"Sapienza" Università di Roma

Scuola di Ingegneria Aerospaziale

DOTTORATO DI RICERCA XXIII CICLO

Tesi di Dottorato

Design of Microwave Absorbing Structure and Microwave Shielding Structure by using Composite Materials, Nanomaterials and Evolutionary Computation

Anno Accademico 2010 / 2011

Dottorando: Ing. Davide Micheli

Tutor: Dr. Gabriele Gradoni

Supervisore: Prof. Mario Marchetti

This page intentionally left blank

Prefazione

Questa tesi raccoglie il lavoro di tre anni di ricerche e studi nel settore dei nanomateriali, nanostrutture ed in generale dei compositi avanzati effettuati presso la Scuola di Ingegneria Aerospaziale della "Sapienza" Università di Roma.
In particolare lo scopo è stato quello di approfondire l'interazione tra campi elettromagnetici ed alcune tipologie di compositi avanzati basati essenzialmente su strutture in carbonio e nanomateriali. Questo tentativo ha richiesto un approccio multidisciplinare tra diversi settori scientifici che comprendono quello dei materiali, delle strutture, dei processi di fabbricazione, delle nanotecnologie e dell'elettromagnetismo, i cui concetti di base sono, in questo contesto, dati per acquisiti e per il cui approfondimento si rimanda a testi specifici.
L'obiettivo principale è stato quello di utilizzare queste conoscenze trasversali per progettare e costruire nuovi materiali/strutture in grado di assorbire efficacemente i campi elettromagnetici in un ampio intervallo di frequenze ed angoli d'incidenza con molteplici applicazioni anche se l'ambito su cui si è lavorato è quello aerospaziale.
Per ottimizzare questi materiali/strutture si è fatto ricorso all'utilizzazione di algoritmi evoluzionistici che sono entrati a pieno titolo nello studio multidisciplinare con uno stretto collegamento tra la teoria sviluppata e le prove di laboratorio atte a validare sperimentalmente i modelli matematici proposti.

Un ringraziamento particolare è rivolto al Prof. Mario Marchetti che in modo lungimirante ha proposto questo tema di studio.

Davide Micheli

This page intentionally left blank

Contents and Subject Index

This page intentionally left blank

Acronyms

CNFs	Carbon Nanofibers
CNTs	Carbon Nanotubes
DB	Data Base
DSEM	Directional Shielding Effectiveness Measurements
EM	Electromagnetic
EMC	Electromagnetic Compatibility
EMI	Electromagnetic Interference
GA	Genetic Algorithm
MSS	Microwave Shielding Structure
MUT	Material Under Test
MWCNTs	Multi Wall Carbon Nanotubes
NRL	Naval Research Laboratory
OF	Objective Function
PEC	Perfect Electric Conductor
PSO	Particle Swarm Optimization
RAM	Radar Absorbing Material
RAS	Radar Absorbing Structure
RC	Reflection Coefficient
SEM	Scanning Electron Microscope
TC	Transmission Coefficient
TE	Transversal Electric
TEM	Transversal Electric and Magnetic
TEM	Transmission Electron Microscope
TM	Transversal Magnetic
XRD	X-Ray Diffraction
WPO	Winning Particle Optimization

This page intentionally left blank

Introduction

This Thesis is focused on scientific research on composite materials electromagnetic characterization and electric conductive polymers applications. Mainly two different composite materials types are taken into account, those based on epoxy-resin and those achieved through pyrolisis of a phenolic-resin more often known as Carbon-Carbon.

The use of such structures is relevant in aerospace/aeronautics, for electromagnetic (EM) protection from natural phenomena (lightning), and intentional interference with radar absorbing materials (RAM), in nuclear physics, for nuclear EM pulses (NEMP) protection, in electromagnetic compatibility (EMC), for equipment-level shielding, high-intensity radiated fields (HIRF) protection, anechoic chambers (for the realizations of wedges and pyramidal arrays), and human exposure mitigation.

In order to modulate the electromagnetic characteristics, like electrical conductivity and microwave absorbing capability, the epoxy-resin composite materials taken into account, are reinforced using carbon nanomaterials in different weight percentage.

The microwave absorbing capability of these fancy materials is analyzed, and numerical design of wide frequency band microwave absorbing structures and microwave shielding structures are presented and discussed in details in terms of both microwave reflection loss and transmission attenuation i.e., shielding effectiveness.

In this Thesis, different branches of research field are applied: nanotechnology, electromagnetic wave propagation theory, composite materials manufacturing, evolutionary computation, and all of them are used to design the “quasi perfect absorber” from electromagnetic point of view.

Traditional composites are loaded by graphene/graphite micrometric mixtures. In this work, we propose an inhomogeneous multilayer absorber made of micrometric graphite (at different wt%), and nanometric carbon particles (SWCNTs, MWCNTs, CNFs, at different wt%). Thus, an improvement of the traditional absorbers has been achieved upon optimization through an in-house genetic algorithm (GA), Particle swarm Optimization (PSO), and winning particle optimization (WPO), this last appositely developed.

Main goal of the work is to achieve lower values (< -10 dB) of both reflection and transmission coefficients for angular apertures within 40°.
The evolutionary computation codes are flexible in the selection of the algorithm parameters such as frequency band, incidence angular range, overall maximum multilayer thickness, possibility to decide if the design optimization procedure must privilege thickness minimization and/or losses maximization. With respect to the present literature, the developed method considers the absorbing capability taking into account both the reflection and the transmission properties of the entire multilayer structure. Moreover, the absorbing properties of the multilayer structures have been analyzed considering oblique incidence at fixed angles within a finite range.

This work is organized into six main chapters.

Chapter 1 describes electromagnetic theory of plane multilayer structures made of lossy materials. Electromagnetic theory about propagation in no-lossy and lossy materials is also discussed using examples to clarify concepts. Reflection and Transmission Coefficients are discussed, oblique incidence and Snell's law, Transverse Impedance, Brewster angle and Critical Angle, Complex Waves, Zenneck Waves, are introduced. At the end, Surface Plasmons are analyzed and simulated using genetic algorithm.

Chapter 2 describes composite materials manufacturing, chemical/physical analysis, and problems in manufacturing large tiles of composite materials. Composite materials considered here are based on epoxy matrix reinforced with several species of filler in particular carbon nanomaterials are considered. These latter have been chosen taking into account the lowest market prices: the economic aspects, normally neglected in small laboratory applications, are on the contrary important in real applications where the amount of carbon nanopowders could be relatively high. In such scenario a good compromise in terms of cost/performances has been obtained using industrial grade multiwall carbon nanotubes (MWCNTs, about 300 $/kg), graphite micropowder (about 40 $/kg), and carbon nanofibers (CNFs, about 30 $/g).

As far as composite materials manufacturing is concerned, the main problem discussed is nanopowders dispersion in relatively high weight percentages within the epoxy-matrix. In fact, microwave absorption properties of the composites are definitively compromised if dispersion is not good enough.

Chapter 3 is related to the electromagnetic characterization of composite materials used to build microwave absorbing and shielding structures.
The electromagnetic characterization of composite materials consists in determining the dielectric properties like electrical permittivity, which in turns can be used in order to compute microwave electrical conductivity, skin depth penetration, etc. Several measuring methods are possible: wave guide, coaxial line, free space antennas, resonant cavities, and so on. In this work, the wave guide method has been adopted: the reason for such choice is due to the problems intrinsically existing with other methods where mechanical machining of composite materials is required, thus affecting the final dielectric permittivity values determination. Meanings of microwave scattering parameters, electrical conductivity, and permittivity are discussed. Main algorithms used to convert values of scattering parameters measured by Vector Network Analyzer into permittivity are shown.

Chapter 4 deals with the algorithms adopted for the numerical design of microwave absorbing and shielding structures.
In order to modeling absorbing structures where the microwave absorbing performances are the best obtainable in a wider frequency band and for all possible microwave incidence angles, transmissions line equations have been applied to multilayer structures. Here in particular each layer can assume the dielectric properties of one particular composite material in the data base composed by all composite materials electromagnetically characterized. In such model, the number and the thickness of each layer determine the entire multilayer structure electromagnetic wave absorbing properties.
Frequency band considered is in the range 5-18 GHz. Two main design scenarios have been considered, the first classically called radar absorbing material (RAM) where the multilayer structure is supposed baked with a perfect electric conductor (PEC), the second baptized microwave shielding structure (MSS) where at the end of

multilayer structure there are again free space conditions for microwave propagation. Such last scenario is useful in application where the composite material posses also mechanical structural properties and is used in place of metal structure (aircraft structure applications).
Since the absorber's overall thickness is sometimes an important constraint in the design process, then the design and optimization algorithms are capable to take into account simultaneously for both, i.e., electromagnetic performances and overall thickness of the multilayer structure. For such kind of problems, evolutionary computation represents a promising method, assuring at the same time good global performances and reasonable computation time. In this work, a new algorithm called winning particle optimization (WPO) is presented and applied. In order to check the soundness of WPO results, an in-house built genetic algorithm (GA) and Particle Swarm Optimization (PSO) are presented and applied too, and final results compared.

Chapter 5 presents the experimental validation of the developed electromagnetic absorbing and shielding mathematical theoretical model. Validation is obtained comparing measurements and simulations of reflection loss (RL), and shielding effectiveness of some realized microwave absorbing and shielding structures based on carbon nanostructured composite materials. Measurements of (RL) in free space using NRL Arch technique are performed on large RAM multilayer structure tiles obtained by numerical design and optimization process.
Measurements of shielding effectiveness in free space using directional shielding effectiveness measurement (DSEM), developed by us and Università Politecnica delle Marche (Dipartimento di Elettromagnetismo e Bioingegneria), are performed on materials and multilayer structures obtained by numerical design and optimization techniques presented. All the cited equipments i.e., NRL arch system, DSEM system, sample holders system, have been appositely in-house manufactured.

Chapter 6, is focused on carbon-carbon (CC) composite materials. Electromagnetic characterization is shown and electrical conductivity, absorbing and shielding properties discussed. NRL arch and DSEM measurements are presented and analyzed. Due to high electrical conductivity of CC, measurements using wave-guide

methods do not permit us to determine the absorption and electrical conductivity properties in a precise way. Then a microwave wave-guide has been built using CC, and the attenuation of microwave signal measured using vector network analyzer.
Using the measured attenuation values, the electrical conductivity of CC has been computed.

This page intentionally left blank

Chapter 1

Electromagnetic wave planes propagation in lossy multilayer structure

1.1 Reflection Coefficient and Transmission coefficient for electromagnetic normal wave plane propagation in a multilayer structure

In this chapter, the electromagnetic model of multilayer structure is analyzed starting from Maxwell's equations. Matrix formalism is adopted and final reflection coefficient and transmission coefficient of multilayer structure is obtained.
Important analysis concerning oblique incidence in lossy material and plasmonic resonance in metamaterials is discussed, this last obtained by an in-house built genetic algorithm able to optimize a single layer structure and to find the best values of permittivity and permeability of metamaterial able to generate surface Plasmon.

All sections reported in this chapter are investigated because useful to understand the phenomena taking place when an electromagnetic field acts through a lossy multilayer structure made of dielectric materials.

Chapter 1 stars with the electromagnetic theory of multilayer plane.

Let us to consider a multilayer system like in Fig. 1.1.1, where $n_m = \sqrt{\mu_0 \varepsilon_0}\sqrt{\mu_{rm} \varepsilon_{rm}}$ is the refraction index of generic *m*-th layer and $\eta_m = \sqrt{\frac{\mu_0}{\varepsilon_0}}\sqrt{\frac{\mu_{rm}}{\varepsilon_{rm}}}$ is the intrinsic wave impedance of the generic *m*-th layer, E_m^+ is the transmitted electric field and E_m^- is the reflected electric field within the generic *m*-th layer, $d_m = z_m - z_{m-1}$ is the thickness of the generic *m*-th layer [1].
The wave number of generic *m*-th layer $\mathbf{k}_m = \omega\sqrt{\mu_0 \varepsilon_0}\sqrt{\mu_{rm} \varepsilon_{rm}}$ depends on dielectric characteristics of materials and by the angular frequency ω. In particular as will be shown later, it is a vector whose components are in the *x* and *z* axes. Usually in most scenarios, only the component along *z* axes are taken into account and the vector became a scalar quantity.

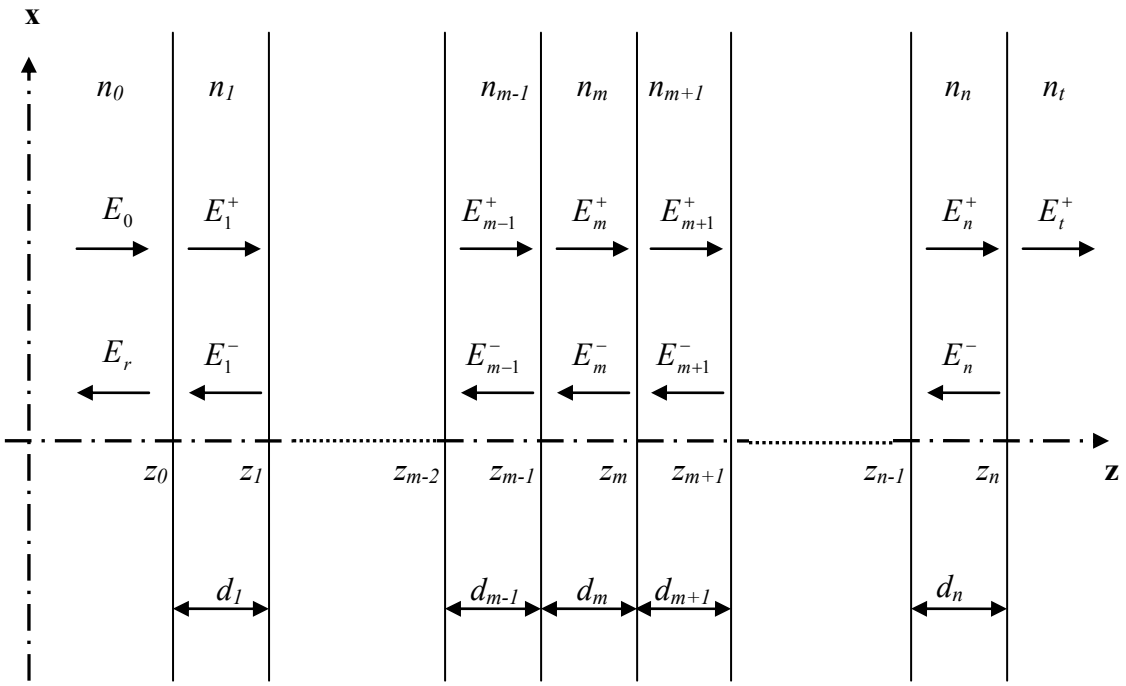

Fig. (1.1.1). Multilayer system

Considering now the interface between m and $m+1$ layers; the boundary conditions which explicit the continuity of the tangential components for electric and magnetic fields can be written as follows

$$\begin{cases} E_m^+ e^{-jk_m z_m} + E_m^- e^{+jk_m z_m} = E_{m+1}^+ e^{-jk_{m+1} z_m} + E_{m+1}^- e^{+jk_{m+1} z_m} \\ H_m^+ e^{-jk_m z_m} - H_m^- e^{+jk_m z_m} = H_{m+1}^+ e^{-jk_{m+1} z_m} - H_{m+1}^- e^{+jk_{m+1} z_m} \end{cases}$$

(1.1.0)

Using the intrinsic wave impedance definition, we can rewrite the equations (1.1.0) as

$$E_m^+ e^{-jk_m z_m} + E_m^- e^{+jk_m z_m} = E_{m+1}^+ e^{-jk_{m+1} z_m} + E_{m+1}^- e^{+jk_{m+1} z_m}$$

(1.1.1)

$$\frac{E_m^+}{\eta_m} e^{-jk_m z_m} - \frac{E_m^-}{\eta_m} e^{+jk_m z_m} = \frac{E_{m+1}^+}{\eta_{m+1}} e^{-jk_{m+1} z_m} - \frac{E_{m+1}^-}{\eta_{m+1}} e^{+jk_{m+1} z_m}$$

(1.1.2)

The (1.1.2) can be rewritten as

$$\frac{\eta_{m+1}}{\eta_m}E_m^+e^{-jk_mz_m}-\frac{\eta_{m+1}}{\eta_m}E_m^-e^{+jk_mz_m}=E_{m+1}^+e^{-jk_{m+1}z_m}-E_{m+1}^-e^{+jk_{m+1}z_m}$$

(1.1.3)

Now summing and subtracting the (1.1.1) and (1.1.3) member to member, we have

$$\left(1+\frac{\eta_{m+1}}{\eta_m}\right)E_m^+e^{-jk_mz_m}+\left(1-\frac{\eta_{m+1}}{\eta_m}\right)E_m^-e^{+jk_mz_m}=2E_{m+1}^+e^{-jk_{m+1}z_m}$$

(1.1.4)

$$\left(1-\frac{\eta_{m+1}}{\eta_m}\right)E_m^+e^{-jk_mz_m}+\left(1+\frac{\eta_{m+1}}{\eta_m}\right)E_m^-e^{+jk_mz_m}=2E_{m+1}^-e^{+jk_{m+1}z_m}$$

(1.1.5)

Then the relation between the fields in the medium $m+1$ and m are:

$$\frac{1}{2}\left(1+\frac{\eta_{m+1}}{\eta_m}\right)E_m^+e^{-jk_mz_m}+\frac{1}{2}\left(1-\frac{\eta_{m+1}}{\eta_m}\right)E_m^-e^{+jk_mz_m}=E_{m+1}^+e^{-jk_{m+1}z_m}$$

(1.1.6)

$$\frac{1}{2}\left(1-\frac{\eta_{m+1}}{\eta_m}\right)E_m^+e^{-jk_mz_m}+\frac{1}{2}\left(1+\frac{\eta_{m+1}}{\eta_m}\right)E_m^-e^{+jk_mz_m}=E_{m+1}^-e^{+jk_{m+1}z_m}$$

(1.1.7)

Where m is an integer number within the closed interval $[0,n]$.

The equations (1.1.6), (1.1.7) can be rewritten in the matrix form:

$$\begin{bmatrix} E_{m+1}^{+}e^{-jk_{m+1}z_m} \\ E_{m+1}^{-}e^{+jk_{m+1}z_m} \end{bmatrix} = \frac{1}{2}\left(1+\frac{\eta_{m+1}}{\eta_m}\right)\cdot\begin{bmatrix} 1 & \dfrac{\left(1-\frac{\eta_{m+1}}{\eta_m}\right)}{\left(1+\frac{\eta_{m+1}}{\eta_m}\right)} \\ \dfrac{\left(1-\frac{\eta_{m+1}}{\eta_m}\right)}{\left(1+\frac{\eta_{m+1}}{\eta_m}\right)} & 1 \end{bmatrix}\cdot\begin{bmatrix} E_m^{+}e^{-jk_m z_m} \\ E_m^{-}e^{+jk_m z_m} \end{bmatrix}$$

(1.1.8)

Calling:

$$R_{(m+1),m} = \frac{\left(1-\frac{\eta_{m+1}}{\eta_m}\right)}{\left(1+\frac{\eta_{m+1}}{\eta_m}\right)} = \frac{\left(\frac{\eta_m-\eta_{m+1}}{\eta_m}\right)}{\left(\frac{\eta_m+\eta_{m+1}}{\eta_m}\right)} = \frac{\eta_m-\eta_{m+1}}{\eta_m+\eta_{m+1}}$$

(1.1.9)

We have:

$$\begin{bmatrix} E_{m+1}^{+}e^{-jk_{m+1}z_m} \\ E_{m+1}^{-}e^{+jk_{m+1}z_m} \end{bmatrix} = \frac{1}{2}\left(1+\frac{\eta_{m+1}}{\eta_m}\right)\cdot\begin{bmatrix} 1 & R_{(m+1),m} \\ R_{(m+1),m} & 1 \end{bmatrix}\cdot\begin{bmatrix} E_m^{+}e^{-jk_m z_m} \\ E_m^{-}e^{+jk_m z_m} \end{bmatrix}.$$

(1.1.10)

Now let us to consider the interface separating the last two regions, $t=n+1$ and n. Posing $m=n$ in the equation (1.1.10), we obtain the relation between the electric field in t and n medium:

$$\begin{bmatrix} E_t^{+}e^{-jk_t z_n} \\ E_t^{-}e^{+jk_{t1}z_n} \end{bmatrix} = \frac{1}{2}\left(1+\frac{\eta_t}{\eta_n}\right)\cdot\begin{bmatrix} 1 & R_{t,n} \\ R_{t,n} & 1 \end{bmatrix}\cdot\begin{bmatrix} E_n^{+}e^{-jk_n z_n} \\ E_n^{-}e^{+jk_n z_n} \end{bmatrix},$$

(1.1.11)

In the medium $t=n+1$, the reflected electric field is zero, i.e., $E_t^{-}=0$ while $E_t^{+}=E_t$.

$$\begin{bmatrix} E_t^{+}e^{-jk_t z_n} \\ 0 \end{bmatrix} = \frac{1}{2}\left(1-\frac{\eta_t}{\eta_n}\right)\begin{bmatrix} 1 & R_{t,n} \\ R_{t,n} & 1 \end{bmatrix}\begin{bmatrix} E_n^{+}e^{-jk_n z_n} \\ E_n^{-}e^{+jk_n z_n} \end{bmatrix},$$

(1.1.12)

Now calling the quantity:

$$\overline{\overline{V_{t,n}}} = \frac{1}{2}\left(1-\frac{\eta_t}{\eta_n}\right)\begin{bmatrix} 1 & R_{t,n} \\ R_{t,n} & 1 \end{bmatrix},$$

(1.1.13)

We have:

$$\begin{bmatrix} E_t^+ e^{-jk_t z_n} \\ 0 \end{bmatrix} = \overline{\overline{V_{t,n}}} \begin{bmatrix} E_n^+ e^{-jk_n z_n} \\ E_n^- e^{+jk_n z_n} \end{bmatrix}.$$

(1.1.14)

The above equation relate the field in the last two layers; now since we are interested in relating the field transmitted in the last medium *t,* and the field forward in the first medium of the multilayer structure, we need a recursive relation capable to take into account for the fields into the intermediate layers.

To obtain such relationship we can multiply each term of equation (1.1.6) for the quantity (1.1.15)

$$e^{-jk_{m+1}(z_{m+1}-z_m)}$$

(1.1.15)

i.e.,

$$\frac{1}{2}\left(1+\frac{\eta_{m+1}}{\eta_m}\right)E_m^+ e^{-jk_m z_m} e^{-jk_{m+1}(z_{m+1}-z_m)} + \frac{1}{2}\left(1-\frac{\eta_{m+1}}{\eta_m}\right)E_m^- e^{+jk_m z_m} e^{-jk_{m+1}(z_{m+1}-z_m)} =$$
$$= E_{m+1}^+ e^{-jk_{m+1} z_m} e^{-jk_{m+1}(z_{m+1}-z_m)}$$

obtaining

$$\frac{1}{2}\left(1+\frac{\eta_{m+1}}{\eta_m}\right)E_m^+ e^{-jk_m z_m} e^{-jk_{m+1}(z_{m+1}-z_m)} + \frac{1}{2}\left(1-\frac{\eta_{m+1}}{\eta_m}\right)E_m^- e^{+jk_m z_m} e^{-jk_{m+1}(z_{m+1}-z_m)} =$$
$$= E_{m+1}^+ e^{-jk_{m+1} z_{m+1}}$$

(1.1.16)

and each term of equation (1.1.7) for the quantity (1.1.17)

$$e^{+jk_{m+1}(z_{m+1}-z_m)}$$

(1.1.17)

i.e.,

$$\frac{1}{2}\left(1-\frac{\eta_{m+1}}{\eta_m}\right)E_m^+e^{-jk_mz_m}e^{+jk_{m+1}(z_{m+1}-z_m)}+\frac{1}{2}\left(1+\frac{\eta_{m+1}}{\eta_m}\right)E_m^-e^{+jk_mz_m}e^{+jk_{m+1}(z_{m+1}-z_m)}=$$
$$=E_{m+1}^-e^{+jk_{m+1}z_m}e^{+jk_{m+1}(z_{m+1}-z_m)}$$

obtaining

$$\frac{1}{2}\left(1-\frac{\eta_{m+1}}{\eta_m}\right)E_m^+e^{-jk_mz_m}e^{+jk_{m+1}(z_{m+1}-z_m)}+\frac{1}{2}\left(1+\frac{\eta_{m+1}}{\eta_m}\right)E_m^-e^{+jk_mz_m}e^{+jk_{m+1}(z_{m+1}-z_m)}=$$
$$=E_{m+1}^-e^{+jk_{m+1}z_{m+1}}$$

(1.1.18)

Equations (1.1.16), (1.1.18), will be used in order to relate the field in the intermediate layers up to arrive to the starting medium where it is propagating the forward wave i.e., $0\le m\le n-1$.

In matrix form, we have:

$$\begin{bmatrix}E_{m+1}^+e^{-jk_{m+1}z_{m+1}}\\E_{m+1}^-e^{+jk_{m+1}z_{m+1}}\end{bmatrix}=\overline{\overline{V_{(m+1),m}}}\cdot\begin{bmatrix}E_m^+e^{-jk_mz_m}\\E_m^-e^{+jk_mz_m}\end{bmatrix},$$

(1.1.19)

where we have called:

$$\overline{\overline{V_{(m+1),m}}}=\frac{1}{2}\left(1+\frac{\eta_{m+1}}{\eta_m}\right)\begin{bmatrix}e^{-jk_{m+1}(z_{m+1}-z_m)} & \dfrac{\left(1-\frac{\eta_{m+1}}{\eta_m}\right)}{\left(1+\frac{\eta_{m+1}}{\eta_m}\right)}e^{-jk_{m+1}(z_{m+1}-z_m)}\\ \dfrac{\left(1-\frac{\eta_{m+1}}{\eta_m}\right)}{\left(1+\frac{\eta_{m+1}}{\eta_m}\right)}e^{+jk_{m+1}(z_{m+1}-z_m)} & e^{+jk_{m+1}(z_{m+1}-z_m)}\end{bmatrix}$$

(1.1.20)

Now calling the quantity within the matrix as before:

$$R_{(m+1),m} = \frac{\left(1 - \frac{\eta_{m+1}}{\eta_m}\right)}{\left(1 + \frac{\eta_{m+1}}{\eta_m}\right)} = \frac{\eta_m - \eta_{m+1}}{\eta_m + \eta_{m+1}}$$

(1.1.21)

we obtain:

$$\overline{\overline{V_{(m+1),m}}} = \frac{1}{2}\left(1 + \frac{\eta_{m+1}}{\eta_m}\right)\begin{bmatrix} e^{-jk_{m+1}(z_{m+1}-z_m)} & R_{(m+1),m}e^{-jk_{m+1}(z_{m+1}-z_m)} \\ R_{(m+1),m}e^{+jk_{m+1}(z_{m+1}-z_m)} & e^{+jk_{m+1}(z_{m+1}-z_m)} \end{bmatrix}$$

(1.1.22)

From equation (1.1.22) we are finally able to write the relationship between first and last layer, and as a consequence the transmitted electromagnetic field into last *t* medium, is related to the impinging electromagnetic field forward to first layer as in following equation:

$$\begin{bmatrix} E_t^+ e^{-jk_t z_n} \\ 0 \end{bmatrix} = \overline{\overline{V_{t,0}}} \cdot \begin{bmatrix} E_0 \\ E_r \end{bmatrix}$$

(1.1.23)

where

$$\overline{\overline{V_{t,0}}} = \overline{\overline{V_{t,n}}} \cdot \overline{\overline{V_{n,n-1}}} \cdot \overline{\overline{V_{n,n-2}}} \cdots\cdots\cdots \overline{\overline{V_{1,0}}}$$

(1.1.24)

Matrix equation (1.1.23) represents a system of two equations in two unknown solutions: $E_t^+ = E_t$ i.e., the amplitude of transmitted field and E_r i.e., the amplitude of reflected field, as a function of the forward electric field E_0. As a consequence it is possible to obtain the reflection coefficient *RC* and the transmission coefficient *TC*.

$$RC = \frac{|E_r|^2}{|E_0|^2}$$

(1.1.25)

$$TC = \frac{n_t}{n_0}\frac{|E_t|^2}{|E_0|^2} = \frac{\sqrt{\frac{\mu_0}{\varepsilon_0}}}{\eta_t}\mu_{rt}\frac{|E_t|^2}{|E_0|^2} = \frac{\mu_{rt}}{\mu_{r0}}\frac{\eta_0}{\eta_t}\frac{|E_t|^2}{|E_0|^2}$$

$$\frac{\sqrt{\frac{\mu_0}{\varepsilon_0}}}{\eta_0}\mu_{r0}$$

(1.1.26)

Where:

μ_{rt} is the relative part of the magnetic permeability of layer *t*

μ_{r0} is the relative part of the magnetic permeability of free space

ε_{rt} is the relative part of the electric permittivity of layer *t*

ε_{r0} is the relative part of the electric permittivity of free space

$\eta_t = \sqrt{\frac{\mu_0}{\varepsilon_0}}\sqrt{\frac{\mu_{rt}}{\varepsilon_{rt}}}$ is the intrinsic wave impedance of layer *t*

$\eta_0 = \sqrt{\frac{\mu_0}{\varepsilon_0}}\sqrt{\frac{\mu_{r0}}{\varepsilon_{r0}}} = \sqrt{\frac{\mu_0}{\varepsilon_0}} \cong 377$ ohm, where $\mu_{r0} = \varepsilon_{r0} = 1,$

$\mu_0 = 4\pi \cdot 10^7$ henry/metro

$\varepsilon_0 = 8.854 \cdot 10^{-12}$ farad/metro

η_0 is the intrinsic wave impedance of free space, which is supposed to be the initial medium where the electromagnetic wave is propagating before impinging on materials.

$n_t = \sqrt{\mu_{rt}\varepsilon_{rt}}$ is the refraction index of the *t*-layer

$n_0 = \sqrt{\mu_{r0}\varepsilon_{r0}} = 1$ is the refraction index of the free space, supposing that initial medium is free space.

In equation (1.1.26) we used the relationship between wave impedance η and refraction index n:

$$\eta = \sqrt{\frac{\mu_0}{\varepsilon_0}}\sqrt{\frac{\mu_r}{\varepsilon_r}} = \sqrt{\frac{\mu_0}{\varepsilon_0}}\sqrt{\frac{\mu_r}{\varepsilon_r}}\sqrt{\frac{\mu_r}{\mu_r}} = \sqrt{\frac{\mu_0}{\varepsilon_0}}\frac{\mu_r}{\sqrt{\mu_r\varepsilon_r}} = \eta_0\frac{\mu_r}{\sqrt{\mu_r\varepsilon_r}} = \eta_0\frac{\mu_r}{n}.$$

(1.1.27)

Now in order to write the expression of *RC* and *TC*, as a function of the electric field, we use the equation (1.1.23):

$$\begin{bmatrix} E_t^+ e^{-jk_t z_n} \\ 0 \end{bmatrix} = \overline{\overline{V_{t,0}}} \cdot \begin{bmatrix} E_0 \\ E_r \end{bmatrix} \Rightarrow \begin{bmatrix} E_t^+ e^{-jk_t z_n} \\ 0 \end{bmatrix} = \begin{bmatrix} V_{t,0}(1,1) & V_{t,0}(1,2) \\ V_{t,0}(2,1) & V_{t,0}(2,2) \end{bmatrix} \cdot \begin{bmatrix} E_0 \\ E_r \end{bmatrix}$$

(1.1.28)

We can rewrite the equation above as:

$$E_t^+ e^{-jk_t z_n} = V_{t,0}(1,1)E_0 + V_{t,0}(1,2)E_r$$

(1.1.29)

$$0 = V_{t,0}(2,1)E_0 + V_{t,0}(2,2)E_r .$$

(1.1.30)

From equation (1.1.30) we have:

$$E_r = -\frac{V_{t,0}(2,1)}{V_{t,0}(2,2)} E_0$$

(1.1.31)

From equation (1.31) we obtain the expression for the reflection coefficient *RC*:

$$\boxed{RC = \frac{|E_r|^2}{|E_0|^2} = \frac{|V_{t,0}(2,1)|^2}{|V_{t,0}(2,2)|^2}}$$

(1.1.32)

$$\boxed{RC(dB) = 10Log_{10}\frac{|E_r|^2}{|E_0|^2} = 10Log_{10}\frac{|V_{t,0}(2,1)|^2}{|V_{t,0}(2,2)|^2} = 20Log_{10}\frac{|V_{t,0}(2,1)|}{|V_{t,0}(2,2)|}}.$$

(1.1.33)

Substituting the expression of E_r, i.e., equation (1.1.31), in equation (1.1.29) it follows;

$$E_t^+ e^{-jk_t z_n} = V_{t,0}(1,1)E_0 - V_{t,0}(1,2)\frac{V_{t,0}(2,1)}{V_{t,0}(2,2)}E_0$$

(1.1.34)

$$E_t = e^{+jk_t z_n}\left(V_{t,0}(1,1) - V_{t,0}(1,2)\frac{V_{t,0}(2,1)}{V_{t,0}(2,2)}\right)E_0$$

(1.1.35)

$$\left|E_t\right| = \left|e^{+jk_t z_n}\right| \cdot \left|\left(V_{t,0}(1,1) - V_{t,0}(1,2)\frac{V_{t,0}(2,1)}{V_{t,0}(2,2)}\right)\right| \cdot \left|E_0\right|$$

(1.1.36)

$$\left|E_t\right|^2 = 1 \cdot \left|\left(V_{t,0}(1,1) - V_{t,0}(1,2)\frac{V_{t,0}(2,1)}{V_{t,0}(2,2)}\right)\right|^2 \cdot \left|E_0\right|^2$$

(1.1.37)

$$\frac{\left|E_t\right|^2}{\left|E_0\right|^2} = \left|\left(V_{t,0}(1,1) - V_{t,0}(1,2)\frac{V_{t,0}(2,1)}{V_{t,0}(2,2)}\right)\right|^2$$

(1.1.38)

Now from complex number theory we know that:

if

$A = (a + jb)$

$B = (c + jd)$

then

$$\begin{aligned}
&|A-B|^2 = |(a+jb)-(c+jd)|^2 = \Re[(a+jb)-(c+jd)][(a-jb)-(c-jd)] = \\
&= [(a+jb)(a-jb)-(a+jb)(c-jd)-(c+jd)(a-jb)+(c+jd)(c-jd)] = \\
&= [(a+jb)(a-jb)-(a+jb)(c-jd)-(c+jd)(a-jb)+(c+jd)(c-jd)] = \\
&= \left[a^2+b^2-(ac-jad+jbc+bd)-(ac-jbc+jad+bd)+c^2+d^2\right] = \\
&= \left[a^2+b^2-2(ac+bd)+c^2+d^2\right] = \\
&= \Re\left[AA^* - (AB^*+BA^*)+BB^*\right] = \\
&= \Re\left[AA^* - 2AB^*+BB^*\right] = \\
&= \left[AA^* - 2\Re(AB^*)+BB^*\right]
\end{aligned}$$

(1.1.39)

As a consequence, it follows:

$$\frac{|E_t|^2}{|E_0|^2} = \left(V_{t,0}(1,1) - V_{t,0}(1,2)\frac{V_{t,0}(2,1)}{V_{t,0}(2,2)} \right)\left(V_{t,0}^*(1,1) - V_{t,0}^*(1,2)\frac{V_{t,0}^*(2,1)}{V_{t,0}^*(2,2)} \right) =$$

$$= \left[V_{t,0}(1,1)V_{t,0}^*(1,1) - 2\Re\left(V_{t,0}(1,1)V_{t,0}^*(1,2)\frac{V_{t,0}^*(2,1)}{V_{t,0}^*(2,2)} \right) + V_{t,0}(1,2)\frac{V_{t,0}(2,1)}{V_{t,0}(2,2)}V_{t,0}^*(1,2)\frac{V_{t,0}^*(2,1)}{V_{t,0}^*(2,2)} \right] =$$

$$= \left[|V_{t,0}(1,1)|^2 - 2\Re\left(V_{t,0}(1,1)V_{t,0}^*(1,2)\frac{V_{t,0}^*(2,1)}{V_{t,0}^*(2,2)} \right) + \frac{|V_{t,0}(1,2)|^2 |V_{t,0}(2,1)|^2}{|V_{t,0}(2,2)^2|} \right].$$

(1.1.40)

Substituting equation (1.1.40) in equation (1.1.26) we obtain the transmission coefficient for a multilayer structure:

$$TC = \frac{n_t}{n_0}\frac{|E_t|^2}{|E_0|^2} = \frac{n_t}{n_0}\left[|V_{t,0}(1,1)|^2 - 2\Re\left(V_{t,0}(1,1)V_{t,0}^*(1,2)\frac{V_{t,0}^*(2,1)}{V_{t,0}^*(2,2)} \right) + \frac{|V_{t,0}(1,2)|^2 |V_{t,0}(2,1)|^2}{|V_{t,0}(2,2)^2|} \right] =$$

$$= \frac{\mu_{rt}}{\mu_{r0}}\frac{\eta_0}{\eta_t}\frac{|E_t|^2}{|E_0|^2} = \frac{\mu_{rt}}{\mu_{r0}}\frac{\eta_0}{\eta_t}\left[|V_{t,0}(1,1)|^2 - 2\Re\left(V_{t,0}(1,1)V_{t,0}^*(1,2)\frac{V_{t,0}^*(2,1)}{V_{t,0}^*(2,2)} \right) + \frac{|V_{t,0}(1,2)|^2 |V_{t,0}(2,1)|^2}{|V_{t,0}(2,2)^2|} \right]$$

(1.1.41)

$$TC(dB) = 10Log_{10}\left\{ \frac{\mu_{rt}}{\mu_{r0}}\frac{\eta_0}{\eta_t}\left[|V_{t,0}(1,1)|^2 - 2\Re\left(V_{t,0}(1,1)V_{t,0}^*(1,2)\frac{V_{t,0}^*(2,1)}{V_{t,0}^*(2,2)} \right) + \frac{|V_{t,0}(1,2)|^2 |V_{t,0}(2,1)|^2}{|V_{t,0}(2,2)^2|} \right] \right\}$$

(1.1.42)

In the case of oblique incidence in lossy media, η_t and μ_{rt} could be complex numbers. In such scenario *TC* become complex too and hence in order to avoid complex *TC* we should consider the absolute value of $\frac{\mu_{rt}}{\mu_{r0}}\frac{\eta_0}{\eta_t}$.

1.2 Reflection and Transmission coefficient related to scattering parameters

Let us to consider the structure depicted in Fig.(1.2.1) [3], composed of different materials where the last and first layers are supposed infinite in length. Suppose the:

T_{21} the transmission coefficient from layer 1 to layer 2;

T_{12} the transmission coefficient from layer 2 to layer 1;

T_{32} the transmission coefficient from layer 2 to layer 3;

T_{23} the transmission coefficient from layer 3 to layer 2;

Γ_{12} the reflection coefficient from layer 1 to layer 2;

Γ_{21} the reflection coefficient from layer 2 to layer 1;

Γ_{23} the reflection coefficient from layer 2 to layer 3;

Γ_{32} the reflection coefficient from layer 3 to layer 2; this last is zero since we suppose layer 3 of infinite length;

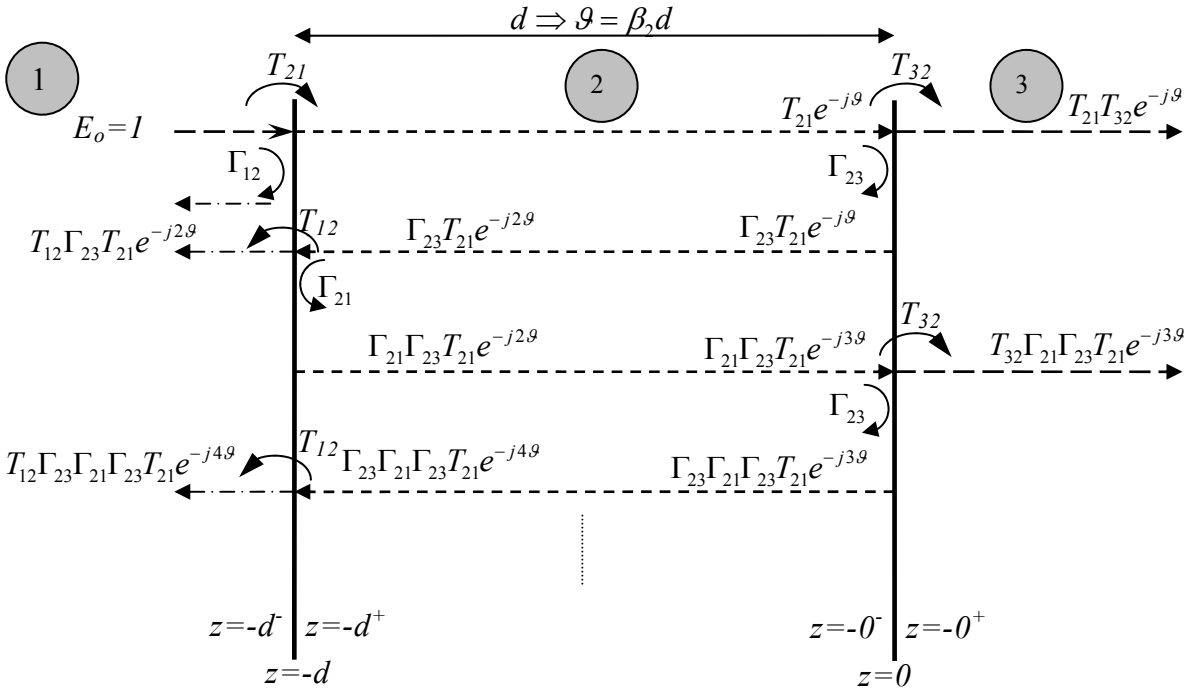

Fig. (1.2.1). Reflection and Transmission coefficient related to scattering parameters

Now we can write the total reflection coefficient at $z=-d^-$ as the contribution of all reflected waves. We suppose the medium linear and exactly symmetrical from transmission and reflection at both faces:

$$\Gamma_{(z=-d)} = \Gamma_{12} + T_{12}\Gamma_{23}T_{21}e^{-j2\vartheta} + T_{12}\Gamma_{23}\Gamma_{21}\Gamma_{23}T_{21}e^{-j4\vartheta} + \ldots\ldots\ldots =$$
$$\Gamma_{(z=-d)} = \Gamma_{12} + T_{12}T_{21}\Gamma_{23}e^{-j2\vartheta} + T_{12}T_{21}\Gamma_{23}^2\Gamma_{21}e^{-j4\vartheta} + \ldots\ldots\ldots =$$
$$\Gamma_{(z=-d)} = \Gamma_{12} + T_{12}T_{21}\Gamma_{23}\Gamma_{21}^0e^{-j2\vartheta} + T_{12}T_{21}\Gamma_{23}^2\Gamma_{21}^1e^{-j4\vartheta} + \ldots\ldots\ldots = \Gamma_{12} + T_{12}T_{21}\sum_{i=1}^{\infty}\Gamma_{23}^i\Gamma_{21}^{i-1}e^{-j2i\vartheta}$$
$$\Gamma_{(z=-d)} = \Gamma_{12} + \frac{T_{12}T_{21}}{\Gamma_{21}}\sum_{i=1}^{\infty}\Gamma_{23}^i\Gamma_{21}^ie^{-j2i\vartheta} = \Gamma_{12} + \frac{T_{12}T_{21}}{\Gamma_{21}}\sum_{i=1}^{\infty}\left(\Gamma_{23}\Gamma_{21}e^{-j2\vartheta}\right)^i$$

(1.2.1)

Calling $q = \Gamma_{23}\Gamma_{21}e^{-j2\vartheta}$ then if $|q| < 1$ the series converges to:

$$\sum_{i=1}^{\infty}x^i = \frac{1}{1-q} - 1 = \frac{1}{1-\Gamma_{23}\Gamma_{21}e^{-j2\vartheta}} - 1 = \frac{\Gamma_{23}\Gamma_{21}e^{-j2\vartheta}}{1-\Gamma_{23}\Gamma_{21}e^{-j2\vartheta}}$$

(1.2.2)

as a consequence

$$\Gamma_{(z=-d)} = \Gamma_{12} + \frac{T_{12}T_{21}}{\Gamma_{21}}\sum_{i=1}^{\infty}\left(\Gamma_{23}\Gamma_{21}e^{-j2\vartheta}\right)^i = \Gamma_{12} + \frac{T_{12}T_{21}}{\Gamma_{21}}\frac{\Gamma_{23}\Gamma_{21}e^{-j2\vartheta}}{1-\Gamma_{23}\Gamma_{21}e^{-j2\vartheta}} = \Gamma_{12} + \frac{T_{12}T_{21}\Gamma_{23}e^{-j2\vartheta}}{1-\Gamma_{23}\Gamma_{21}e^{-j2\vartheta}}$$

(1.2.3)

Now since we supposed:

$$\Gamma_{21} = -\Gamma_{12}$$
$$T_{12} = 1 + \Gamma_{12}$$
$$T_{21} = 1 + \Gamma_{21} = 1 - \Gamma_{12}$$

(1.2.4)

then substituting in (1.2.3) we have

$$\Gamma_{(z=-d)} = \Gamma_{12} + \frac{T_{12}T_{21}\Gamma_{23}e^{-j2\vartheta}}{1-\Gamma_{23}\Gamma_{21}e^{-j2\vartheta}} = \Gamma_{12} + \frac{(1+\Gamma_{12})(1-\Gamma_{12})\Gamma_{23}e^{-j2\vartheta}}{1+\Gamma_{23}\Gamma_{12}e^{-j2\vartheta}} =$$

$$\Gamma_{(z=-d)} = \frac{\Gamma_{12} + \Gamma_{12}^2\Gamma_{23}e^{-j2\vartheta} + (1-\Gamma_{12}^2)\Gamma_{23}e^{-j2\vartheta}}{1+\Gamma_{23}\Gamma_{12}e^{-j2\vartheta}} =$$

$$\Gamma_{(z=-d)} = \frac{\Gamma_{12} + \Gamma_{12}^2\Gamma_{23}e^{-j2\vartheta} + \Gamma_{23}e^{-j2\vartheta} - \Gamma_{12}^2\Gamma_{23}e^{-j2\vartheta}}{1+\Gamma_{23}\Gamma_{12}e^{-j2\vartheta}} =$$

$$\Gamma_{(z=-d)} = \frac{\Gamma_{12} + \Gamma_{23}e^{-j2\vartheta}}{1+\Gamma_{23}\Gamma_{12}e^{-j2\vartheta}}$$

(1.2.5)

supposing $\Gamma_{12} = -\Gamma_{23}$ i.e., *free space, medium, free space*, then:

$$\boxed{S_{11} = \Gamma_{(z=-d)} = \frac{\Gamma_{12} + \Gamma_{23}e^{-j2\vartheta}}{1+\Gamma_{23}\Gamma_{12}e^{-j2\vartheta}} = \frac{\Gamma_{12} - \Gamma_{12}e^{-j2\vartheta}}{1-\Gamma_{12}^2e^{-j2\vartheta}} = \frac{\Gamma_{12}(1-e^{-j2\vartheta})}{1-\Gamma_{12}^2e^{-j2\vartheta}}}$$

(1.2.6)

where ***S11*** is a scattering parameter we will see later in chapter 3. It is adopted for dielectric characterization of nanostrucutred composite materials, by using wave-guide method and vector network analyzer.

Calling P the propagation factor $\boxed{P = e^{-j\vartheta} = e^{-j\beta_2 d} = e^{-\gamma d}}$ and $\Gamma_{12} = \Gamma$ then we can rewrite:

$$\boxed{S_{11} = \Gamma_{(z=-d)} = \frac{\Gamma(1-P^2)}{1-\Gamma^2P^2}}$$

(1.2.7)

As far as global transmission coefficient is concerned, we have:

$$T_{(z=0^+)} = T_{21}T_{32}e^{-j\vartheta} + T_{32}T_{21}\Gamma_{23}\Gamma_{21}e^{-j3\vartheta} + \Gamma_{21}^2\Gamma_{23}^2T_{21}T_{32}e^{-j5\vartheta} + ...$$

(1.2.8)

$$T_{(z=0^+)} = T_{21}T_{32}\sum_{i=0}^{\infty}\Gamma_{23}^i\Gamma_{21}^ie^{-j(2i+1)\vartheta} = T_{21}T_{32}e^{-j\vartheta}\sum_{i=0}^{\infty}\left(\Gamma_{21}\Gamma_{23}e^{-j2\vartheta}\right)^i$$

(1.2.9)

now due to the geometric series:

$$\sum_{i=0}^{\infty} x^i = \frac{1-x^{i+1}}{1-x} = \frac{1}{1-x} \qquad if \quad |x|<1$$

now since:

$\Gamma_{21} = -\Gamma_{12}$
$T_{12} = 1+\Gamma_{12}$
$T_{21} = 1+\Gamma_{21} = 1-\Gamma_{12}$
$T_{32} = 1+\Gamma_{32} = 1-\Gamma_{23}$

(1.2.10)

then calling $x = \Gamma_{21}\Gamma_{23}e^{-j2\vartheta}$ we have:

$$T_{(z=0^+)} = T_{21}T_{32}e^{-j\vartheta}\sum_{i=0}^{\infty}\left(\Gamma_{21}\Gamma_{23}e^{-j2\vartheta}\right)^i = T_{21}T_{32}e^{-j\vartheta}\frac{1}{1-\Gamma_{21}\Gamma_{23}e^{-j2\vartheta}} = \frac{(1-\Gamma_{12})(1-\Gamma_{23})e^{-j\vartheta}}{1+\Gamma_{12}\Gamma_{23}e^{-j2\vartheta}}$$

(1.2.11)

suppose $\Gamma_{12} = -\Gamma_{23}$ i.e., *free space, medium, free space*, then:

$$\boxed{S_{21} = T_{(z=0^+)} = \frac{(1-\Gamma_{12})(1+\Gamma_{12})e^{-j\vartheta}}{1-\Gamma_{12}^2e^{-j2\vartheta}} = \frac{(1-\Gamma_{12}^2)e^{-j\vartheta}}{1-\Gamma_{12}^2e^{-j2\vartheta}}}$$

(1.2.12)

where ***S21*** is the scattering parameter we will se later in chapter 3. It is adopted for dielectric characterization of nanostrucutred composite materials, by using wave-guide method and vector network analyzer.

Calling P the propagation factor $\boxed{P = e^{-j\vartheta} = e^{-j\beta_2 d} = e^{-\gamma d}}$ and $\Gamma_{12} = \Gamma$ then we can rewrite:

$$\boxed{S_{21} = T_{(z=0^+)} = \frac{P(1-\Gamma^2)}{1-\Gamma^2P^2}}$$

(1.2.13)

1.3 Oblique incidence and Snell's Laws

With some redefinition, the formalism of transfer matrices and wave impedance for normal incidence translate almost verbatim to the case of oblique incidence [2].
By separating the field into *transverse* and *longitudinal* components with respect to the direction the dielectric are stacked (the *z*-direction), we show that the transverse components satisfy the identical transfer matrix relationship as in the case of normal incidence, provided we replace the media impedance η by the transverse impedances η_T defined below. Fig.(1.2.1), depicts plane waves forward from both side onto a planar interface separating two media with relative permittivity $\varepsilon^I, \mu^I, \varepsilon^{II}, \mu^{II}$. Both cases of *parallel* and *perpendicular* polarization are shown.

In *parallel* polarization, also known as p-polarization, π-polarization, or TM polarization, the electric field lie on the plane of incidence and the magnetic field are perpendicular to that plane (along the y-direction) and transverse to the z-direction.

In *perpendicular* polarization, also known as s-polarization, σ-polarization, or TE polarization, the electric field are perpendicular to the plane of incidence (along the y-direction), and the magnetic field lie on that plane. The figure shows the angle of incidence and reflection to be the same on either side. This is the Snell's law for reflection and it is a consequence of the boundary conditions for electric and magnetic field. Figure also implies that the two planes of incidence and two planes of reflection all coincide with the xz-plane. This is also a consequence of the boundary conditions.

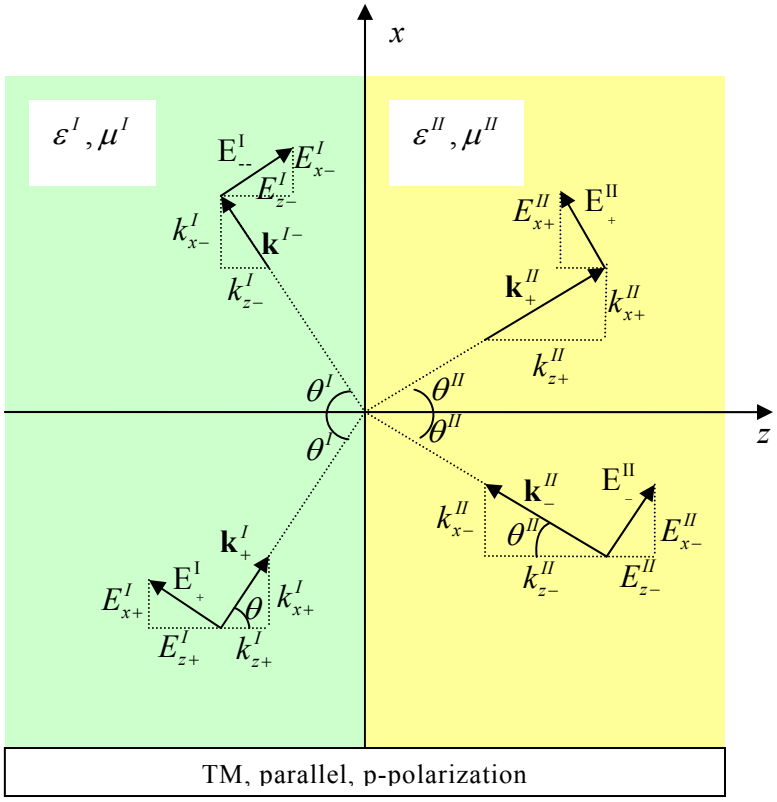

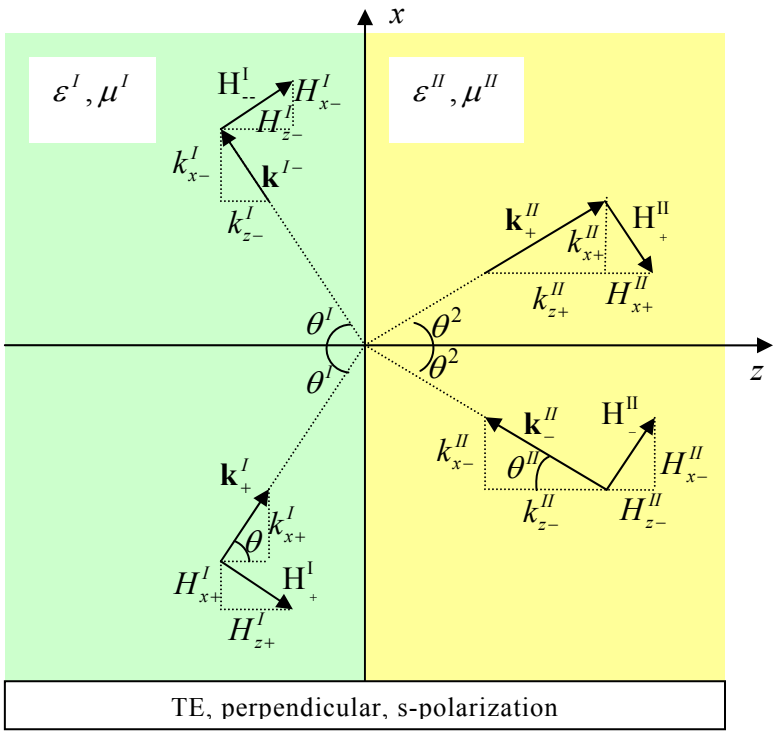

Fig. 1.3.1. Oblique incidence for TM and TE polarized waves

Starting with arbitrary wave vectors:

$$k_{\pm}^{I} = \hat{x}k_{x\pm}^{I} + \hat{y}k_{y\pm}^{I} + \hat{z}k_{z\pm}^{I}$$
$$k_{\pm}^{II} = \hat{x}k_{x\pm}^{II} + \hat{y}k_{y\pm}^{II} + \hat{z}k_{z\pm}^{II},$$

(1.3.1)

The forward refracted and reflected electric field at the two sides will have the general forms:

$\mathbf{E}_{+}^{I}e^{-j\mathbf{k}_{+}^{I}\cdot\mathbf{r}}$, Forward electric field in layer I;

$\mathbf{E}_{-}^{I}e^{-j\mathbf{k}_{-}^{I}\cdot\mathbf{r}}$, Reflected electric field in layer I;

$\mathbf{E}_{+}^{II}e^{-j\mathbf{k}_{+}^{II}\cdot\mathbf{r}}$, Refracted electric field in layer II;

$\mathbf{E}_{-}^{II}e^{-j\mathbf{k}_{-}^{II}\cdot\mathbf{r}}$, Reflected electric field in layer II;

The boundary conditions state that the net *transverse* (tangential) component of the electric field must be continuous across the interface.
Assuming that the interface is at *z=0*, we can write this condition in a form that applies to both polarizations:

$$\mathbf{E}_{T+}^{I}e^{-j\mathbf{k}_{+}^{I}\cdot\mathbf{r}} + \mathbf{E}_{T-}^{I}e^{-j\mathbf{k}_{-}^{I}\cdot\mathbf{r}} = \mathbf{E}_{T+}^{II}e^{-j\mathbf{k}_{+}^{II}\cdot\mathbf{r}} + \mathbf{E}_{T-}^{II}e^{-j\mathbf{k}_{-}^{I}\cdot\mathbf{r}} \qquad \text{at } z=0$$

(1.3.2)

Where the subscript *T* denotes the transverse (with respect to *z*) part of vector, that is, $\mathbf{E}_T = \hat{z}\times(\mathbf{E}\times\hat{z}) = \mathbf{E} - \hat{z}E_z$. Setting *z=0* in the propagation phase factors, we obtain:

$$\mathbf{E}_{T+}^{I}e^{-j\left(k_{x+}^{I}x+k_{y+}^{I}y\right)} + \mathbf{E}_{T-}^{I}e^{-j\left(k_{x-}^{I}x+k_{y-}^{I}y\right)} = \mathbf{E}_{T+}^{II}e^{-j\left(k_{x+}^{II}x+k_{y+}^{II}y\right)} + \mathbf{E}_{T-}^{2}e^{-j\left(k_{x-}^{II}x+k_{y-}^{II}y\right)}$$

(1.3.3)

For the two sides to match at *all* points on the interface, the phase factors must be equal to each other for all *x* and *y*:

$$e^{-j\left(k_{x+}^{I}x+k_{y+}^{I}y\right)} = e^{-j\left(k_{x-}^{II}x+k_{y-}^{II}y\right)} = e^{-j\left(k_{x+}^{II}x+k_{y+}^{II}y\right)} = e^{-j\left(k_{x-}^{II}x+k_{y-}^{II}y\right)},$$

(phase matching)

(1.3.4)

and this requires the *x*- and *y*-components of the wave vectors to be equal:

$$k_{x+}^{I} = k_{x-}^{I} = k_{x+}^{II} = k_{x-}^{II}$$
$$k_{y+}^{I} = k_{y-}^{I} = k_{y+}^{II} = k_{y-}^{II}$$

(1.3.5)

If the left plane of incidence is the *xz*-plane, so that $k_{y+}^{I} = 0$, than all *y*-components of the wave vectors will be zero, implying that all plane of incidence and reflection will coincide with *xz*-plane. In terms of forward and reflected angles $\theta_{\pm}^{I}, \theta_{\pm}^{II}$, the condition on the *x*-components read:

$$k^{I} \sin\theta_{+}^{I} = k^{I} \sin\theta_{-}^{I} = k^{II} \sin\theta_{+}^{II} = k^{II} \sin\theta_{-}^{II}$$

(1.3.6)

This implies the Snell's law of reflection:

$$\boxed{\begin{aligned} k^{I} \sin\theta_{+}^{I} &= k^{I} \sin\theta_{-}^{I} \quad \Rightarrow \quad \theta_{+}^{I} = \theta_{-}^{I} = \theta^{I} \\ k^{II} \sin\theta_{+}^{II} &= k^{II} \sin\theta_{-}^{II} \quad \Rightarrow \quad \theta_{+}^{II} = \theta_{-}^{II} = \theta^{II} \end{aligned}}$$

(Snell's law of reflection)

(1.3.7)

And also the Snell's law of refraction:

$$k^{I} \sin\theta^{I} = k^{II} \sin\theta^{II}$$

(1.3.8)

Since the wave number k can be written also as:

$$k = \omega\sqrt{\mu_0\varepsilon_0}\sqrt{\mu_r\varepsilon_r} = \frac{\omega}{c}\sqrt{\mu_r\varepsilon_r} = k_0\sqrt{\mu_r\varepsilon_r} = k_0 n$$

(1.3.9)

Where:

$\omega = 2\pi f$ is the frequency in radiant;

c is the speed of light;

n is the index of refraction;

$$k_0 n^I \sin\theta^I = k_0 n^{II} \sin\theta^{II}$$

$$\Downarrow$$

$$\boxed{n^I \sin\theta^I = n^{II} \sin\theta^{II}}$$

(Snel's law of refraction)

(1.3.10)

It follows that the wave vector shown in Fig. (1.3.1) will be explicitly:

$$\mathbf{k}^I = \mathbf{k}_+^I = k_x^I \hat{x} + k_z^I \hat{z} = k^I \sin\theta^I \hat{x} + k^I \cos\theta^I \hat{z}$$

$$\mathbf{k}_-^1 = k_x^1 \hat{x} - k_z^1 \hat{z} = k^I \sin\theta^I \hat{x} - k^I \cos\theta^I \hat{z}$$

$$\mathbf{k}^{II} = \mathbf{k}_+^{II} = k_x^{II} \hat{x} + k_z^{II} \hat{z} = k^{II} \sin\theta^{II} \hat{x} + k^{II} \cos\theta^{II} \hat{z}$$

$$\mathbf{k}_-^1 = k_x^{II} \hat{x} - k_z^{II} \hat{z} = k^{II} \sin\theta^{II} \hat{x} - k^{II} \cos\theta^{II} \hat{z}$$

where in general :

$$k_x = k \sin\theta$$

$$k_z = k \cos\theta$$

$$k_z^2 = k^2 - k_x^2 = k^2 - k^2 \sin^2\theta = k^2 \cos^2\theta$$

(1.3.11)

The net transverse electric fields at arbitrary locations on either side of the interface are given by Eq.(1.3.2). Using Eq. (1.3.11), we have:

$$\mathbf{E}_T^I(x,z) = \mathbf{E}_{T+}^I e^{-j\mathbf{k}_+^I \cdot \mathbf{r}} + \mathbf{E}_{T-}^1 e^{-j\mathbf{k}_-^I \cdot \mathbf{r}} = \mathbf{E}_{T+}^I e^{-j\left(k_x^I \hat{x} + k_z^I \hat{z}\right)} + \mathbf{E}_{T-}^I e^{-j\left(k_x^I \hat{x} - k_z^I \hat{z}\right)} =$$
$$= \left(\mathbf{E}_{T+}^I e^{-jk_z^I \hat{z}} + \mathbf{E}_{T-}^I e^{jk_z^I \hat{z}}\right) e^{-jk_x^I \hat{x}}$$

$$\mathbf{E}_T^{II}(x,z) = \mathbf{E}_{T+}^{II} e^{-j\mathbf{k}_+^{II} \cdot \mathbf{r}} + \mathbf{E}_{T-}^{II} e^{-j\mathbf{k}_-^{II} \cdot \mathbf{r}} = \mathbf{E}_{T+}^{II} e^{-j\left(k_x^{II} \hat{x} + k_z^{II} \hat{z}\right)} + \mathbf{E}_{T-}^{II} e^{-j\left(k_x^{II} \hat{x} - k_z^{II} \hat{z}\right)} =$$
$$= \left(\mathbf{E}_{T+}^{II} e^{-jk_z^{II} \hat{z}} + \mathbf{E}_{T-}^{II} e^{jk_z^{II} \hat{z}}\right) e^{-jk_x^{II} \hat{x}}$$

(1.3.12)

In analyzing multilayer dielectrics stacked along the *z*-direction, the phase factors $e^{-jk_x^I x} = e^{-jk_x^{II} x}$ will be common at all interfaces, and therefore, we can ignore it and restore it at the end of the calculations, if so desired. Thus, we write Eq.(1.3.12) as:

$$\mathbf{E}_T^I(z) = \mathbf{E}_{T+}^I e^{-jk_z^I \hat{z}} + \mathbf{E}_{T-}^I e^{jk_z^I \hat{z}}$$

$$\mathbf{E}_T^{II}(z) = \mathbf{E}_{T+}^{II} e^{-jk_z^{II} \hat{z}} + \mathbf{E}_{T-}^{II} e^{jk_z^{II} \hat{z}}$$

(1.3.12)

1.4 Transverse Impedance

An obliquely-moving wave will have in general, both TM and TE components [4]-[5]-[6].

We summarize these in compact form, where E_T stands for either E_{TE} or E_{TM}:

$$E_T(z) = E_{T+}e^{-jk_z z} + E_{T-}e^{jk_z z}$$
$$H_T(z) = \frac{1}{\eta_T}\left[E_{T+}e^{-jk_z z} - E_{T-}e^{jk_z z}\right]$$

(1.4.1)

The transverse impedance η_T stands for either η_{TE} or η_{TM}:

$$\eta_T = \begin{cases} \eta_{TE} = \dfrac{\eta}{\cos\theta} & \text{TE, perpendicular, s - polarization} \\ \eta_{TM} = \eta\cos\theta & \text{TM, parallel, p - polarization} \end{cases}$$

(1.4.2)

Because $\eta = \eta_0 \dfrac{\mu_r}{n}$, it is convenient to define also a *transverse* refractive index [3]:

$$n_T = \eta_0 \frac{\mu_r}{\eta_T} = \begin{cases} n_{TE} = \eta_0 \dfrac{\mu_r}{\eta_{TE}} = \eta_0 \dfrac{\mu_r}{\eta}\cos\theta & \text{TE, perpendicular, s - polarization} \\ n_{TM} = \eta_0 \dfrac{\mu_r}{\eta_{TE}} = \eta_0 \dfrac{\mu_r}{\eta\cos\theta} & \text{TM, parallel, p - polarization} \end{cases}$$

(1.4.3)

Recalling that

$k_x = k\sin\theta$

$k_z = k\cos\theta$

Then

$$\frac{k_x}{k} = \sin\theta$$
$$\frac{k_z}{k} = \cos\theta$$

(1.4.4)

Then we can express impedances, reflection coefficient, and field expressions in terms of wavenumbers:

$$\eta_T = \begin{cases} \eta_{TE} = \dfrac{\eta}{\cos\theta} = \dfrac{k\eta}{k_z} = \dfrac{\omega\sqrt{\mu\varepsilon}\sqrt{\dfrac{\mu}{\varepsilon}}}{k_z} = \dfrac{\omega\mu}{k_z} \\ \eta_{TM} = \eta\cos\theta = \dfrac{k_z\eta}{k} = \dfrac{k_z\sqrt{\dfrac{\mu}{\varepsilon}}}{\omega\sqrt{\mu\varepsilon}} = \dfrac{k_z}{\omega\varepsilon} \end{cases}$$

(1.4.5)

1.5 Fresnel Reflection and Transmission Coefficient

In the simple case of Fig.(1.3.1), the reflection coefficient for the two polarization case are [2]-[5]-[6]:

$$\rho_{TE} = \frac{\eta_{TE}^{II} - \eta_{TE}^{I}}{\eta_{TE}^{II} + \eta_{TE}^{I}} = \frac{\dfrac{\eta^{II}}{\cos\theta^{II}} - \dfrac{\eta^{I}}{\cos\theta^{I}}}{\dfrac{\eta^{II}}{\cos\theta^{II}} + \dfrac{\eta^{I}}{\cos\theta^{I}}} = \frac{\dfrac{\eta_0\mu_r^{II}}{n^{II}\cos\theta^{II}} - \dfrac{\eta_0\mu_r^{I}}{n^{I}\cos\theta^{I}}}{\dfrac{\eta_0\mu_r^{II}}{n^{II}\cos\theta^{II}} + \dfrac{\eta_0\mu_r^{I}}{n^{I}\cos\theta^{I}}} = \frac{\mu_r^{II}n^{I}\cos\theta^{I} - \mu_r^{I}n^{II}\cos\theta^{II}}{\mu_r^{II}n^{I}\cos\theta^{I} + \mu_r^{I}n^{II}\cos\theta^{II}}$$

(1.5.1)

$$\rho_{TM} = \frac{\eta_{TM}^{II} - \eta_{TM}^{I}}{\eta_{TM}^{II} + \eta_{TM}^{I}} = \frac{\eta^{II}\cos\theta^{II} - \eta^{I}\cos\theta^{I}}{\eta^{II}\cos\theta^{II} + \eta^{I}\cos\theta^{I}} = \frac{\dfrac{\eta_0\mu_r^{II}}{n^{II}}\cos\theta^{2} - \dfrac{\eta_0\mu_r^{I}}{n^{I}}\cos\theta^{I}}{\dfrac{\eta_0\mu_r^{II}}{n^{II}}\cos\theta^{II} + \dfrac{\eta_0\mu_r^{I}}{n^{I}}\cos\theta^{I}} = \frac{\mu_r^{II}n^{I}\cos\theta^{II} - \mu_r^{I}n^{II}\cos\theta^{I}}{\mu_r^{II}n^{I}\cos\theta^{II} + \mu_r^{I}n^{II}\cos\theta^{I}}$$

(1.5.2)

The corresponding transmission coefficient will be:

$$\tau_{TE} = 1 + \rho_{TE} = 1 + \frac{\eta_{TE}^{II} - \eta_{TE}^{I}}{\eta_{TE}^{II} + \eta_{TE}^{I}} = \frac{\eta_{TE}^{II} + \eta_{TE}^{I} + \eta_{TE}^{II} - \eta_{TE}^{I}}{\eta_{TE}^{II} + \eta_{TE}^{I}} = \frac{2\eta_{TE}^{II}}{\eta_{TE}^{II} + \eta_{TE}^{I}}$$

(1.5.3)

$$\tau_{TE} = 1 + \rho_{TE} = 1 + \frac{\mu_r^{II} n^I \cos\theta^I - \mu_r^I n^{II} \cos\theta^{II}}{\mu_r^{II} n^I \cos\theta^I + \mu_r^I n^{II} \cos\theta^{II}} = \frac{2\mu_r^{II} n^I \cos\theta^I}{\mu_r^{II} n^I \cos\theta^I + \mu_r^I n^{II} \cos\theta^{II}}$$

(1.5.4)

$$\tau_{TM} = 1 + \rho_{TM} = 1 + \frac{\eta_{TM}^{II} - \eta_{TM}^I}{\eta_{TM}^{II} + \eta_{TM}^I} = \frac{\eta_{TM}^{II} + \eta_{TM}^I + \eta_{TM}^{II} - \eta_{TM}^I}{\eta_{TM}^{II} + \eta_{TM}^I} = \frac{2\eta_{TM}^{II}}{\eta_{TM}^{II} + \eta_{TM}^I}$$

(1.5.5)

$$\tau_{TM} = 1 + \rho_{TM} = 1 + \frac{\mu_r^{II} n^I \cos\theta^{II} - \mu_r^I n^{II} \cos\theta^I}{\mu_r^{II} n^I \cos\theta^{II} + \mu_r^I n^{II} \cos\theta^I} = \frac{2\mu_r^{II} n^I \cos\theta^{II}}{\mu_r^{II} n^I \cos\theta^{II} + \mu_r^I n^{II} \cos\theta^I}$$

(1.5.6)

Note that at *grazing angle* of incidence $\theta \to 90^\circ$, the reflection coefficient tend to $\rho_{TE} \to -1$ and $\rho_{TM} \to 1$, regardless of the refractive indices n^I, n^{II}.

One consequence of this property is in wireless communications where the effect of the ground reflections causes the power of the propagating radio wave to attenuate with the *fourth* (instead of the *second*) power of the distance, thus limiting the propagation range.

We note also that equations (1.5.1) and (1.5.2) remain valid when one or both of the media are lossy. For example, if the right medium is lossy with complex refractive index $n^{II} = n_r^{II} - jn_i^{II}$, then the Snell's law, $n^I \sin\theta^I = n^{II} \sin\theta^{II}$, is still valid but with a complex valued θ^{II}.

Since in case of lossy media the wave numbers and refraction and possibly incidence angle become complex-valued then sometimes, in order to avoid unnecessary complex algebra, it proves convenient to recast reflection coefficient and fields expressions in terms of wavenumbers. Using the expressions found in the previous section and reported below:

$$\eta_{TE} = \frac{\omega\mu}{k_z}$$

$$\eta_{TM} = \frac{k_z}{\omega\varepsilon}$$

We can rewrite the Fresnel Reflection and Transmission Coefficient in terms of wave numbers:

$$\rho_{TE} = \frac{\eta_{TE}^{II} - \eta_{TE}^{I}}{\eta_{TE}^{II} + \eta_{TE}^{I}} = \frac{\dfrac{\omega\mu^{II}}{k_z^{II}} - \dfrac{\omega\mu^{I}}{k_z^{I}}}{\dfrac{\omega\mu^{II}}{k_z^{II}} + \dfrac{\omega\mu^{I}}{k_z^{I}}} = \frac{\dfrac{\mu^{II}}{k_z^{II}} - \dfrac{\mu^{I}}{k_z^{I}}}{\dfrac{\mu^{II}}{k_z^{II}} + \dfrac{\mu^{I}}{k_z^{I}}} = \frac{\dfrac{k_z^{I}\mu^{II} - k_z^{II}\mu^{I}}{k_z^{II}k_z^{I}}}{\dfrac{k_z^{I}\mu^{II} + k_z^{II}\mu^{I}}{k_z^{II}k_z^{I}}} = \frac{k_z^{I}\mu^{II} - k_z^{II}\mu^{I}}{k_z^{I}\mu^{II} + k_z^{II}\mu^{I}}$$

(1.5.7)

$$\rho_{TM} = \frac{\eta_{TM}^{II} - \eta_{TM}^{I}}{\eta_{TM}^{II} + \eta_{TM}^{I}} = \frac{\dfrac{k_z^{II}}{\omega\varepsilon^{II}} - \dfrac{k_z^{I}}{\omega\varepsilon^{I}}}{\dfrac{k_z^{II}}{\omega\varepsilon^{II}} + \dfrac{k_z^{I}}{\omega\varepsilon^{I}}} = \frac{\dfrac{k_z^{II}}{\varepsilon^{II}} - \dfrac{k_z^{I}}{\varepsilon^{I}}}{\dfrac{k_z^{II}}{\varepsilon^{II}} + \dfrac{k_z^{I}}{\varepsilon^{I}}} = \frac{\dfrac{\varepsilon^{I}k_z^{II} - \varepsilon^{II}k_z^{I}}{\varepsilon^{II}\varepsilon^{I}}}{\dfrac{\varepsilon^{I}k_z^{II} + \varepsilon^{II}k_z^{I}}{\varepsilon^{II}\varepsilon^{I}}} = \frac{k_z^{II}\varepsilon^{I} - k_z^{I}\varepsilon^{II}}{k_z^{II}\varepsilon^{I} + k_z^{I}\varepsilon^{II}}$$

(1.5.8)

The corresponding transmission coefficient will be:

$$\tau_{TE} = 1 + \rho_{TE} = 1 + \frac{k_z^{I}\mu^{II} - k_z^{II}\mu^{I}}{k_z^{I}\mu^{II} + k_z^{II}\mu^{I}} = \frac{k_z^{I}\mu^{II} + k_z^{II}\mu^{I} + k_z^{I}\mu^{II} - k_z^{II}\mu^{I}}{k_z^{I}\mu^{II} + k_z^{II}\mu^{I}} = \frac{2k_z^{I}\mu^{II}}{k_z^{I}\mu^{II} + k_z^{II}\mu^{I}}$$

(1.5.9)

$$\tau_{TM} = 1 + \rho_{TM} = 1 + \frac{\varepsilon^{I}k_z^{II} - \varepsilon^{II}k_z^{I}}{\varepsilon^{I}k_z^{II} + \varepsilon^{II}k_z^{I}} = \frac{\varepsilon^{I}k_z^{II} + \varepsilon^{II}k_z^{I} + \varepsilon^{I}k_z^{II} - \varepsilon^{II}k_z^{I}}{\varepsilon^{I}k_z^{II} + \varepsilon^{II}k_z^{I}} = \frac{2\varepsilon^{I}k_z^{II}}{\varepsilon^{I}k_z^{II} + \varepsilon^{II}k_z^{I}}$$

(1.5.10)

In the case of Fig. (1.1.1), the reflection coefficient expressed by Eq. (1.1.32) and (1.1.33) will computed for TE and TM propagation using the expression of η_{TE} and η_{TM}.

The same procedure can be applied for the transmission coefficient expressed by the Eq.(1.1.41) and (1.142).

1.6 Maximum angle and Critical angle

As the angle of incidence θ^I varies over $0 \le \theta^I \le 90^o$, the angle of refraction θ^{II} will have a corresponding range of variation. It can be determined by solving for θ^I from Snel's law, $n^I \sin\theta^I = n^{II} \sin\theta^{II}$

$$\sin\theta^{II} = \frac{n^I}{n^{II}} \sin\theta^I$$

(1.6.1)

If $n^I < n^{II}$ as in Fig.(1.6.1) where: $n^I = \sqrt{\mu^I \varepsilon^I}$ and $n^{II} = \sqrt{\mu^{II} \varepsilon^{II}}$, and where $\mu'^I \varepsilon^I, \mu'^{II} \varepsilon^{II}$ are the relative part of permeability and permittivity of both media, (we assume lossless dielectrics here), then Eq. (1.6.1) implies that

$$\sin\theta^{II} = \frac{n^I}{n^{II}} \sin\theta^I < \sin\theta^I$$

(1.6.2)

$$\theta^{II} < \theta^I$$

(1.6.3)

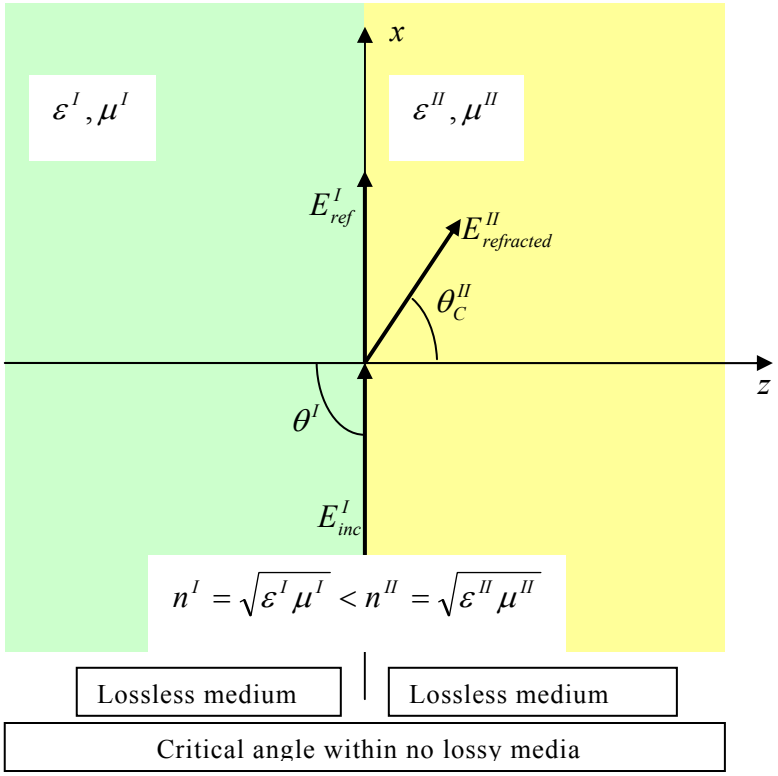

Fig. 1.6.1 Critical angle within no lossy media

Thus, if the forward wave is from a lighter to a denser medium, the refracted angle is always smaller than the angle of incidence . The maximum value of θ^{II}, denoted here by θ^{II}_C, is obtained when θ^I has its maximum, $\theta^I = 90^\circ$

$$if \quad n^I < n^{II} \Rightarrow \quad \sin\theta^{II}_C = \frac{n^I}{n^{II}} \tag{1.6.4}$$

as a consequence the critical angle can be expressed as

$$if \quad n^I < n^{II} \Rightarrow \quad \theta^{II}_C = \arcsin\left(\frac{n^I}{n^{II}}\right) \tag{1.6.5}$$

Thus, if $n^I < n^{II}$ and the incidence angle range are $0 \le \theta^I \le 90^\circ$ the refracted angle can range within the range $0 \le \theta^{II} \le \theta_C^{II}$.

On the other hand, if $n^I > n^{II}$ like in Fig.(1.6.2), and the forward wave is from a denser onto a lighter medium, then

$$\sin\theta^{II} = \frac{n^I}{n^{II}} \sin\theta^I > \sin\theta^I$$

(1.6.6)

or

$$\theta^{II} > \theta^I$$

(1.6.7)

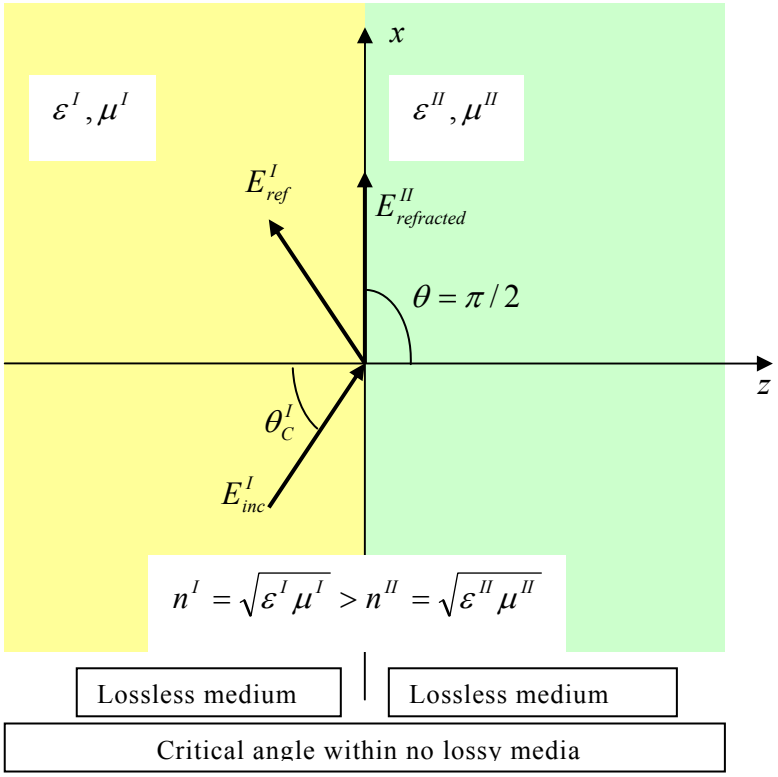

Fig. 1.6.2 Critical angle within no lossy media

Therefore, θ^{II} will reach the maximum value of 90° before θ^I does. The corresponding maximum value of θ satisfies Snell's law,

$$\sin\theta^{II} = n^I \sin\theta_C^I = n^{II} \sin(\pi/2) = n^{II}$$

(1.6.8)

or,

$$\boxed{if \quad n^I > n^{II} \Rightarrow \quad \sin\theta_C^I = \frac{n^{II}}{n^I}}$$

(1.6.9)

as a consequence the critical angle can be expressed as

$$\boxed{if \quad n^I > n^{II} \Rightarrow \quad \theta_C^I = \arcsin\left(\frac{n^{II}}{n^I}\right)}$$

(1.6.10)

This angle is called the critical angle of incidence. If the forward wave were from the right, θ_C^I would be the maximum angle of refraction according to the above discussion. If $\theta^I \le \theta_C^I$, there is normal refraction into the lighter medium. But, if θ^I exceeds θ_C^I, the forward wave cannot be refracted and gets completely reflected back into the denser medium. This phenomenon is called *total internal reflection*. When $\theta^I > \theta_C^I$, the fields on the right side of the interface are not zero, but do not propagate away to the right. Instead, they decay exponentially with the distance z. There is no transfer of power (on the average) to the right. The interface becomes a perfect mirror, with zero transmittance into the lighter medium.

1.7 Brewster angle

Let us to suppose the situation shown in Fig.(1.7.1), where in both media relative permeability are fixed to 1 and where relative permittivity can be greater than 1 only in the second media [2]. The TM Brewster angle is defined as the angle of incidence at which the TM Fresnel reflection coefficient vanishes, $\rho_{TM} = 0$. The TE coefficient $\rho_{TE} = 0$ cannot vanish for any angle θ, for non-magnetic materials .

Fig. (1.7.1) depicts the TM Brewster angle.

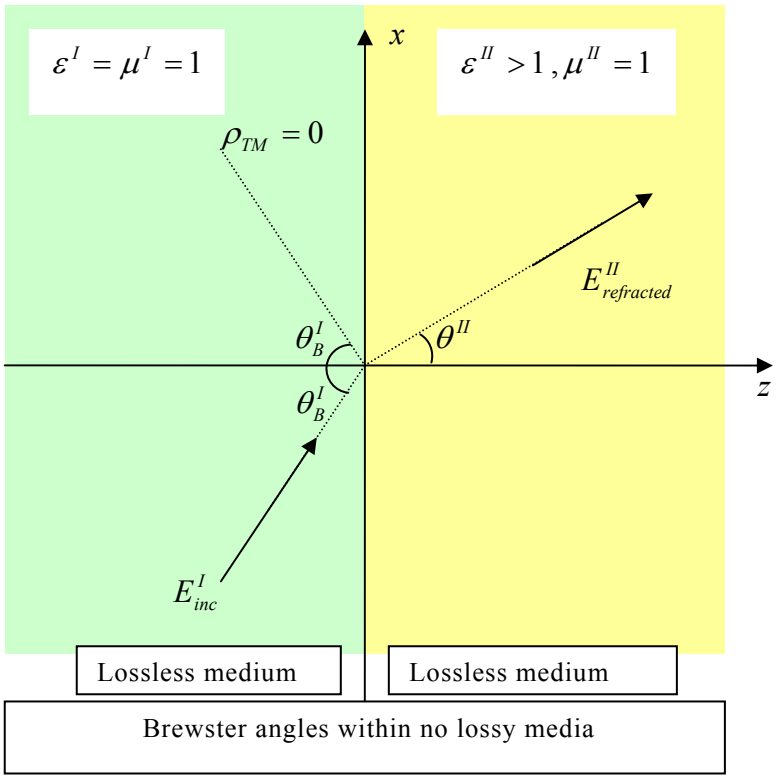

Fig. 1.6.1 Brewster angle within no lossy media

The TM Brewster angle is also called the polarizing angle because if a mixture of TM and TE waves are forward on a dielectric interface at that angle, only the TE or perpendicularly polarized waves will be reflected.

$$\rho_{TM} = \frac{\eta^{II}_{TM} - \eta^{I}_{TM}}{\eta^{II}_{TM} + \eta^{I}_{TM}} = \frac{k^{II}_z \varepsilon^I - k^I_z \varepsilon^{II}}{k^{II}_z \varepsilon^I + k^I_z \varepsilon^{II}} = 0 \quad \Rightarrow \quad \eta^{II}_{TM} - \eta^{I}_{TM} = 0 \quad \Rightarrow \quad \eta^{II}_{TM} = \eta^{I}_{TM}$$

(1.7.1)

but

$$\eta_{TM}^{II} = \eta_{TM}^{I} \quad \Rightarrow \quad \eta^{II}\cos\theta^{II} = \eta^{I}\cos\theta_{B\_TM}^{I}$$

(1.7.1)

From Snell's law

$$n^{I}\sin\theta^{I} = n^{II}\sin\theta^{II} \quad \Rightarrow \quad \sin\theta^{II} = \frac{n^{I}}{n^{II}}\sin\theta^{I} \quad \Rightarrow \quad \sin^{2}\theta^{II} = \left(\frac{n^{I}}{n^{II}}\right)^{2}\sin^{2}\theta^{I}$$

where

$$n = \frac{c}{v} = \frac{\dfrac{1}{\sqrt{\mu_0\varepsilon_0}}}{\dfrac{1}{\sqrt{\mu_0\varepsilon_0\mu_r\varepsilon_r}}} = \sqrt{\mu_r\varepsilon_r}$$

from (1.7.1)

$$\frac{\eta^{II}}{\eta^{I}}\cos\theta^{II} = \cos\theta_{B\_TM}^{I}$$

(1.7.2)

$$\frac{\eta^{II}}{\eta^{I}} = \frac{\sqrt{\dfrac{\mu^{II}}{\varepsilon^{II}}}}{\sqrt{\dfrac{\mu^{I}}{\varepsilon^{I}}}} = \sqrt{\frac{\mu^{II}\varepsilon^{I}}{\mu^{I}\varepsilon^{II}}} \quad \Rightarrow \quad \sqrt{\frac{\mu^{II}\varepsilon^{I}}{\mu^{I}\varepsilon^{II}}}\cos\theta^{II} = \cos\theta_{B\_TM}^{I}$$

(1.7.3)

Since $\cos\theta^{II} = \sqrt{1-\sin^{2}\theta^{II}}$ and $\cos\theta^{I} = \sqrt{1-\sin^{2}\theta^{I}}$

$$\sqrt{\frac{\mu^{II}\varepsilon^{I}}{\mu^{I}\varepsilon^{II}}}\sqrt{1-\sin^{2}\theta^{II}} = \sqrt{1-\sin^{2}\theta_{B\_TM}^{I}}$$

(1.7.4)

Using Snell's law

$$\sqrt{\frac{\mu^{II}\varepsilon^{I}}{\mu^{I}\varepsilon^{II}}}\sqrt{1-\left[\left(\frac{n^{I}}{n^{II}}\right)^{2}\sin^{2}\theta_{B\_TM}^{I}\right]} = \sqrt{1-\sin^{2}\theta_{B\_TM}^{I}}$$

(1.7.5)

Squaring both sides, we obtain

$$\frac{\mu^{II}\varepsilon^{I}}{\mu^{I}\varepsilon^{II}}\left[1-\left(\frac{n^{I}}{n^{II}}\right)^{2}\sin^{2}\theta^{I}_{B\_TM}\right]=1-\sin^{2}\theta^{I}_{B\_TM}$$

(1.7.6)

$$\left[\frac{\mu^{II}\varepsilon^{I}}{\mu^{I}\varepsilon^{II}}-\frac{\mu^{II}\varepsilon^{I}}{\mu^{I}\varepsilon^{II}}\left(\frac{n^{I}}{n^{II}}\right)^{2}\sin^{2}\theta^{I}_{B\_TM}\right]=1-\sin^{2}\theta^{I}_{B\_TM}$$

(1.7.7)

$$\sin^{2}\theta^{I}_{B\_TM}-\frac{\mu^{II}\varepsilon^{I}}{\mu^{I}\varepsilon^{II}}\left(\frac{n^{I}}{n^{II}}\right)^{2}\sin^{2}\theta^{I}_{B\_TM}=1-\frac{\mu^{II}\varepsilon^{I}}{\mu^{I}\varepsilon^{II}}$$

(1.7.9)

$$\sin^{2}\theta^{I}_{B\_TM}\left[1-\frac{\mu^{II}\varepsilon^{I}}{\mu^{I}\varepsilon^{II}}\left(\frac{n^{I}}{n^{II}}\right)^{2}\right]=1-\frac{\mu^{II}\varepsilon^{I}}{\mu^{I}\varepsilon^{II}}$$

(1.7.10)

$$\sin^{2}\theta^{I}_{B\_TM}=\frac{\left[1-\dfrac{\mu^{II}\varepsilon^{I}}{\mu^{I}\varepsilon^{II}}\right]}{\left[1-\dfrac{\mu^{II}\varepsilon^{I}}{\mu^{I}\varepsilon^{II}}\left(\dfrac{n^{I}}{n^{II}}\right)^{2}\right]}=\frac{\left[\dfrac{\mu^{I}\varepsilon^{II}-\mu^{II}\varepsilon^{I}}{\mu^{I}\varepsilon^{II}}\right]}{\left[\dfrac{\mu^{I}\varepsilon^{II}\left(n^{II}\right)^{2}-\mu^{II}\varepsilon^{I}\left(n^{I}\right)^{2}}{\mu^{I}\varepsilon^{II}\left(n^{II}\right)^{2}}\right]}$$

(1.7.11)

$$\sin^{2}\theta^{I}_{B\_TM}=\frac{\left[\dfrac{\mu^{I}\varepsilon^{II}-\mu^{II}\varepsilon^{I}}{1}\right]}{\left[\dfrac{\mu^{I}\varepsilon^{II}\left(n^{II}\right)^{2}-\mu^{II}\varepsilon^{I}\left(n^{I}\right)^{2}}{\left(n^{II}\right)^{2}}\right]}=\frac{\mu^{I}\varepsilon^{II}-\mu^{II}\varepsilon^{I}}{1}\frac{\left(n^{II}\right)^{2}}{\mu^{I}\varepsilon^{II}\left(n^{II}\right)^{2}-\mu^{II}\varepsilon^{I}\left(n^{I}\right)^{2}}$$

(1.7.12)

$$\theta^{I}_{B\_TM}=\arcsin\sqrt{\frac{\left(n^{II}\right)^{2}\left(\mu^{I}\varepsilon^{II}-\mu^{II}\varepsilon^{I}\right)}{\mu^{I}\varepsilon^{II}\left(n^{II}\right)^{2}-\mu^{II}\varepsilon^{I}\left(n^{I}\right)^{2}}}$$

(1.7.13)

$$\theta_{B\_TM}^{I} = \arcsin\sqrt{\frac{\dfrac{\left(n^{II}\right)^2\left(\mu^{I}\varepsilon^{II}-\mu^{II}\varepsilon^{I}\right)}{\mu^{II}\varepsilon^{II}}}{\dfrac{\mu^{I}\varepsilon^{II}\left(n^{II}\right)^2-\mu^{II}\varepsilon^{I}\left(n^{I}\right)^2}{\mu^{II}\varepsilon^{II}}}} = \arcsin\sqrt{\frac{\left(n^{II}\right)^2\left(\dfrac{\mu^{I}\varepsilon^{II}}{\mu^{II}\varepsilon^{II}}-\dfrac{\mu^{II}\varepsilon^{I}}{\mu^{II}\varepsilon^{II}}\right)}{\dfrac{\mu^{I}\varepsilon^{II}}{\mu^{II}\varepsilon^{II}}\left(n^{II}\right)^2-\dfrac{\mu^{II}\varepsilon^{I}}{\mu^{II}\varepsilon^{II}}\left(n^{I}\right)^2}}$$

(1.7.13)

$$\boxed{\theta_{B\_TM}^{I} = \arcsin\sqrt{\frac{\left(\dfrac{\mu^{I}}{\mu^{II}}-\dfrac{\varepsilon^{I}}{\varepsilon^{II}}\right)\left(n^{II}\right)^2}{\dfrac{\mu^{I}}{\mu^{II}}\left(n^{II}\right)^2-\dfrac{\varepsilon^{I}}{\varepsilon^{II}}\left(n^{I}\right)^2}}}$$

(1.7.14)

Alternatively, starting from (1.7.6), i.e., $\dfrac{\mu^{II}\varepsilon^{I}}{\mu^{I}\varepsilon^{II}}\left[1-\left(\dfrac{n^{I}}{n^{II}}\right)^2\sin^2\theta_{B\_TM}^{I}\right]=1-\sin^2\theta_{B\_TM}^{I}$,

and substituting $n^{I}=\sqrt{\mu^{I}\varepsilon^{I}}$ and $n^{II}=\sqrt{\mu^{II}\varepsilon^{II}}$ we obtain

$$\frac{\mu^{II}\varepsilon^{I}}{\mu^{I}\varepsilon^{II}}-\frac{\mu^{II}\varepsilon^{I}}{\mu^{I}\varepsilon^{II}}\left(\frac{\mu^{I}\varepsilon^{I}}{\mu^{II}\varepsilon^{II}}\right)\sin^2\theta_{B\_TM}^{I}=1-\sin^2\theta_{B\_TM}^{I}$$

(1.7.15)

$$\frac{\mu^{II}\varepsilon^{I}}{\mu^{I}\varepsilon^{II}}-\left(\frac{\varepsilon^{I}}{\varepsilon^{II}}\right)^2\sin^2\theta_{B\_TM}^{I}=1-\sin^2\theta_{B\_TM}^{I}$$

(1.7.16)

$$\sin^2\theta_{B\_TM}^{I}\left[1-\left(\frac{\varepsilon^{I}}{\varepsilon^{II}}\right)^2\right]=\left[1-\frac{\mu^{II}\varepsilon^{I}}{\mu^{I}\varepsilon^{II}}\right]$$

(1.7.17)

$$\sin^2\theta_{B\_TM}^{I}=\frac{\left[\dfrac{\mu^{I}\varepsilon^{II}-\mu^{II}\varepsilon^{I}}{\mu^{I}\varepsilon^{II}}\right]}{\left[\dfrac{\left(\varepsilon^{II}\right)^2-\left(\varepsilon^{II}\right)^2}{\left(\varepsilon^{II}\right)^2}\right]}=\frac{\mu^{I}\varepsilon^{II}-\mu^{II}\varepsilon^{I}}{\mu^{I}\varepsilon^{II}}\frac{\left(\varepsilon^{II}\right)^2}{\left(\varepsilon^{II}+\varepsilon^{I}\right)\left(\varepsilon^{II}-\varepsilon^{I}\right)}$$

(1.7.18)

$$\sin^2\theta^I_{B\_TM} = \frac{\varepsilon^{II}}{\mu^I}\frac{\left(\mu^I\varepsilon^{II} - \mu^{II}\varepsilon^I\right)}{\left(\varepsilon^{II} + \varepsilon^I\right)\left(\varepsilon^{II} - \varepsilon^I\right)}$$

(1.7.19)

$$\boxed{\theta^I_{B\_TM} = \arcsin\sqrt{\frac{\varepsilon^{II}}{\mu^I}\frac{\left(\mu^I\varepsilon^{II} - \mu^{II}\varepsilon^I\right)}{\left(\varepsilon^{II} + \varepsilon^I\right)\left(\varepsilon^{II} - \varepsilon^I\right)}}}$$

(1.7.20)

Supposing non magnetic materials, we have:

$$\boxed{\theta^I_{B\_TM} = \arcsin\sqrt{\frac{\varepsilon^{II}\left(\varepsilon^{II} - \varepsilon^I\right)}{\left(\varepsilon^{II} + \varepsilon^I\right)\left(\varepsilon^{II} - \varepsilon^I\right)}} = \arcsin\sqrt{\frac{\varepsilon^{II}}{\left(\varepsilon^{II} + \varepsilon^I\right)}} = \arctan\sqrt{\frac{\varepsilon^{II}}{\varepsilon^I}}}$$

(1.7.21)

An in-house built Genetic Algorithm has been developed in order to find the permittivity and permeability for an infinite extended layer made of no-lossy materials. The purpose of objective function was to reduce as much as possible the reflection coefficient at the *free space-layer* interface for a certain frequency of incoming electromagnetic wave. Impinging electromagnetic wave is supposed in the incidence angular range 0÷90 deg.

Output of optimization process is the following:

$\varepsilon^I = 1 + j0$

$\mu^I = 1 + j0$

$\varepsilon^{II} = 3 + j0$

$\mu^{II} = 1 + j0$

Frequency of incidence wave = 1 GHz;

Then Brewster and Critical angles are respectively:

$$\theta^I_B = \arcsin\sqrt{\frac{\varepsilon^{II}}{\left(\varepsilon^{II} + \varepsilon^I\right)}} = \arcsin\sqrt{\frac{3}{(3+1)}} = 60^\circ$$

since on the right of interface the medium is denser than medium on the left then

$$\theta^I_C = \arcsin\left(\frac{n^I}{n^{II}}\right) = \arcsin\left(\frac{1}{\sqrt{3}}\right) = 35.26^\circ$$

Reflection and transmission coefficients are shown in Fig.(1.7.2) and (1.7.3)

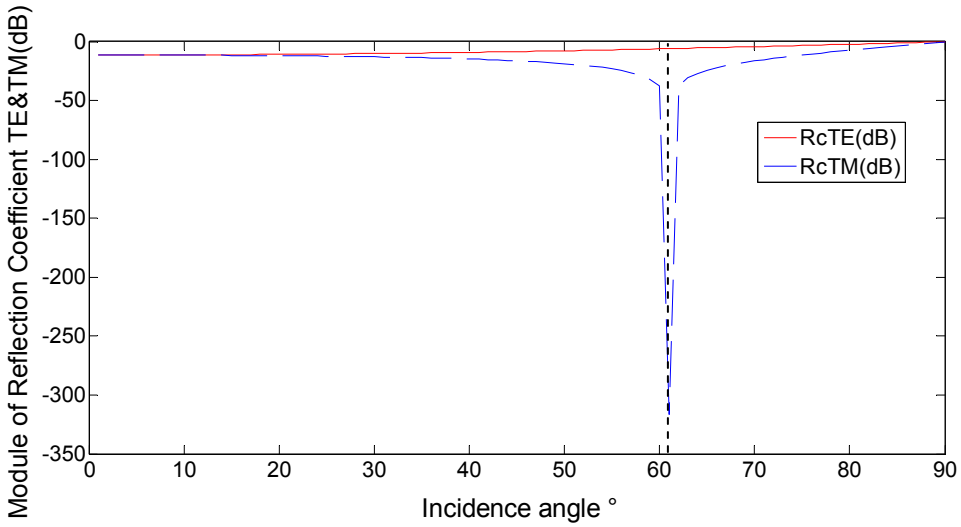

Fig.(1.7.2). Module in dB of reflection coefficient for TE and TM mode

It is to be noticed that when the incidence angle approach the Brewster value, the reflection coefficient became very small.

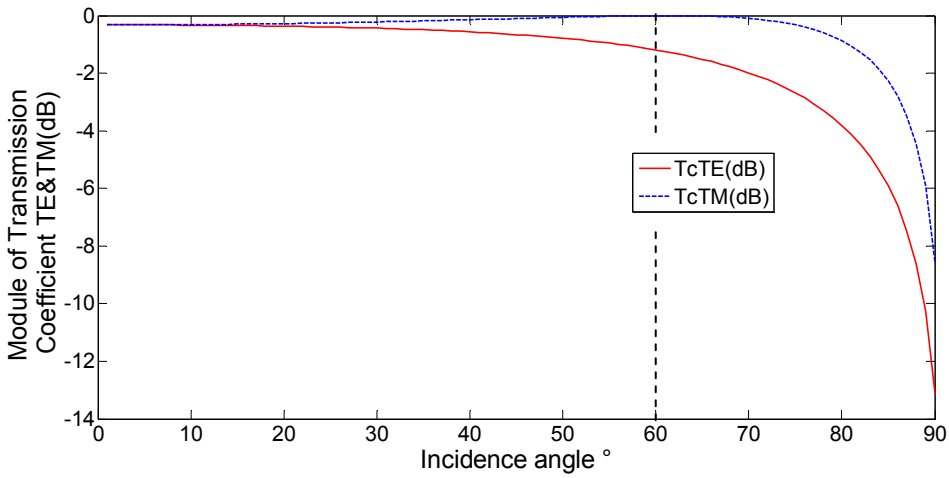

Fig.(1.7.3). Module in dB of transmission coefficient for TE and TM mode

Transmission and reflection coefficients have been computed adopting matrix formalism shown in equations (1.1.33) and (1.1.42).

It is possible to notice that when the incidence angle approach the Brewster angle, the TM transmission coefficient tend to its *maximum*.

In Fig. (1.6.4), the real part of wave number *Kx* and *Kz* along *x* and *z* axes are shown. Since materials are no-lossy materials, the imaginary part of wave numbers are zeroed.

It is noticeable that the component *Kz* is always greater than *Kx* which means that the propagation of electromagnetic wave inside the materials take place mainly along longitudinal *z* direction.

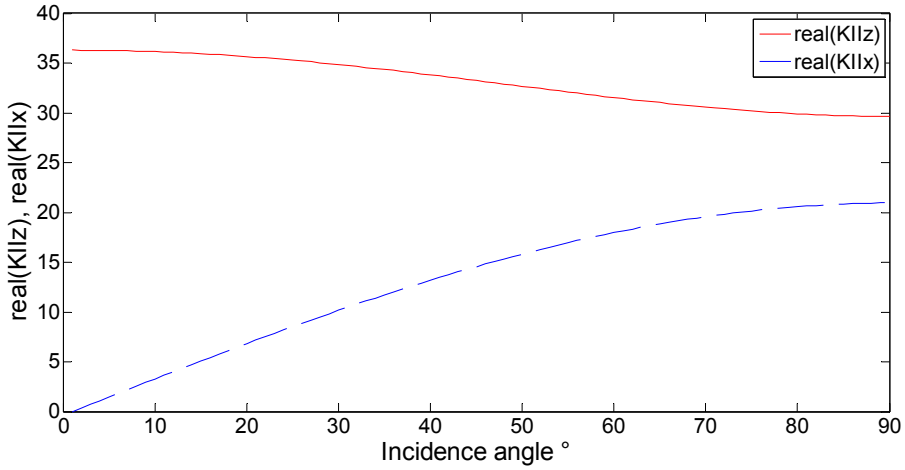

Fig.(1.7.4). Real part of wave number *Kx* and *Kz* along two propagation axes

In order to study TE Brewster angle, suppose the situation depicted on Fig. (1.7.5). Here the second media has relative permeability greater than 1 and relative permittivity set to 1. Materials are no-lossy materials.

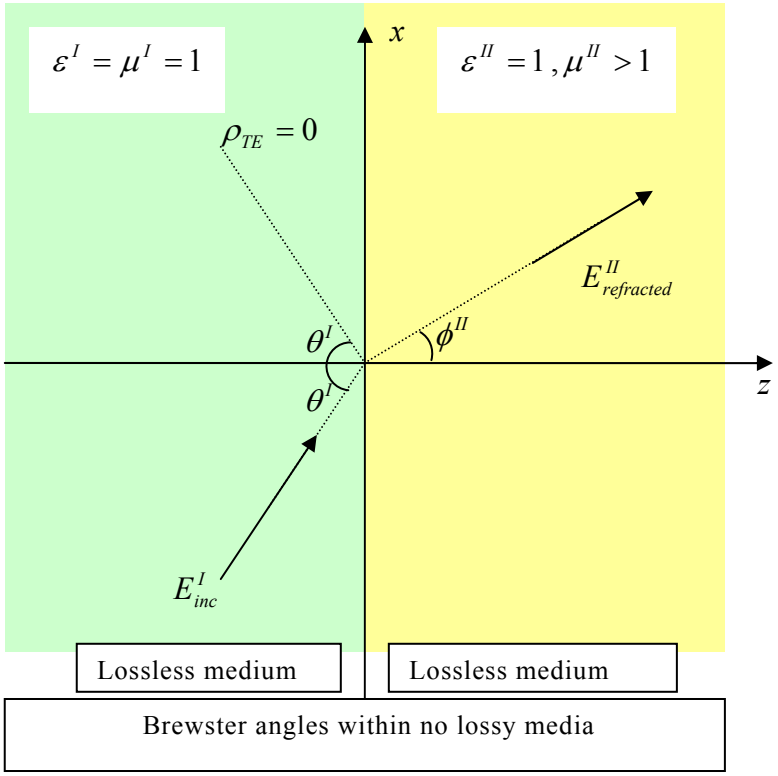

Fig. 1.7.5 Brewster angle within no lossy media

$$\rho_{TE} = \frac{\eta^{II}_{TE} - \eta^{I}_{TE}}{\eta^{II}_{TE} + \eta^{I}_{TE}} = 0 \quad \Rightarrow \quad \eta^{II}_{TE} - \eta^{I}_{TE} = 0 \quad \Rightarrow \quad \eta^{II}_{TE} = \eta^{I}_{TE}$$

(1.7.22)

but

$$\eta^{II}_{TE} = \eta^{I}_{TE} \quad \Rightarrow \quad \frac{\eta^{II}}{\cos\theta^{II}} = \frac{\eta^{I}}{\cos\theta^{I}_{B\_TE}}$$

(1.7.23)

From Snell's law

$$n^I \sin\theta^I = n^{II} \sin\theta^{II} \quad \Rightarrow \quad \sin\theta^{II} = \frac{n^I}{n^{II}} \sin\theta^I \quad \Rightarrow \quad \sin^2\theta^{II} = \left(\frac{n^I}{n^{II}}\right)^2 \sin^2\theta^I$$

where:

$$n = \frac{c}{v} = \frac{\dfrac{1}{\sqrt{\mu_0 \varepsilon_0}}}{\dfrac{1}{\sqrt{\mu_0 \varepsilon_0 \mu_r \varepsilon_r}}} = \sqrt{\mu_r \varepsilon_r}$$

from (1.7.1)

$$\frac{\eta^I}{\eta^{II}} \cos\theta^{II} = \cos\theta^I_{B\_TE}$$

(1.7.24)

$$\frac{\eta^I}{\eta^{iI}} = \frac{\sqrt{\dfrac{\mu^I}{\varepsilon^I}}}{\sqrt{\dfrac{\mu^{II}}{\varepsilon^{II}}}} = \sqrt{\frac{\mu^I \varepsilon^{II}}{\mu^{II} \varepsilon^I}} \quad \Rightarrow \quad \sqrt{\frac{\mu^I \varepsilon^{II}}{\mu^{II} \varepsilon^I}} \cos\theta^{II} = \cos\theta^I_{B\_TE}$$

(1.7.25)

Since

$\cos\theta^{II} = \sqrt{1 - \sin^2\theta^{II}}$ and $\cos\theta^I = \sqrt{1 - \sin^2\theta^I}$

$$\sqrt{\frac{\mu^I \varepsilon^{II}}{\mu^{II} \varepsilon^I}} \sqrt{1 - \sin^2\theta^{II}} = \sqrt{1 - \sin^2\theta^I_{B\_TE}}$$

(1.7.26)

Using Snell's law

$$\sqrt{\frac{\mu^I \varepsilon^{II}}{\mu^{II} \varepsilon^I}} \sqrt{1 - \left(\frac{n^I}{n^{II}}\right)^2 \sin^2\theta^I_{B\_TE}} = \sqrt{1 - \sin^2\theta^I_{B\_TE}}$$

(1.7.27)

Squaring both sides, we obtain

$$\frac{\mu^I \varepsilon^{II}}{\mu^{II} \varepsilon^I} \left[1 - \left(\frac{n^I}{n^{II}}\right)^2 \sin^2\theta^I_{B\_TE}\right] = 1 - \sin^2\theta^I_{B\_TE}$$

(1.7.28)

$$\left[\frac{\mu^I \varepsilon^{II}}{\mu^{II} \varepsilon^I} - \frac{\mu^I \varepsilon^{II}}{\mu^{II} \varepsilon^I} \left(\frac{n^I}{n^{II}}\right)^2 \sin^2\theta^I_{B\_TE}\right] = 1 - \sin^2\theta^I_{B\_TE}$$

(1.7.29)

substituting $n^I = \sqrt{\mu^I \varepsilon^I}$ and $n^{II} = \sqrt{\mu^{II} \varepsilon^{II}}$ we obtain

$$\left[\frac{\mu^I \varepsilon^{II}}{\mu^{II} \varepsilon^I} - \frac{\mu^I \varepsilon^{II}}{\mu^{II} \varepsilon^I}\left(\frac{\mu^I \varepsilon^I}{\mu^{II} \varepsilon^{II}}\right)\sin^2 \theta^I_{B\_TE}\right] = 1 - \sin^2 \theta^I_{B\_TE}$$

(1.7.30)

$$\left[\frac{\mu^I \varepsilon^{II}}{\mu^{II} \varepsilon^I} - \left(\frac{\mu^I}{\mu^{II}}\right)^2 \sin^2 \theta^I_{B\_TE}\right] = 1 - \sin^2 \theta^I_{B\_TE}$$

(1.7.31)

$$\sin^2 \theta^I_{B\_TE}\left[1 - \left(\frac{\mu^I}{\mu^{II}}\right)^2\right] = \left[1 - \frac{\mu^I \varepsilon^{II}}{\mu^{II} \varepsilon^I}\right]$$

(1.7.32)

$$\sin^2 \theta^I_{B\_TE} = \frac{\left[1 - \frac{\mu^I \varepsilon^{II}}{\mu^{II} \varepsilon^I}\right]}{\left[1 - \left(\frac{\mu^I}{\mu^{II}}\right)^2\right]} = \frac{\left[\frac{\mu^{II} \varepsilon^I - \mu^I \varepsilon^{II}}{\mu^{II} \varepsilon^I}\right]}{\left[\frac{\left(\mu^{Ii}\right)^2 - \left(\mu^I\right)^2}{\left(\mu^{Ii}\right)^2}\right]} = \frac{\mu^{II} \varepsilon^I - \mu^I \varepsilon^{II}}{\mu^{II} \varepsilon^I} \frac{\left(\mu^{II}\right)^2}{\left(\mu^{II}\right)^2 - \left(\mu^I\right)^2}$$

(1.7.33)

$$\sin^2 \theta^I_{B\_TE} = \frac{\mu^{II}}{\varepsilon^I} \frac{\left(\mu^{II} \varepsilon^I - \mu^I \varepsilon^{II}\right)}{\left(\mu^{II}\right)^2 - \left(\mu^I\right)^2} = \frac{\mu^{II}}{\varepsilon^I} \frac{\left(\mu^{II} \varepsilon^I - \mu^I \varepsilon^{II}\right)}{\left(\mu^{II} + \mu^I\right)\left(\mu^{II} - \mu^I\right)}$$

(1.7.34)

$$\boxed{\theta^I_{B\_TE} = \arcsin\sqrt{\frac{\mu^{II}}{\varepsilon^I} \frac{\left(\mu^{II} \varepsilon^I - \mu^I \varepsilon^{II}\right)}{\left(\mu^{II} + \mu^I\right)\left(\mu^{II} - \mu^I\right)}}}$$

(1.7.35)

Supposing only magnetic materials, we have:

$$\theta_{B\_TE}^{I} = \arcsin\sqrt{\frac{\mu^{II}\left(\mu^{II}-\mu^{I}\right)}{\left(\mu^{II}+\mu^{I}\right)\left(\mu^{II}-\mu^{I}\right)}} = \arcsin\sqrt{\frac{\mu^{II}}{\left(\mu^{II}+\mu^{I}\right)}} = \arctan\sqrt{\frac{\mu^{II}}{\mu^{I}}}$$

(1.7.36)

Again using Genetic algorithm supposing to find the following interface where the materials are:

$\varepsilon^{I} = 1 + j0$

$\mu^{I} = 1 + j0$

$\varepsilon^{II} = 1 + j0$

$\mu^{II} = 3 + j0$

Frequency of incidence wave = 1 GHz;

Then Brewster and Critical angles are respectively:

$$\theta_{B\_TE}^{I} = \arcsin\sqrt{\frac{\mu^{II}}{\left(\mu^{II}+\mu^{I}\right)}} = \arcsin\sqrt{\frac{3}{(3+1)}} = 60°$$

and since on the right of interface the medium is denser than medium on the left then

$$\theta_{C}^{I} = \arcsin\left(\frac{n^{I}}{n^{II}}\right) = \arcsin\left(\frac{1}{\sqrt{3}}\right) = 35.26^{\circ}$$

Reflection and transmission coefficient are shown on Fig.(1.7.5) and (1.7.6)

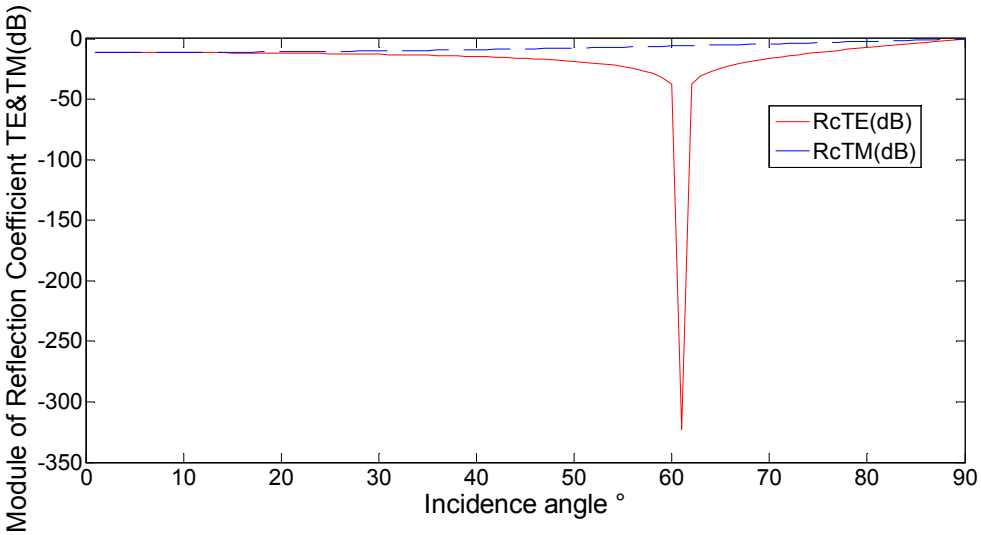

Fig.(1.7.6). Module in dB of reflection coefficient for TE and TM mode

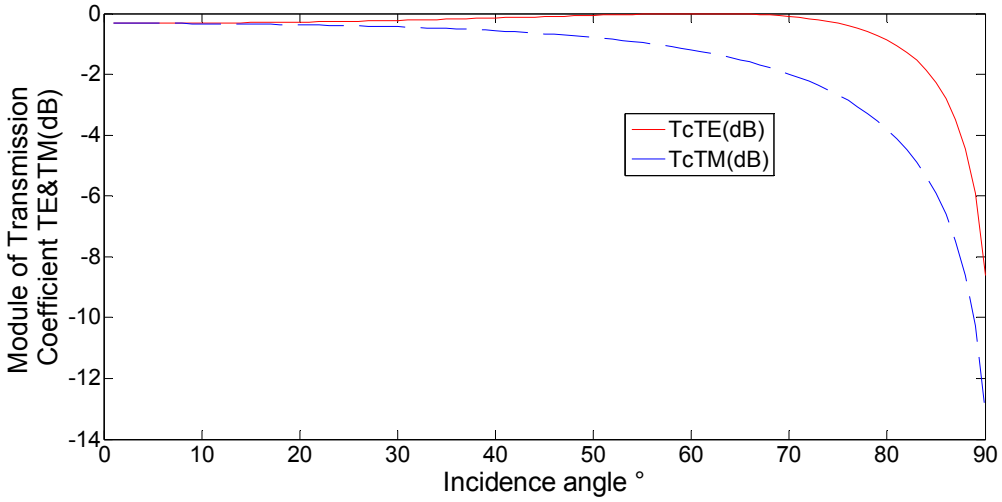

Fig.(1.7.6). Module in dB of transmission coefficient for TE and TM mode

Transmission and reflection coefficients have been computed adopting matrix formalism shown in equations (1.1.33) and (1.1.42).

It is possible to notice that when the incidence angle approaches the Brewster angle, the TE transmission coefficient tend to its *maximum*.

In Fig. (1.6.7) the real part of wave number *Kx* and *Kz* along transversal *x* and longitudinal *z* axes are shown. Since there is non losses materials the imaginary part of wave number are zeroed. It is noticeable that the component *Kz* is always greater than *Kx*.

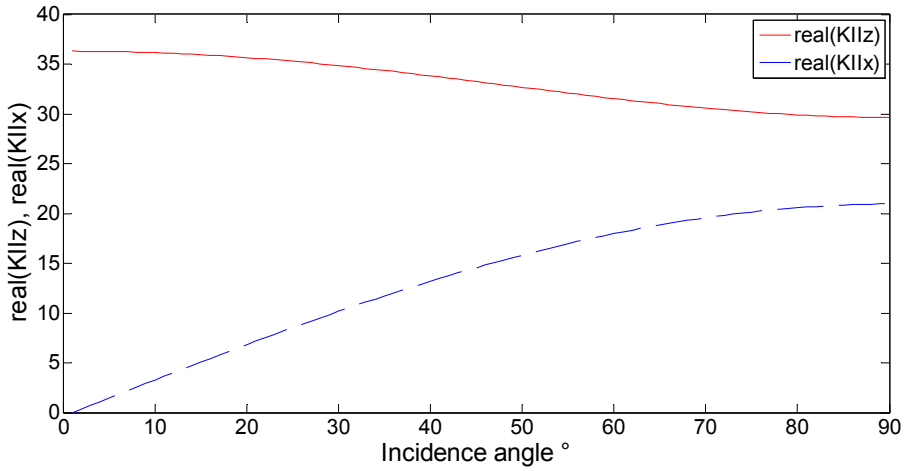

Fig.(1.7.7). Real part of wave number *Kx* and *Kz* along two propagation axes

1.8 Complex waves

When electromagnetic propagation take place in lossy media, *complex wave* phenomena could happens [2]-[3]-[4]-[5]. Lossy media are in general described adopting complex values for electric permittivity and complex values for magnetic permeability:

$$\varepsilon_r = \varepsilon_r' - j\varepsilon_r''$$

Complex relative permittivity

(1.8.1)

$$\mu_r = \mu_r' - j\mu_r''$$

Complex relative permeability

(1.8.2)

As a consequence, both, refraction index and intrinsic wave impedance become complex quantity:

$$n = \sqrt{\mu_r \varepsilon_r} = \sqrt{\left(\mu_r' - j\mu_r''\right)\left(\varepsilon_r' - j\varepsilon_r''\right)}$$
$$\eta = \sqrt{\frac{\mu}{\varepsilon}} = \sqrt{\frac{\mu_0}{\varepsilon_0}}\sqrt{\frac{\mu_r' - j\mu_r''}{\varepsilon_r' - j\varepsilon_r''}}$$

(1.8.3)

The refraction angle depends on refraction index and become complex too.
Let us to consider an example where two medium are as in Fig. (1.8.1), and suppose them to be lossy material.

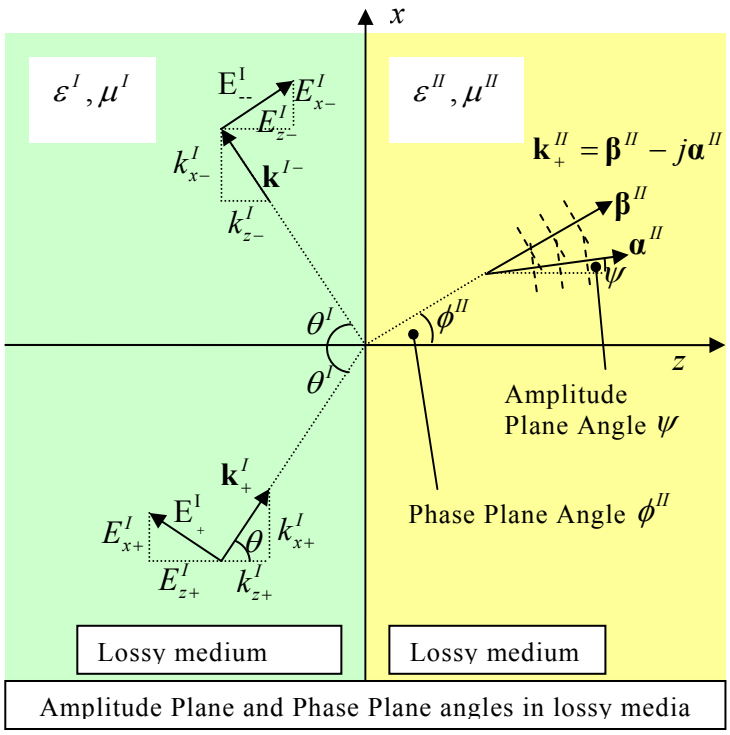

Fig. 1.8.1 Complex wave in lossy media

In oblique incidence problems, the wave number ***k***, become complex-valued and the transmitted wave is complex too.

$$\mathbf{k} = \boldsymbol{\beta} - j\boldsymbol{\alpha}$$

(1.8.4)

In a more general form, we can write the expression for the wave number ***k*** considering the component along $\hat{x}$ and $\hat{z}$ axes*:*

$$\mathbf{k}^{II} = \boldsymbol{\beta}^{II} - j\boldsymbol{\alpha}^{II} = k_x^{II}\hat{x} + k_z^{II}\hat{z} = \left(\beta_x^{II} - j\alpha_x^{II}\right)\hat{x} + \left(\beta_z^{II} - j\alpha_z^{II}\right)\hat{z}$$

(1.8.5)

where ***k*** have to satisfy the constraint:

$$\mathbf{k} \bullet \mathbf{k} = \omega^2 \mu\varepsilon = \mu_0\varepsilon_0\left(\mu_r' - j\mu_r''\right)\left(\varepsilon_r' - j\varepsilon_r''\right)$$

(1.8.6)

The space dependence of the transmitted field have the general form:

$$e^{-jk_z^{II}z}e^{-jk_x^{II}x} = e^{-j\left(\beta_z^{II}-j\alpha_z^{II}\right)z}e^{-j\left(\beta_x^{II}-j\alpha_x^{II}\right)x} = e^{-\left(\alpha_z^{II}+\alpha_x^{II}\right)}e^{-j\left(\beta_z^{II}z+\beta_x^{II}x\right)}$$

(1.8.7)

For the wave to attenuate at large distances into the right medium, it is required that $\alpha_z^{II} > 0$.

Usual propagation requires that $\alpha_x^{II} = 0$. This corresponds to a real valued wave numbers $k_x^{II}\hat{x} = \beta_x^{II}\hat{x}$.

The wave numbers k_z^I, k_z^{II} are related to $k_x^I = k_x^{II} = k_x$ though:

$$\begin{aligned}
k_x^{I^2} &= \mathbf{k}^{I^2}\sin^2\theta^I \\
k_x^{II^2} &= \mathbf{k}^{II^2}\sin^2\theta^{II} \\
k_z^{I^2} &= \mathbf{k}^{I^2} - k_x^{I^2} = \omega^2\mu^I\varepsilon^I - k_x^{I^2} = \mathbf{k}^{I^2} - \mathbf{k}^{I^2}\sin^2\theta^I = \mathbf{k}^{I^2}\cos^2\theta^I \\
k_z^{II^2} &= \mathbf{k}^{II^2} - k_x^{II^2} = \omega^2\mu^{II}\varepsilon^I - k_x^{II^2} = \mathbf{k}^{II^2} - \mathbf{k}^{II^2}\sin^2\theta^{II} = \mathbf{k}^{II^2}\cos^2\theta^{II}
\end{aligned}$$

(1.8.8)

In calculating k_z^I, k_z^{II} by taking square roots of the above expression, it is necessary, in complex wave problems, to get the correct signs of their imaginary parts; such the *evanescent waves* are described correctly. This leads us to define an "evanescent" square root as follows.

Let $\varepsilon_r = \varepsilon_r' - j\varepsilon_r''$, $\mu_r = \mu_r' - j\mu_r''$ with $\varepsilon_r'' > 0, \quad \mu_r'' > 0$, for an absorbing medium, then

$$k_z = sqrte\left[\mathbf{k}^2 - k_x^2\right] = sqrte\left[\omega^2\mu_0\varepsilon_0\left(\varepsilon_r' - j\varepsilon_r''\right)\left(\mu_r' - j\mu_r''\right) - k_x^2\right] = sqrte\left[\mathbf{k}^2\cos^2\theta^I\right] =$$

$$= \begin{cases} \sqrt{\omega^2\mu_0\varepsilon_0\left(\varepsilon_r' - j\varepsilon_r''\right)\left(\mu_r' - j\mu_r''\right) - k_x^2} & if \quad \varepsilon_r'' \neq 0, \ \mu_r'' \neq 0 \\ -j\sqrt{k_x^2 - \omega^2\mu_0\varepsilon_0\varepsilon_r'\mu_r'} & if \quad \varepsilon_r'' = 0, \ \mu_r'' = 0 \end{cases}$$

(1.8.9)

If $\varepsilon_r'' = 0,\ \mu_r'' = 0$ and $\left[\omega^2\mu_0\varepsilon_0\left(\varepsilon_r' - j\varepsilon_r''\right)\left(\mu_r' - j\mu_r''\right) - k_x^2\right] > 0$, then the two expression give the same answer. But if $\varepsilon_r'' = 0,\ \mu_r'' = 0$ and $\left[\omega^2\mu_0\varepsilon_0\left(\varepsilon_r' - j\varepsilon_r''\right)\left(\mu_r' - j\mu_r''\right) - k_x^2\right] < 0$, then k_z is correctly calculated form the second expression.

In fact:

- if $\varepsilon_r'' = 0,\ \mu_r'' = 0$ and $k_z^2 = \mathbf{k}^2 - k_x^2 = \left[\omega^2\mu_0\varepsilon_0\varepsilon_r'\mu_r' - k_x^2\right] > 0$ then
- $k_z = \sqrt{\mathbf{k}^2 - k_x^2} = \sqrt{\omega^2\mu_0\varepsilon_0\varepsilon_r'\mu_r' - k_x^2} = -j\sqrt{-\left(\omega^2\mu_0\varepsilon_0\varepsilon_r'\mu_r' - k_x^2\right)} = -j\sqrt{k_x^2 - \omega^2\mu_0\varepsilon_0\varepsilon_r'\mu_r'}$

  e.g., $k_z = \sqrt{4} = -j\sqrt{-4} = -j\left(j\sqrt{4}\right) = 2 \quad \Rightarrow \quad e^{-jk_z} = e^{-j2}$,

  i.e., propagation along *z* axes

but if

- if $\varepsilon_r'' = 0,\ \mu_r'' = 0$ and $k_z^2 = \mathbf{k}^2 - k_x^2 = \left[\omega^2\mu_0\varepsilon_0\varepsilon_r'\mu_r' - k_x^2\right] < 0$ then
- $k_z = \sqrt{\mathbf{k}^2 - k_x^2} = \sqrt{\omega^2\mu_0\varepsilon_0\varepsilon_r'\mu_r' - k_x^2} = j\sqrt{k_x^2 - \omega^2\mu_0\varepsilon_0\varepsilon_r'\mu_r'}$

  e.g., $k_z = \sqrt{-4} = j\sqrt{4} = j2 \quad \Rightarrow \quad e^{-jk_z} = e^{-j(j2)} = e^{-j(j2)} = e^{2}$ which is not evanescent, as a consequence for the evanescent wave propagation is required that:

- $k_z = -j\sqrt{k_x^2 - \mathbf{k}} = -j\sqrt{k_x^2 - \omega^2\mu_0\varepsilon_0\varepsilon_r'\mu_r'}$

  e.g., $k_z = \sqrt{-4} = -j\left(\sqrt{4}\right) = -j2 \quad \Rightarrow \quad e^{-jk_z} = e^{-j(-j2)} = e^{-2}$ which is evanescent, as a the *evanescent wave behavior* along z axes require

The constant *amplitude-plane angle* and the constant *phase-plane angle* are given by

$$\phi = \arctan\frac{\beta_x^I}{\beta_z^{II}} = \arctan\frac{\Re\left(k_x^I\right)}{\Re\left(k_z^{II}\right)}$$
$$\psi = \arctan\frac{\alpha_x^I}{\alpha_z^{II}} = \arctan\frac{\Im\left(k_x^I\right)}{\Im\left(k_z^{II}\right)}$$

(1.8.10)

1.9 Snell's law in lossy media

Let us to consider two dielectric medium as in Fig. (1.8.1), where $\varepsilon_r = \varepsilon_r' - j\varepsilon_r''$, $\mu_r = \mu_r' - j\mu_r''$, $n = n_r - jn_i = \sqrt{\mu_r \varepsilon_r}$ we can write the Snell's law of refraction as:

$$n^I \sin\theta^I = n^{II} \sin\theta^{II}$$

$$\left(n_r^I - jn_i^I\right)\sin\theta^I = \left(n_r^{II} - jn_i^{II}\right)\sin\theta^{II}$$

$$\left(\varepsilon_r^{I'} - j\varepsilon_r^{I''}\right)\left(\mu_r^{I'} - j\mu_r^{I''}\right)\sin\theta^I = \left(\varepsilon_r^{II'} - j\varepsilon_r^{II''}\right)\left(\mu_r^{II'} - j\mu_r^{II''}\right)\sin\theta^{II}$$

$$\left(\varepsilon_r^{I'}\mu_r^{I'} - j\varepsilon_r^{I'}\mu_r^{I''} - j\varepsilon_r^{I''}\mu_r^{I'} - \varepsilon_r^{I''}\mu_r^{I''}\right)\sin\theta^I = \left(\varepsilon_r^{II'}\mu_r^{II'} - j\varepsilon_r^{II'}\mu_r^{II''} - j\varepsilon_r^{II''}\mu_r^{II'} - \varepsilon_r^{II''}\mu_r^{II''}\right)\sin\theta^{II}$$

$$\left[\left(\varepsilon_r^{I'}\mu_r^{I'} - \varepsilon_r^{I''}\mu_r^{I''}\right) - j\left(\varepsilon_r^{I'}\mu_r^{I''} + \varepsilon_r^{I''}\mu_r^{I'}\right)\right]\sin\theta^I = \left[\left(\varepsilon_r^{II'}\mu_r^{II'} - \varepsilon_r^{II''}\mu_r^{II''}\right) - j\left(\varepsilon_r^{II'}\mu_r^{II''} + \varepsilon_r^{II''}\mu_r^{II'}\right)\right]\sin\theta^{II}$$

(1.9.1)

$$\left(\varepsilon_r^{I'}\mu_r^{I'} - \varepsilon_r^{I''}\mu_r^{I''}\right)\sin\theta^I - j\left(\varepsilon_r^{I'}\mu_r^{I''} + \varepsilon_r^{I''}\mu_r^{I'}\right)\sin\theta^I = \left(\varepsilon_r^{II'}\mu_r^{II'} - \varepsilon_r^{II''}\mu_r^{II''}\right)\sin\theta^{II} - j\left(\varepsilon_r^{II'}\mu_r^{II''} + \varepsilon_r^{II''}\mu_r^{II'}\right)\sin\theta^{II}$$

$$\left(\varepsilon_r^{I'}\mu_r^{I'} - \varepsilon_r^{I''}\mu_r^{I''}\right)\sin\theta^I - \left(\varepsilon_r^{II'}\mu_r^{II'} - \varepsilon_r^{II''}\mu_r^{II''}\right)\sin\theta^{II} = j\left[\left(\varepsilon_r^{I'}\mu_r^{I''} + \varepsilon_r^{I''}\mu_r^{I'}\right)\sin\theta^I - \left(\varepsilon_r^{II'}\mu_r^{II''} + \varepsilon_r^{II''}\mu_r^{II'}\right)\sin\theta^{II}\right]$$

(1.9.2)

Using Eq. **(1.8.1)** we cab find the complex expression for the refracted angle θ^{II}:

$$\sin\theta^{II} = \frac{\left[\left(\varepsilon_r^{I'}\mu_r^{I'} - \varepsilon_r^{I''}\mu_r^{I''}\right) - j\left(\varepsilon_r^{I'}\mu_r^{I''} + \varepsilon_r^{I''}\mu_r^{I'}\right)\right]}{\left[\left(\varepsilon_r^{II'}\mu_r^{II'} - \varepsilon_r^{II''}\mu_r^{II''}\right) - j\left(\varepsilon_r^{II'}\mu_r^{II''} + \varepsilon_r^{II''}\mu_r^{II'}\right)\right]}\sin\theta^I$$

(1.9.3)

$$\sin\theta^{II} = \frac{\left[\left(\varepsilon_r^{I'}\mu_r^{I'} - \varepsilon_r^{I''}\mu_r^{I''}\right) - j\left(\varepsilon_r^{I'}\mu_r^{I''} + \varepsilon_r^{I''}\mu_r^{I'}\right)\right]\left[\left(\varepsilon_r^{II'}\mu_r^{II'} - \varepsilon_r^{II''}\mu_r^{II''}\right) + j\left(\varepsilon_r^{II'}\mu_r^{II''} + \varepsilon_r^{II''}\mu_r^{II'}\right)\right]}{\left[\left(\varepsilon_r^{II'}\mu_r^{II'} - \varepsilon_r^{II''}\mu_r^{II''}\right) - j\left(\varepsilon_r^{II'}\mu_r^{II''} + \varepsilon_r^{II''}\mu_r^{II'}\right)\right]\left[\left(\varepsilon_r^{II'}\mu_r^{II'} - \varepsilon_r^{II''}\mu_r^{II''}\right) + j\left(\varepsilon_r^{II'}\mu_r^{II''} + \varepsilon_r^{II''}\mu_r^{II'}\right)\right]}\sin\theta^I$$

(1.9.4)

$$\sin\theta^{II} = \frac{\begin{array}{c}\left(\varepsilon_r^{I'}\mu_r^{I'} - \varepsilon_r^{I''}\mu_r^{I''}\right)\left(\varepsilon_r^{II'}\mu_r^{II'} - \varepsilon_r^{II''}\mu_r^{II''}\right) + j\left(\varepsilon_r^{I'}\mu_r^{I'} - \varepsilon_r^{I''}\mu_r^{I''}\right)\left(\varepsilon_r^{II'}\mu_r^{II''} + \varepsilon_r^{II''}\mu_r^{II'}\right) + \\ -j\left(\varepsilon_r^{I'}\mu_r^{I''} + \varepsilon_r^{I''}\mu_r^{I'}\right)\left(\varepsilon_r^{II'}\mu_r^{II'} - \varepsilon_r^{II''}\mu_r^{II''}\right) + \left(\varepsilon_r^{I'}\mu_r^{I''} + \varepsilon_r^{I''}\mu_r^{I'}\right)\left(\varepsilon_r^{II'}\mu_r^{II''} + \varepsilon_r^{II''}\mu_r^{II'}\right)\end{array}}{\left[\left(\varepsilon_r^{II'}\mu_r^{II'} - \varepsilon_r^{II''}\mu_r^{II''}\right)^2 + \left(\varepsilon_r^{II'}\mu_r^{II''} + \varepsilon_r^{II''}\mu_r^{II'}\right)^2\right]}\sin\theta^I$$

(1.9.5)

$$\sin\theta^{II}=\frac{\begin{array}{l}\left(\varepsilon_r^{I'}\mu_r^{I'}\varepsilon_r^{II'}\mu_r^{II'}-\varepsilon_r^{I'}\mu_r^{I'}\varepsilon_r^{II''}\mu_r^{II''}-\varepsilon_r^{I''}\mu_r^{I''}\varepsilon_r^{II'}\mu_r^{II'}+\varepsilon_r^{I''}\mu_r^{I''}\varepsilon_r^{II''}\mu_r^{II''}\right)+\\+j\left(\varepsilon_r^{I'}\mu_r^{I'}\varepsilon_r^{II'}\mu_r^{II''}+\varepsilon_r^{I'}\mu_r^{I'}\varepsilon_r^{II''}\mu_r^{II'}-\varepsilon_r^{I''}\mu_r^{I''}\varepsilon_r^{II'}\mu_r^{II''}-\varepsilon_r^{I''}\mu_r^{I''}\varepsilon_r^{II''}\mu_r^{II'}\right)+\\-j\left(\varepsilon_r^{I'}\mu_r^{I''}\varepsilon_r^{II'}\mu_r^{II'}-\varepsilon_r^{I'}\mu_r^{I''}\varepsilon_r^{II''}\mu_r^{II''}+\varepsilon_r^{I''}\mu_r^{I'}\varepsilon_r^{II'}\mu_r^{II'}-\varepsilon_r^{I''}\mu_r^{I'}\varepsilon_r^{II''}\mu_r^{II''}\right)+\\+\left(\varepsilon_r^{I'}\mu_r^{I''}\varepsilon_r^{II'}\mu_r^{II''}+\varepsilon_r^{I'}\mu_r^{I''}\varepsilon_r^{II''}\mu_r^{II'}+\varepsilon_r^{I''}\mu_r^{I'}\varepsilon_r^{II'}\mu_r^{II''}+\varepsilon_r^{I''}\mu_r^{I'}\varepsilon_r^{II''}\mu_r^{II'}\right)\end{array}}{\left[\left(\varepsilon_r^{II'}\mu_r^{II'}-\varepsilon_r^{II''}\mu_r^{II''}\right)^2+\left(\varepsilon_r^{II'}\mu_r^{II''}+\varepsilon_r^{II''}\mu_r^{II'}\right)^2\right]}\sin\theta^{I}$$

(1.9.6)

$$\sin\theta^{II}=\frac{\begin{array}{l}\left(\varepsilon_r^{I'}\mu_r^{I'}\varepsilon_r^{II'}\mu_r^{II'}-\varepsilon_r^{I'}\mu_r^{I'}\varepsilon_r^{II''}\mu_r^{II''}-\varepsilon_r^{I''}\mu_r^{I''}\varepsilon_r^{II'}\mu_r^{II'}+\varepsilon_r^{I''}\mu_r^{I''}\varepsilon_r^{II''}\mu_r^{II''}\right)+\\+\left(\varepsilon_r^{I'}\mu_r^{I''}\varepsilon_r^{II'}\mu_r^{II''}+\varepsilon_r^{I'}\mu_r^{I''}\varepsilon_r^{II''}\mu_r^{II'}+\varepsilon_r^{I''}\mu_r^{I'}\varepsilon_r^{II'}\mu_r^{II''}+\varepsilon_r^{I''}\mu_r^{I'}\varepsilon_r^{II''}\mu_r^{II'}\right)+\\+j\left(\varepsilon_r^{I'}\mu_r^{I'}\varepsilon_r^{II'}\mu_r^{II''}+\varepsilon_r^{I'}\mu_r^{I'}\varepsilon_r^{II''}\mu_r^{II'}-\varepsilon_r^{I''}\mu_r^{I''}\varepsilon_r^{II'}\mu_r^{II''}-\varepsilon_r^{I''}\mu_r^{I''}\varepsilon_r^{II''}\mu_r^{II'}\right)+\\+j\left(+\varepsilon_r^{I'}\mu_r^{I''}\varepsilon_r^{II'}\mu_r^{II''}-\varepsilon_r^{I'}\mu_r^{I''}\varepsilon_r^{II''}\mu_r^{II'}-\varepsilon_r^{I''}\mu_r^{I'}\varepsilon_r^{II'}\mu_r^{II''}+\varepsilon_r^{I''}\mu_r^{I'}\varepsilon_r^{II''}\mu_r^{II'}\right)+\end{array}}{\left[\left(\varepsilon_r^{II'}\mu_r^{II'}-\varepsilon_r^{II''}\mu_r^{II''}\right)^2+\left(\varepsilon_r^{II'}\mu_r^{II''}+\varepsilon_r^{II''}\mu_r^{II'}\right)^2\right]}\sin\theta^{I}$$

(1.9.7)

$$\theta^{II}=\arcsin\left(\frac{\begin{array}{l}\left(\varepsilon_r^{I'}\mu_r^{I'}\varepsilon_r^{II'}\mu_r^{II'}-\varepsilon_r^{I'}\mu_r^{I'}\varepsilon_r^{II''}\mu_r^{II''}-\varepsilon_r^{I''}\mu_r^{I''}\varepsilon_r^{II'}\mu_r^{II'}+\varepsilon_r^{I''}\mu_r^{I''}\varepsilon_r^{II''}\mu_r^{II''}\right)+\\+\left(\varepsilon_r^{I'}\mu_r^{I''}\varepsilon_r^{II'}\mu_r^{II''}+\varepsilon_r^{I'}\mu_r^{I''}\varepsilon_r^{II''}\mu_r^{II'}+\varepsilon_r^{I''}\mu_r^{I'}\varepsilon_r^{II'}\mu_r^{II''}+\varepsilon_r^{I''}\mu_r^{I'}\varepsilon_r^{II''}\mu_r^{II'}\right)+\\+j\left(\varepsilon_r^{I'}\mu_r^{I'}\varepsilon_r^{II'}\mu_r^{II''}+\varepsilon_r^{I'}\mu_r^{I'}\varepsilon_r^{II''}\mu_r^{II'}-\varepsilon_r^{I''}\mu_r^{I''}\varepsilon_r^{II'}\mu_r^{II''}-\varepsilon_r^{I''}\mu_r^{I''}\varepsilon_r^{II''}\mu_r^{II'}\right)+\\+j\left(+\varepsilon_r^{I'}\mu_r^{I''}\varepsilon_r^{II'}\mu_r^{II''}-\varepsilon_r^{I'}\mu_r^{I''}\varepsilon_r^{II''}\mu_r^{II'}-\varepsilon_r^{I''}\mu_r^{I'}\varepsilon_r^{II'}\mu_r^{II''}+\varepsilon_r^{I''}\mu_r^{I'}\varepsilon_r^{II''}\mu_r^{II'}\right)\end{array}}{\left[\left(\varepsilon_r^{II'}\mu_r^{II'}-\varepsilon_r^{II''}\mu_r^{II''}\right)^2+\left(\varepsilon_r^{II'}\mu_r^{II''}+\varepsilon_r^{II''}\mu_r^{II'}\right)^2\right]}\sin\theta^{I}\right)$$

(1.9.8)

1.10 Zenneck Surface Wave

In previous section, lossy materials and complex waves have been introduced. When lossy materials are considered then the TM or TE reflection coefficients can vanish for a complex angle θ, or equivalently for a complex valued wave vector $\mathbf{k} = \boldsymbol{\beta} - \mathbf{j}\boldsymbol{\alpha}$ even though the left medium is lossless. Brewster angle in lossy media leads to the so-called Zenneck surface wave [2]. The constant phase plane and constant amplitude plane in both media are shown in Fig. (1.10.1). On the lossless side, vectors $\boldsymbol{\beta}$ and $\boldsymbol{\alpha}$, are necessarily orthogonal to each other.

Although the Zenneck wave attenuates both along the *x*- and *z*-directions, the attenuation constant along *x* tends to be much smaller than that along *z*.

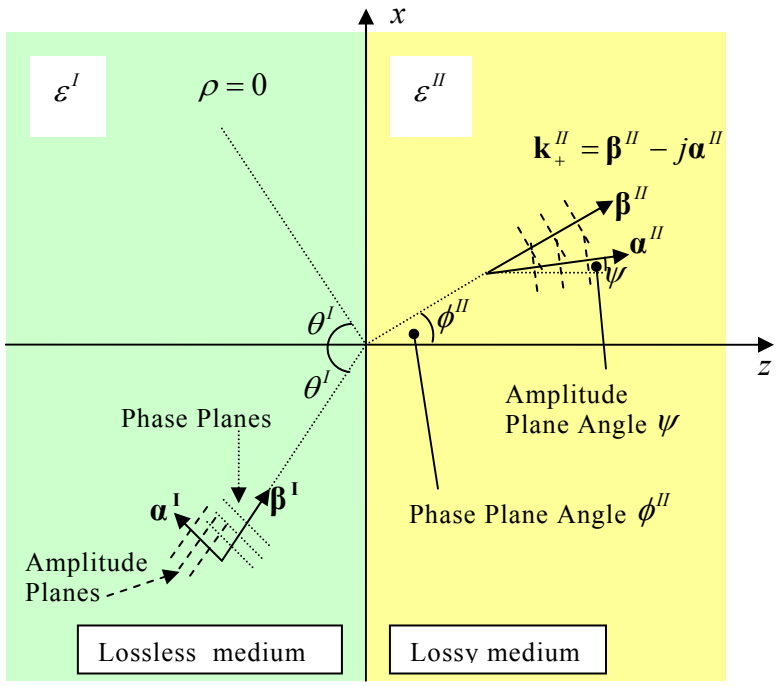

Fig. 1.10.1 Amplitude Plane and Phase Plane angles for the Zenneck wave

We can observe that as a function of permittivity ε^{II} and permeability μ^{II}, the TE or TM reflection coefficient can vanish. This means that there will be angles of electromagnetic wave at which ρ_{TM} or ρ_{TE} will be zeroed.

For the ***TM case*** the condition $\rho_{TM} = 0$ require:

$$\boxed{\rho_{TM} = \frac{\eta_{TM}^{II} - \eta_{TM}^{I}}{\eta_{TM}^{II} + \eta_{TM}^{I}} = \frac{\varepsilon^{I} k_z^{II} - \varepsilon^{II} k_z^{I}}{\varepsilon^{I} k_z^{II} + \varepsilon^{II} k_z^{I}} = 0}$$

(1.10.1)

This condition is verified if the numerator is zeroed:

$$\varepsilon^{I} k_z^{II} = \varepsilon^{II} k_z^{I}$$

(1.10.2)

This condition may be rewritten in the equivalent form:

$$\omega^2 \varepsilon^{I} \mu^{I} k_z^{II} \mu^{II} = \omega^2 \varepsilon^{II} \mu^{II} k_z^{I} \mu^{I}$$

(1.10.3)

Which is equivalent to

$$\left(k^{I}\right)^2 k_z^{II} \mu^{II} = \left(k^{II}\right)^2 k_z^{I} \mu^{I}$$

(1.10.4)

Using the relations which come from Maxwell's equations:

$$\left(k_x^{I}\right)^2 + \left(k_z^{I}\right)^2 = \left(k^{I}\right)^2$$
$$\left(k_x^{II}\right)^2 + \left(k_z^{II}\right)^2 = \left(k^{II}\right)^2$$

(1. 10.5)

and considering that due to the boundary conditions $k_x^{I} = k_x^{II}$, the relation above can be rewritten as

$$\left(k_x\right)^2 + \left(k_z^{I}\right)^2 = \left(k^{I}\right)^2$$
$$\left(k_x\right)^2 + \left(k_z^{II}\right)^2 = \left(k^{II}\right)^2$$

(1. 10.6)

Finally, we can rewrite a system of three equations in three complex unknowns k_x, k_z^{I}, k_z^{II}:

$$\begin{cases} \left(k^{I}\right)^2 k_z^{II}\mu^{II} = \left(k^{II}\right)^2 k_z^{I}\mu^{I} \\ \left(k_x\right)^2 + \left(k_z^{I}\right)^2 = \left(k^{I}\right)^2 \\ \left(k_x\right)^2 + \left(k_z^{II}\right)^2 = \left(k^{II}\right)^2 \end{cases}$$

(1. 10.7)

To solve the equations above we rename $k_x = x, \quad k_z^{I} = y, \quad k_z^{II} = z,$:

$$\begin{cases} \left(k^{I}\right)^2 z\mu^{II} = \left(k^{II}\right)^2 y\mu^{I} \\ x^2 + y^2 = \left(k^{I}\right)^2 \\ x^2 + z^2 = \left(k^{II}\right)^2 \end{cases} \Rightarrow \begin{cases} z = \dfrac{\mu^{I}\left(k^{II}\right)^2}{\mu^{II}\left(k^{I}\right)^2} y \\ x^2 + y^2 = \left(k^{I}\right)^2 \\ x^2 = \left(k^{II}\right)^2 - z^2 = \left(k^{II}\right)^2 - \dfrac{\left(\mu^{I}\right)^2\left(k^{II}\right)^4}{\left(\mu^{II}\right)^2\left(k^{I}\right)^4} y^2 \end{cases}$$

(1. 10.8)

Then substituting the last equation in x into the second of the system, we have the value for y:

$$\begin{cases} z = \dfrac{\mu^{I}\left(k^{II}\right)^2}{\mu^{II}\left(k^{I}\right)^2} y \\ \left(k^{II}\right)^2 - \dfrac{\left(\mu^{I}\right)^2\left(k^{II}\right)^4}{\left(\mu^{II}\right)^2\left(k^{I}\right)^4} y^2 + y^2 = \left(k^{I}\right)^2 \quad \Rightarrow y^2 = \dfrac{\left(k^{I}\right)^2 - \left(k^{II}\right)^2}{\left[1 - \dfrac{\left(\mu^{I}\right)^2\left(k^{II}\right)^4}{\left(\mu^{II}\right)^2\left(k^{I}\right)^4}\right]} \\ x^2 = \left(k^{II}\right)^2 - \dfrac{\left(\mu^{I}\right)^2\left(k^{II}\right)^4}{\left(\mu^{II}\right)^2\left(k^{I}\right)^4} y^2 \end{cases}$$

(1. 10.9)

Then substituting the second equation in y into the first and last of the system we obtain the value for z and x:

$$\begin{cases} z = \dfrac{\mu^I \left(k^{II}\right)^2}{\mu^{II} \left(k^I\right)^2} \sqrt{\dfrac{\left(k^I\right)^2 - \left(k^{II}\right)^2}{\left[1 - \dfrac{\left(\mu^I\right)^2 \left(k^{II}\right)^4}{\left(\mu^{II}\right)^2 \left(k^I\right)^4}\right]}} \\ y^2 = \dfrac{\left(k^I\right)^2 - \left(k^{II}\right)^2}{\left[1 - \dfrac{\left(\mu^I\right)^2 \left(k^{II}\right)^4}{\left(\mu^{II}\right)^2 \left(k^I\right)^4}\right]} \\ x^2 = \left(k^{II}\right)^2 - \dfrac{\left(\mu^I\right)^2 \left(k^{II}\right)^4}{\left(\mu^{II}\right)^2 \left(k^I\right)^4} \dfrac{\left[\left(k^I\right)^2 - \left(k^{II}\right)^2\right]}{\left[1 - \dfrac{\left(\mu^I\right)^2 \left(k^{II}\right)^4}{\left(\mu^{II}\right)^2 \left(k^I\right)^4}\right]} = \left(k^{II}\right)^2 - \dfrac{\left(\mu^I\right)^2 \left(k^{II}\right)^4}{\cancel{\left(\mu^{II}\right)^2 \left(k^I\right)^4}} \dfrac{\left[\left(k^I\right)^2 - \left(k^{II}\right)^2\right]}{\left[\dfrac{\left(\mu^{II}\right)^2 \left(k^I\right)^4 - \left(\mu^I\right)^2 \left(k^{II}\right)^4}{\cancel{\left(\mu^{II}\right)^2 \left(k^I\right)^4}}\right]} \end{cases}$$

(1. 10.10)

$$\begin{cases} z = \dfrac{\mu^I \left(k^{II}\right)^2}{\mu^{II} \left(k^I\right)^2} \sqrt{\dfrac{\left(k^I\right)^2 - \left(k^{II}\right)^2}{\left[\dfrac{\left(\mu^{II}\right)^2 \left(k^I\right)^4 - \left(\mu^I\right)^2 \left(k^{II}\right)^4}{\left(\mu^{II}\right)^2 \left(k^I\right)^4}\right]}} \\ y = \sqrt{\dfrac{\left(k^I\right)^2 - \left(k^{II}\right)^2}{\left[\dfrac{\left(\mu^{II}\right)^2 \left(k^I\right)^4 - \left(\mu^I\right)^2 \left(k^{II}\right)^4}{\left(\mu^{II}\right)^2 \left(k^I\right)^4}\right]}} \\ x^2 = \left(k^{II}\right)^2 - \dfrac{\left(\mu^I\right)^2 \left(k^{II}\right)^4 \left[\left(k^I\right)^2 - \left(k^{II}\right)^2\right]}{\left[\dfrac{\left(\mu^{II}\right)^2 \left(k^I\right)^4 - \left(\mu^I\right)^2 \left(k^{II}\right)^4}{1}\right]} = \left(k^{II}\right)^2 - \dfrac{\left(\mu^I\right)^2 \left(k^{II}\right)^4 \left(k^I\right)^2 - \left(\mu^I\right)^2 \left(k^{II}\right)^4 \left(k^{II}\right)^2}{\left(\mu^{II}\right)^2 \left(k^I\right)^4 - \left(\mu^I\right)^2 \left(k^{II}\right)^4} \end{cases}$$

(1. 10.11)

$$\begin{cases} z = \dfrac{\mu^I \left(k^{II}\right)^2}{\mu^{II} \left(k^I\right)^2} \sqrt{\dfrac{\left(\mu^{II}\right)^2 \left(k^I\right)^4 \left(k^I\right)^2 - \left(\mu^{II}\right)^2 \left(k^I\right)^4 \left(k^{II}\right)^2}{\left(\mu^{II}\right)^2 \left(k^I\right)^4 - \left(\mu^I\right)^2 \left(k^{II}\right)^4}} \\ y = \sqrt{\dfrac{\left(\mu^{II}\right)^2 \left(k^I\right)^4 \left(k^I\right)^2 - \left(\mu^{II}\right)^2 \left(k^I\right)^4 \left(k^{II}\right)^2}{\left(\mu^{II}\right)^2 \left(k^I\right)^4 - \left(\mu^I\right)^2 \left(k^{II}\right)^4}} \\ x^2 = \dfrac{\left(\mu^{II}\right)^2 \left(k^I\right)^4 \left(k^{II}\right)^2 \cancel{- \left(\mu^I\right)^2 \left(k^{II}\right)^4 \left(k^{II}\right)^2} - \left(\mu^I\right)^2 \left(k^{II}\right)^4 \left(k^I\right)^2 \cancel{+ \left(\mu^I\right)^2 \left(k^{II}\right)^4 \left(k^{II}\right)^2}}{\left(\mu^{II}\right)^2 \left(k^I\right)^4 - \left(\mu^I\right)^2 \left(k^{II}\right)^4} \end{cases}$$

(1. 10.12)

$$\begin{cases} k_z^{II} = z = \dfrac{\mu^I \left(k^{II}\right)^2}{\mu^{II}\left(k^I\right)^2}\sqrt{\dfrac{\left(\mu^{II}\right)^2\left(k^I\right)^4\left(k^I\right)^2 - \left(\mu^{II}\right)^2\left(k^I\right)^4\left(k^{II}\right)^2}{\left(\mu^{II}\right)^2\left(k^I\right)^4 - \left(\mu^I\right)^2\left(k^{II}\right)^4}} \\ k_z^I = y = \sqrt{\dfrac{\left(\mu^{II}\right)^2\left(k^I\right)^4\left(k^I\right)^2 - \left(\mu^{II}\right)^2\left(k^I\right)^4\left(k^{II}\right)^2}{\left(\mu^{II}\right)^2\left(k^I\right)^4 - \left(\mu^I\right)^2\left(k^{II}\right)^4}} \\ k_x = x = \sqrt{\dfrac{\left(\mu^{II}\right)^2\left(k^I\right)^4\left(k^{II}\right)^2 - \left(\mu^I\right)^2\left(k^{II}\right)^4\left(k^I\right)^2}{\left(\mu^{II}\right)^2\left(k^I\right)^4 - \left(\mu^I\right)^2\left(k^{II}\right)^4}} \end{cases}$$

(1. 10.13)

which, using the expression $\left(k^I\right)^2 = \omega^2\mu^I\varepsilon^I$, $\left(k^{II}\right)^2 = \omega^2\mu^{II}\varepsilon^{II}$ is equivalent to:

$$\begin{cases} k_z^{II} = z = \dfrac{\mu^I\omega^2\mu^{II}\varepsilon^{II}}{\mu^{II}\omega^2\mu^I\varepsilon^I}\sqrt{\dfrac{\left(\mu^{II}\right)^2\omega^4\left(\mu^I\varepsilon^I\right)^2\omega^2\left(\mu^I\varepsilon^I\right) - \left(\mu^{II}\right)^2\omega^4\left(\mu^I\varepsilon^I\right)^2\omega^2\left(\mu^{II}\varepsilon^{II}\right)}{\left(\mu^{II}\right)^2\omega^4\left(\mu^I\varepsilon^I\right)^2 - \left(\mu^I\right)^2\omega^4\left(\mu^{II}\varepsilon^{II}\right)^2}} \\ k_z^I = y = \sqrt{\dfrac{\left(\mu^{II}\right)^2\omega^4\left(\mu^I\varepsilon^I\right)^2\omega^2\left(\mu^I\varepsilon^I\right) - \left(\mu^{II}\right)^2\omega^4\left(\mu^I\varepsilon^I\right)^2\omega^2\left(\mu^{II}\varepsilon^{II}\right)}{\left(\mu^{II}\right)^2\omega^4\left(\mu^I\varepsilon^I\right)^2 - \left(\mu^I\right)^2\omega^4\left(\mu^{II}\varepsilon^{II}\right)^2}} \\ k_x = x = \sqrt{\dfrac{\left(\mu^{II}\right)^2\left(\omega^2\mu^I\varepsilon^I\right)^2\omega^2\mu^{II}\varepsilon^{II} - \left(\mu^I\right)^2\left(\omega^2\mu^{II}\varepsilon^{II}\right)^2\omega^2\mu^I\varepsilon^I}{\left(\mu^{II}\right)^2\left(\omega^2\mu^I\varepsilon^I\right)^2 - \left(\mu^I\right)^2\left(\omega^2\mu^{II}\varepsilon^{II}\right)^2}} = \\ \quad = \sqrt{\dfrac{\left(\mu^{II}\right)^2\omega^4\left(\mu^I\varepsilon^I\right)^2\omega^2\left(\mu^{II}\varepsilon^{II}\right) - \left(\mu^I\right)^2\omega^4\left(\mu^{II}\varepsilon^{II}\right)^2\omega^2\left(\mu^I\varepsilon^I\right)}{\left(\mu^{II}\right)^2\omega^4\left(\mu^I\varepsilon^I\right)^2 - \left(\mu^I\right)^2\omega^4\left(\mu^{II}\varepsilon^{II}\right)^2}} = \\ \quad = \sqrt{\dfrac{\left(\mu^{II}\right)^2\omega^4\left(\mu^I\right)^2\left(\varepsilon^I\right)^2\omega^2\left(\mu^{II}\right)\left(\varepsilon^{II}\right) - \left(\mu^I\right)^2\omega^4\left(\mu^{II}\right)^2\left(\varepsilon^{II}\right)^2\omega^2\left(\mu^I\right)\left(\varepsilon^I\right)}{\left(\mu^{II}\right)^2\omega^4\left(\mu^I\right)^2\left(\varepsilon^I\right)^2 - \left(\mu^I\right)^2\omega^4\left(\mu^{II}\right)^2\left(\varepsilon^{II}\right)^2}} \\ \quad = \omega\sqrt{\dfrac{\left(\varepsilon^I\right)^2\left(\mu^{II}\right)\left(\varepsilon^{II}\right) - \left(\varepsilon^{II}\right)^2\left(\mu^I\right)\left(\varepsilon^I\right)}{\left(\varepsilon^I\right)^2 - \left(\varepsilon^{II}\right)^2}} \end{cases}$$

(1. 10.14)

which is equivalent to:

$$\begin{cases} k_z^{II} = z = \omega \dfrac{\varepsilon^{II}}{\varepsilon^{I}} \sqrt{\dfrac{\left(\varepsilon^{I}\right)^2\left(\mu^{I}\varepsilon^{I}\right)-\left(\varepsilon^{I}\right)^2\left(\mu^{II}\varepsilon^{II}\right)}{\left(\varepsilon^{I}\right)^2-\left(\varepsilon^{II}\right)^2}} = \omega\varepsilon^{II}\sqrt{\dfrac{\left(\mu^{I}\varepsilon^{I}\right)-\left(\mu^{II}\varepsilon^{II}\right)}{\left(\varepsilon^{I}\right)^2-\left(\varepsilon^{II}\right)^2}} \\ k_z^{I} = y = \omega\sqrt{\dfrac{\left(\varepsilon^{I}\right)^2\left(\mu^{I}\varepsilon^{I}\right)-\left(\varepsilon^{I}\right)^2\left(\mu^{II}\varepsilon^{II}\right)}{\left(\varepsilon^{I}\right)^2-\left(\varepsilon^{II}\right)^2}} = \omega\varepsilon^{I}\sqrt{\dfrac{\left(\mu^{I}\varepsilon^{I}\right)-\left(\mu^{II}\varepsilon^{II}\right)}{\left(\varepsilon^{I}\right)^2-\left(\varepsilon^{II}\right)^2}} \\ k_x = x = \omega\sqrt{\dfrac{\left(\varepsilon^{I}\right)^2\left(\mu^{II}\varepsilon^{II}\right)-\left(\varepsilon^{II}\right)^2\left(\mu^{I}\varepsilon^{I}\right)}{\left(\varepsilon^{I}\right)^2-\left(\varepsilon^{II}\right)^2}} \end{cases}$$

(1. 10.15)

In a scenario where $\mu^{I} = \mu^{II} = \mu_0$, we can rewrite the expressions of wave numbers as:

$$\begin{cases} k_z^{II} = z = \omega \dfrac{\varepsilon^{II}}{\varepsilon^{I}} \sqrt{\mu_0}\sqrt{\dfrac{\left(\varepsilon^{I}\right)^2\left(\varepsilon^{I}\right)-\left(\varepsilon^{I}\right)^2\left(\varepsilon^{II}\right)}{\left(\varepsilon^{I}\right)^2-\left(\varepsilon^{II}\right)^2}} = \omega\dfrac{\varepsilon^{II}}{\varepsilon^{I}}\sqrt{\mu_0}\sqrt{\dfrac{\left(\varepsilon^{I}\right)^2\left[\left(\varepsilon^{I}\right)-\left(\varepsilon^{II}\right)\right]}{\left[\left(\varepsilon^{I}\right)-\left(\varepsilon^{II}\right)\right]\left[\left(\varepsilon^{I}\right)+\left(\varepsilon^{II}\right)\right]}} \\ k_z^{I} = y = \omega\sqrt{\mu_0}\sqrt{\dfrac{\left(\varepsilon^{I}\right)^2\left[\left(\varepsilon^{I}\right)-\left(\varepsilon^{II}\right)\right]}{\left[\left(\varepsilon^{I}\right)-\left(\varepsilon^{II}\right)\right]\left[\left(\varepsilon^{I}\right)+\left(\varepsilon^{II}\right)\right]}} = \omega\sqrt{\mu_0}\sqrt{\dfrac{\left(\varepsilon^{I}\right)^2}{\left[\left(\varepsilon^{I}\right)+\left(\varepsilon^{II}\right)\right]}} \\ k_x = x = \omega\sqrt{\mu_0}\sqrt{\dfrac{\left(\varepsilon^{I}\right)^2\left(\varepsilon^{II}\right)-\left(\varepsilon^{II}\right)^2\left(\varepsilon^{I}\right)}{\left(\varepsilon^{I}\right)^2-\left(\varepsilon^{II}\right)^2}} = \omega\sqrt{\mu_0}\sqrt{\dfrac{\left(\varepsilon^{I}\right)^2\left(\varepsilon^{II}\right)-\left(\varepsilon^{II}\right)^2\left(\varepsilon^{I}\right)}{\left[\left(\varepsilon^{I}\right)-\left(\varepsilon^{II}\right)\right]\left[\left(\varepsilon^{I}\right)+\left(\varepsilon^{II}\right)\right]}} \end{cases}$$

(1. 10.16)

$$\begin{cases} k_z^{II} = z = \omega \dfrac{\varepsilon^{II}}{\varepsilon^{I}} \sqrt{\mu_0}\sqrt{\dfrac{\left(\varepsilon^{I}\right)^2\left(\varepsilon^{I}\right)-\left(\varepsilon^{I}\right)^2\left(\varepsilon^{II}\right)}{\left(\varepsilon^{I}\right)^2-\left(\varepsilon^{II}\right)^2}} = \omega\dfrac{\varepsilon^{II}}{\varepsilon^{I}}\dfrac{\sqrt{\mu_0}\left(\varepsilon^{I}\right)}{\sqrt{\left[\left(\varepsilon^{I}\right)+\left(\varepsilon^{II}\right)\right]}} = \dfrac{\omega\varepsilon^{II}\sqrt{\mu_0}}{\sqrt{\varepsilon^{I}+\varepsilon^{II}}} \\ k_z^{I} = y = \omega\sqrt{\mu_0}\sqrt{\dfrac{\left(\varepsilon^{I}\right)^2\left[\left(\varepsilon^{I}\right)-\left(\varepsilon^{II}\right)\right]}{\left[\left(\varepsilon^{I}\right)-\left(\varepsilon^{II}\right)\right]\left[\left(\varepsilon^{I}\right)+\left(\varepsilon^{II}\right)\right]}} = \dfrac{\omega\varepsilon^{I}\sqrt{\mu_0}}{\sqrt{\varepsilon^{I}+\varepsilon^{II}}} \\ k_x = x = \omega\sqrt{\mu_0}\sqrt{\dfrac{\left(\varepsilon^{I}\right)^2\left(\varepsilon^{II}\right)-\left(\varepsilon^{II}\right)^2\left(\varepsilon^{I}\right)}{\left(\varepsilon^{I}\right)^2-\left(\varepsilon^{II}\right)^2}} = \omega\sqrt{\mu_0}\sqrt{\dfrac{\left(\varepsilon^{I}\right)^2\left(\varepsilon^{II}\right)-\left(\varepsilon^{I}\right)\left(\varepsilon^{II}\right)^2}{\left[\left(\varepsilon^{I}\right)-\left(\varepsilon^{II}\right)\right]\left[\left(\varepsilon^{I}\right)+\left(\varepsilon^{II}\right)\right]}} \end{cases}$$

(1. 10.17)

$$\begin{cases} k_z^{II} = z = \omega\dfrac{\varepsilon^{II}}{\varepsilon^{I}}\sqrt{\mu_0}\sqrt{\dfrac{\left(\varepsilon^{I}\right)^2\left(\varepsilon^{I}\right)-\left(\varepsilon^{I}\right)^2\left(\varepsilon^{II}\right)}{\left(\varepsilon^{I}\right)^2-\left(\varepsilon^{II}\right)^2}} = \omega\dfrac{\varepsilon^{II}}{\varepsilon^{I}}\dfrac{\sqrt{\mu_0}\left(\varepsilon^{I}\right)}{\sqrt{\left[\left(\varepsilon^{I}\right)+\left(\varepsilon^{II}\right)\right]}} = \dfrac{\omega\varepsilon^{II}\sqrt{\mu_0}}{\sqrt{\varepsilon^{I}+\varepsilon^{II}}} \\ k_z^{I} = y = \omega\sqrt{\mu_0}\sqrt{\dfrac{\left(\varepsilon^{I}\right)^2\left[\left(\varepsilon^{I}\right)-\left(\varepsilon^{II}\right)\right]}{\left[\left(\varepsilon^{I}\right)-\left(\varepsilon^{II}\right)\right]\left[\left(\varepsilon^{I}\right)+\left(\varepsilon^{II}\right)\right]}} = \dfrac{\omega\varepsilon^{I}\sqrt{\mu_0}}{\sqrt{\varepsilon^{I}+\varepsilon^{II}}} \\ k_x = x = \omega\sqrt{\mu_0}\sqrt{\dfrac{\left(\varepsilon^{I}\right)^2\left(\varepsilon^{II}\right)-\left(\varepsilon^{I}\right)\left(\varepsilon^{II}\right)^2}{\left[\left(\varepsilon^{I}\right)-\left(\varepsilon^{II}\right)\right]\left[\left(\varepsilon^{I}\right)+\left(\varepsilon^{II}\right)\right]}} = \omega\sqrt{\mu_0}\sqrt{\dfrac{\left(\varepsilon^{I}\right)\left(\varepsilon^{II}\right)\left[\left(\varepsilon^{I}\right)-\left(\varepsilon^{II}\right)\right]}{\left[\left(\varepsilon^{I}\right)-\left(\varepsilon^{II}\right)\right]\left[\left(\varepsilon^{I}\right)+\left(\varepsilon^{II}\right)\right]}} \end{cases}$$

(1. 10.18)

$$\begin{cases} k_z^{II} = z = \omega\dfrac{\varepsilon^{II}}{\varepsilon^{I}}\sqrt{\mu_0}\sqrt{\dfrac{\left(\varepsilon^{I}\right)^2\left(\varepsilon^{I}\right)-\left(\varepsilon^{I}\right)^2\left(\varepsilon^{II}\right)}{\left(\varepsilon^{I}\right)^2-\left(\varepsilon^{II}\right)^2}} = \omega\dfrac{\varepsilon^{II}}{\varepsilon^{I}}\dfrac{\sqrt{\mu_0}\left(\varepsilon^{I}\right)}{\sqrt{\left[\left(\varepsilon^{I}\right)+\left(\varepsilon^{II}\right)\right]}} = \dfrac{\omega\varepsilon^{II}\sqrt{\mu_0}}{\sqrt{\varepsilon^{I}+\varepsilon^{II}}} \\ k_z^{I} = y = \omega\sqrt{\mu_0}\sqrt{\dfrac{\left(\varepsilon^{I}\right)^2\left[\left(\varepsilon^{I}\right)-\left(\varepsilon^{II}\right)\right]}{\left[\left(\varepsilon^{I}\right)-\left(\varepsilon^{II}\right)\right]\left[\left(\varepsilon^{I}\right)+\left(\varepsilon^{II}\right)\right]}} = \dfrac{\omega\varepsilon^{I}\sqrt{\mu_0}}{\sqrt{\varepsilon^{I}+\varepsilon^{II}}} \\ k_x = x = \omega\sqrt{\mu_0}\sqrt{\dfrac{\left(\varepsilon^{I}\right)^2\left(\varepsilon^{II}\right)-\left(\varepsilon^{I}\right)\left(\varepsilon^{II}\right)^2}{\left[\left(\varepsilon^{I}\right)-\left(\varepsilon^{II}\right)\right]\left[\left(\varepsilon^{I}\right)+\left(\varepsilon^{II}\right)\right]}} = \omega\sqrt{\mu_0}\sqrt{\dfrac{\left(\varepsilon^{I}\right)\left(\varepsilon^{II}\right)}{\left[\left(\varepsilon^{I}\right)+\left(\varepsilon^{II}\right)\right]}} \end{cases}$$

(1. 10.19)

If both media are lossless, then both $\mathbf{k}^{I},\mathbf{k}^{II}$ are real and equations (1.10.19) yield the usual Brewster angle formulas, that is,

$$\tan\theta_{TM}^{I} = \frac{k_x}{k_z^{I}} = \frac{\omega\sqrt{\mu_0}\sqrt{\dfrac{\left(\varepsilon^{I}\right)\left(\varepsilon^{II}\right)}{\left[\left(\varepsilon^{I}\right)+\left(\varepsilon^{II}\right)\right]}}}{\dfrac{\omega\varepsilon^{I}\sqrt{\mu_0}}{\sqrt{\varepsilon^{I}+\varepsilon^{II}}}} = \frac{\dfrac{\sqrt{\varepsilon^{I}}\sqrt{\varepsilon^{II}}}{\sqrt{\varepsilon^{I}+\varepsilon^{II}}}}{\dfrac{\varepsilon^{I}}{\sqrt{\varepsilon^{I}+\varepsilon^{II}}}} = \frac{\sqrt{\varepsilon^{II}}}{\sqrt{\varepsilon^{I}}} = \frac{n^{II}}{n^{I}}$$

$$\tan\theta_{TM}^{II} = \frac{k_x}{k_z^{II}} = \frac{n^{I}}{n^{II}}$$

(1. 10.20)

where θ^{I} is the Brewster angle seen from media on the left side before the interface while θ^{II} is the Brewster angle seen from media on the right side after the interface.

Using $k_x^I = k_x^{II} = k_x = \beta_x - j\alpha_x$ the space-dependence of the fields at the two sides is as follows:

$$e^{-j\left(k_x^I x + k_z^I z\right)} = e^{-j\left[\left(\beta_x^I x - j\alpha_x^I x\right) + \left(\beta_z^I z - j\alpha_z^I z\right)\right]} = e^{-\left(\alpha_x^I x + \alpha_z^I z\right)} e^{-j\left(\beta_x^I x + \beta_z^I z\right)} \qquad \text{for } z \le 0$$

(1. 10.21)

$$e^{-j\left(k_x^{II} x + k_z^{II} z\right)} = e^{-j\left[\left(\beta_x^{II} x - j\alpha_x^{II} x\right) + \left(\beta_z^{II} z - j\alpha_z^{II} z\right)\right]} = e^{-\left(\alpha_x^{II} x + \alpha_z^{II} z\right)} e^{-j\left(\beta_x^{II} x + \beta_z^{II} z\right)} \qquad \text{for } z \ge 0$$

(1. 10.22)

Thus, in order for the fields not to grow exponentially with distance and to be confined near the interface it must be:

$$\boxed{\alpha_x^I = \alpha_x^{II} > 0, \quad \alpha_z^I < 0, \quad \alpha_z^{II} > 0}$$

(1. 10.23)

Now in order to rewrite the (1.10.15) separating the real and imaginary part of wave number, we can replace permittivity and permeability using their complex number in order to take into account for real and imaginary part:

$$\begin{cases} k_z^{II} = z = \omega\varepsilon^{II}\sqrt{\dfrac{\left(\mu^I\varepsilon^I\right) - \left(\mu^{II}\varepsilon^{II}\right)}{\left(\varepsilon^I\right)^2 - \left(\varepsilon^{II}\right)^2}} = \omega\left(\varepsilon_r^{II} - j\varepsilon_i^{II}\right)\sqrt{\dfrac{\left(\mu_r^I - j\mu_i^I\right)\left(\varepsilon_r^I - j\varepsilon_i^I\right) - \left(\mu_r^{II} - j\mu_i^{II}\right)\left(\varepsilon_r^{II} - j\varepsilon_i^{II}\right)}{\left(\varepsilon_r^I - j\varepsilon_i^I\right)^2 - \left(\varepsilon_r^{II} - j\varepsilon_i^{II}\right)^2}} \\ k_z^I = \omega\varepsilon^I\sqrt{\dfrac{\left(\mu^I\varepsilon^I\right) - \left(\mu^{II}\varepsilon^{II}\right)}{\left(\varepsilon^I\right)^2 - \left(\varepsilon^{II}\right)^2}} = \omega\left(\varepsilon_r^I - j\varepsilon_i^I\right)\sqrt{\dfrac{\left(\mu_r^I - j\mu_i^I\right)\left(\varepsilon_r^I - j\varepsilon_i^I\right) - \left(\mu_r^{II} - j\mu_i^{II}\right)\left(\varepsilon_r^{II} - j\varepsilon_i^{II}\right)}{\left(\varepsilon_r^I - j\varepsilon_i^I\right)^2 - \left(\varepsilon_r^{II} - j\varepsilon_i^{II}\right)^2}} \\ k_x = \omega\sqrt{\dfrac{\left(\varepsilon^I\right)^2\left(\mu^{II}\varepsilon^{II}\right) - \left(\varepsilon^{II}\right)^2\left(\mu^I\varepsilon^I\right)}{\left(\varepsilon^I\right)^2 - \left(\varepsilon^{II}\right)^2}} = \\ \quad = \omega\sqrt{\dfrac{\left(\varepsilon_r^I - j\varepsilon_i^I\right)^2\left(\mu_r^{II} - j\mu_i^{II}\right)\left(\varepsilon_r^{II} - j\varepsilon_i^{II}\right) - \left(\varepsilon_r^{II} - j\varepsilon_i^{II}\right)^2\left(\mu_r^I - j\mu_i^I\right)\left(\varepsilon_r^I - j\varepsilon_i^I\right)}{\left(\varepsilon_r^I - j\varepsilon_i^I\right)^2 - \left(\varepsilon_r^{II} - j\varepsilon_i^{II}\right)^2}} \end{cases}$$

(1. 10.24)

$$\begin{cases} k_z^{II} = \omega\left(\varepsilon_r^{II} - j\varepsilon_i^{II}\right)\sqrt{\dfrac{\mu_r^I\varepsilon_r^I - j\mu_r^I\varepsilon_i^I - j\mu_i^I\varepsilon_r^I - \mu_i^I\varepsilon_i^I - \mu_r^{II}\varepsilon_r^{II} + j\mu_r^{II}\varepsilon_i^{II} + j\mu_i^{II}\varepsilon_r^{II} + \mu_i^{II}\varepsilon_i^{II}}{\left(\varepsilon_r^I\right)^2 - \left(\varepsilon_i^I\right)^2 - 2j\varepsilon_r^I\varepsilon_i^I - \left(\varepsilon_r^{II}\right)^2 + \left(\varepsilon_i^{II}\right)^2 + 2j\varepsilon_r^{II}\varepsilon_i^{II}}} \\ k_z^I = \omega\left(\varepsilon_r^I - j\varepsilon_i^I\right)\sqrt{\dfrac{\mu_r^I\varepsilon_r^I - j\mu_r^I\varepsilon_i^I - j\mu_i^I\varepsilon_r^I - \mu_i^I\varepsilon_i^I - \mu_r^{II}\varepsilon_r^{II} + j\mu_r^{II}\varepsilon_i^{II} + j\mu_i^{II}\varepsilon_r^{II} + \mu_i^{II}\varepsilon_i^{II}}{\left(\varepsilon_r^I\right)^2 - \left(\varepsilon_i^I\right)^2 - 2j\varepsilon_r^I\varepsilon_i^I - \left(\varepsilon_r^{II}\right)^2 + \left(\varepsilon_i^{II}\right)^2 + 2j\varepsilon_r^{II}\varepsilon_i^{II}}} \\ k_x = \sqrt{\dfrac{\left[\left(\varepsilon_r^I\right)^2 - \left(\varepsilon_i^I\right)^2 - 2j\varepsilon_r^I\varepsilon_i^I\right]\left[\mu_r^{II}\varepsilon_r^{II} - j\mu_r^{II}\varepsilon_i^{II} - j\mu_i^{II}\varepsilon_r^{II} - \mu_i^{II}\varepsilon_i^{II}\right] + \\ -\left[\left(\varepsilon_r^{II}\right)^2 - \left(\varepsilon_i^{II}\right)^2 - 2j\varepsilon_r^{II}\varepsilon_i^{II}\right]\left[\mu_r^I\varepsilon_r^I - j\mu_r^I\varepsilon_i^I - j\mu_i^I\varepsilon_r^I - \mu_i^I\varepsilon_i^I\right]}{\left(\varepsilon_r^I\right)^2 - \left(\varepsilon_i^I\right)^2 - 2j\varepsilon_r^I\varepsilon_i^I - \left(\varepsilon_r^{II}\right)^2 + \left(\varepsilon_i^{II}\right)^2 + 2j\varepsilon_r^{II}\varepsilon_i^{II}}} \end{cases}$$

(1. 10.26)

$$k_z^{II} = \omega\left(\varepsilon_r^{II} - j\varepsilon_i^{II}\right)\sqrt{\dfrac{\left(\mu_r^I\varepsilon_r^I - \mu_i^I\varepsilon_i^I - \mu_r^{II}\varepsilon_r^{II} + \mu_i^{II}\varepsilon_i^{II}\right) - j\left(\mu_r^I\varepsilon_i^I + \mu_i^I\varepsilon_r^I - \mu_r^{II}\varepsilon_i^{II} - \mu_i^{II}\varepsilon_r^{II}\right)}{\left(\varepsilon_r^I\right)^2 - \left(\varepsilon_i^I\right)^2 - \left(\varepsilon_r^{II}\right)^2 + \left(\varepsilon_i^{II}\right)^2 - 2j\left(\varepsilon_r^I\varepsilon_i^I - \varepsilon_r^{II}\varepsilon_i^{II}\right)}}$$

$$k_z^I = \omega\left(\varepsilon_r^I - j\varepsilon_i^I\right)\sqrt{\dfrac{\left(\mu_r^I\varepsilon_r^I - \mu_i^I\varepsilon_i^I - \mu_r^{II}\varepsilon_r^{II} + \mu_i^{II}\varepsilon_i^{II}\right) - j\left(\mu_r^I\varepsilon_i^I + \mu_i^I\varepsilon_r^I - \mu_r^{II}\varepsilon_i^{II} - \mu_i^{II}\varepsilon_r^{II}\right)}{\left(\varepsilon_r^I\right)^2 - \left(\varepsilon_i^I\right)^2 - \left(\varepsilon_r^{II}\right)^2 + \left(\varepsilon_i^{II}\right)^2 - 2j\left(\varepsilon_r^I\varepsilon_i^I - \varepsilon_r^{II}\varepsilon_i^{II}\right)}}$$

$$k_x = \sqrt{\dfrac{\begin{array}{l} +\left[\left(\varepsilon_r^I\right)^2\mu_r^{II}\varepsilon_r^{II} - j\left(\varepsilon_r^I\right)^2\mu_r^{II}\varepsilon_i^{II} - j\left(\varepsilon_r^I\right)^2\mu_i^{II}\varepsilon_r^{II} - j\left(\varepsilon_r^I\right)^2\mu_i^{II}\varepsilon_i^{II}\right] + \\ -\left[\left(\varepsilon_i^I\right)^2\mu_r^{II}\varepsilon_r^{II} - j\left(\varepsilon_i^I\right)^2\mu_r^{II}\varepsilon_i^{II} - j\left(\varepsilon_i^I\right)^2\mu_i^{II}\varepsilon_r^{II} - j\left(\varepsilon_i^I\right)^2\mu_i^{II}\varepsilon_i^{II}\right] + \\ -2\left[j\varepsilon_r^{II}\varepsilon_i^{II}\mu_r^{II}\varepsilon_r^{II} + \varepsilon_r^{II}\varepsilon_i^{II}\mu_r^{II}\varepsilon_i^{II} + \varepsilon_r^{II}\varepsilon_i^{II}\mu_i^{II}\varepsilon_r^{II} + \varepsilon_r^{II}\varepsilon_i^{II}\mu_i^{II}\varepsilon_i^{II}\right] + \\ -\left[\left(\varepsilon_r^{II}\right)^2\mu_r^I\varepsilon_r^I - j\left(\varepsilon_r^{II}\right)^2\mu_r^I\varepsilon_i^I - j\left(\varepsilon_r^{II}\right)^2\mu_i^I\varepsilon_r^I - j\left(\varepsilon_r^{II}\right)^2\mu_i^I\varepsilon_i^I\right] + \\ +\left[\left(\varepsilon_i^{II}\right)^2\mu_r^I\varepsilon_r^I - j\left(\varepsilon_i^{II}\right)^2\mu_r^I\varepsilon_i^I - j\left(\varepsilon_i^{II}\right)^2\mu_i^I\varepsilon_r^I - j\left(\varepsilon_i^{II}\right)^2\mu_i^I\varepsilon_i^I\right] + \\ +2\left[j\varepsilon_r^I\varepsilon_i^I\mu_r^I\varepsilon_r^I + \varepsilon_r^I\varepsilon_i^I\mu_r^I\varepsilon_i^I + \varepsilon_r^I\varepsilon_i^I\mu_i^I\varepsilon_r^I + \varepsilon_r^I\varepsilon_i^I\mu_i^I\varepsilon_i^I\right] \end{array}}{\left(\varepsilon_r^I\right)^2 - \left(\varepsilon_i^I\right)^2 - \left(\varepsilon_r^{II}\right)^2 + \left(\varepsilon_i^{II}\right)^2 - 2j\left(\varepsilon_r^I\varepsilon_i^I - \varepsilon_r^{II}\varepsilon_i^{II}\right)}}$$

(1. 10.27)

$$k_z^{II} = \omega\left(\varepsilon_r^{II} - j\varepsilon_i^{II}\right)\sqrt{\frac{\left(\mu_r^I\varepsilon_r^I - \mu_i^I\varepsilon_i^I - \mu_r^{II}\varepsilon_r^{II} + \mu_i^{II}\varepsilon_i^{II}\right) - j\left(\mu_r^I\varepsilon_i^I + \mu_i^I\varepsilon_r^I - \mu_r^{II}\varepsilon_i^{II} - \mu_i^{II}\varepsilon_r^{II}\right)}{\left(\varepsilon_r^I\right)^2 - \left(\varepsilon_i^I\right)^2 - \left(\varepsilon_r^{II}\right)^2 + \left(\varepsilon_i^{II}\right)^2 - 2j\left(\varepsilon_r^I\varepsilon_i^I - \varepsilon_r^{II}\varepsilon_i^{II}\right)}}$$

$$k_z^I = \omega\left(\varepsilon_r^I - j\varepsilon_i^I\right)\sqrt{\frac{\left(\mu_r^I\varepsilon_r^I - \mu_i^I\varepsilon_i^I - \mu_r^{II}\varepsilon_r^{II} + \mu_i^{II}\varepsilon_i^{II}\right) - j\left(\mu_r^I\varepsilon_i^I + \mu_i^I\varepsilon_r^I - \mu_r^{II}\varepsilon_i^{II} - \mu_i^{II}\varepsilon_r^{II}\right)}{\left(\varepsilon_r^I\right)^2 - \left(\varepsilon_i^I\right)^2 - \left(\varepsilon_r^{II}\right)^2 + \left(\varepsilon_i^{II}\right)^2 - 2j\left(\varepsilon_r^I\varepsilon_i^I - \varepsilon_r^{II}\varepsilon_i^{II}\right)}}$$

$$k_x = \sqrt{\frac{\begin{aligned}&+\left[\left(\varepsilon_r^I\right)^2\mu_r^{II}\varepsilon_r^{II} - j\left(\varepsilon_r^I\right)^2\mu_r^{II}\varepsilon_i^{II} - j\left(\varepsilon_r^I\right)^2\mu_i^{II}\varepsilon_r^{II} - j\left(\varepsilon_r^I\right)^2\mu_i^{II}\varepsilon_i^{II}\right]+\\&+\left[-\left(\varepsilon_i^I\right)^2\mu_r^{II}\varepsilon_r^{II} + j\left(\varepsilon_i^I\right)^2\mu_r^{II}\varepsilon_i^{II} + j\left(\varepsilon_i^I\right)^2\mu_i^{II}\varepsilon_r^{II} + j\left(\varepsilon_i^I\right)^2\mu_i^{II}\varepsilon_i^{II}\right]+\\&+\left[-2j\varepsilon_r^{II}\varepsilon_i^{II}\mu_r^{II}\varepsilon_r^{II} - 2\varepsilon_r^{II}\varepsilon_i^{II}\mu_r^{II}\varepsilon_i^{II} - 2\varepsilon_r^{II}\varepsilon_i^{II}\mu_i^{II}\varepsilon_r^{II} - 2\varepsilon_r^{II}\varepsilon_i^{II}\mu_i^{II}\varepsilon_i^{II}\right]+\\&+\left[-\left(\varepsilon_r^{II}\right)^2\mu_r^I\varepsilon_r^I + j\left(\varepsilon_r^{II}\right)^2\mu_r^I\varepsilon_i^I + j\left(\varepsilon_r^{II}\right)^2\mu_i^I\varepsilon_r^I + j\left(\varepsilon_r^{II}\right)^2\mu_i^I\varepsilon_i^I\right]+\\&+\left[\left(\varepsilon_i^{II}\right)^2\mu_r^I\varepsilon_r^I - j\left(\varepsilon_i^{II}\right)^2\mu_r^I\varepsilon_i^I - j\left(\varepsilon_i^{II}\right)^2\mu_i^I\varepsilon_r^I - j\left(\varepsilon_i^{II}\right)^2\mu_i^I\varepsilon_i^I\right]+\\&+\left[2j\varepsilon_r^I\varepsilon_i^I\mu_r^I\varepsilon_r^I + 2\varepsilon_r^I\varepsilon_i^I\mu_r^I\varepsilon_i^I + 2\varepsilon_r^I\varepsilon_i^I\mu_i^I\varepsilon_r^I + 2\varepsilon_r^I\varepsilon_i^I\mu_i^I\varepsilon_i^I\right]\end{aligned}}{\left(\varepsilon_r^I\right)^2 - \left(\varepsilon_i^I\right)^2 - \left(\varepsilon_r^{II}\right)^2 + \left(\varepsilon_i^{II}\right)^2 - 2j\left(\varepsilon_r^I\varepsilon_i^I - \varepsilon_r^{II}\varepsilon_i^{II}\right)}}$$

(1. 10.28)

An in-house built Genetic Algorithm has been developed in order to find permittivity and permeability for an infinite extended layer made of lossy materials. The purpose of Objective function was to reduce as much as possible the reflection coefficient at the interface between free space and material for a certain frequency of the incoming electromagnetic wave. Electromagnetic wave is supposed in the incidence angular range 0÷90 deg.

Output of optimization process is the following example of dielectric interface where the media on the right of interface is a lossy dielectric as can be noticed by the imaginary part of permittivity greater than 0:

$\varepsilon^I = 1 + j0$

$\mu^I = 1 + j0$

$\varepsilon^{II} = 54.15 - j22.99$

$\mu^I = 1 + j0$

Frequency of incidence wave = 1 GHz;

Zenneck angle and Critical angle before and after the interface are:

$$\theta_B^I = \left|\arctan\left(\frac{n^{II}}{n^I}\right)\right| = \left|\arctan\left(\frac{\sqrt{54.15 - j22.99}}{1}\right)\right| = 82.7277^\circ$$

Since on the right of interface the medium is denser than medium on the left then

$$\theta_C^{II} = \arcsin\left(\frac{n^I}{n^{II}}\right) = \arcsin\left(\frac{1}{\sqrt{54.15 - j22.99}}\right) = 7.4896^\circ$$

Reflection and transmission coefficient are shown on Fig.(1.10.2) and (1.10.3)

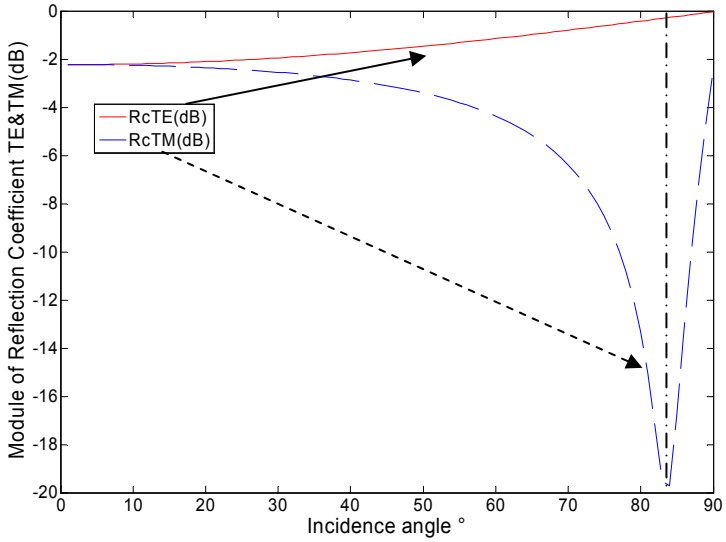

Fig.(1.10.2). Module in dB of reflection coefficient TE / TM

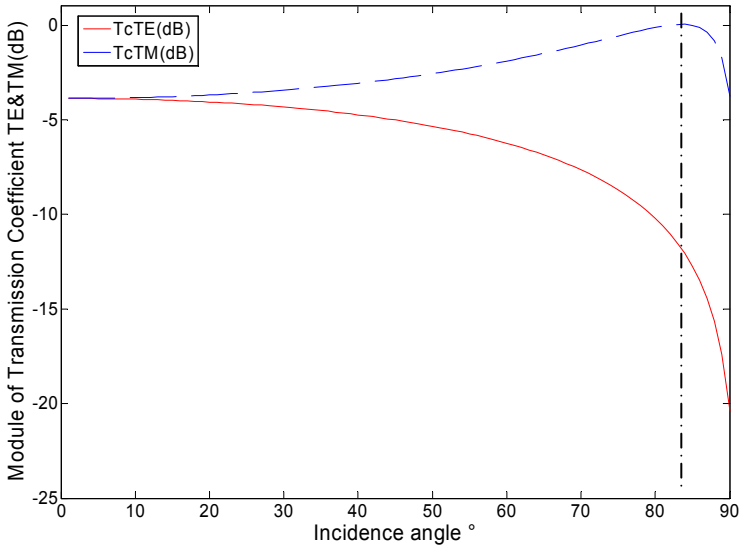

Fig.(1.10.3). Module in dB of transmission coefficient TE / TM

Transmission and reflection coefficients have been computed adopting matrix formalism shown in equations (1.1.33) and (1.1.42).

It is also useful to observe curves related to real and imaginary part of wavenumbers along *x* and *z* axes.

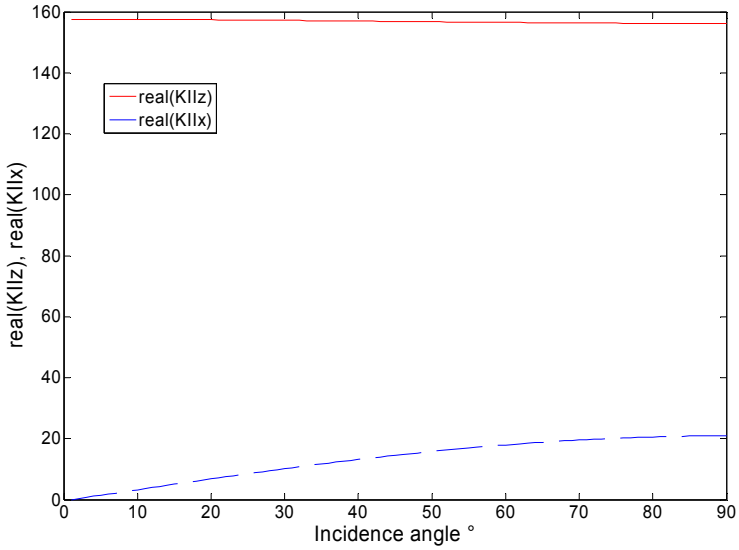

Fig.(1.10.4). Real part of wave number within the second medium on the right of interface

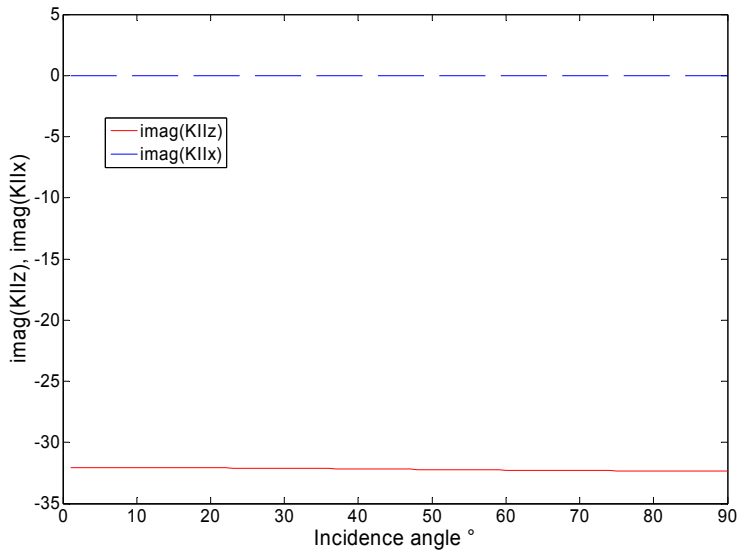

Fig.(1.10.5). Imaginary part of wave number within the second medium on the right of interface

In particular real part of *Kz* is greater than real part of *Kx* and this is mean that wave propagation phenomena is greater along *z* than along *x* direction. As far as imaginary part of wavenumber is concerned, it can be noticed that along *z* axes the value is

negative. Since for convention we decided to express the wave number as $k_z = \beta_z - j\alpha_z$ this mean that $\alpha_z > 0$.

As a consequence, along *z* axes the field changes as:

$$e^{-jk_z z} = e^{-j(\beta_z - j\alpha_z)z} = e^{-j\beta_z z} e^{-j(-j\alpha_z)z} = e^{-j\beta_z z} e^{-\alpha_z z} .$$

Along the *x* axes the field changes as

$$e^{-jk_x x} = e^{-j(\beta_x - j\alpha_x)x} = e^{-j\beta_x z} e^{-j(-j\alpha_x)x} = e^{-j\beta_x x} e^{-\alpha_x x}$$

$$\alpha_x = 0 \quad \Rightarrow \quad e^{-jk_x x} = e^{-j\beta_x x}$$

(1.10.24)

Eq.(1.10.24) seem to satisfy the conditions (1.10.23) of Zenneck surface waves except for $\alpha_x = 0$ which instead should be $\alpha_x > 0$ i.e., attenuation along *x* axes too.

In the similar way, for the ***TE case*** the condition $\rho_{TE} = 0$ require:

$$\boxed{\rho_{TE} = \frac{\eta_{TE}^{II} - \eta_{TE}^{I}}{\eta_{TE}^{II} + \eta_{TE}^{I}} = \frac{k_z^I \mu^{II} - k_z^{II} \mu^I}{k_z^I \mu^{II} + k_z^{II} \mu^I} = 0}$$

(1.10.25)

This condition is verified if the numerator is zeroed:

$$\mu^I k_z^{II} = \mu^{II} k_z^I$$

(1.10.26)

This condition may be rewritten in the equivalent form:

$$\omega^2 \varepsilon^I \varepsilon^{II} \mu^I k_z^{II} = \omega^2 \varepsilon^I \varepsilon^{II} \mu^{II} k_z^I$$

(1.10.27)

Which is equivalent to

$$\left(k^I\right)^2 k_z^{II} \varepsilon^{II} = \left(k^{II}\right)^2 k_z^I \varepsilon^I$$

(1.10.28)

Using the relations:

$$\left(k_x^I\right)^2+\left(k_z^I\right)^2=\left(k^I\right)^2$$
$$\left(k_x^{II}\right)^2+\left(k_z^{II}\right)^2=\left(k^{II}\right)^2$$

(1.10.29)

And since due to the boundary conditions $k_x^I=k_x^{II}$, the relation above can be rewritten as

$$\left(k_x\right)^2+\left(k_z^I\right)^2=\left(k^I\right)^2$$
$$\left(k_x\right)^2+\left(k_z^{II}\right)^2=\left(k^{II}\right)^2$$

(1.10.30)

Finally we can rewrite a system of three equations in three complex unknowns k_x,k_z^I,k_z^{II}:

$$\begin{cases}\left(k^I\right)^2 k_z^{II}\varepsilon^{II}=\left(k^{II}\right)^2 k_z^I\varepsilon^I\\ \left(k_x\right)^2+\left(k_z^I\right)^2=\left(k^I\right)^2\\ \left(k_x\right)^2+\left(k_z^{II}\right)^2=\left(k^{II}\right)^2\end{cases}$$

(1.10.31)

$$\begin{cases}\left(k^I\right)^2 z\varepsilon^{II}=\left(k^{II}\right)^2 y\varepsilon^I\\ (x)^2+(y)^2=\left(k^I\right)^2\\ (x)^2+(z)^2=\left(k^{II}\right)^2\end{cases}$$

(1.10.32)

then substituting the expression of *z* into third equation we have

$$\begin{cases}z=\dfrac{\varepsilon^I}{\varepsilon^{II}}\dfrac{\left(k^{II}\right)^2}{\left(k^I\right)^2}y\\ (x)^2+(y)^2=\left(k^I\right)^2\\ (x)^2=\left(k^{II}\right)^2-(z)^2=\left(k^{II}\right)^2-\dfrac{\left(\varepsilon^I\right)^2}{\left(\varepsilon^{II}\right)^2}\dfrac{\left(k^{II}\right)^4}{\left(k^I\right)^4}y^2\end{cases}$$

(1.10.33)

then substituting the expression of x into second equation we have

$$\begin{cases} z = \dfrac{\varepsilon^I}{\varepsilon^{II}} \dfrac{\left(k^{II}\right)^2}{\left(k^I\right)^2} y \\ (y)^2 = \left(k^I\right)^2 - (x)^2 = \left(k^I\right)^2 - \left(k^{II}\right)^2 + \dfrac{\left(\varepsilon^I\right)^2}{\left(\varepsilon^{II}\right)^2} \dfrac{\left(k^{II}\right)^4}{\left(k^I\right)^4} y^2 \\ (x)^2 = \left(k^{II}\right)^2 - (z)^2 = \left(k^{II}\right)^2 - \dfrac{\left(\varepsilon^I\right)^2}{\left(\varepsilon^{II}\right)^2} \dfrac{\left(k^{II}\right)^4}{\left(k^I\right)^4} y^2 \end{cases}$$

(1.10.34)

then, substituting y into first and third equation we have:

$$\begin{cases} z^2 = \dfrac{\left(\varepsilon^I\right)^2}{\left(\varepsilon^{II}\right)^2} \dfrac{\left(k^{II}\right)^4}{\left(k^I\right)^4} y^2 = \dfrac{\left(\varepsilon^I\right)^2}{\left(\varepsilon^{II}\right)^2} \dfrac{\left(k^{II}\right)^4}{\left(k^I\right)^4} \dfrac{\left(k^I\right)^2 - \left(k^{II}\right)^2}{\dfrac{\left(\varepsilon^{II}\right)^2\left(k^I\right)^4 - \left(\varepsilon^I\right)^2\left(k^{II}\right)^4}{\left(\varepsilon^{II}\right)^2\left(k^I\right)^4}} \\ y^2 - \dfrac{\left(\varepsilon^I\right)^2}{\left(\varepsilon^{II}\right)^2} \dfrac{\left(k^{II}\right)^4}{\left(k^I\right)^4} y^2 = \left(k^I\right)^2 - \left(k^{II}\right)^2 \quad \Rightarrow \quad y^2 = \dfrac{\left(k^I\right)^2 - \left(k^{II}\right)^2}{\dfrac{\left(\varepsilon^{II}\right)^2\left(k^I\right)^4 - \left(\varepsilon^I\right)^2\left(k^{II}\right)^4}{\left(\varepsilon^{II}\right)^2\left(k^I\right)^4}} \\ x^2 = \left(k^{II}\right)^2 - \dfrac{\left(\varepsilon^I\right)^2}{\left(\varepsilon^{II}\right)^2} \dfrac{\left(k^{II}\right)^4}{\left(k^I\right)^4} \dfrac{\left(k^I\right)^2 - \left(k^{II}\right)^2}{\dfrac{\left(\varepsilon^{II}\right)^2\left(k^I\right)^4 - \left(\varepsilon^I\right)^2\left(k^{II}\right)^4}{\left(\varepsilon^{II}\right)^2\left(k^I\right)^4}} \end{cases}$$

(1. 10.35)

$$\begin{cases} z^2 = \dfrac{\left(\varepsilon^I\right)^2\left(k^I\right)^2\left(k^{II}\right)^4 - \left(\varepsilon^I\right)^2\left(k^{II}\right)^2\left(k^{II}\right)^4}{\left(\varepsilon^{II}\right)^2\left(k^I\right)^4 - \left(\varepsilon^I\right)^2\left(k^{II}\right)^4} \\ y^2 = \dfrac{\left(\varepsilon^{II}\right)^2\left(k^I\right)^4\left(k^I\right)^2 - \left(\varepsilon^{II}\right)^2\left(k^I\right)^4\left(k^{II}\right)^2}{\left(\varepsilon^{II}\right)^2\left(k^I\right)^4 - \left(\varepsilon^I\right)^2\left(k^{II}\right)^4} \\ x^2 = \dfrac{\left(\varepsilon^{II}\right)^2\left(k^I\right)^4\left(k^{II}\right)^2 - \left(\varepsilon^I\right)^2\left(k^{II}\right)^4\left(k^{II}\right)^2}{\left(\varepsilon^{II}\right)^2\left(k^I\right)^4 - \left(\varepsilon^I\right)^2\left(k^{II}\right)^4} - \dfrac{\left(\varepsilon^I\right)^2\left(k^I\right)^2\left(k^{II}\right)^4 - \left(\varepsilon^I\right)^2\left(k^{II}\right)^2\left(k^{II}\right)^4}{\left(\varepsilon^{II}\right)^2\left(k^I\right)^4 - \left(\varepsilon^I\right)^2\left(k^{II}\right)^4} \end{cases}$$

(1. 10.36)

$$\begin{cases} z^2 = \dfrac{\left(\varepsilon^I\right)^2\left(k^I\right)^2\left(k^{II}\right)^4 - \left(\varepsilon^I\right)^2\left(k^{II}\right)^2\left(k^{II}\right)^4}{\left(\varepsilon^{II}\right)^2\left(k^I\right)^4 - \left(\varepsilon^I\right)^2\left(k^{II}\right)^4} \\ y^2 = \dfrac{\left(\varepsilon^{II}\right)^2\left(k^I\right)^4\left(k^I\right)^2 - \left(\varepsilon^{II}\right)^2\left(k^I\right)^4\left(k^{II}\right)^2}{\left(\varepsilon^{II}\right)^2\left(k^I\right)^4 - \left(\varepsilon^I\right)^2\left(k^{II}\right)^4} \\ x^2 = \dfrac{\left(\varepsilon^{II}\right)^2\left(k^I\right)^4\left(k^{II}\right)^2 - \cancel{\left(\varepsilon^I\right)^2\left(k^{II}\right)^4\left(k^{II}\right)^2} - \left(\varepsilon^I\right)^2\left(k^I\right)^2\left(k^{II}\right)^4 + \cancel{\left(\varepsilon^I\right)^2\left(k^{II}\right)^2\left(k^{II}\right)^4}}{\left(\varepsilon^{II}\right)^2\left(k^I\right)^4 - \left(\varepsilon^I\right)^2\left(k^{II}\right)^4} \end{cases}$$

(1. 10.37)

$$\begin{cases} z^2 = \dfrac{\left(\varepsilon^I\right)^2\left(k^I\right)^2\left(k^{II}\right)^4 - \left(\varepsilon^I\right)^2\left(k^{II}\right)^2\left(k^{II}\right)^4}{\left(\varepsilon^{II}\right)^2\left(k^I\right)^4 - \left(\varepsilon^I\right)^2\left(k^{II}\right)^4} \\ y^2 = \dfrac{\left(\varepsilon^{II}\right)^2\left(k^I\right)^4\left(k^I\right)^2 - \left(\varepsilon^{II}\right)^2\left(k^I\right)^4\left(k^{II}\right)^2}{\left(\varepsilon^{II}\right)^2\left(k^I\right)^4 - \left(\varepsilon^I\right)^2\left(k^{II}\right)^4} \\ x^2 = \dfrac{\left(\varepsilon^{II}\right)^2\left(k^I\right)^4\left(k^{II}\right)^2 - \left(\varepsilon^I\right)^2\left(k^I\right)^2\left(k^{II}\right)^4}{\left(\varepsilon^{II}\right)^2\left(k^I\right)^4 - \left(\varepsilon^I\right)^2\left(k^{II}\right)^4} \end{cases}$$

(1. 10.38)

which using the expression $\left(k^I\right)^2 = \omega^2\mu^I\varepsilon^I$, $\left(k^{II}\right)^2 = \omega^2\mu^{II}\varepsilon^{II}$ and $x = k_x$, $y = k_z^I$, $z = k_z^{II}$: is equivalent to:

$$\begin{cases} k_z^{II} = \sqrt{\dfrac{\left(\varepsilon^I\right)^2\left(\omega^2\mu^I\varepsilon^I\right)\left(\omega^2\mu^{II}\varepsilon^{II}\right)^2 - \left(\varepsilon^I\right)^2\left(\omega^2\mu^{II}\varepsilon^{II}\right)\left(\omega^2\mu^{II}\varepsilon^{II}\right)^2}{\left(\varepsilon^{II}\right)^2\left(\omega^2\mu^I\varepsilon^I\right)^2 - \left(\varepsilon^I\right)^2\left(\omega^2\mu^{II}\varepsilon^{II}\right)^2}} \\ k_z^I = \sqrt{\dfrac{\left(\varepsilon^{II}\right)^2\left(\omega^2\mu^I\varepsilon^I\right)^2\left(\omega^2\mu^I\varepsilon^I\right) - \left(\varepsilon^{II}\right)^2\left(\omega^2\mu^I\varepsilon^I\right)^2\left(\omega^2\mu^{II}\varepsilon^{II}\right)}{\left(\varepsilon^{II}\right)^2\left(\omega^2\mu^I\varepsilon^I\right)^2 - \left(\varepsilon^I\right)^2\left(\omega^2\mu^{II}\varepsilon^{II}\right)^2}} \\ k_x = \sqrt{\dfrac{\left(\varepsilon^{II}\right)^2\left(\omega^2\mu^I\varepsilon^I\right)^2\left(\omega^2\mu^{II}\varepsilon^{II}\right) - \left(\varepsilon^I\right)^2\left(\omega^2\mu^I\varepsilon^I\right)\left(\omega^2\mu^{II}\varepsilon^{II}\right)^2}{\left(\varepsilon^{II}\right)^2\left(\omega^2\mu^I\varepsilon^I\right)^2 - \left(\varepsilon^I\right)^2\left(\omega^2\mu^{II}\varepsilon^{II}\right)^2}} \end{cases}$$

(1. 10.39)

$$\begin{cases} k_z^{II} = \sqrt{\dfrac{\left(\varepsilon^I\right)^2\omega^2\left(\mu^I\right)\left(\varepsilon^I\right)\omega^4\left(\mu^{II}\right)^2\left(\varepsilon^{II}\right)^2-\omega^2\left(\varepsilon^I\right)^2\omega^4\left(\mu^{II}\right)\left(\varepsilon^{II}\right)\left(\mu^{II}\right)^2\left(\varepsilon^{II}\right)^2}{\omega^4\left(\varepsilon^{II}\right)^2\left(\mu^I\right)^2\left(\varepsilon^I\right)^2-\omega^4\left(\varepsilon^I\right)^2\left(\mu^{II}\right)^2\left(\varepsilon^{II}\right)^2}} \\ k_z^I = \sqrt{\dfrac{\left(\varepsilon^{II}\right)^2\omega^4\left(\mu^I\right)^2\left(\varepsilon^I\right)^2\omega^2\left(\mu^I\right)\left(\varepsilon^I\right)-\left(\varepsilon^{II}\right)^2\omega^4\left(\mu^I\right)^2\left(\varepsilon^I\right)^2\omega^2\left(\mu^{II}\right)\left(\varepsilon^{II}\right)}{\omega^4\left(\varepsilon^{II}\right)^2\left(\mu^I\right)^2\left(\varepsilon^I\right)^2-\omega^4\left(\varepsilon^I\right)^2\left(\mu^{II}\right)^2\left(\varepsilon^{II}\right)^2}} \\ k_x = \sqrt{\dfrac{\left(\varepsilon^{II}\right)^2\omega^4\left(\mu^I\right)^2\left(\varepsilon^I\right)^2\omega^2\left(\mu^{II}\right)\left(\varepsilon^{II}\right)-\left(\varepsilon^I\right)^2\omega^2\left(\mu^I\right)\left(\varepsilon^I\right)\omega^4\left(\mu^{II}\right)^2\left(\varepsilon^{II}\right)^2}{\left(\varepsilon^{II}\right)^2\omega^4\left(\mu^I\right)^2\left(\varepsilon^I\right)^2-\omega^4\left(\varepsilon^I\right)^2\left(\mu^{II}\right)^2\left(\varepsilon^{II}\right)^2}} \end{cases}$$

(1. 10.40)

$$\boxed{\begin{cases} k_z^{II} = \omega\mu^{II}\sqrt{\dfrac{\left(\mu^I\right)\left(\varepsilon^I\right)-\left(\mu^{II}\right)\left(\varepsilon^{II}\right)}{\left(\mu^I\right)^2-\left(\mu^{II}\right)^2}} \\ k_z^I = \omega\mu^I\sqrt{\dfrac{\left(\mu^I\right)\left(\varepsilon^I\right)-\left(\mu^{II}\right)\left(\varepsilon^{II}\right)}{\left(\mu^I\right)^2-\left(\mu^{II}\right)^2}} \\ k_x = \omega\sqrt{\dfrac{\left(\mu^I\right)^2\left(\mu^{II}\right)\left(\varepsilon^{II}\right)-\left(\mu^I\right)\left(\varepsilon^I\right)\left(\mu^{II}\right)^2}{\left(\mu^I\right)^2-\left(\mu^{II}\right)^2}} \end{cases}}$$

(1. 10.41)

in the case where $\varepsilon^I = \varepsilon^{II} = \varepsilon_0$ then we have:

$$\begin{cases} k_z^{II} = \omega\mu^{II}\sqrt{\varepsilon_0}\sqrt{\dfrac{\left(\mu^I\right)-\left(\mu^{II}\right)}{\left(\mu^I\right)^2-\left(\mu^{II}\right)^2}} = \omega\mu^{II}\sqrt{\varepsilon_0}\sqrt{\dfrac{\left(\mu^I-\mu^{II}\right)}{\left(\mu^I+\mu^{II}\right)\left(\mu^I-\mu^{II}\right)}} \\ k_z^I = \omega\mu^I\sqrt{\varepsilon_0}\sqrt{\dfrac{\left(\mu^I\right)-\left(\mu^{II}\right)}{\left(\mu^I\right)^2-\left(\mu^{II}\right)^2}} = \omega\mu^I\sqrt{\varepsilon_0}\sqrt{\dfrac{\left(\mu^I-\mu^{II}\right)}{\left(\mu^I+\mu^{II}\right)\left(\mu^I-\mu^{II}\right)}} \\ k_x = \omega\sqrt{\varepsilon_0}\sqrt{\dfrac{\left(\mu^I\right)^2\left(\mu^{II}\right)-\left(\mu^I\right)\left(\mu^{II}\right)^2}{\left(\mu^I\right)^2-\left(\mu^{II}\right)^2}} = \omega\sqrt{\varepsilon_0}\sqrt{\dfrac{\mu^I\mu^{II}\cancel{\left(\mu^I-\mu^{II}\right)}}{\left(\mu^I+\mu^{II}\right)\cancel{\left(\mu^I-\mu^{II}\right)}}} \end{cases}$$

(1. 10.42)

$$\begin{cases} k_z^{II} = \dfrac{\omega\mu^{II}\sqrt{\varepsilon_0}}{\left(\mu^I + \mu^{II}\right)} \\ k_z^{I} = \dfrac{\omega\mu^{I}\sqrt{\varepsilon_0}}{\left(\mu^I + \mu^{II}\right)} \\ k_x = \omega\sqrt{\varepsilon_0}\sqrt{\dfrac{\mu^I\mu^{II}}{\left(\mu^I + \mu^{II}\right)}} \end{cases}$$

(1. 10.43)

If both media are lossless, then both $\mathbf{k}^I, \mathbf{k}^{II}$ are real and equations (1.9.40) yield the usual Brewster angle formulas, that is,

$$\tan\theta_{TE}^I = \frac{k_x}{k_z^I} = \frac{\omega\sqrt{\varepsilon_0}\sqrt{\dfrac{\mu^I\mu^{II}}{\left(\mu^I+\mu^{II}\right)}}}{\dfrac{\omega\mu^I\sqrt{\varepsilon_0}}{\left(\mu^I+\mu^{II}\right)}} = \frac{\dfrac{\sqrt{\mu^I}\sqrt{\mu^{II}}}{\sqrt{\mu^I+\mu^{II}}}}{\dfrac{\mu^I}{\sqrt{\mu^I+\mu^{II}}}} = \frac{\sqrt{\mu^{II}}}{\sqrt{\mu^I}} = \frac{n^{II}}{n^I}$$

$$\tan\theta_{TE}^{II} = \frac{k_x}{k_z^{II}} = \frac{n^I}{n^{II}}$$

(1.10.44)

Using $k_x = k_x^I = k_x^{II} = \beta_x - j\alpha_x$ the space-dependence of the fields at the two sides is as follows:

$$e^{-j\left(k_x^I x + k_z^I z\right)} = e^{-j\left[\left(\beta_x^I x - j\alpha_x^I x\right) + \left(\beta_z^I z - j\alpha_z^I z\right)\right]} = e^{-\left(\alpha_x^I x + \alpha_z^I z\right)} e^{-j\left(\beta_x^I x + \beta_z^I z\right)} \qquad \text{for } z \le 0$$

(1. 10.45)

$$e^{-j\left(k_x^{II} x + k_z^{II} z\right)} = e^{-j\left[\left(\beta_x^{II} x - j\alpha_x^{II} x\right) + \left(\beta_z^{II} z - j\alpha_z^{II} z\right)\right]} = e^{-\left(\alpha_x^{II} x + \alpha_z^{II} z\right)} e^{-j\left(\beta_x^{II} x + \beta_z^{II} z\right)} \qquad \text{for } z \ge 0$$

(1. 10.46)]

Thus, in order for the fields not to grow exponentially with distance and to be confined near the interface it must be:

$$\alpha_x^I = \alpha_x^{II} > 0, \quad \alpha_z^I < 0, \quad \alpha_z^{II} > 0$$

(1.10.47)

1.11 Surface Plasmons

Surface plasmons or polaritons are waves that are propagating along the interface between two different media and attenuate exponentially perpendicularly to the interface in both media [3]. It has been shown that a surface Plasmon can be excited in matter through two different structures, namely the Otto and the Kretschmann configurations [3]. Such a phenomenon relies on the plasma nature of a good conductor irradiated by optical and higher-energy beams.

Less studied and understood is the excitation of plasmons (or polaritons) at microwave frequencies. Numerical results have been showed in [7] for a selected metallic structure. Here, we investigate the microwave plasmonic resonance analytically, from first-principles, extending the forward-backward matrix formalism to include also evanescent plane waves [8].

Furthermore, we use an optimization algorithm, the genetic algorithm (GA), to meet the inverse electromagnetic problem: how to excite an electromagnetic plasmon in a given structure at a given frequency?

We found that this is possible at microwave frequencies, for both TE and TM propagation modes, only using an ultra-thin low-lossy (double negative) metamaterial [9]-[10]-[11], whose parameters are given by the GA itself. This is confirmed by

inspection of the reflection coefficient (RC) and the angle between constant amplitude-plane and phase-plane.

Obtained structure is a modified Kretschmann configuration, with identical dielectrics (in selected cases, the free space), at both sides of the metamaterial slab. It is to be noticed that asurface (plasm onic-like) resonance is obtained also for the TE case, mainly ascribed to the presence of a dominant real part of the permeability, with respect to the real part of the permittivity

Using $k_x = k_x^I = k_x^{II} = \beta_x - j\alpha_x$ the space-dependence of the fields at the two sides is as follows:

$$e^{-j\left(k_x^I x + k_z^I z\right)} = e^{-j\left[\left(\beta_x^I x - j\alpha_x^I x\right) + \left(\beta_z^I z - j\alpha_z^I z\right)\right]} = e^{-\left(\alpha_x^I x + \alpha_z^I z\right)} e^{-j\left(\beta_x^I x + \beta_z^I z\right)} \qquad \text{for } z \le 0$$

(1.11.1)

$$e^{-j\left(k_x^{II} x + k_z^{II} z\right)} = e^{-j\left[\left(\beta_x^{II} x - j\alpha_x^{II} x\right) + \left(\beta_z^{II} z - j\alpha_z^{II} z\right)\right]} = e^{-\left(\alpha_x^{II} x + \alpha_z^{II} z\right)} e^{-j\left(\beta_x^{II} x + \beta_z^{II} z\right)} \qquad \text{for } z \ge 0$$

(1.11.2)

Thus, in order for the fields to attenuate exponentially with distance along *x* but above all along *z* direction and to be confined only near the interface along *x* direction it must be:

$$\boxed{\beta_x^I = \beta_x^{II} > 0, \quad \alpha_z^{II} > \alpha_x^I = \alpha_x^{II} \ge 0, \quad \beta_x^I = \beta_x^{II} >> \beta_z^{II} \to 0, \quad \alpha_z^I < 0, \quad \alpha_z^{II} > 0,}$$

(1.11.3)

i.e., $\boxed{real\left(k_x\right) + imag\left(k_z^{II}\right) - real\left(k_z^{II}\right)}$ must be maximized

(1.11.4)

With respect to Zenneck surface waves here $\alpha_x^I = \alpha_x^{II} \ge 0, \quad \alpha_z^I < 0, \quad \alpha_z^{II} > 0$, the conditions which must be satisfied in Plasmon surface are especially those related to the real part of wave number.

When a plasmonic resonance occurs, energy is localized nearby the interface, along the *x* direction, where the attenuation is negligible, whereas strong attenuation takes place along the *z* direction. In this case, the plasmonic condition is

$$\alpha_x^I = \alpha_x^{II} \to 0, \quad \alpha_z^I < 0, \quad \alpha_z^{II} > 0$$

(1.11.5)

For a Plasmon excitation, the main conditions to be satisfied are those related to the real part of wave numbers: this is the basic difference with the Zenneck surface wave excitation.

In order to optimize a structure of material able to excite a plasmonic resonance at microwave frequencies, an in-house genetic algorithm (GA) has been implemented to find the optimum solution in terms of permittivity, permeability, and thickness of a single layer structure [12].The action of GA code results in the minimization of imaginary part of wave number along longitudinal *z*-axes and the maximization of real part of wave number along *x*-axes. In other words, GA optimizes the structure finding the best dielectric materials where the propagation along *z*-axes is minimized while the propagation along *x*-axes is maximized, meeting the plasmonic conditions.
Our code has degrees of freedom in choosing double/single negative permittivity and permeability. With this constraint, the final optimized material can be right handed or left handed [3]. One further condition is used obtain low lossy materials, normally needed by a plasmonic resonance [7], and in a practical scenario to make the manufacturing process easy.
Since we are handling a lossy material, the oblique incidence excites the plasmonic resonance by total internal reflection of surface Zenneck waves. Obtained structure is a modified Kretschmann configuration, with identical dielectrics (in selected cases, the free space), at both sides of the metamaterial slab. It is to be noticed that a surface (plasmonic-like) resonance is obtained also for the TE case, mainly ascribed to the presence of a dominant real part of the permeability, with respect to the real part of the permittivity. Results are of interest in the transformation of the surface waves, as they are conceived to obtain absorbing medium, screens and, the possibility of controlling it through a design tool, in the emerging transformation optics.

1.11.1 Simulation of TE Plasmonic Resonance using Genetic Algorithm

In the scenario supposed for TE plasmonic resonance Genetic algorithm optimized the following values for permeability, permittivity, and thickness of material:

- Chosen Frequency=1 GHz, (frequency set by operator)
- Incidence angle from 0 to 90 deg, (angular range of wave incidence set by operator)
- $\mu_r^l = -30.20 - j2.56$, (permeability optimized by genetic algorithm)

- $\varepsilon_r^I = -9.32 - j0.96$, (permittivity optimized by genetic algorithm)
- Layer thickness=0.031 mm, (thickness optimized by genetic algorithm)

In Fig. (1.11.1.1), scheme of layers structure is shown. Frees pace along z-axes and transversal dimension along x-axes are considered not limited.

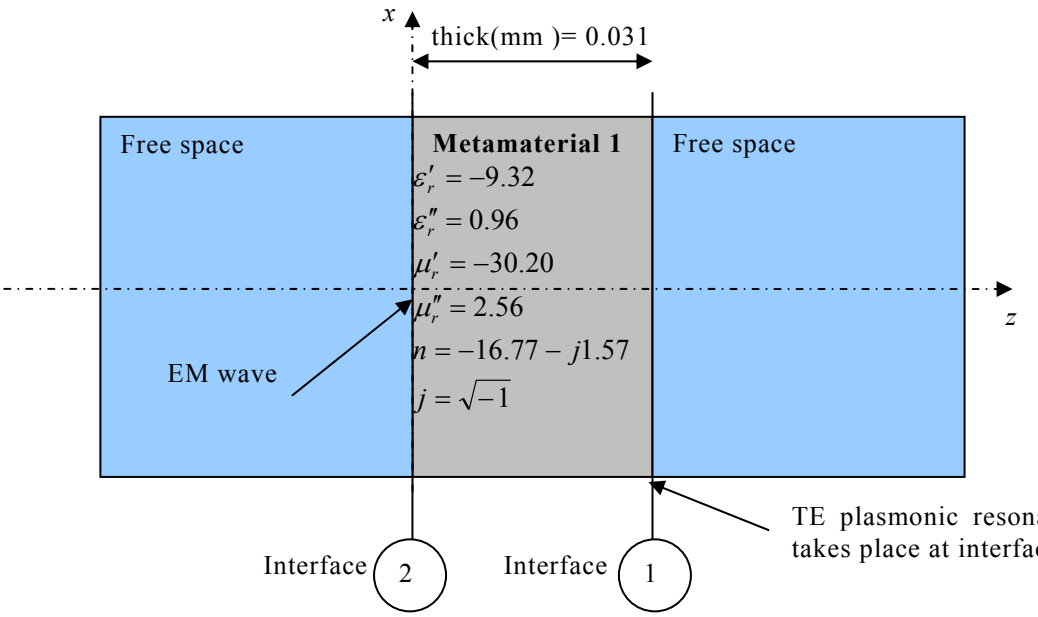

Fig. (1.11.1.1). Layer Interfaces structure scheme for TE plasmonic resonance

In Fig. (1.11.1.2), Reflection, and Transmission coefficient (dB) at interfaces denominated 1 and 2 are reported. Plasmonic resonance can be noticed in Fig. (1.11.1.2a) where a notch for reflection coefficient take place at interface 1.

Transmission and reflection coefficients have been computed adopting matrix formalism shown in equations (1.1.33) and (1.1.42).

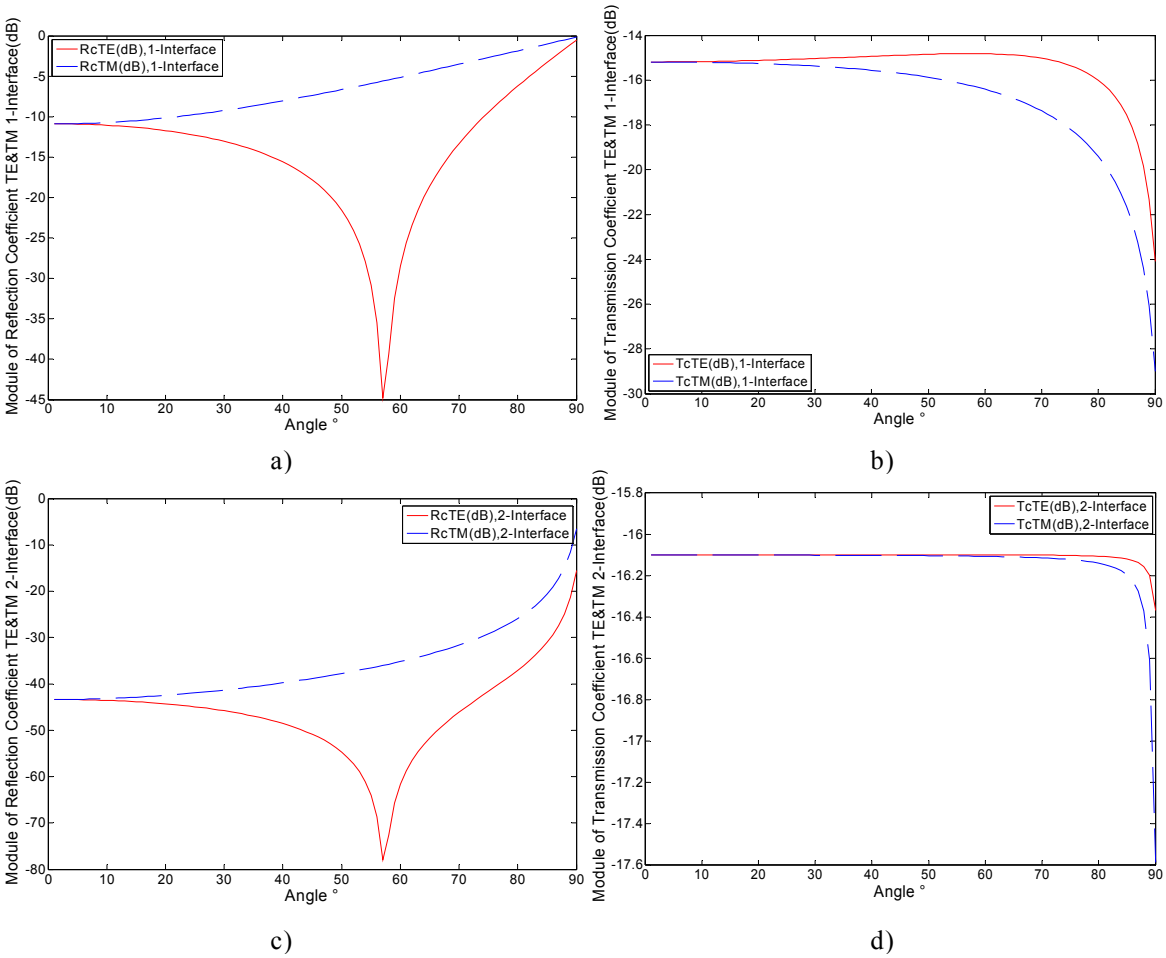

Fig. (1.11.1.2).

a,b) Reflection and Transmission coefficients at interface 1 (metamaterial-free space)

c,d) Reflection and Transmission coefficients at interface 2 (free space-metamaterial)

Real and imaginary part of *Kx* and *Kz* wave numbers are plotted in Fig. (1.11.1.3): Here the real part of *Kx*, i.e., propagation factor along *x*-axes, is greater with respect to that along *z*-azes and the imaginary part of *Kx* along *x*-axes i.e., attenuation factor along *x*-axes, is zero i.e., no attenuation along *x*-axes take place. On the contrary, attenuation along *z*-axes happens since imaginary part of *Kz* along *z*-axes exists.

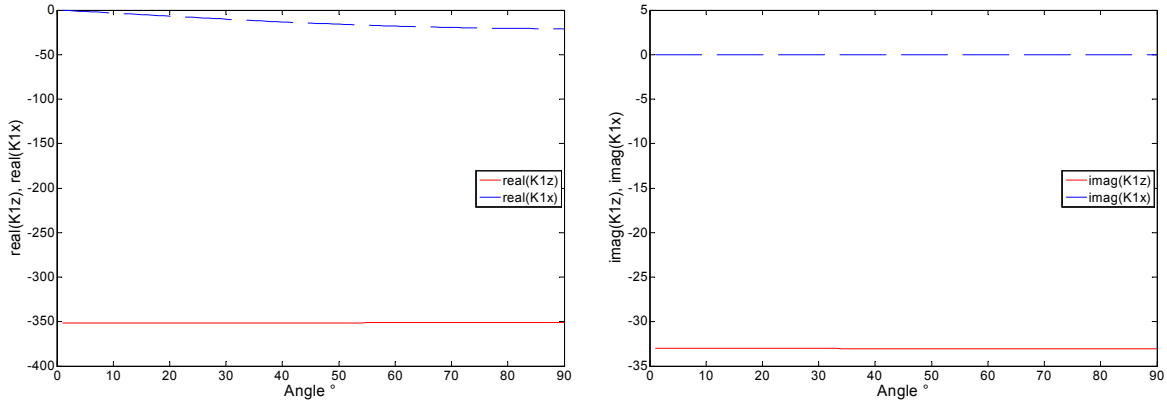

a) b)

Fig. (1.11.1.3).

a,b) Real and Imaginary components of wave number along x-axes and z-axes at interface 1 (metamaterial-free space)

The two required Plasmonic conditions seem to be satisfied since by using metamaterial we obtain:

1. $\varepsilon_r' < -1 (1 = air)$; *and* $\mu_r' < -1 (1 = air)$
2. metamaterial posses little losses in terms of absolute value of permittivity and permeability imaginary components.

Considering values of *Kx* and *Kz,* for an incidence angle close to *60 deg*, the propagation of electromagnetic wave across metamaterial can be described as:

$$e^{-jk_x\hat{x}} \cdot e^{-jk_z\hat{z}} = e^{-j(-25-j0)\hat{x}} \cdot e^{-j(-150-j33)\hat{z}} = e^{j25\hat{x}} \cdot 1 \cdot e^{j150\hat{z}} e^{-33\hat{z}} = e^{j(25\hat{x}+150\hat{z})} e^{-33\hat{z}}$$

Factor $e^{-33\hat{z}}$ is an attenuation factor when *z>0* as in Fig. (1.11.1.1).

In our code, the value of metamaterial refraction index is:

$$n = sign\_WaveNumber \times \sqrt{(mu_r' - jmu_r'') \times (e_r' - je_r'')} = -16.77 - j1.57$$

Where

sign_WaveNumber=-1 for metamaterial where real part of permittivity and permeability are both contemporary negative.

Fig. (1.11.1.4), show the departure between phase- and amplitude-planes of TE scenarios. This behavior confirms the presence of low lossy in the metamaterial slabs.

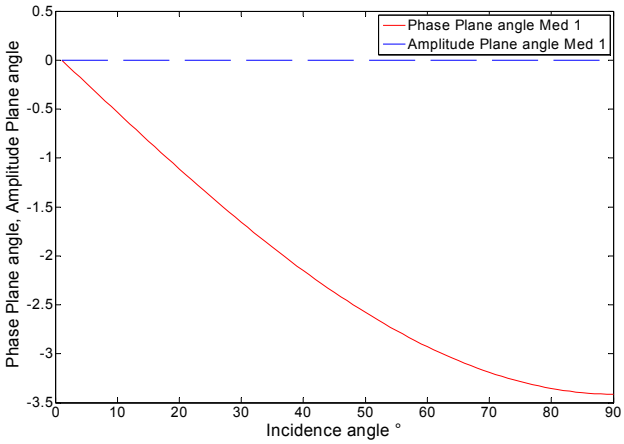

Fig. (1.11.1.4).

Departure between phase- and amplitude-planes of TE scenarios on metamaterials

1.11.2 Simulation of TM Plasmonic Resonance using Genetic Algorithm

In the scenario supposed for TM plasmonic resonance Genetic algorithm optimized the following values for permeability, permittivity and thickness of material:

- Chosen Frequency=1 GHz, (frequency set by operator)
- Incidence angle from 0 to 90 deg, (angular range of wave incidence set by operator)
- $\mu_r^I = -15.46 - j1.71$, (permeability optimized by genetic algorithm)
- $\varepsilon_r^I = -50.84 - j5.81$, (permittivity optimized by genetic algorithm)
- Layer thickness=6.1×10^{-4} mm, (thickness optimized by genetic algorithm)

In Fig. (1.11.2.1) the scheme of layers structure is shown. Frees pace along *z*-axes and transversal dimension along *x*-axes are considered not limited.

In Fig. (1.11.2.2), Reflection, and Transmission coefficient (dB) at interfaces denominated 1 and 2 are reported. Plasmonic resonance can be noticed in Fig. (1.11.2.2a), where a notch for reflection coefficient take place at interface 1. Transmission and reflection coefficients have been computed adopting matrix formalism shown in equations (1.1.33) and (1.1.42).

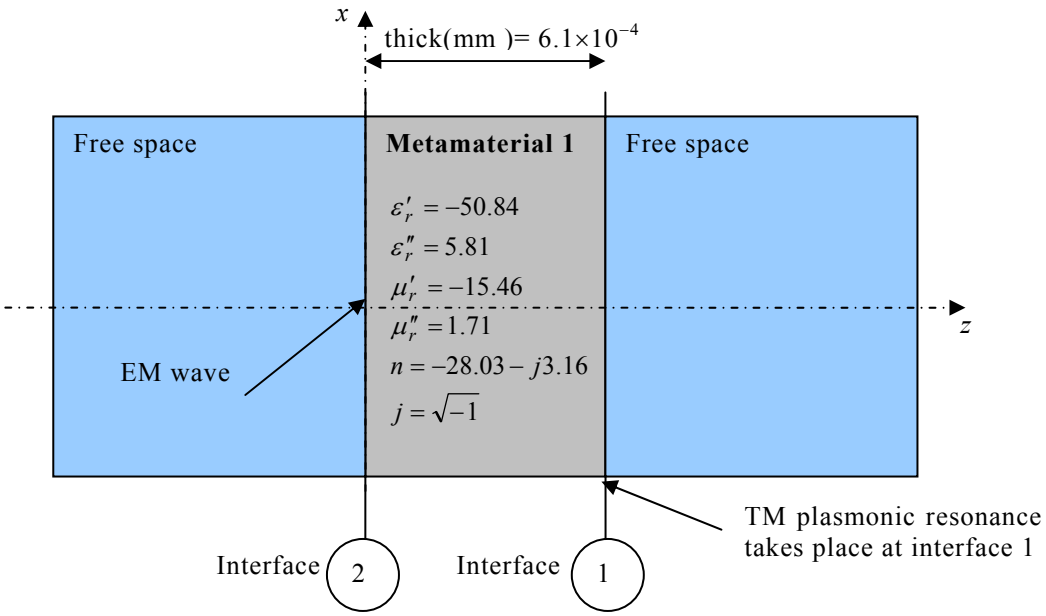

Fig. (1.11.2.1). Layer Interfaces structure scheme for TM plasmonic resonance

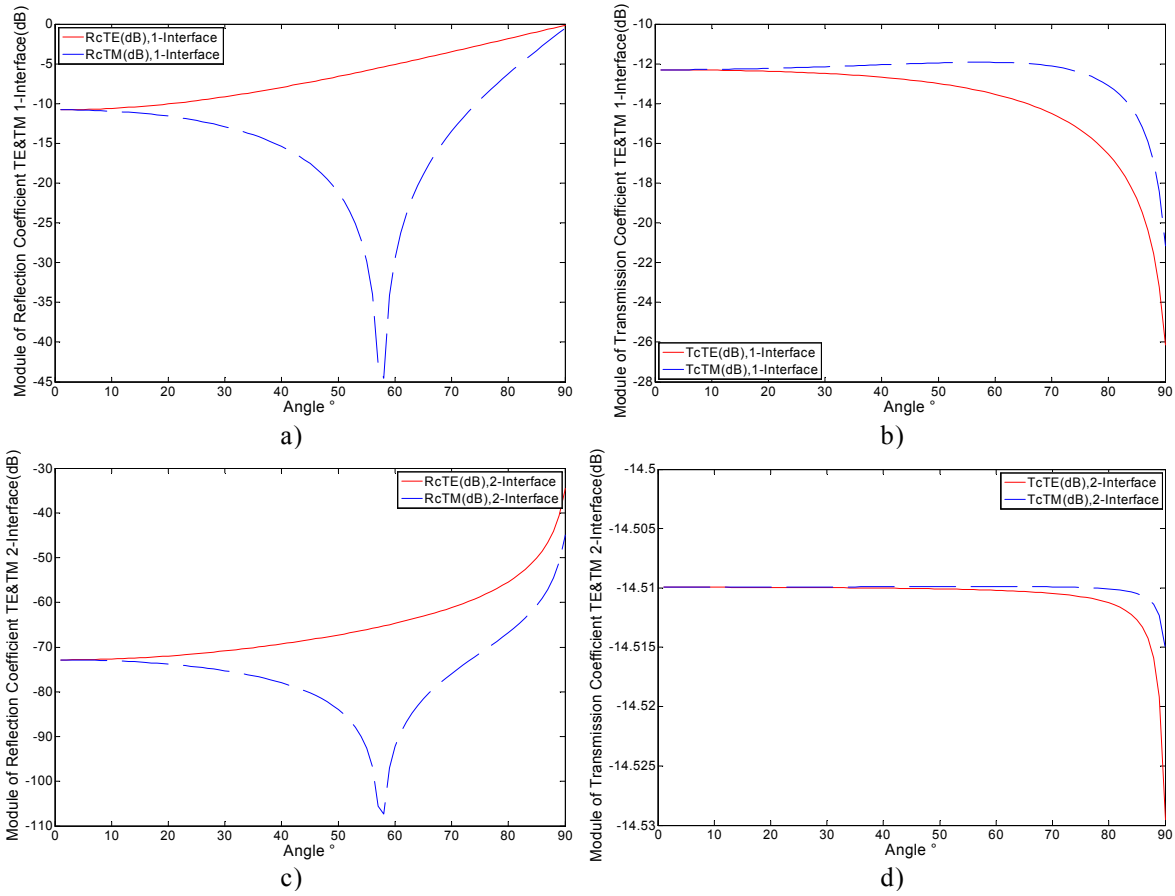

Fig. (1.11.2.2).

a,b) Reflection and Transmission coefficients at interface 1 (metamaterial-free space)

c,d) Reflection and Transmission coefficients at interface 2 (free space-metamaterial)

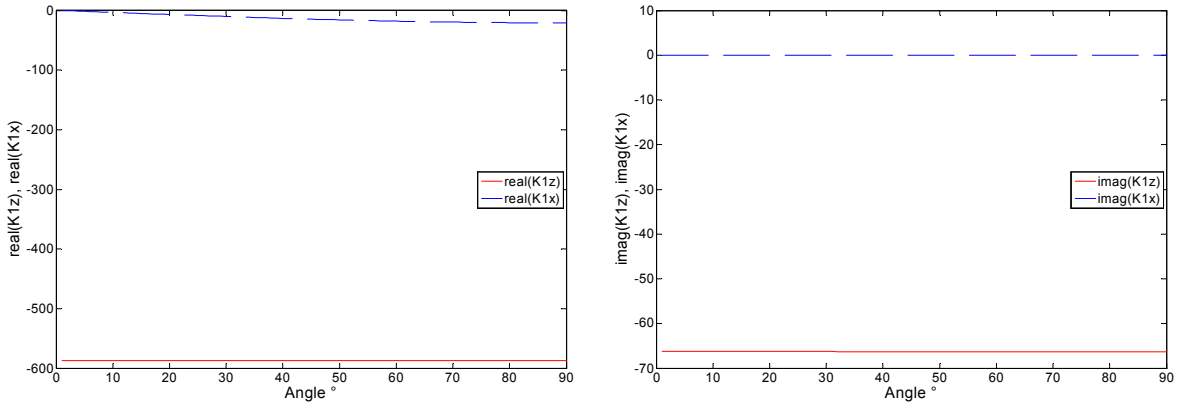

a) b)

Fig. (1.11.2.3).

a,b) Real and Imaginary components of wave number along x-axes and z-axes at interface 1 (metamaterial-free space)

The two required Plasmonic conditions seems to be satisfied since by using metamaterial we obtain:

1. $\varepsilon_r' < -1 (1 = air); and \quad \mu_r' < -1 (1 = air)$

2. metamaterial posses little losses in terms of absolute value of permittivity and permeability imaginary components.

Considering values of *Kx* and *Kz,* for an incidence angle close to *60 deg*, the propagation of electromagnetic wave across metamaterial can be described as:

$$e^{-jk_x\hat{x}} \cdot e^{-jk_z\hat{z}} = e^{-j(-25-j0)\hat{x}} \cdot e^{-j(-590-j67)\hat{z}} = e^{j25\hat{x}} \cdot 1 \cdot e^{j590\hat{z}} e^{-67\hat{z}} = e^{j(25\hat{x}+590\hat{z})} e^{-67\hat{z}}$$

Factor $e^{-67\hat{z}}$ is an attenuation factor when *z>0* as in Fig. (1.11.2.1).

The value of refraction index of metamaterials is:

$n = sign\_WaveNumber \times \sqrt{(mu_r' - jmu_r'') \times (e_r' - je_r'')}$ = -28.0355 - j3.1617i

Where

sign_WaveNumber=-1 for metamaterials where real part of permittivity and permeability are both contemporary negative.

Fig. (1.11.1.4), show the departure between phase- and amplitude-planes of TE scenarios. This behavior confirms the presence of low lossy in the metamaterial slabs.

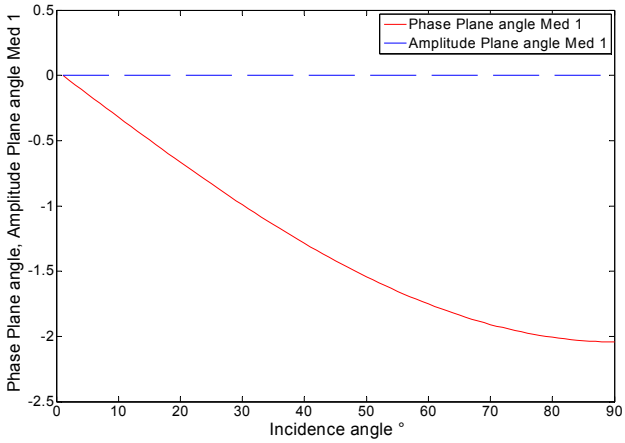

Fig. (1.11.1.4).

Departure between phase- and amplitude-planes of TM scenarios on metamaterials

1.12 Conclusion

In this chapter mathematical model of electromagnetic multilayer structure has been presented and reflection and transmission coefficient determined. Lossy materials have been assumed and complex waves introduced in order to take into account for losses. Brewster angle in no lossy and Zenneck wave in lossy materials have been analyzed. At the end plasmonic resonance has been introduced and simulated by using genetic algorithm. All the analysis have been made in order to give to the reader the theoretical instruments needed to understand the methods adopted to design microwave multilayer absorbers.

1.13 Reference Table

[1] S.Barbarino, "Campi Elettromagnetici"

[2] Sophocles J.Orfanidis, "Electromagnetic wave and Antennas"

[3] Julius Adam Stratton. Electromagnetic Theory, IEEE Press & John Wiley-Interscience, 2007, ISBN 9780470131534.

[4] Jin Au Kong "Electromagnetic wave Theory", *A JOHN WILEY & SONS, INC., PUBLICATION, 1986*

[5] Pozar "Microwave Engineering" third edition, *A JOHN WILEY & SONS, INC., PUBLICATION*

[6] Ramo, Whinnery, Van Duzer, Fields and Waves in Communications Electronics, JohnWiley and Son, 1994.

[7] CHRISTOPHE CALOZ, TATSUO ITOH, "ELECTROMAGNETIC METAMATERIALS: TRANSMISSION LINE THEORY AND MICROWAVE APPLICATIONS", *A JOHN WILEY & SONS, INC., PUBLICATION, 2006*

[8] Nader Engheta, Richard W. Ziolkowski. Metamaterials: Physics and Engineering Explorations, IEEE Press, 2006.

[9] Mark L. Brongersma, Pieter G. Kik. Surface Plasmon Nanophotonics, Springer, 2007.

[10] Caloz, C.; Cheng-Jung Lee; Smith, D.R.; Pendry, J.B.; Itoh, T.; "Existence and properties of microwave surface plasmons at the interface between a right-handed and a left-handed media," Antennas and Propagation Society International Symposium, 2004. IEEE , vol. 3, pp. 3151- 3154 Vol.3, 20-25 June 2004

[11] Lockyear, Matthew J.; Hibbins, Alastair P.; Sambles; J. Roy. "Microwave Surface-Plasmon-Like Modes on Thin Metamaterials," Phys. Rev. Lett., vol. 7, no. 2, 2009.

[12] D. Micheli, R. Pastore, C. Apollo, M. Marchetti, G. Gradoni, F.Moglie and V. Mariani Primiani. "Carbon Based Nanomaterial Composites in RAM and Microwave Shielding Applications," in Proc. of the 9th IEEE Nanotechnology Symposium, July, Genova (IT), 2009.

Chapter 2
Nanomaterials characterization and Composite materials manufacturing

2.1 Introduction

This chapter focuses on characterization of nanomaterials adopted to built electrically conductive composite materials and in nanostructured composite materials manufacturing. Typical problems occurring in large composite material tiles manufacturing are also analyzed. At the first a brief introduction about electrically conductive composite materials is reported [1]. After that composite material manufacturing is analyzed and discussed.

In formulating an electrically conductive composite material, a polymer is combined with highly conductive rigid particles. Electrical conductivity is accomplished though a certain level of particle-to-particle contact or close proximity. It is difficult to draw definite conclusions about electrical conductivity since it depends also from electromagnetic solicitation type, i.e., DC or AC current and type of electromagnetic wave propagation i.e., direct contact or plane wave incidence on the composite material, [2][3].

In the uncured polymeric material, the conductive particles are considered to be touching or near touching with little electrical conductivity. During the curing process, the polymer shrinkage due to chemical action of curing-cross-linking and the physical action of thermal contraction as the elastomer is cooled to room temperature causes the particle to be pressed and percolated together forming the conductive path. In general, the resistivity of conductive elastomer is closely related to the resistivity of the filler [4].

Numerous other factors can affect the conductive properties of the filler loaded composite, including filler type, loading level, particle distributions, particle size, intrinsic conductivity of filler, process condition plating, and compounding.

However, the most basic factors are particle conductivity, loading level and particle shape. The filler concentration i.e. the filler in weight % with respect to the polymer, or the volume loading level of the filler is relevant in the percolation regime of the composite i.e., the threshold at which the composite changes form an insulator to a conductor.

At low filler loadings, where the filler particles are isolated with no contact between them, the composite remains an insulator although its dielectric properties may change significantly [5]. Upon the increase of the filler loading and the resulting

close proximity of the conduct filler particles, electrons can travel the polymeric gap between the conductive particles, allowing current to flow. This is called the hopping and tunneling effect [6]. The ability of an electron to jump a gap under a given voltage field increases exponentially with decreasing separation between particles. As the filler loading is increased further and reaches a critical point, the conductive particles contact one another, and a continuous network is established. The sudden and precipitous drop in resistivity is achieved through a generation of a continuous network, which is defined as percolation threshold [7].

At the percolation threshold, a majority of the filler particles are in contact with at least two of their nearest neighbors, thereby forming a continuous chain or network. An electrical charge now can now pass through the composite via this network without encountering the high-resistance polymer resin. Additional filler loading beyond the percolation threshold does not greatly reduce the resistivity of the composite [8].

The percolation behavior is primarily affected by the surface chemistry of the filler and its wettability by the polymer melt, the rheology of the polymer melt, the parameters of the solidification process, the crystallinity of semicrystalline polymer, and the parameters of the mixing process [9].

For a certain filler volume, the shape of the particles plays a critical role in where percolation occurs. The more structured or elaborately shaped the particle, the more likely it is to contact a nearest neighbor and form a continuous network. Perfectly spherical fillers, which arguably have the least elaborate and the least structured shape, can require as much as 40% loading to reach the percolation threshold. Carbon-black particles are more irregularly shaped and often have long branches reaching out form the main body of the particle reaching percolation threshold for loadings in the range 5% to 35% [10].

In other words, the greater the aspect ratio of the particles, the smaller the loading level needed to reach the percolation threshold [3].

In addition, the mixing process plays an important role in the percolation and conductivity of the conductive composite material. For instance, with an increase in mixing time and hence the specific energy input incorporated during the mixing process, the homogeneity of the spatial distribution of the conductive particle in the

matrix is improved and dielectric permittivity of composite material at microwave frequencies has not sharp changes [11].

Nanomaterials and nanocomposite materials provide a potential approach to EMI shielding, microwave absorber, lightening strike protection. With the arrival of nanotechnology, it was discovered that the ability to create small particles with high aspect ratio, could expand the capability to create and modify materials. For example carbon nanotechnology creates nanotubes, fullerenes and nanodiamonds. Carbon nanotube (CNTs) are produced in many variants; the most important classifications is single- (SWCNTs).or multiwall carbon nanotube (MWCNTs).

They provide unique properties, such as (a) they are probably the best conductors of electricity on a nanoscale; (b) thermal conductivity comparable that of diamonds along the tube axis; and (c) they are probably the stiffest, strongest, toughest nanofiber. Carbon nanotube (CNTs) reinforced conductive polymer composite have been explored for EMI shielding and absorber applications [11]. The effect of the length and aggregate size of MWCNTs on the alternate current (AC) conductance of epoxy-based composite reveals the percolation threshold for the filler to be as low as 0.5 wt%. These properties, along with their mechanical reinforcing/stiffening capabilities, have made CNTs extremely attractive candidates for reinforcements of conductive polymer composite [12]. The tendency of CNTs to form ropes [13], provides very long conductive pathways even at ultra-low loadings, which may be exploited in EMI shielding composites. gasket, radar absorbing materials (RAM) for stealth applications.

Composite materials considered in this book are based on epoxy matrix reinforced with several species of carbon nanomaterials. These latter have been chosen taking into account the lowest market prices: the economic aspects, normally neglected in small laboratory applications, are on the contrary important in real applications where the amount of carbon nanopowders could be relatively high. In such scenario a good compromise in terms of cost/performances has been obtained using industrial grade multiwall carbon nanotubes (MWCNTs, about 300 $/kg), graphite micropowder (about 40 $/kg), and carbon nanofibers (CNFs, about 30 $/g).

2.2 Carbon powders adopted and main properties

In this book carbon powders has been widely adopted for samples and large tile of composite materials.

Carbon materials and epoxy-resin considered in the experiments are:

- Micro Graphite (granular size < 20 μm), bought at SigmaAldrich;
- SWCNTs (Single Wall Carbon Nanotubes), bought at Carbolex (diameter around 1-2 nm, length 5-30 μm); http://www.nanotube-suppliers.com
- CNFs (Carbon NanoFibers), bought at SigmaAldrich (diameter around 75 nm, length 50-100 μm); http://www.sigmaaldrich.com/sigma-aldrich/home.html
- MWCNTs (Multi-Wall Carbon Nanotubes type NANOCYLTM NC7000), bought at NANOCYL (diameter around 9.5 nm, length 1.5 μm, purity 90%) http://www.nanocyl.com
- Epoxy-resin is: PrimeTM 20LV(density 1.123 g/cm3), Hardner(density 0.936 g/cm3); http://www.gurit.com/

Carbon materials weight ratio (wt%) with respect to the polymer (epoxy-resin) are mainly in the range 0.5-3 wt%. Scanning electron microscope (SEM) analysis has been widely adopted in laboratory using VEGA TESCAN SEM model www.tescan.com. There are excellent reviews and books on the synthesis and the physical properties of carbon nanotube and therefore, in this section, only a brief summary of the fundamentals and general approaches for the synthesis of carbon nanotubes is presented. There are single-wall carbon nanotube or SWCNTs, and multi-wall carbon nanotube or MWCNTs.

A given multi-wall carbon nanotube can typically be composed of a mixture of cylindrical tubes having different helicity or no helicity, thereby resembling turbostratic graphite. Typical dimensions of multi-wall carbon nanotube are outer diameter: 2-20 nm, inner diameter: 1-3 nm, and length: 1-100 μm. The intertubular distance is 0.340 nm, which is slightly larger than the interplanar distance in graphite. Multi-wall carbon nanotube consists of several nested coaxial singlewall tubules. The arrangement of the carbon atoms in the hexagonal network of the multi-wall carbon nanotube is often helicoidal, resulting in the formation of chiral tubes.

Carbon nanotubes (CNTs) have attracted considerable attention for the construction of nano and micro-devices since the discovery of CNTs by Iijima in 1991 [14]. A single walled carbon nanotube (SWCNT) can be imagined as a rolledup cylinder formed from a two-dimensional graphene sheets with caps at both ends. According to theoretical calculations, CNTs have extraordinary mechanical, thermal, and electrical properties due to their unique carbon structure as well as the nano-scale. Fig.(2.2.1), depict a qualitative structure of a SWCNT and a MWCNT.

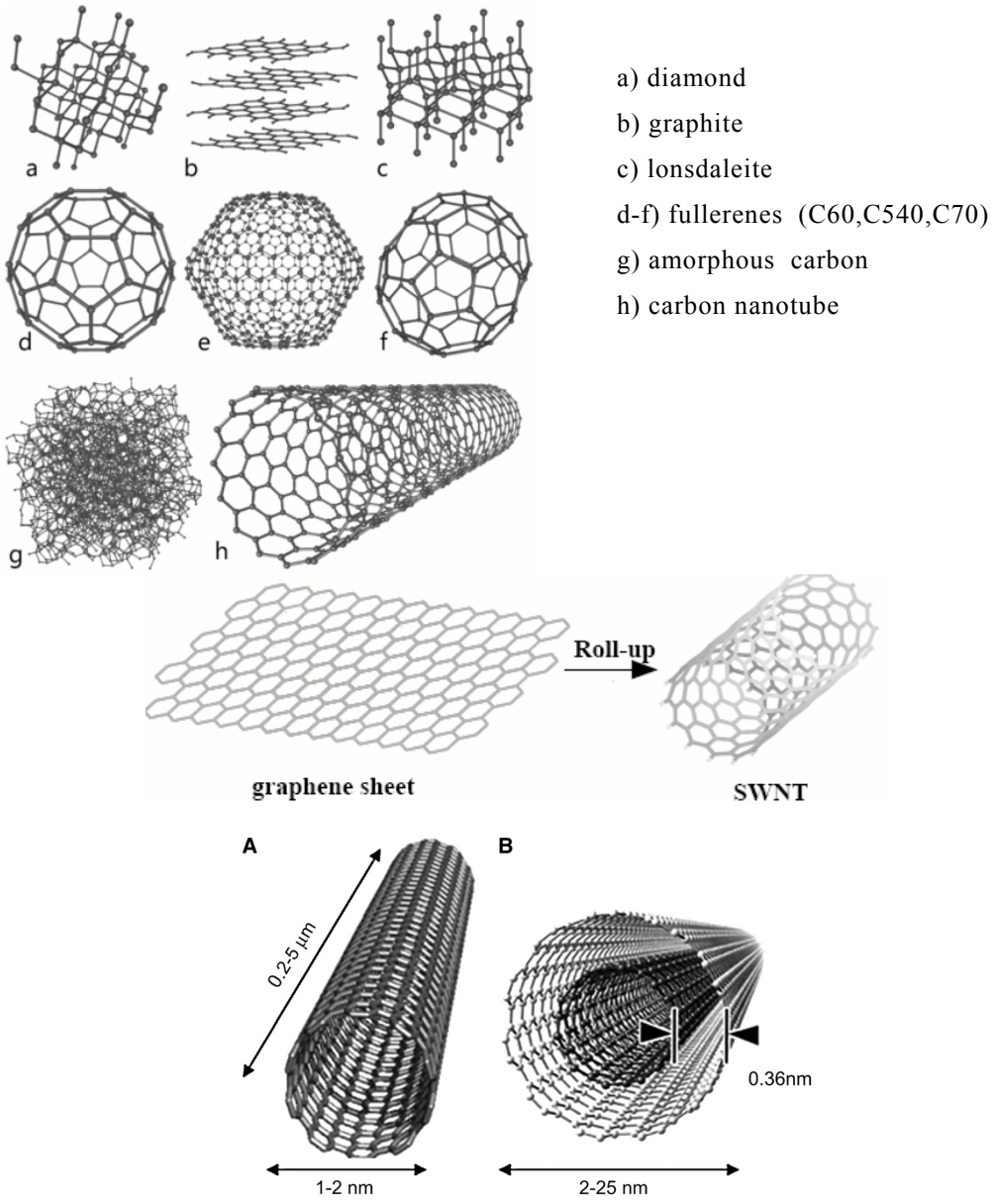

Fig.2.2.1. Different form of Carbon materials and CNT

A) Single Wall Carbon Nanotube B) Multi Wall Carbon Nanotube

Some specific defect-free forms of SWNTs showed remarkable mechanical properties and metallic behavior [15].

Main properties of CNTs are briefly shown in Tab. (2.2.1)

PARAMETER	**CARBON NANOTUBE**	**REFERENCE**
Density	0.6 ÷100 nm	50 nm-large and some nanometers-thick ribbons through E.B. Lithography
Length	Some thousands nanometers	-
Density	1,33 ÷ 1.40 gr/cm3	Aluminium alloys : 2.7 gr/ cm3 Carbon fibers: 1.74 ÷ 1.94 gr/cm3
Tensile strength	45 GPa	High Strength steels : 2 GPa Carbon fibers: 3.5 GPa
Young modulus	≈ 1÷ 4 TPa	Carbon fibers : 0.23÷ 0.52 TPa
Elasticity	Pliability up to very high angle without fracture	Metals and carbon fibers break over lower pliability angles
Electrical properties	Metal/semiconductor	It depends on the nanotube structure
Density current	$1*10^9$ A/ cm^2 (estimated)	Copper wire melting point at $1*10^6$ A/ cm^2
Field emission	Activation of phosphorus compounds at ≈ 1÷3 V with 1 μm spacing electrodes	50÷100 V/μm for molibdenum
Thermal conductivity	6000 W/m°K	Very pure diamond : 3320 W/m°K
Thermal Stability	Stable up to 2800 °C in vacuum and 750 °C in atmosphere	Microchip joints melt within 600÷1000 °C
Chemical properties	Functionalisation according with carbon chemistry	

Tab.2.2.1. Main Properties of Carbon Nanotube

One of the critical challenges faced currently by researchers in the nanotechnology and nanoscience fields is the inability and the lack of instruments to observe measure and manipulate the materials at the nanometer level by manifesting at the

macroscopic level. In the past, the studies have been focused mainly on the collective behaviors and properties of a large number of nanostructured materials. The properties and behaviors observed and measured are typically group characteristics. A better fundamental understanding and various potential applications increasingly demand the ability and instrumentation to observe measure and manipulate the individual nanomaterials and nanostructures.

Characterization and manipulation of individual nanostructures require not only extreme sensitivity and accuracy, but also atomic-level resolution. It therefore leads to various microscopy that play a central role in characterization and measurements of nanostructured materials and nanostructures. These include: X-ray diffraction (XRD) [16,17] various electron microscopy (EM) including scanning electron microscopy (SEM) and transmission microscopy (TEM),[18,19] and scanning probe microscopy (SPM).[20]

SEM [21] is one of the most widely used techniques used in characterization of nanomaterials and nanostructures.

The resolution of the SEM approaches a few nanometers, and the instruments can operate at magnifications that are easily adjusted from - 10 to over 300,000. Not only does the SEM produce topographical information as optical microscopes do, it also provides the chemical composition information near the surface.

In a typical SEM, a source of electrons is focused into a beam, with a very fine spot size of -5 nm and having energy ranging from a few hundred eV to 50KeV that is rastered over the surface of the specimen by deflection coils. As the electrons strike and penetrate the surface, a number of interactions occur that result in the emission of electrons and photons from the sample, and SEM images are produced by collecting the emitted electrons on a cathode ray tube (CRT). Various SEM techniques are differentiated on the basis of what is subsequently detected and imaged, and the principle images produced in the SEM are of three types: secondary electron images, backscattered electron images and elemental X-ray maps.

When a high-energy primary electron interacts with an atom, it undergoes either inelastic scattering with atomic electrons or elastic scattering with the atomic nucleus. In an inelastic collision with an electron, the primary electron transfers part of its energy to the other electron. When the energy transferred is large enough, the other electron will emit from the sample. If the emitted electron has energy of less

than 50 eV, it is referred to as a secondary electron. Backscattered electrons are the high energy electrons that are elastically scattered and essentially possess the same energy as the forward or primary electrons. The probability of backscattering increases with the atomic number of the sample material.

Although backscattering images cannot be used for elemental identification, useful contrast can develop between regions of the specimen that differ widely in atomic number, Z. An additional electron interaction in the SEM is that the primary electron collides with and ejects a core electron from an atom in the sample. The excited atom will decay to its ground state by emitting either a characteristic X-ray photon or an Auger electron, both of which have been used for chemical characterization. Combining with chemical analytical capabilities, SEM not only provides the image of the morphology and microstructures of bulk and nanostructured materials and devices, but can also provide detailed information of chemical composition and distribution. The theoretical limit to an instrument's resolving power is determined by the wavelengths of the electron beam used and the numerical aperture of the system. The resolving power, R, of an instrument is defined as:

$$R = \frac{\lambda}{2NA} \tag{2.2.1}$$

where A is the wavelength of electrons used and NA is the numerical aperture, which is engraved on each objective by condenser lens system, providing a measure of the electron gathering ability of the objective, or the electron providing ability of the condenser. In order to verify and characterize CNTs and CNFs morphology, SEM analysis has been widely adopted in laboratory using VEGA TESCAN SEM model.

In the subsequent figures, pictures of SWCNTs , MWCNTs and CNFs are shown.

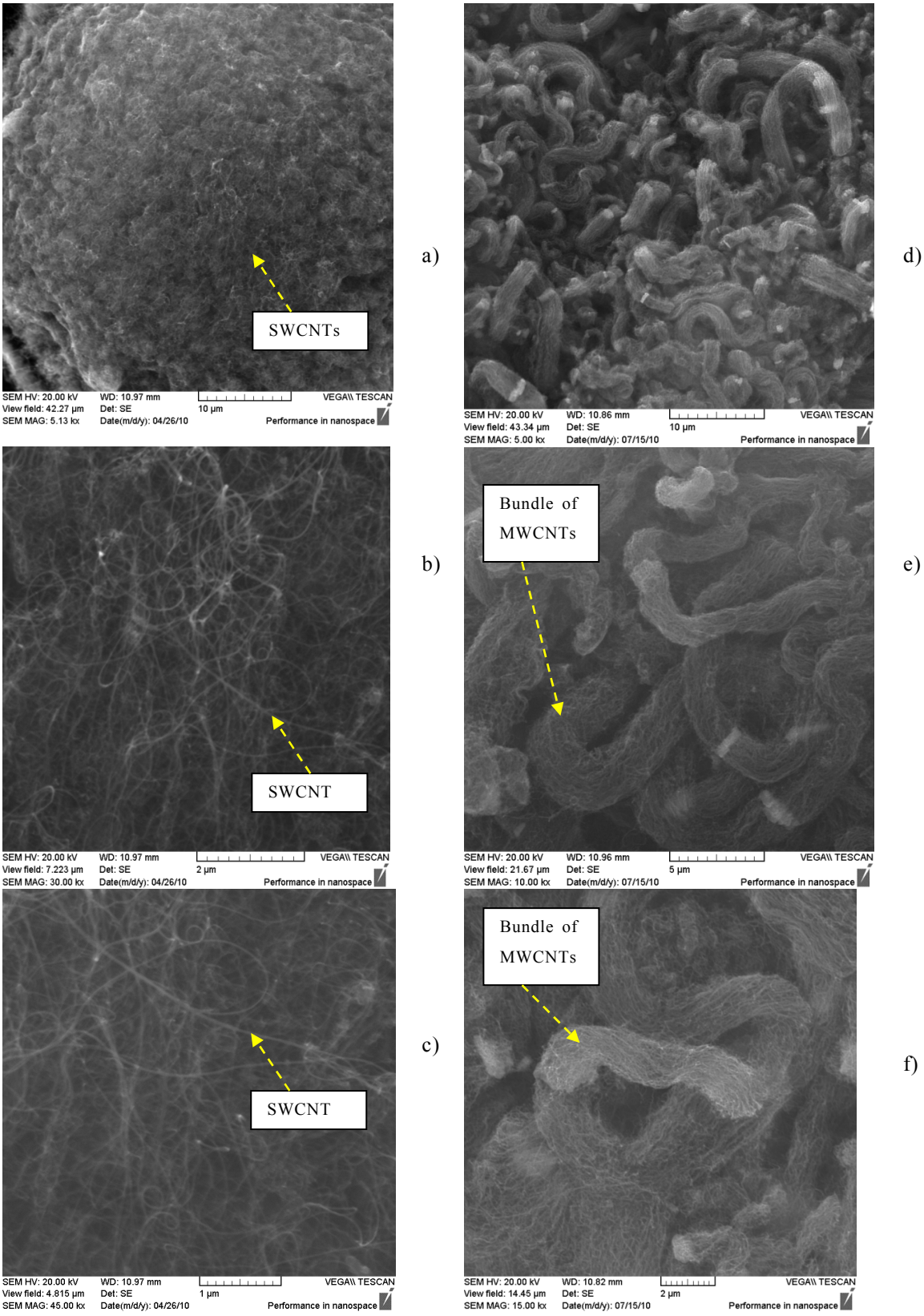

Fig. 2.2.3. a) SWCNT zoom 5x (10µm scale), b) SWCNT zoom 30x (2µm scale), c) SWCNT zoom 45x (1µm scale), d) MWCNT zoom 5x (10µm scale), e) MWCNT zoom 10x (5µm scale), f) MWCNT zoom 15x (2µm scale).

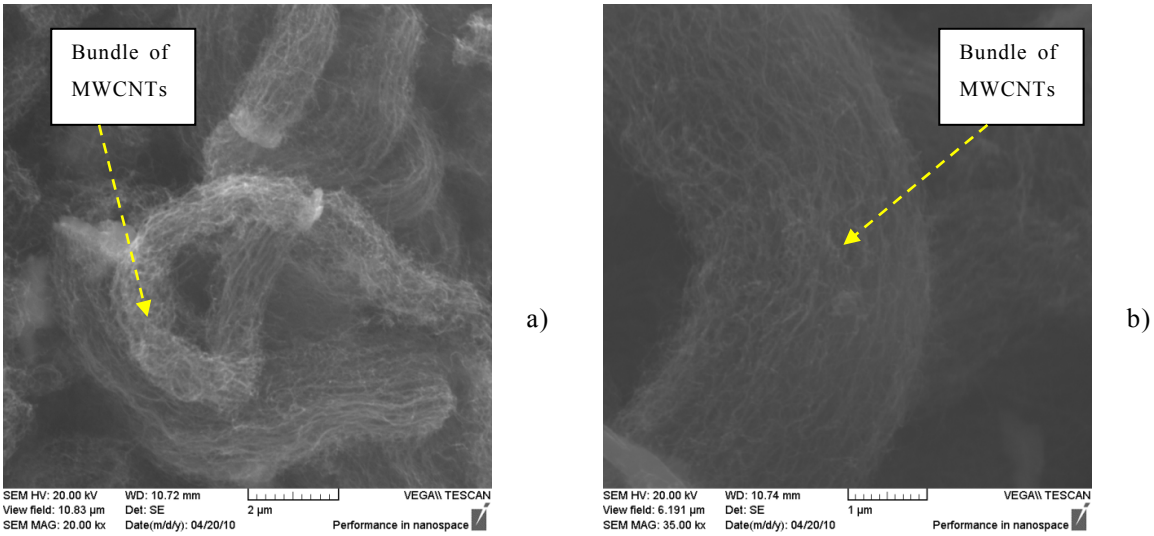

Fig. 2.2.4. a) MWCNTs zoom 20x (2µm scale), b) MWCNTs zoom 35x (1µm scale).

In Fig. (2.2.3), a), b), c), Pictures of functionalized SWCNTs are shown. Functionalization process is described later but it is used to purify CNTs from impurities due to the manufacturing process of CNTs.

In Fig. (2.2.3), d), e), f), Pictures of MWCNTs are shown. Comparing dimensions of SWCNTs and MWCNTs, it can be observed about 0.05 µm for SWCNTs average diameters and about 2 µm for MWCNTs average diameters, i.e., such type of MWCNTs are typically 40 times greater then SWCNTs.

Even topologies of CNTs network appear different; in fact MWCNTs are like ropes of bundled MWCNTs. This fact is well visible in Fig. (2.2.4), where picture of a bundle of MWCNTs is shown.

Such agglomerations of MWCNTs represent a bad problems in composite materials manufacturing, in fact, MWCNTs are not easy to deagglomerate and to disperse within epoxy resin matrix.

In polymerization process, epoxy-resin tend to spirally wrap CNTs, but when such type of dense CNTs agglomeration take place, the polymerization process sometimes fail and localized parts of composite material remain in a fluid status without completing the polymerization phase.

This is why we tried to break and to deagglomerate MWCNTs by means of sonication. Sonication [22] is process where ultrasound is used to drastically reduce

the size of particle agglomerates. Ultrasonic cavitation generates high shear forces that break particle agglomerates into single dispersed particles. The mixing of powders into liquids is a common step in the formulation of various products, such as paint, ink, shampoo, beverages, or polishing media. The individual particles in fact are held together by attraction forces of various physical and chemical nature, including Van Der Waals forces and liquid surface tension. The attraction forces must be overcome on order to deagglomerate and disperse the particles into liquid media. For the dispersing and deagglomeration of powders in liquids, high intensity ultrasonication is an interesting alternative to high pressure homogenizers and rotor-stator-mixers.

In Fig. (2.2.5), a),b), pictures of sonicated free MWCNTs are shown. Comparing these pictures to that of Fig. (2.2.3), d),e), it is possible to observe that some deagglomeration action take place.

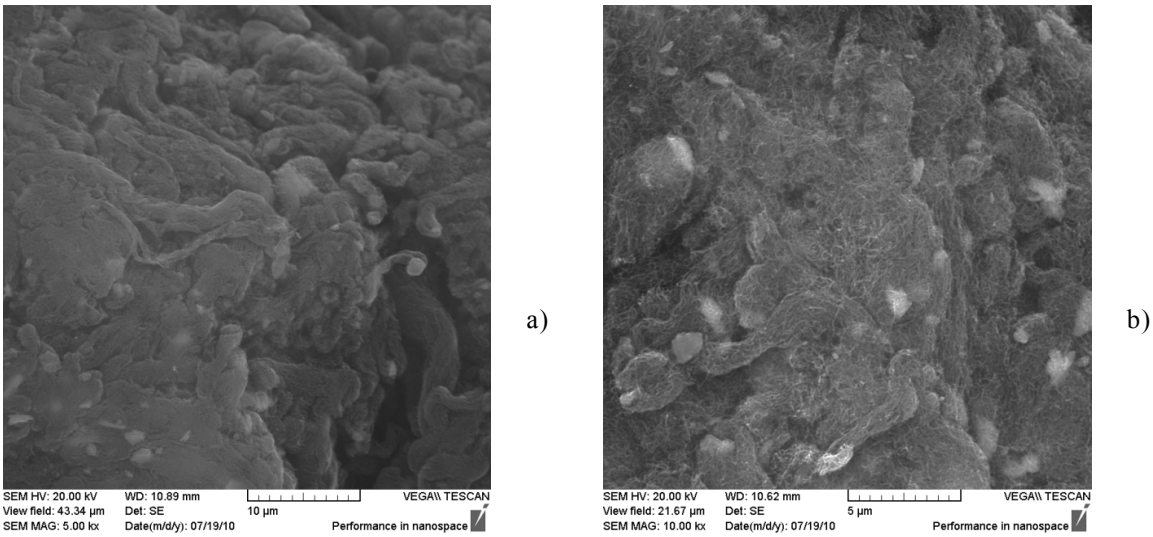

Fig. 2.2.5. a) Sonicated MWCNTs zoom 5x (10µm scale),

b) Sonicated MWCNTs zoom 10x (5µm scale).

In order to be aware about dimensions when talking of carbon nanopowders, we report a comparison between the more known human hair, carbon fiber (CF) and such nanomaterials, like SWCNTs and MWCNTs and carbon nanofiber (CNFs).

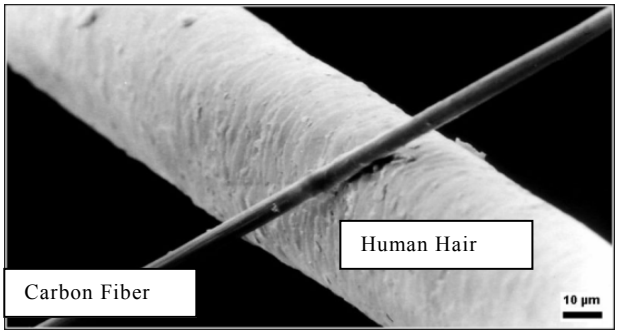

a) taken on the web

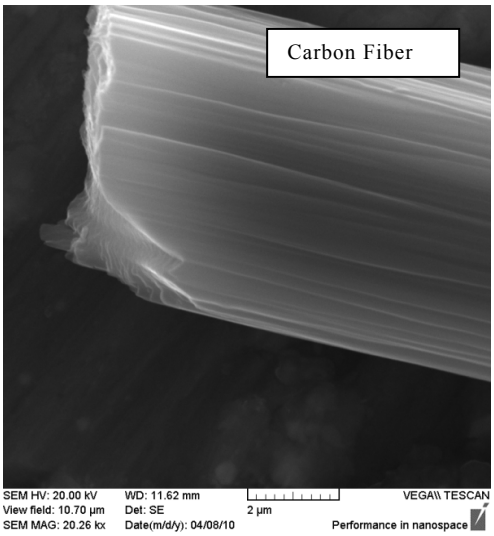

b)

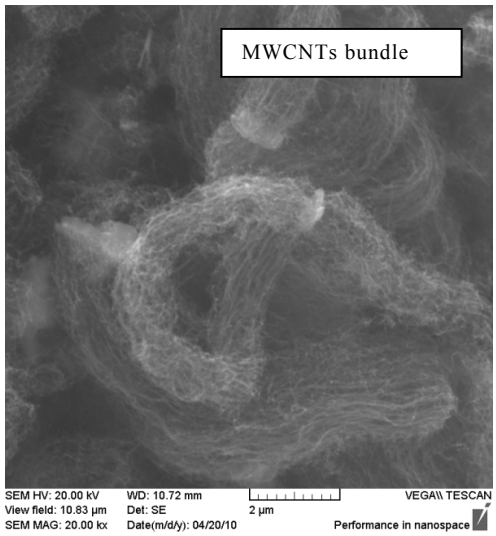

d)

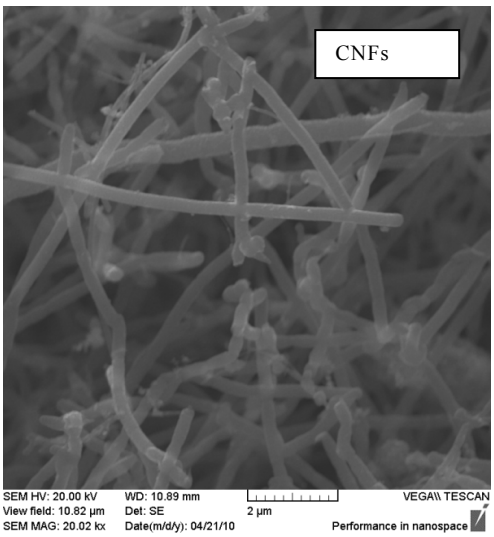

c)

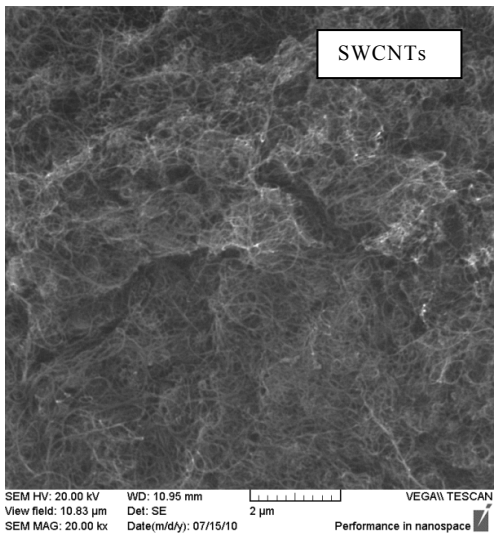

e)

Fig. 2.2.6. a) Carbon Fiber and Human Hair, b) Carbon Fiber (CF) zoom 20x (2µm scale), c) Carbon Nanofiber (CNFs) zoom 20x (2µm scale), d) Multi Wall Carbon Nanotube (MWCNTs) zoom 20x (2µm scale), e) Single Wall Carbon Nanotube (SWCNTs) zoom 20x (2µm scale).

In the following picture CNFs are shown in different scale.

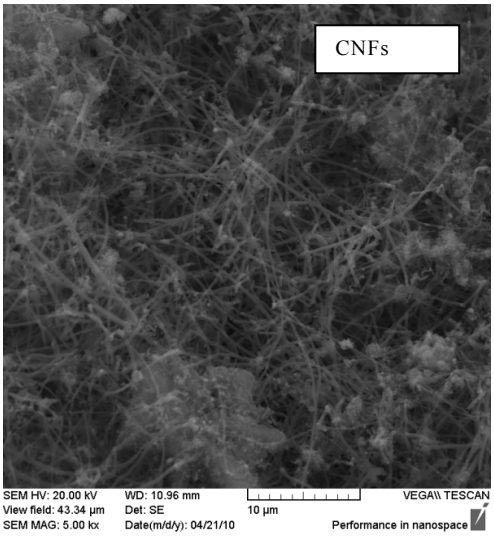

a)

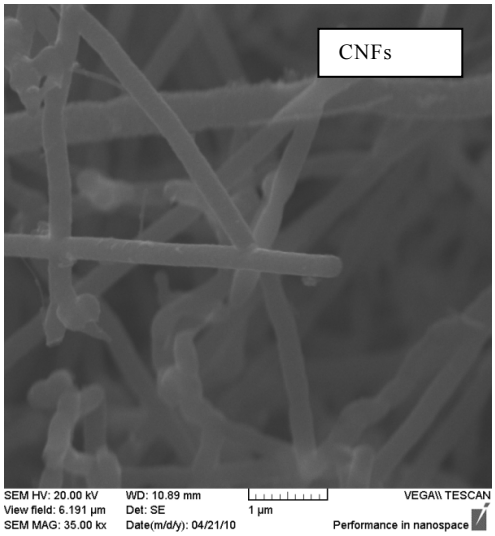

d)

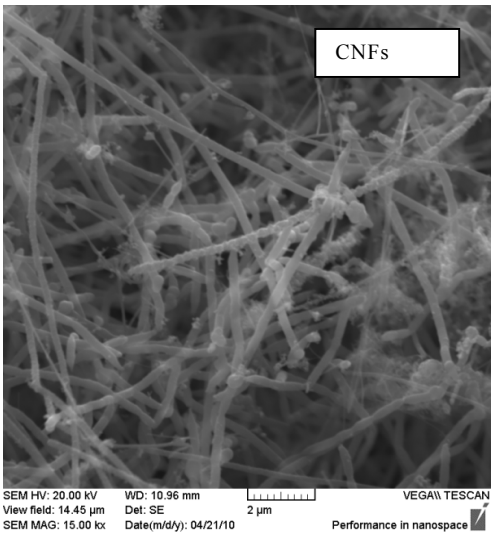

b)

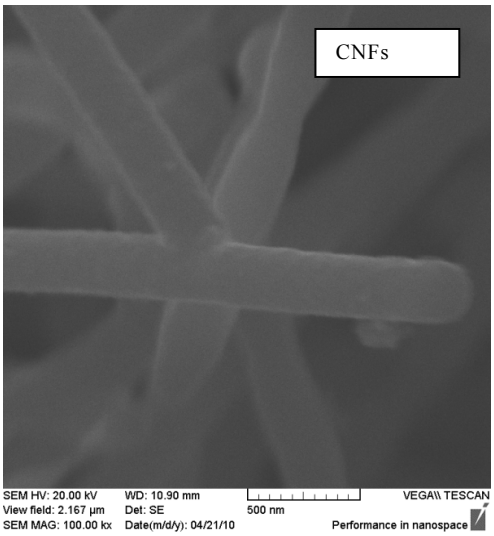

e)

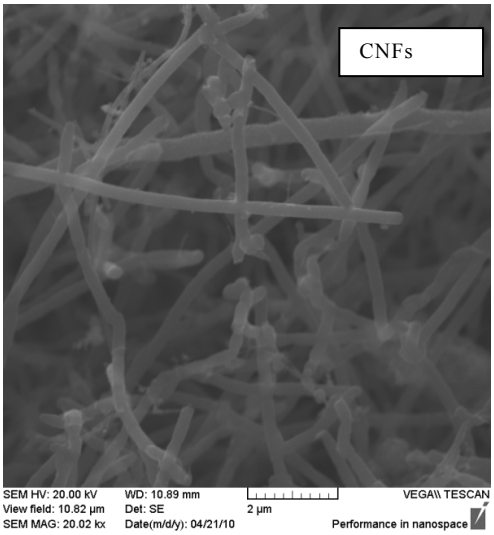

c)

Fig. 2.2.7. a) CNFs zoom 5x (10µm scale), b) CNFs zoom 15x (2µm scale), c) CNFs zoom 20x (2µm scale), d) CNFs zoom 35x (1µm scale), e) CNFs zoom 100x (0.5µm scale),

2.3 Nanostrucutred composite materials manufacturing

Manufacturing of carbon based nanostrucutred composite materials using epoxy-resin, is achieved through the following steps:

- Mixing and sonication of epoxy-resin and carbon nanopowders in the desired weigh percentage;
- Degassing;
- Hardener adding;
- Composite curing by oven treatment.

First step is crucial in preparation of homogeneous composite materials. In Fig. (2.3.1), pictures of composite materials preparation are shown. A priori and a posteriori sonication phase pictures are shown.

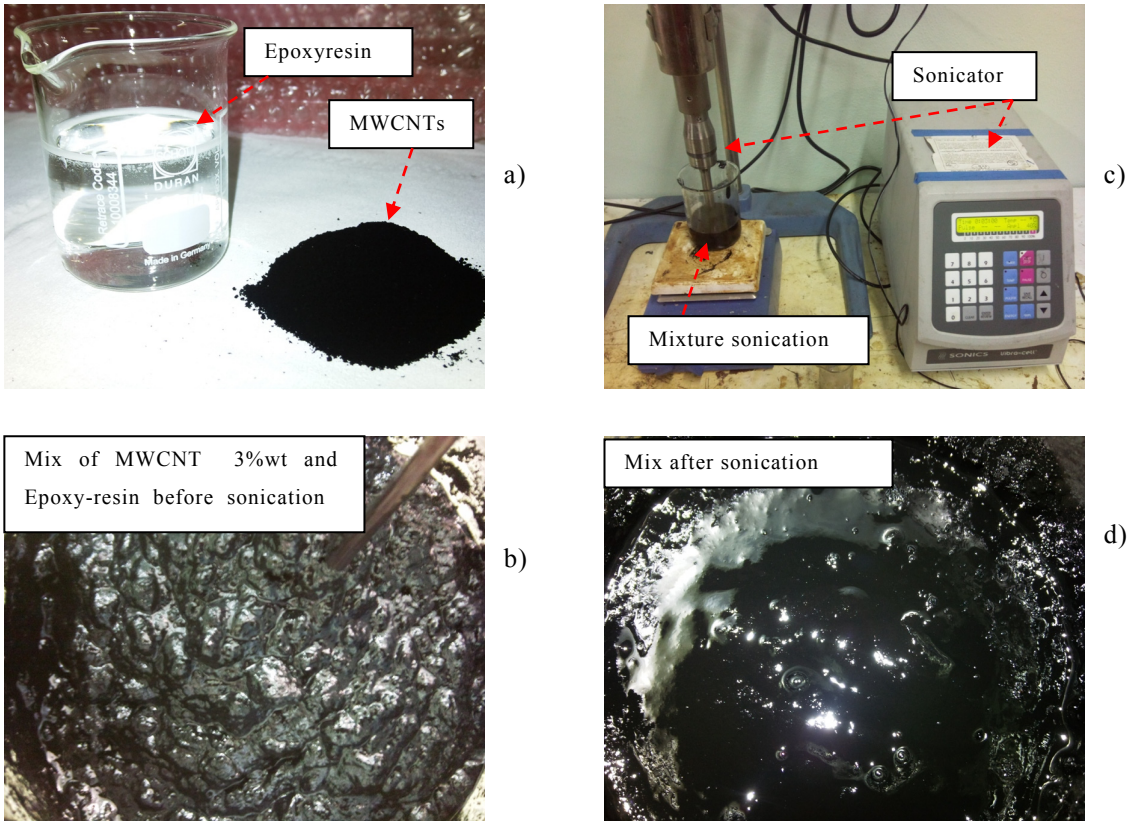

Fig. 2.3.1. a) Ingredients: Epoxyresin and MWCNTs, b) MWCNTs 3%wt and epoxy-resin manually mixed before sonication, c) Sonication process, d) MWCNTs 3%wt and epoxy-resin mixture after sonication

Degassing step consists in reducing the number of small air bubbles within the composite material when it is in liquid status. In our experience we observed that when sonication procedure is deeply performed (freq=20 KHz, amplitude 30% for about 10-15 minutes), then the amount of remaining air bubbles is very little and they do not affect dielectric properties at microwave frequencies. As a consequence degassing procedure can be avoided with less manufacturing time consuming. Since a deep sonication phase transmits kinetic energy and tends to increase the temperature of composite material, then in order to avoid premature polymerization when hardener is added, we organized the entire procedure at temperature around 0 C° i.e., well below the curing temperature of epoxy-resin we used which is 50 C°.

The nanostructured composite material manufacturing process is termed with the injection of described liquid mixture in the appropriate sample holder and by curing all with appropriate oven treatment. In Fig. (2.3.2), sample holder and oven are shown. In our case, Curing process requires about sixteen hours at temperature of 50 C°.

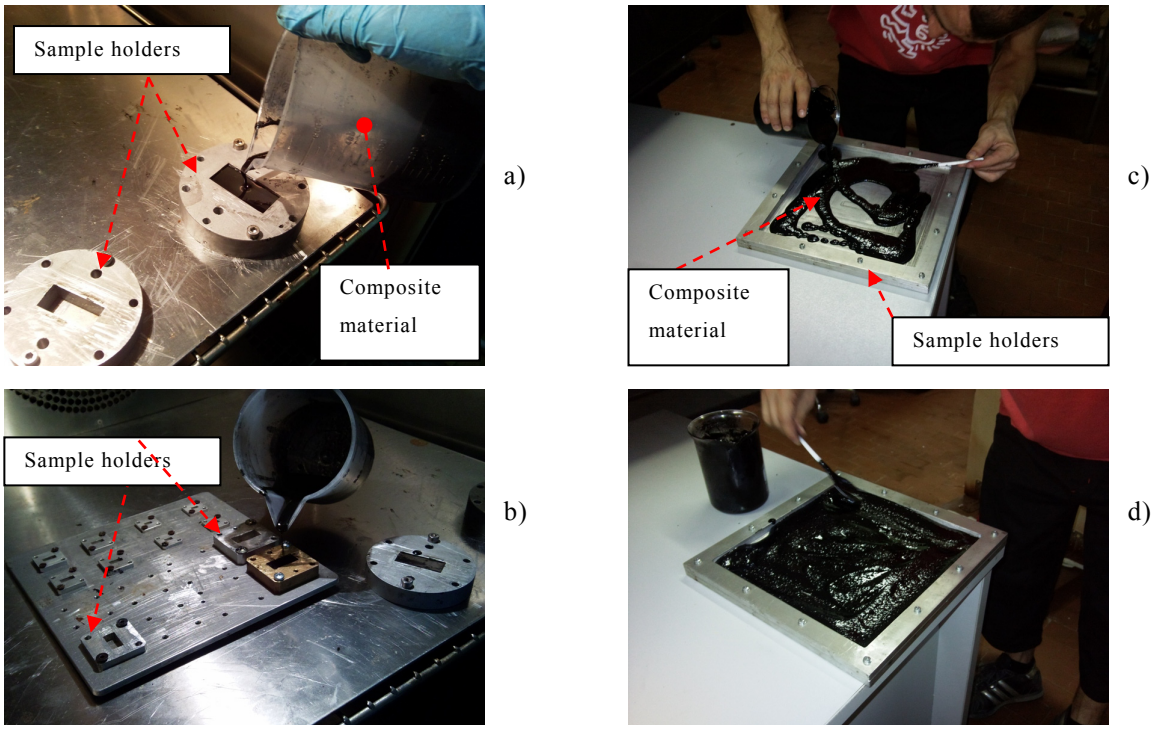

Fig. 2.3.2. a) Sample holder filled with composite material for wave guide analysis in the frequency band 4-8 GHz, b) Sample holder filled with composite material for wave guide analysis in the frequency band 8-18 GHz, c,d) Sample holder filled with composite material for free space electromagnetic analysis.

Final results after oven treatment are shown in Fig.(2.3.3).

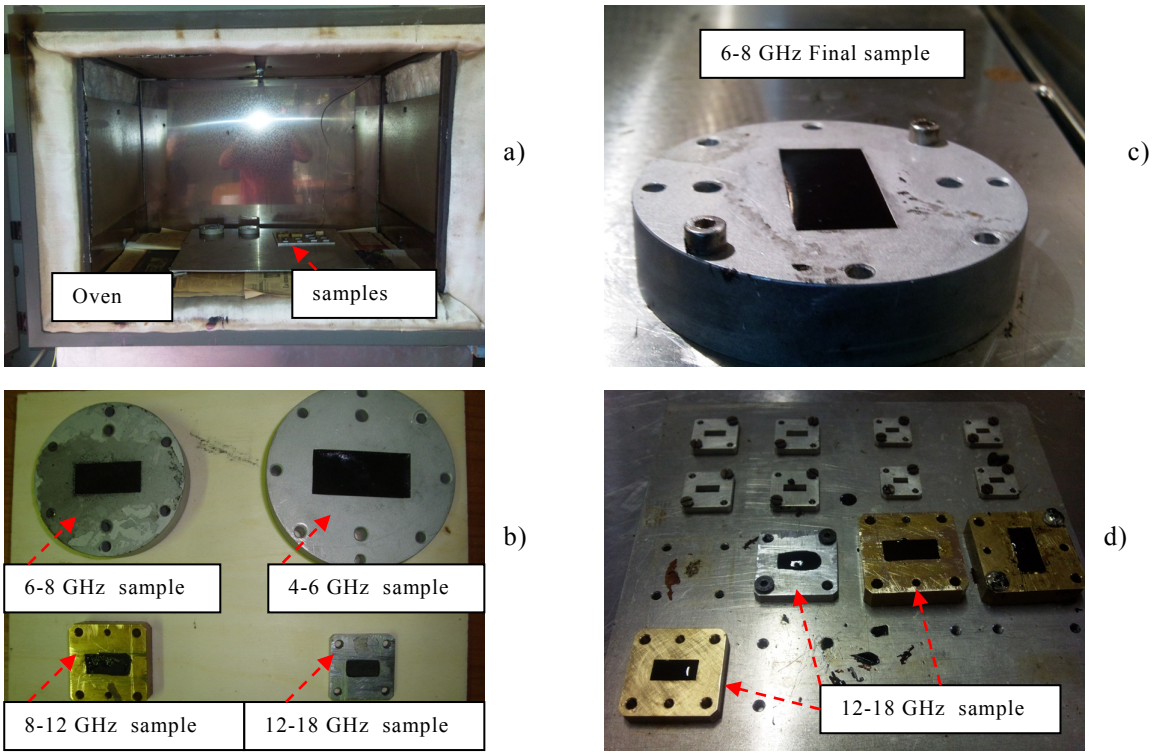

Fig. 2.3.3. a) Oven treatment: 16 hours and 50 C°, b,c,d) Final sample within sample holders for wave guide measurement of electromagnetic properties of composite materials in the band 4-18 GHz.

Each layer of multilayer tile is accurately defined in thickness by using an in-house built press shown in Fig.(2.3.4).

Each layer is built over the other. Starting from the last layer, one after one layers are added to the previous and tuned in thickness using press. Some holes on the upper plate of press allow surplus of material to flow out.

Each layer require about 16 hours to complete polymerization as a consequence the current process of multilayer manufacturing requires several days to be successfully completed.

Such method allows adjusting thickness of each layer with an average uncertainty of about 0.5 mm.

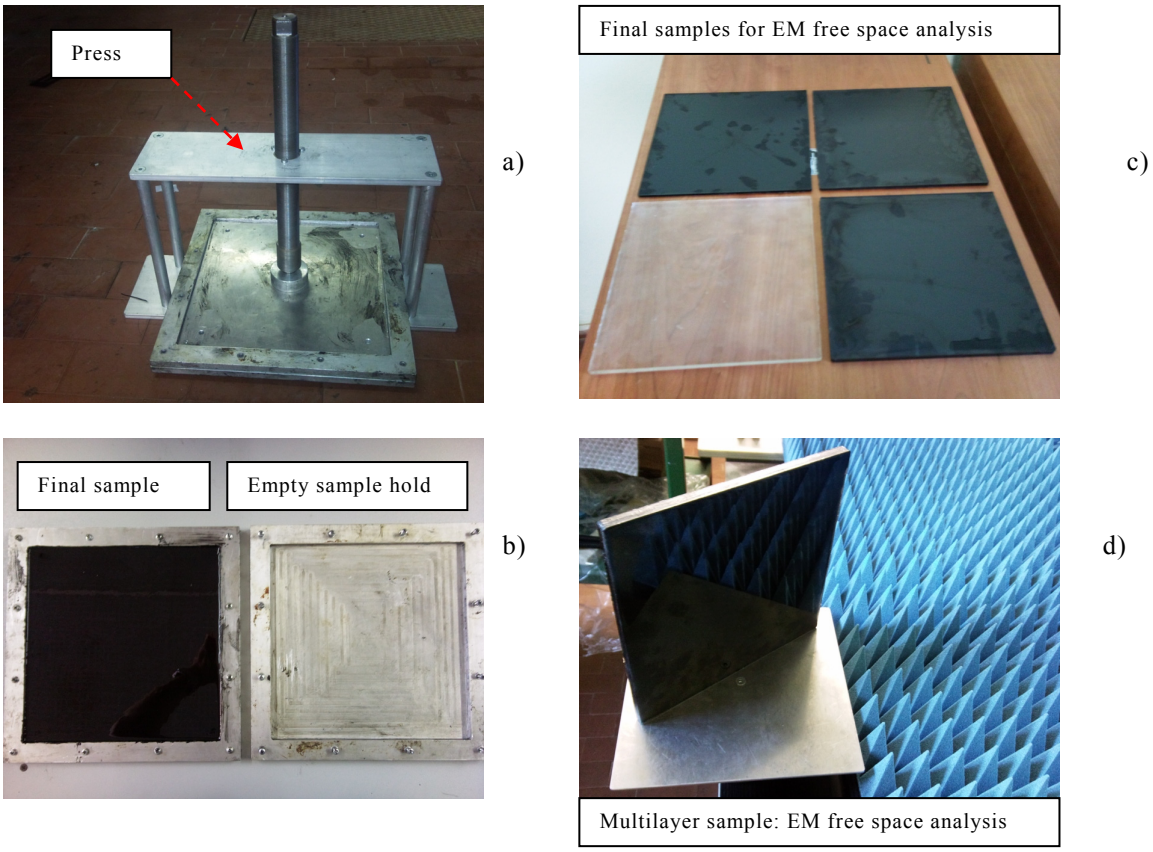

Fig. 2.3.4. a) Press to make multilayer structure. b,c,d) 200x200 mm tiles for free space electromagnetic measurements analysis

2.4 Problems in composite materials manufacturing

Several factors can induce failures in manufacturing nanostructured composite materials, major of them are: wrong cure temperature cycle and to much high concentration of carbon nanopowders. Presence of high concentration of carbon nanopowders can modify the composite cure temperature so for each epoxy-resin type some trials are required prior to find the optimal method to produce nanostructured composite materials.

In our experience when the weigh percentage of carbon nanopowders i.e., CNTs or CNFs wt%, with respect to epoxy-resin are greater than 5% it is quite hard to homogeneously disperse them within the epoxy-resin matrix. Such criticism become difficult to overcome if the dimensions of the composite materials we want make are greater than of usual little samples used in laboratory to characterize the materials. In

Fig.(2.4.1) we compare the preparation of composite materials based on MWCNTs for weight percentage of 2% and 5% with respect to epoxy-resin. We can notice that 5wt% appear almost as a solid material which is hard to disperse and deagglomerate using sonication. In other words this means that some parts of materials will result denser than the others and as a consequence in a large sample, the electromagnetic properties of composite material will be differently affected from point to point in a non controllable manner.

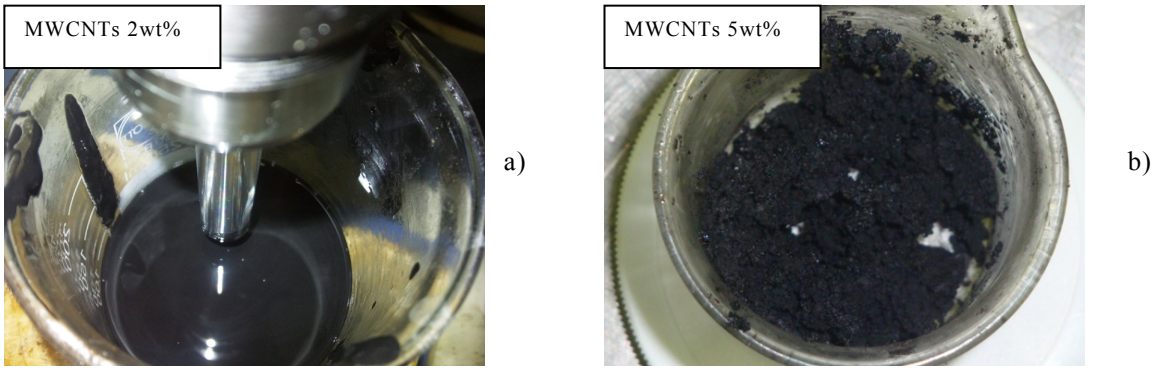

Fig. 2.4.1. a) composite material mix of MWCNTs 2wt% b) composite material mix of MWCNTs 5wt%

Relatively high weigh percentage of carbon nanopowders produce also another problem, in fact, since dispersion and deagglomeration time consuming increases with the weigh percentage of nanomaterials then also the mechanical energy transferred to the mixture increases.

In this condition when we add the hardener it could happen that polymerization process start while we are still mixing the compound or injecting it in the sample holder shape.

The immediate consequence is a failure in composite material manufacturing process. In Fig.(2.4.2), shows a filed trial during a 200x200 mm tile manufacturing using CNFs 3wt%. It is possible to observe the bad surface condition of the tile. This happened since polymerization process started while we were still injecting liquid composite material in the sample holder.

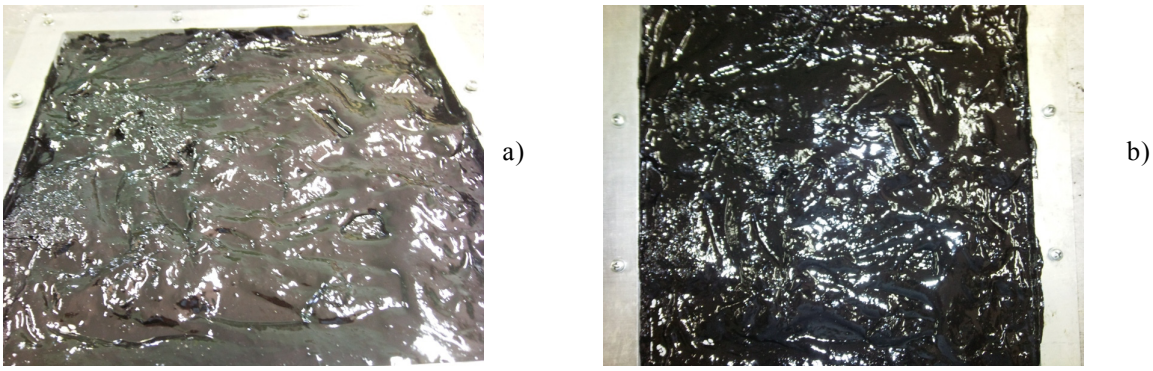

Fig. 2.4.2. a,b) early polymerization of composite materials containing CNFs 3%wt, while it was injected in the sample holder 200x200x10 mm

Manufacturing of multilayer structure is also quite difficult since each layer is added over the previous layers and each time the oven treatment is required for composite curing phase. So supposing to have four layers and sixteen hours of oven treatment for each layer, than an amount of about four days is the working time required to complete the structure.

In Fig,(2.4.3), pictures of two multilayer layers structure are shown. In a) is possible to observe the first layer based on 2mm of MWCNTs 3wt%: in b) the final double layer structure is obtained adding a second layer of 4mm epoxy-resin on the first layer.

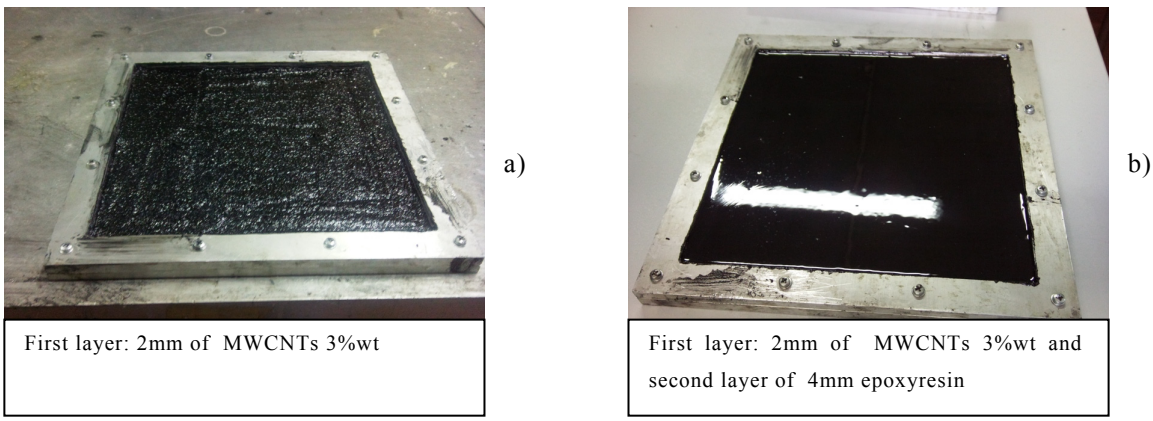

Fig. 2.4.3. Multilayer structure manufacturing. a) first layer based on 2mm MWCNTs 3%wt, b) second layer of 4mm Epoxyresin deposited above the first layer in the sample holder 200x200x10 mm

2.5 Epoxy-resin and MWCNTs composite SEM surface analisys

In Fig. (2.5.1), SEM pictures of surface of some samples loaded with MWCNTs are taken. In particular it can be noticed that surface of sample in Fig (2.5.1.b) appear smother than the other.

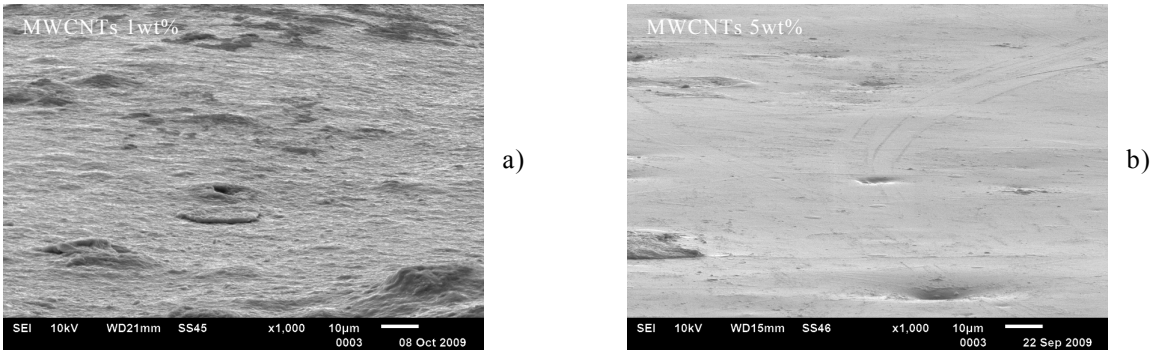

Fig. 2.5.1. SEM surface analysis. a) composite with MWCNTs 1%wt, a) composite with MWCNTs 5%wt

2.6 Conlusion

In this chapter carbon powders used to build composite materials based on epoxy-resin have been presented and scanning electron microscope pictures shown.

Reasons conducting us to adopt certain carbon nanomaterials have been weighted taking into account market price and large amount of carbon nanomaterials needed in an industrial scenario

Composite materials manufacturing system has been deeply analyzed taking into account problems too, mainly arising from high weigh concentration of carbon nanomaterials in the epoxy-matrix.

In the next chapter electromagnetic characterization of composite materials is performed.

2.7 Reference Table

[1] Xingcun Colin Tong, "Advanced Materials and Design for Electromagnetic Interference Shielding", *CRC Press*, 2009
[2] Z. Ounaiesa,*, C. Parkb, K.E. Wiseb, E.J. Siochic, J.S. Harrisonc, "Electrical properties of single wall carbon nanotube reinforced polyimide composites", *Elsevier Science@Direct* 2003.
[3] D. Micheli *, C. Apollo, R. Pastore, M. Marchetti, "X-Band microwave characterization of carbon-based nanocomposite material, absorbing capability comparison and RAS design simulation", *Elsevier Composites Science and Technology 70 (2010) 400–409*, 2010
[4] Bhattacharya, S. "Metal-filled Polymers". *New York: Marcel Dekker*. 1986.
[5] Kalyon, D.M., E. Birinci, B.Karuv, and S.Walsh. 2002.,"Electrical properties of composites as affected by the degree of mixedness of the conductive filler in the polymer matrix.", *Polymer Engineering and Science* 42: 1609-1617.
[6] Bigg, D. M., "The Effect of compounding on the conductive properties of EMI shielding compounds." *Advances in Polymer Technology 4: 255-266.,* 1984.
[7] Weber, M, and Kamal., "Estimation of the volume resistivity of electrically conductive composites.", *Polymer Composites 18(6), 711-725*, 1997
[8] Sichel, E., "Carbon Black-Polymer Composites". *New York: Marcel Dekker*. 1982.
[9] Toshio, J. I. Yuichi, I. Takashi, and Y. Rikio. " Characterization of multi-walled carbon nanotubes/phenylethynyl terminated polymide composite.", Composites Part A: *Applied Science and Manufactoring 35:67-74*, 2004.
[10] Sankaran,S.,S.Dasgupta. K.Ravi Sekhar, and C.Ghosh., "Carbon nanotubes rreinforced syntactic composite foams." *Procedings of ISAMPE National Conference on Composites, 82-82 XII*. 2005.
[11] Davide Micheli, Roberto Pastore, Carmelo Apollo, Mario Marchetti, Gabriele Gradoni, Valter Mariani Primiani, and Franco Moglie, "Design of Broadband Quasi-Perfect Electromagnetic Absorbers using Carbon Nanostructure-Based Composites", IEEE Nanotchnology. 2010.
[12] C. Vieu, F. Carcenac, A. Pepin, Y. Chen, M. Mejias, A. Lebib, L. Manin-Ferlazzo, L. Couraud, and H. Lunois, Appl. Sur- Sci. 164, 11 1 (2000).
[13] Thess, A., Lee, R., Nikolaev, P., Dai, H., Petit, P., Robert, J., Xu, C., Lee, Y.H., Kim, S.G., Rinzler, A.G., Colbert, D. T., Scuseria, G.E., Tomanek, D., Fisher, J.E., and Smalley, R.E., "Crystalline Ropes of Metallic Carbon Nanotubes". Science 273, 1996, 483-487
[14] S. Iijima, "Helical Microtubules of Graphitic Carbon", Nature, 354, 56 (1991).
[15] D
[16] B.D. Cullity and S.R. Stock, Elements of "X-Ray Diffraction, 3rd edition", *Prentice Hall, Upper Saddle River,* NJ, 2001.D
[17] L.H. Schwartz and J.B. Cohen, „Diffraction From Materials, Springer-Verlag, Berlin", 1987.
[18] L. Reimer, "Scanning Electron Microscopy", *Springer-Verlag*, Berlin, 1985.

[19] Z.L. Wang, "Reflected Electron Microscopy and Spectroscopy for Surface Analysis", *Cambridge University Press*, Cambridge, 1996.
[20] D. Bonnell (ed.), "Scanning Probe Microscopy and Spectroscopy", *Wiley-VCH*, New York, 2001.
[21] Guozhong Cao, "NANOSTRUCTURES & NANOMATERIALS Synthesis, Properties & Applications", *Imperial College Press,* 2004
[22] Y. Y. Huang, S. V. Ahir, and E. M. Terentjev. "Dispersion rheology of carbon nanotubes in a polymer matrix," *Physical Review B*, Vol. 73, N. 12, 125422, 2006, pp. 1-9

Chapter 3

Dielectric characterization of Composite Materials and Microwave absorbing properties

3.1 Introduction

In this chapter analysis of electromagnetic properties of epoxy-resin based composite materials are shown.

At the beginning the meaning of electrical conductivity is explored from chemical, physical, and electromagnetic point of view: conductors and dielectric materials are described and the meanings of permittivity and permeability discussed.

In the first part of chapter theoretical analysis are proposed, in the second part some measurement methods of dielectric properties of composite material are presented, in the third part, dielectric properties of manufactured epoxy-resin based composite materials are analyzed. Composite materials are those introduced in the previous chapter and are adopted in microwave absorbing and shielding applications.

3.2 Definition of electrical conductivity from atomic point of view

3.2.1 Electrical conduction in Metals and delocalized Bloch Orbitals

Properties and structure of metals, reveals that *valence electrons* of their atoms, are *delocalized* i.e., they are spread out in all the extension of the crystalline network and they are free to migrate from on place to another under the action of even a weak electric field.

As far as *atomic orbital* of molecules are concerned, when they overlap to each other, their combination give rise to a system of delocalized *molecular orbital* extended on several or even to all of the molecule's atoms.

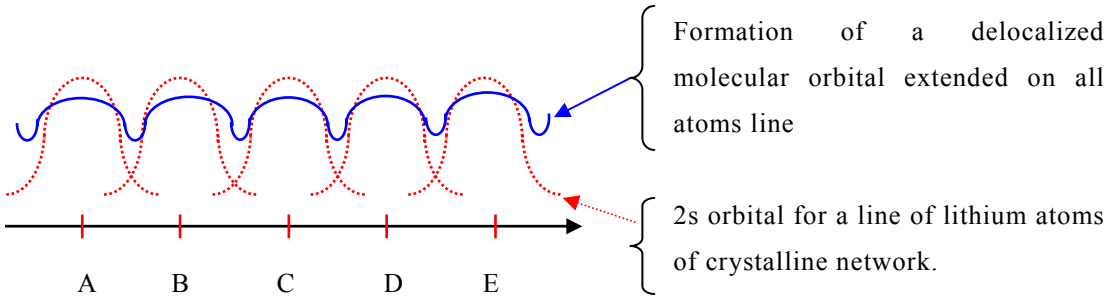

Fig.(3.2.1.1). Delocalized molecular orbital within crystalline structure of metal

A metallic crystal can be considered as a giant molecule made of a great number of atoms where the same principle is applied [1]. In such scenario, due to the compactness of the structure, extended overlapping phenomena between orbitals happens and a new equivalent single atom valence orbital take place. The immediate consequence is that the crystalline or reticular orbital, result completely delocalized embracing the entire reticular network.

Such delocalized orbital describe the valence electron's distribution of atoms within the crystalline reticular network structure of metal. Such orbital are called *Bloch wave function* from the name of author which first introduced this physical model theory.

3.2.2 Energy bands

Molecular orbital of a crystal i.e., of a great number of atoms, differ from that of a single molecule of few atoms due to an important characteristic pertaining their corresponding energetic levels.

In order to have an idea of phenomena we can suppose to build a crystalline network of Sodium (NA) adding step by step one atom to the others. When a second atom B is added to the first atom A, i.e., making the bi-atomic aggregate Na_2, the valence orbital of each single atom are combined together. The results are two distinct molecular orbital each one characterized by a proper energy.

$$\psi_A + \psi_B \quad \text{and} \quad \psi_A - \psi_B$$

Where $\psi_A + \psi_B$ corresponds to a higher energy level, whereas $\psi_A - \psi_B$ corresponds to a lower energy level with respect to the initial single atoms.

Now if we add a third atoms C, making the aggregate Na_3, the valence orbital of three atoms will determine three molecular orbital and their distinct energetic levels will group around the original level ψ_A.

The addition of a new atom increases by one the number of available molecular orbitals so as the corresponding energetic levels. As a consequence for N atoms it will exist N energetic levels. When N is great, say around 10^{23}, the energetic levels are so close to each other to constitute a continuous energy band.

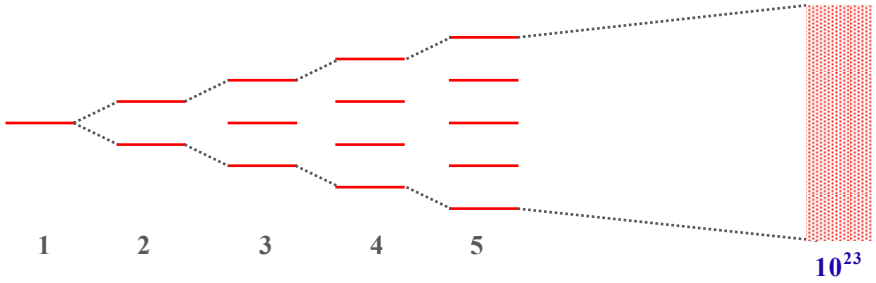

Fig.(3.2.2.1). Continuous band of energy levels

The conductivity properties of a crystal are mainly ascribed to the energy difference between adjacent energy band and by the distribution of electrons within such bands.

- The *band amplitude* resulting by the interaction between atoms within the crystal and the *bands separation,* depends on the inter-nuclear distances ***r***;
- When ***r*** decreases the amplitude of band increases and the gap between adjacent band decreases.

When atoms are at far distance form each other and they are not interacting to each other, the energy levels of electrons are corresponding to that of isolated proper atoms.

Reducing the inter-atomic distances each level give rise to an energy band. The greater the reciprocal atoms interaction, the bigger is the amplitude of the resulting energy band.

This is represented in the next figure.

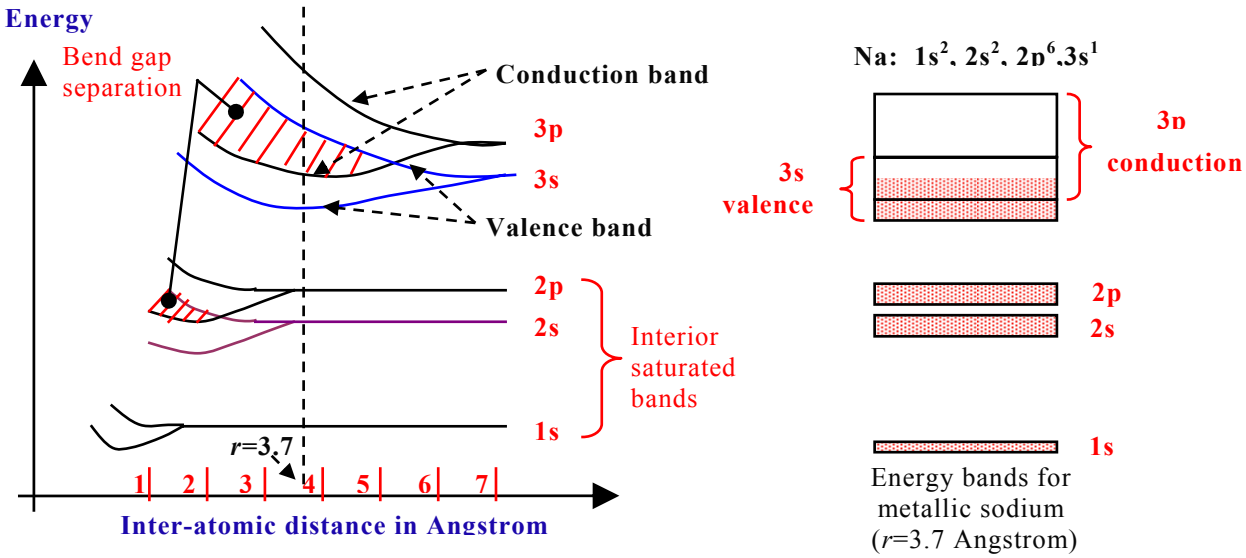

Fig.(3.2.2.2). Band gap separation

Given a certain distance ***r*** between atoms, the higher the energy band, the greater the band amplitude:

- The higher is the extension of the atomic orbital, the grater is the inter-atomic distance at which the interaction between atoms transforms the energetic levels of isolated atoms in energy bands,
  - For this reason the energetic level of ***3s*** and ***3p*** orbital are transformed in band for values of ***r*** where the levels of ***2s*** and ***2p*** orbital are not yet perturbed.
  - The internal level ***1s***, remain unaffected down to very close inter-atomic distances.
- The progressive increasing of band's amplitude with the diminishing of the reciprocal inter-atomic distances can determine the band overlapping:
  - In case of sodium depicted in Fig.(3.2.2.2), at the distance ***r***=3.7 Angstrom, at which are placed the atoms in the crystal network, the fusion happen for the band ***3s*** and ***3p*** which become one only energy band.

The electrons of atoms within the crystal are distributed within the orbitals, corresponding to the energy levels of the different bands, following the Pauli principle. The distribution starts from the low energy level.

Supposing the reported example of sodium, the electrons of deep orbital ***1s, 2s,2p***, do the saturation of the corresponding internal band. The valence's electrons instead (suppose *N* electrons), do the saturation of the first *N*/2 levels of the ***3s*** band which therefore is called valence band (in chemistry, the definition of valence band stay for the band interested to the exchange or put in common of electrons in order to make chemical bonds). The succession of the different growing energy bands follows a scheme in which belts of prohibited energy values for the electrons of the crystal are put between bands of permitted energy values. What happen in the crystal is similar to a single atom where the electrons can stay only on the well defined energy levels and the energy levels between the permitted quantized zones are prohibited.

The electrons in the internal bands are practically localized within the atom of pertinence, whereas the electrons of the valence band are delocalized since they can travel over all the extension of the crystalline reticulum.

In order to better understand what happen to the electrons, we can image two different situations: the first where only one atom of sodium is considered and the second where a reticulum of linearly disposed atoms of sodium is considered.

In the first scenario, the curve relating the potential energy of the electron versus the distance ***r*** from the nucleon is in the picture below shows.

$$E_{coulomb} = -\frac{Ze^2}{r} = -\frac{11e^2}{r}$$

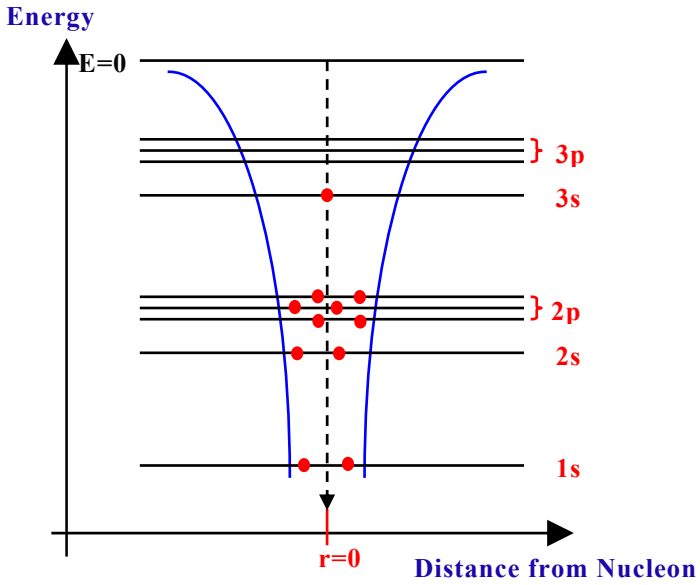

Fig.(3.2.2.3). Electrons distribution allocation in an hypothetical single sodium atom

On the curve are depicted the permitted energy levels for the electrons of atom, the higher the level of the occupied orbital, the greater is its extension and the higher is the average distance of the electron from nucleon.

In the next figure a similar relationship are reported taking into account several sodium atoms disposed along a line.

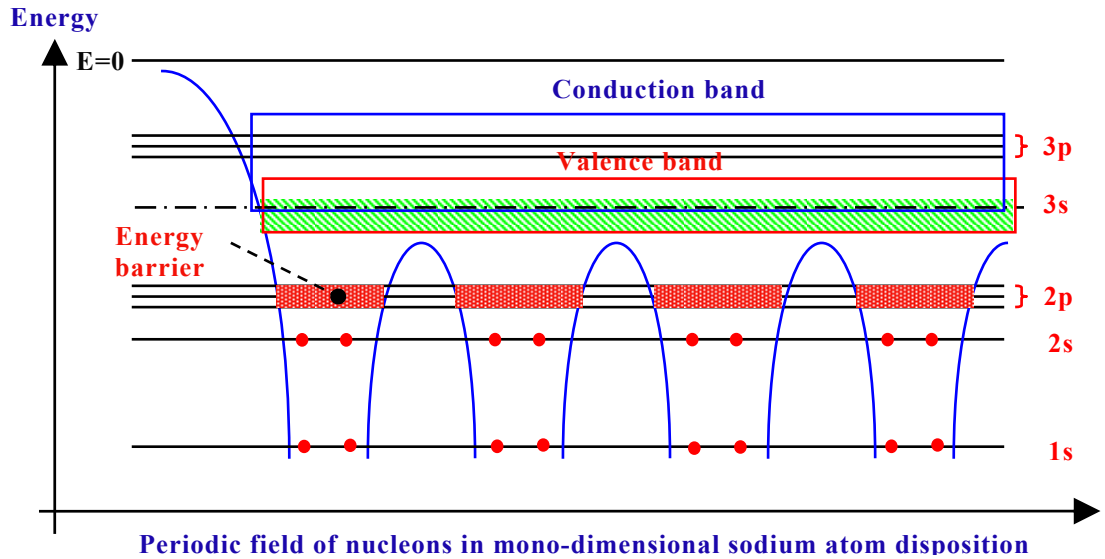

Fig.(3.2.2.4). Electrons distribution allocation in an hypothetical chain of sodium atoms

Between each couple of atoms, the resulting field determines an energy barrier which forbids the electrons of ***1s*** and ***2s*** orbital to change their energy status. In their energy are too low to overcome the barrier. On the other side the electrons of the valence band are instead free to move within the reticulum i.e., in the conduction band overlapped to the valence band.

3.2.3 Conductors Nonconductors and Semiconductors

The model based on bands, is applied to all type of crystalline solids, metallic or non metallic. It is quite effective in interpreting the properties of conductive or nonconductive materials.

Let us to consider the following scheme related to an ideal crystal where the electronic bands are well separated without any overlapping. Distributing the

electrons on the permitted energy levels two main scenarios are possible: in the a) scenario, the valence band are only partially occupied and it contains free levels, whereas in the b) scenario the valence band is fully occupied.

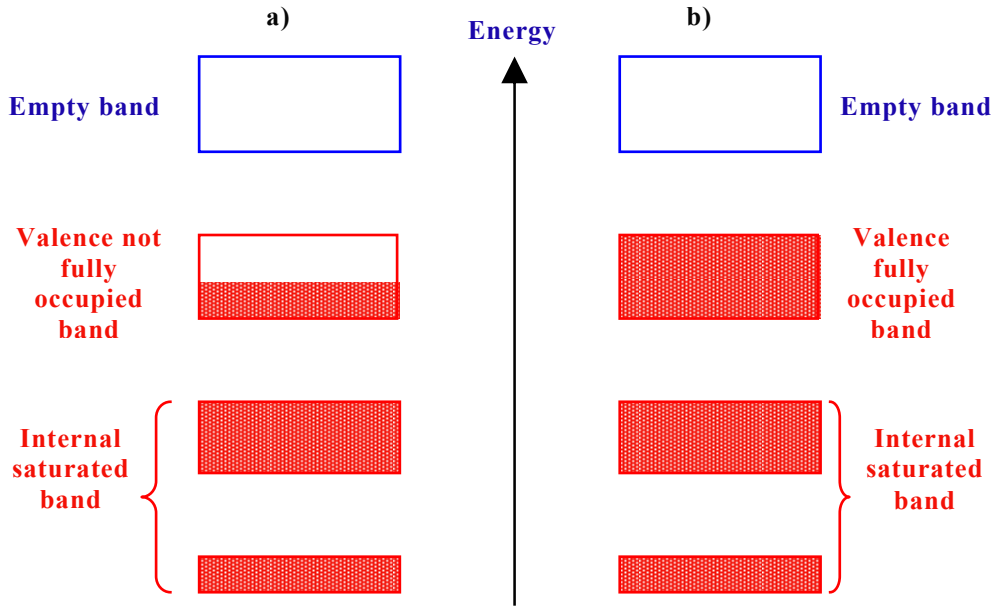

Fig.(3.2.3.1). Conductor and non-conductor model of solid crystal

The orbital corresponding to the valence bands are in both scenarios delocalized, therefore the electrons within such bands can freely change atom moving in in any direction. Nevertheless, the effect of an electric applied field is quite different. The applied electric field tends to make a unidirectional flux of electrons in which the energy of electrons increases due to the electric field.

- In scenario a), the valence band are not fully occupied, there are some free energy levels available above the occupied levels in the absence of electric fields. In such free levels, the electrons which acquire energy under the application of electric field can be moved constituting an ordinate flux i.e., an electric current.
- In scenario b), such promotion of electrons to higher levels is impossible since all the valence band is already fully occupied by electrons moving in all direction. Here there are not levels available for the electrons acquiring energy

in order to be allocated and to constitute an ordinate flux i.e., the electric current.

We can conclude that in the scenario a), the crystal is an electronic conductor since even a weak electric field is able to determine a flux of electrons across the crystal mass. The electric current is $I = dQ/dt$ where Q is the total charge carriers. Such current can also be expressed as: $I = N \cdot q \cdot V_d$, where N is the number of carriers, q is the elementary carrier, V_d is the drift velocity of the carrier.

In b) scenario instead, the crystal is a nonconductor. In fact, the only way to obtain an ordinate unidirectional flux of electrons would be the application of a so high electric field, up to give to some electrons of the valence band the energy needed to promote and transfer them into the next empty band. This last band represents a conduction band since when some electrons pass to it there is a current flux.

This mechanism explains the *breakdown voltage* of dielectric materials.

We can conclude saying that when a solid crystal is characterized by only partially occupied valence bands, it is an electrical conductor, whereas when it is characterized by fully occupied bands or fully empty bands without any reciprocal overlapping, the crystal is a nonconductor. In the following examples, some materials are analyzed. The first material is **lithium**. In the crystalline lithium ***(1s², 2s¹)***, the band ***2s*** and ***2p***, are partially overlapped making together a unique band where supposed N the number of atoms, then $8N$ electrons could be placed (in fact, ***2p*** band has 3 corresponding orbital, $\mathbf{2p_x}$, $\mathbf{2p_y}$, $\mathbf{2p_z}$).

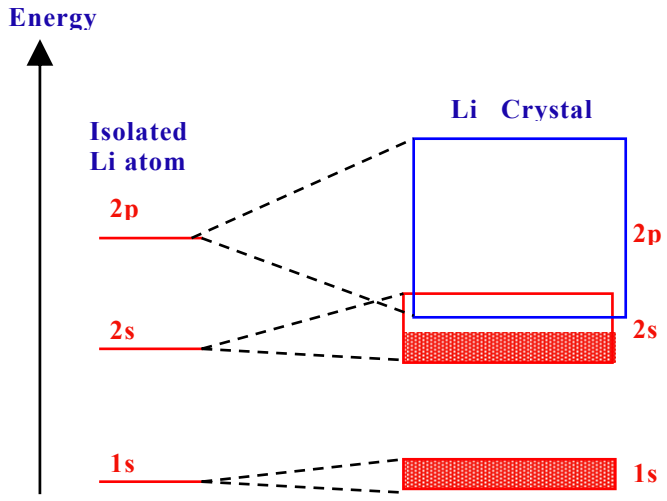

Fig.(3.2.3.2). Lithium atomic energy band model

The valence electrons are able to saturate the first *N/2* levels of ***2s*** band letting completely empty the remaining *N/2* levels of ***2s*** band and all the other levels of the ***2p*** band. As a consequence, immediately above the occupied levels there are many other free levels available for the conduction under the action of electric field.

Some materials like Carbon are characterized by a bands system where the higher occupied band is fully occupied while the next energy band is empty. The prohibited energy gap is not negligible. As an example in the case of diamond, atoms of carbon are tied to each other by means of covalent chain with tetraedic coordination determined by ibrid orbital sp^3 type. The resulting molecular orbital are grouped in two energy bands separated by a large prohibited energy gap of 5.6 eV.

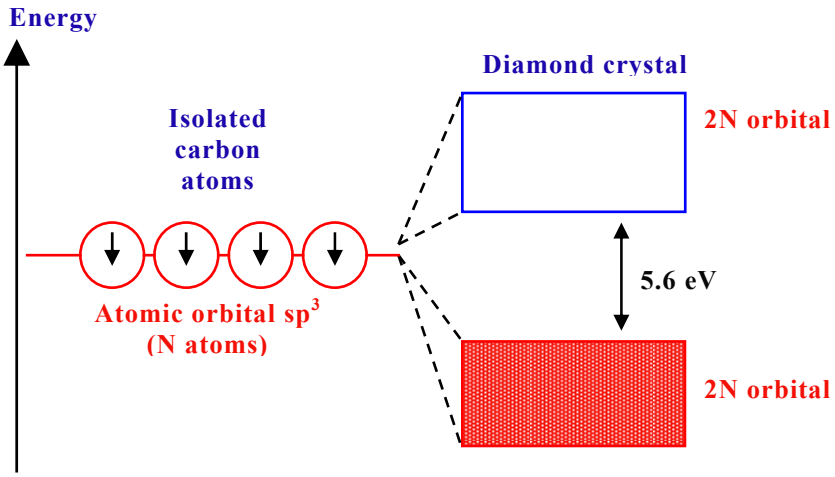

Fig.(3.2.3.3). Diamond atomic energy band model

The four valence electrons completely do the saturation of the lower energy band and due to the high prohibited energy gap (5.6 eV), is almost impossible for the electrons to migrate to the upper empty energy band under the action of external electric field. As a consequence, the diamond is a perfect nonconductive material from electrical point of view.

In case of silica (Si) and germanium (Ge), the scheme is quite similar but the amplitude of the prohibited energy gap is 1.1 eV (Si) and 0.7 eV (Ge). Such band gaps are quite smaller compared to that of diamond and it is possible to transfer a certain number of electrons from one band to the other. Such electrons transferring can take place due to thermal excitation or due to irradiation with appropriate wavelength. Under such conditions, the crystal becomes electrically conductive and, we speak respectively of thermo-conduction and photo-conduction.

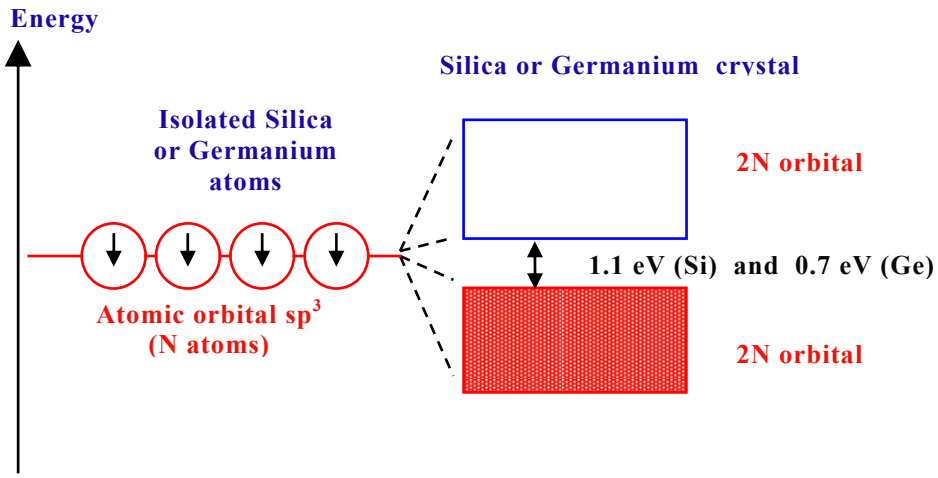

Fig.(3.2.3.4). Silica or Germanium atomic energy band model

Crystals possessing such electronic properties are called intrinsic semiconductors. It has to be noticed that in transferring the electrons from the valence band to the next band the electrons of both bands determine the electric conduction phenomena since both bands present vacant levels.

In particular the conduction determined by the electrons promoted to the band which before were empty is called "*n-type*" since it is considered as due to the motion of negative electric carriers; vice versa, the conduction determined by the electron of the valence band which now it is not anymore saturated is called "*p-type*". Even though the electric conduction is really due to the motion of electrons, it is preferable to threat it as the motion of positive "hall carrier" created by the excited electrons promoted to higher conduction band.

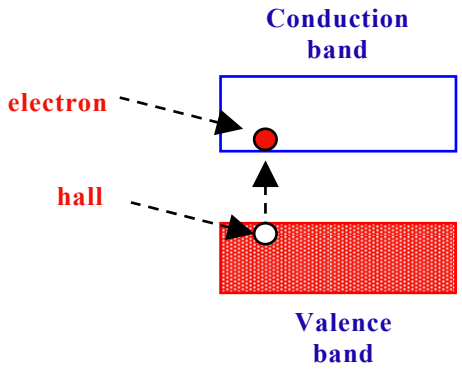

Fig.(3.2.3.5). Conduction in semiconductors in terms of positive and negative charge carriers motion

To the motion of electrons from valence band to conduction band corresponds the migration in the opposite direction of the "hall carriers".

The electric conduction mechanism in semiconductors, explains why differently from metal, when the temperature raises the electric conduction increases or at the same way the resistivity decreases. In fact, the higher the temperature the greater the number of excited electrons promoted from valence band to conduction band.

3.3 Lorentz model for Dielectrics and Conductors

A simple model to study the dielectric properties of a material is obtained by considering the motion of a bound electron in the presence of an applied electric field. As the electric field tries to separate the electron from the positively charged nucleus, it creates an electric dipole moment. Averaging this dipole moment over the volume of the material gives rise to a macroscopic dipole moment per unit volume.

A simple model for the dynamics of the displacement x of the bound electron is as follows [2] , with $\dot{x} = \frac{dx}{dt}$, $\ddot{x} = \frac{d^2x}{dt^2}$:

$$m\ddot{x} = eE - kx - m\gamma\dot{x} \tag{3.3.1}$$

where we assumed that the electric field is acting in the x-direction and that there is a spring-like restoring force $-kx$ due to the binding of the electron to the nucleus, and a friction-type force $-m\gamma\dot{x}$ proportional to the velocity of the electron.

The spring constant k is related to the resonance frequency of the spring via the relationship $\omega_0 = \sqrt{\frac{k}{m}}$, or, $k = m\omega_0^2$

Therefore, we may rewrite Eq. (3.3.1) as

$$\ddot{x} + \gamma\dot{x} + \omega_0^2 x = \frac{e}{m}E \tag{3.3.2}$$

The limit $\omega_0 = 0$ corresponds to unbound electrons and describes the case of good conductors. The frictional term $\gamma\dot{x}$ arises from collisions which tend to slow down

the electron. The parameter γ is a measure of the rate of collisions per unit time, and therefore, $\tau = 1/\gamma$ will represent the mean-time between collisions.

In a typical conductor, $\tau = 1/\gamma$ is of the order of 10^{-14} seconds, for example, for copper, τ = 2.4 × 10^{-14} sec and γ = 4.1 × 10^{13} sec^{-1}. The case of a tenuous, collisionless, plasma can be obtained in the limit $\gamma = 0$. Thus, the above simple model can describe the following cases:

a. *Dielectrics,* $\omega_0 \neq 0, \quad \gamma \neq 0$;

b. *Conductors,* $\omega_0 = 0, \quad \gamma \neq 0$;

c. *Collisionless Plasmas*, $\omega_0 = 0, \quad \gamma = 0$:

The basic idea of this model is that the applied electric field tends to separate positive from negative charges, thus, creating an electric dipole moment. In this sense, the model contains the basic features of other types of polarization in materials, such as ionic/molecular polarization arising from the separation of positive and negative ions by the applied field, or polar materials that have a permanent dipole moment.

3.3.1 Dielectrics

The applied electric field E(t) in Eq. (3.3.2) can have any time dependence. In particular, if we assume it is sinusoidal with frequency ω, $E(t) = Ee^{j\omega t}$, then, Eq. (3.3.2) will have the solution $x(t) = xe^{j\omega t}$, where the phasor x must satisfy:

$$-\omega^2 x + j\omega\gamma x + \omega_0^2 x = \frac{e}{m}E$$

(3.3.1.1)

which is obtained by replacing time derivatives by $\partial t \rightarrow j\omega$. Its solution is:

$$x = \frac{\frac{e}{m}E}{-\omega^2 + j\omega\gamma + \omega_0^2}$$

(3.3.1.2)

The corresponding velocity of the electron will also be sinusoidal where, $v = \dot{x} = j\omega x$. Thus, we have:

$$v = j\omega x = \frac{j\omega \frac{e}{m} E}{-\omega^2 + j\omega\gamma + \omega_0^2}$$

(3.3.1.3)

From Eq. (3.3.1.2) and (3.3.1.3), we can find the polarization per unit volume *P*. We assume that there are *N* such elementary dipoles per unit volume. The individual electric dipole moment is $p = ex$. Therefore, the polarization per unit volume will be:

$$P = Np = Nex = \frac{Ne\frac{e}{m}E}{-\omega^2 + j\omega\gamma + \omega_0^2} = \frac{\frac{Ne^2}{m}E}{-\omega^2 + j\omega\gamma + \omega_0^2} = \varepsilon_0\chi(\omega)E$$

(3.3.1.4)

where

$$\frac{\frac{Ne^2}{m}}{-\omega^2 + j\omega\gamma + \omega_0^2} = \varepsilon_0\chi(\omega) \quad \Rightarrow \quad \chi(\omega) = \frac{\frac{Ne^2}{\varepsilon_0 m}}{-\omega^2 + j\omega\gamma + \omega_0^2}$$

(3.3.1.5)

For a dielectric material, an applied electric field *E*, causes the polarizations of the atoms of molecules of the materials to create electric dipole moment that augment the total displacement flux *D*.

Such <u>electric flux density</u> will be then:

$$D = \varepsilon_0 E + P = \varepsilon_0[1 + \chi(\omega)]E = \varepsilon_0\left[1 + \frac{\frac{Ne^2}{\varepsilon_0 m}}{-\omega^2 + j\omega\gamma + \omega_0^2}\right]E = \varepsilon(\omega)E$$

(3.3.1.6)

where the <u>effective permittivity</u> $\varepsilon(\omega)$ is:

$$\varepsilon(\omega)=\varepsilon_0\left[1+\frac{\dfrac{Ne^2}{\varepsilon_0 m}}{-\omega^2+j\omega\gamma+\omega_0^2}\right]$$

(3.3.1.6)

This can be written in a more convenient form, as follows:

$$\varepsilon(\omega)=\varepsilon_0+\frac{\varepsilon_0\dfrac{Ne^2}{\varepsilon_0 m}}{-\omega^2+j\omega\gamma+\omega_0^2}=\varepsilon_0+\frac{\varepsilon_0\omega_p^2}{-\omega^2+j\omega\gamma+\omega_0^2}$$

(3.3.1.7)

where ω_p^2 is the so called *plasma frequency* of the medium:

$$\boxed{\omega_p^2=\frac{Ne^2}{\varepsilon_0 m}}$$

(3.3.1.8)

The model defined by (3.3.1.8) is known as a "*Lorentz dielectric*." The corresponding

Susceptibility, defined through $\varepsilon(\omega)=\varepsilon_0[1+\chi(\omega)]$ is:

$$\chi(\omega)=\frac{\omega_p^2}{-\omega^2+j\omega\gamma+\omega_0^2}$$

(3.3.1.9)

For a dielectric, we may assume $\omega_0\neq 0$. Then, the low-frequency limit ($\omega = 0$) of Eq. (3.3.1.7), gives the nominal dielectric constant:

$$\varepsilon(0)=\varepsilon_0+\varepsilon_0\frac{\omega_p^2}{\omega_0^2}=\varepsilon_0+\varepsilon_0\frac{ne^2}{m\omega_0^2}$$

(3.3.1.10)

The real and imaginary parts of $\varepsilon(\omega)$ characterize the refractive and absorptive properties of the material. By convention, we define the imaginary part with the negative sign (because we use $e^{j\omega t}$ time dependence):

$$\boxed{\varepsilon(\omega)=\varepsilon'(\omega)-j\varepsilon''(\omega)}$$

(3.3.1.11)

From Eq. (3.3.1.7), taking the real and imaginary part we obtain the components of $\varepsilon(\omega)$:

$$\varepsilon(\omega)=\varepsilon_0+\frac{\varepsilon_0\omega_p^2}{-\omega^2+j\omega\gamma+\omega_0^2}=\frac{\varepsilon_0\left(-\omega^2+j\omega\gamma+\omega_0^2\right)+\varepsilon_0\omega_p^2}{\left(-\omega^2+j\omega\gamma+\omega_0^2\right)}=$$

$$\varepsilon(\omega)=\frac{\left[\varepsilon_0\left(-\omega^2+j\omega\gamma+\omega_0^2\right)+\varepsilon_0\omega_p^2\right]\left(-\omega^2-j\omega\gamma+\omega_0^2\right)}{\left(-\omega^2+j\omega\gamma+\omega_0^2\right)\left(-\omega^2-j\omega\gamma+\omega_0^2\right)}=$$

$$\varepsilon(\omega)=\frac{\varepsilon_0\left[\left(-\omega^2+\omega_0^2\right)^2+\omega^2\gamma^2\right]+\varepsilon_0\omega_p^2\left(-\omega^2-j\omega\gamma+\omega_0^2\right)}{\left(-\omega^2+\omega_0^2\right)^2+\omega^2\gamma^2}=$$

$$\varepsilon(\omega)=\frac{\varepsilon_0\left[\left(-\omega^2+\omega_0^2\right)^2+\omega^2\gamma^2\right]+\varepsilon_0\omega_p^2\left(\omega_0^2-\omega^2\right)-j\omega\varepsilon_0\omega_p^2\gamma}{\left(-\omega^2+\omega_0^2\right)^2+\omega^2\gamma^2}=$$

$$\boxed{\varepsilon'(\omega)=\varepsilon_0+\frac{\varepsilon_0\omega_p^2\left(\omega_0^2-\omega^2\right)}{\left(-\omega^2+\omega_0^2\right)^2+\omega^2\gamma^2}}$$

(3.3.1.11)

$$\boxed{\varepsilon''(\omega)=\frac{\omega\varepsilon_0\omega_p^2\gamma}{\left(-\omega^2+\omega_0^2\right)^2+\omega^2\gamma^2}}$$

(3.3.1.12)

Fig. (3.3.1.1) shows a plot of $\varepsilon'(\omega)$ and $\varepsilon''(\omega)$. Around the resonant frequency ω_0, the real part $\varepsilon'(\omega)$ behaves in an anomalous manner, that is, it drops rapidly with frequency to values less than ε_0 and the material exhibits strong absorbing. The term "*normal dispersion*" refers to an $\varepsilon'(\omega)$ that is an increasing function of ω, as is the case to the far left and right of the resonant frequency.

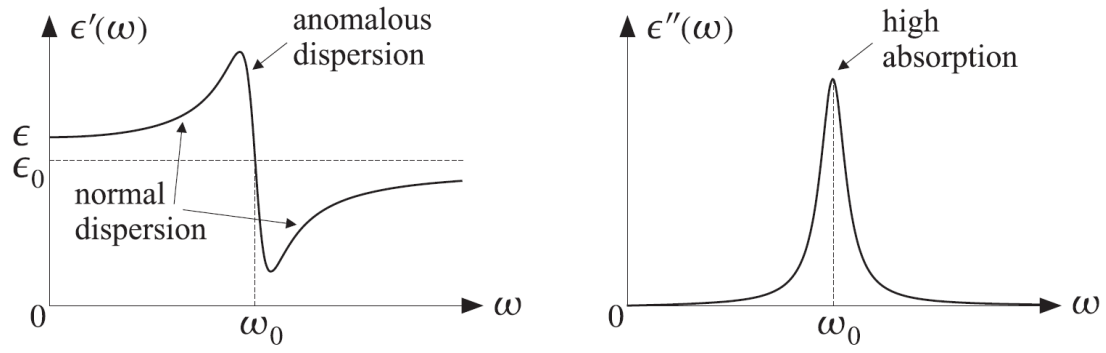

Fig. (3.3.1.1)

Real dielectric materials exhibit, of course, several such resonant frequencies corresponding to various vibrational modes and polarization mechanisms (e.g., electronic, ionic, etc.) The permittivity becomes the sum of such terms:

$$\varepsilon(\omega) = \varepsilon_0 + \sum_i \frac{\varepsilon_0 \dfrac{N_i e_i^2}{m_i \varepsilon_0}}{-\omega^2 + j\omega\gamma_i + \omega_i^2}$$

(3.3.1.12)

3.3.2 Relation between real and imaginary part of permittivity

The analytic properties of the complex permittivity by eq.(3.3.1.11), provide certain relationship between $\varepsilon'(\omega)$ and $\varepsilon''(\omega)$ so that the frequency behavior of one part is not independent of the frequency behavior of the other [3]. This interesting and important relationship, known as Kramers-Kronig relations [4], may be written

$$\varepsilon'(\omega) = \varepsilon_0 + \frac{2}{\pi} P \int_0^\infty \frac{\omega' \varepsilon''(\omega') d\omega'}{\left(\omega'^2 - \omega^2\right)}$$

(3.3.1.13)

$$\varepsilon''(\omega) = -\frac{2\omega}{\pi} P \int_0^\infty \frac{\left[\varepsilon'(\omega') - \varepsilon_0\right] d\omega'}{\left(\omega'^2 - \omega^2\right)}$$

(3.3.1.14)

where *P,* denotes that the principal value of the integral should be taken. They are similar to relations between resistance and reactance functions of frequency in circuit theory.

3.3.3 Conductors

The conductivity properties of a material are described by Ohm's law,

$$\boxed{\mathbf{J} = \sigma \mathbf{E}}$$

(3.3.3.1)

where: **J** is the current density vector (A/m^2), σ is the electrical conductivity (S/m), **E** is the electric field vector (V/m).

To derive this law from our simple model, we use the relationship $J = \rho v$,

$$J = \rho v$$

(3.3.3.2)

where ρ, is the volume density of the conduction charges: $\rho = Ne$ (C/m^3) is the number of charge carriers per unit of volume. It follows from Eq. (3.3.1.3) that:

$$J = \rho v = j\omega \rho x = \frac{j\omega \frac{\rho e}{m} E}{-\omega^2 + j\omega\gamma + \omega_0^2} = \frac{j\omega \frac{Ne^2}{m} E}{-\omega^2 + j\omega\gamma + \omega_0^2} = \sigma(\omega) E$$

(3.3.3.3)

and therefore, we identify the conductivity σ(ω):

$$\sigma(\omega) = \frac{j\omega \frac{Ne^2}{m}}{-\omega^2 + j\omega\gamma + \omega_0^2} = \frac{j\omega\varepsilon_0 \frac{Ne^2}{\varepsilon_0 m}}{-\omega^2 + j\omega\gamma + \omega_0^2} = \frac{j\omega\varepsilon_0 \omega_p^2}{-\omega^2 + j\omega\gamma + \omega_0^2}$$

(3.3.3.4)

We note that $\sigma(\omega)/j\omega$ is essentially the electric susceptibility considered above.

$$\chi(\omega) = \frac{\omega_p^2}{-\omega^2 + j\omega\gamma + \omega_0^2}$$

Indeed, we have $J = Nev = Nej\omega x = j\omega P$, and thus,

$$P = \frac{J}{j\omega} = \frac{\sigma(\omega)}{j\omega} E = \varepsilon_0 \chi(\omega) E$$

(3.3.3.5)

From (3.3.1.7), It follows that

$$\varepsilon(\omega) = \varepsilon_0 + \frac{\varepsilon_0 \omega_p^2}{-\omega^2 + j\omega\gamma + \omega_0^2}$$

$$\Downarrow$$

$$\varepsilon(\omega) - \varepsilon_0 = \frac{\varepsilon_0 \omega_p^2}{-\omega^2 + j\omega\gamma + \omega_0^2} = \varepsilon_0 \chi(\omega)$$

$$\Downarrow$$

$$\varepsilon(\omega) - \varepsilon_0 = \frac{\sigma(\omega)}{j\omega}$$

(3.3.3.6)

As a consequence we obtain

$$\varepsilon(\omega) = \varepsilon_0 + \frac{\sigma(\omega)}{j\omega}$$

(3.3.3.7)

Since in a metal the conduction charges are unbound, we may take $\omega_0 = 0$ in Eq. (3.3.3.4). After canceling a common factor of $j\omega$, we obtain:

$$\sigma(\omega) = \frac{j\omega\varepsilon_0\omega_p^2}{-\omega^2 + j\omega\gamma + \omega_0^2} = \frac{j\omega\varepsilon_0\omega_p^2}{-\omega^2 + j\omega\gamma + 0} = \frac{\varepsilon_0\omega_p^2}{\frac{-\omega^2 + j\omega\gamma}{j\omega}} = \frac{\varepsilon_0\omega_p^2}{\frac{-\omega^2}{j\omega} + \gamma} = \frac{\varepsilon_0\omega_p^2}{\gamma + j\omega}$$

$$\boxed{\sigma(\omega) = \frac{\varepsilon_0\omega_p^2}{\gamma + j\omega} = \frac{\varepsilon_0 \frac{Ne^2}{\varepsilon_0 m}}{\gamma + j\omega} = \frac{Ne^2}{m\gamma + j\omega m}}$$

(3.3.3.7)

The conductivity in general is a complex number function of frequency.

In general terms, the higher the frequency the lower the electrical conductivity of conductor described by (3.3.3.7).

The model defined by (3.3.3.7) is know as the "*Drude model*." The nominal conductivity is obtained at the low-frequency limit, ω = 0:

$$\boxed{\sigma = \frac{\varepsilon_0 \omega_p^2}{\gamma} = \frac{Ne^2}{m\gamma}}$$

(3.3.3.8)

Example 3.3.2.1:

Copper has a mass density of $8.9 \times 10^6\ gr/m^3$ and atomic weight of 63.54 (grams per mole.) Using Avogadro's number of 6×10^{23} atoms per mole, and assuming one conduction electron per atom, we find for the volume density *N*:

$$N = \frac{6\times10^{23}\left[\frac{atoms}{mole}\right]}{63.54\left[\frac{grams}{mole}\right]} \times 8.9\times10^{6}\left[\frac{grams}{m^3}\right] \times \left[\frac{1\ \ electron}{atom}\right] = 8.4\times10^{28}\quad \frac{electrons}{m^3}$$

(3.3.3.9)

it follows that:

$$\sigma = \frac{\varepsilon_0\omega_p^2}{\gamma} = \frac{Ne^2}{m\gamma} = \frac{\left(8.4\times10^{28}\right)\left(1.6\times10^{-19}\right)^2}{\left(9.1\times10^{-31}\right)\left(4.1\times10^{13}\right)} = 5.8\cdot10^{7}\quad \frac{Siemens}{m}$$

(3.3.3.10)

where we used $e = 1.6\times10^{-19}$, $m = 9.1\times10^{-31}$, $\gamma = 4.1\times10^{13}$. The plasma frequency of copper can be calculated by:

$$f_p = \frac{\omega_p}{2\pi} = \frac{1}{2\pi}\sqrt{\frac{Ne^2}{\varepsilon_0 m}} = 2.6\times10^{15}\quad Hz$$

(3.3.3.11)

which lies in the ultraviolet range. For frequencies such that $\omega << \gamma$, the conductivity (3.3.2.7) may be considered to be independent of frequency and equal to the dc value of Eq. (3.3.2.8). This frequency range covers most present-day RF applications. For example, assuming $\omega \le 0.1\gamma$, we find $f \le 0.1\gamma/2\pi = 653\ GHz$.

3.4 Maxwell analysis for Dielectrics and Conductors

In this section we consider the simple case of isotropic (**P** is a vector directed like **E**), linear materials, and we describe the losses on the response of applied fields. The effect of losses can enter though a response to either the electric of magnetic field, or both. An example of material in which the response to the magnetic field leads to losses is the so-called *ferrite* (*ferromagnetic* materials), and in this case the permeability must be a complex quantity $\mu = \mu' - j\mu''$. For materials of interest in wave studies, magnetic response is very weak and the permeability is a real constant that differ very little from the permeability of free space; this will be assumed throughout this section unless otherwise specified.

The previous study of the response of bound electrons in atoms and ions in molecules shown that the total current density resulting from their motion is

$$\mathbf{J} = j\omega\varepsilon\mathbf{E} = j\omega(\varepsilon' - j\varepsilon'')\mathbf{E} \tag{3.4.1}$$

where $\varepsilon = \varepsilon(\omega) = \varepsilon_0(1 + \chi(\omega))$.

If, in addition, the material contains free electrons or holes, there is a conduction current density **J** which is due to the conductivity σ of materials even if it is a not perfect dielectric materials

$$\mathbf{J} = \sigma\mathbf{E} \tag{3.4.2}$$

At sufficiently high frequencies, σ can be complex, but we will assume that frequency is low enough to consider it real (satisfactory though the microwave range).

Then the total current density is

$$\mathbf{J} = j\omega\left(\varepsilon' - j\varepsilon'' - j\frac{\sigma}{\omega}\right)\mathbf{E} \tag{3.4.3}$$

Maxwell's curl equation for **H** become:

$$\nabla \times \mathbf{H} = \mathbf{J} + j\omega\mathbf{D} = \mathbf{J} + j\omega\varepsilon\mathbf{E} = \sigma\mathbf{E} + j\omega\varepsilon\mathbf{E}$$

(3.4.4)

$\sigma\mathbf{E}$ is the conduction current;

$j\omega\varepsilon\mathbf{E}$ is the displacement current;

If $\sigma >> \omega\varepsilon$ then prevail the conduction behavior due to the conduction current

if $\sigma << \omega\varepsilon$ then prevail the conduction behavior due to the displacement current

Substituting the complex permittivity into Eq. (3.4.4) we have

$$\nabla \times \mathbf{H} = \sigma\mathbf{E} + j\omega(\varepsilon' - j\varepsilon'')\mathbf{E} = (\sigma + \omega\varepsilon'' + j\omega\varepsilon')\mathbf{E} =$$
$$= j\omega\left(\frac{\sigma}{j\omega} + \frac{\omega\varepsilon''}{j\omega} + \varepsilon'\right)\mathbf{E} = j\omega\left(\varepsilon' - j\varepsilon'' - j\frac{\sigma}{\omega}\right)\mathbf{E} = j\omega\left[\varepsilon' - j\left(\varepsilon'' + \frac{\sigma}{\omega}\right)\right]\mathbf{E} = j\omega\tilde{\varepsilon}\mathbf{E}$$

(3.4.5)

It has to be noticed that losses due to dielectric dumping $\omega\varepsilon''$ is indistinguishable from losses due to conductivity σ.

3.4.1 Dielectrics

In materials called *dielectrics*, there are usually few free electrons, and any free-electron current component is included in ε'' and σ is taken as 0. On the other hand, in materials considered *conductors* such as metals and semiconductors, the conduction current dominates and the effect of bound electrons ε_b'' is subsumed in the conductivity. Although physically different, the two losses terms enter into equations in the same way through relation $\sigma = \omega\varepsilon''$.

For dielectric materials with real permeability and complex permittivity,

$$\nabla \times \mathbf{H} = j\omega\varepsilon\mathbf{E} = j\omega(\varepsilon' - j\varepsilon'')\mathbf{E}$$

(3.4.1.1)

where conduction current are included in the loss factor ε''.

Wave number is complex and it is

$$k = \omega\sqrt{\mu\left(\varepsilon' - j\varepsilon''\right)} = \beta - j\alpha$$

(3.4.1.2)

the wave number *k* may be separated into real and imaginary parts:

$$jk = \alpha + j\beta = j\omega\sqrt{\mu\left(\varepsilon' - j\varepsilon''\right)} = j\omega\sqrt{\mu\varepsilon'\left[1 - j\left(\frac{\varepsilon''}{\varepsilon'}\right)\right]}$$

(3.4.1.3)

where

$$\alpha = \omega\sqrt{\left(\frac{\mu\varepsilon'}{2}\right)\left[\sqrt{1+\left(\frac{\varepsilon''}{\varepsilon'}\right)^2} - 1\right]}$$

(3.4.1.4)

$$\beta = \omega\sqrt{\left(\frac{\mu\varepsilon'}{2}\right)\left[\sqrt{1+\left(\frac{\varepsilon''}{\varepsilon'}\right)^2} + 1\right]}$$

(3.4.1.5)

The exponential propagation factor for phasor waves is e^{-jkz} and, when *k* is complex, it becomes

$$e^{-jkz} = e^{-\alpha z}e^{-j\beta z}$$

(3.4.1.6)

Thus the wave attenuates as it propagates though the material and the attenuation depends upon the dielectric losses and the conduction losses as would be expected.

The intrinsic impedance, or ratio of electric to magnetic field for a uniform plane wave, becomes

$$\eta = \sqrt{\frac{\mu}{\varepsilon}} = \sqrt{\frac{\mu}{\varepsilon'\left[1 - j\left(\frac{\varepsilon''}{\varepsilon'}\right)\right]}}$$

(3.4.1.7)

An important parameter appearing through (3.4.1.7) is the ratio $\varepsilon''/\varepsilon'$. For low loss materials this ratio is much less than unity. We may refer to such material as an *imperfect dielectric* i.e., dielectric with some losses mechanism. Under these conditions the *attenuation constant* and the *phase constant* may be approximated by expanding both as binomial series:

$$\alpha \approx \frac{k\varepsilon''}{2\varepsilon'}$$

(3.4.1.8)

$$\beta \approx k\left[1+\frac{1}{8}\left(\frac{\varepsilon''}{\varepsilon'}\right)^2\right]$$

(3.4.1.9)

where $k=\omega\sqrt{\mu\varepsilon'}$. Dielectric losses are usually described by "loss tangent" $\tan\delta=\frac{\varepsilon''}{\varepsilon'}$.

It is seen that there is a small increase of the phase constant and therefore, decreasing of the phase velocity when losses are present in a dielectric.

The intrinsic impedance form (3.4.1.7), in this case is

$$\eta \approx \sqrt{\frac{\mu}{\varepsilon'}}\left\{\left[1-\frac{3}{8}\left(\frac{\varepsilon''}{\varepsilon'}\right)^2\right]+j\frac{\varepsilon''}{2\varepsilon'}\right\}$$

(3.4.1.10)

3.4.2 Conductors

In material such as semiconductor where the losses are predominantly conductive,

$$\nabla\times\mathbf{H}=\left(j\omega\varepsilon'+\sigma\right)\mathbf{E}=j\omega\varepsilon'\left[1+\frac{\sigma}{j\omega\varepsilon'}\right]\mathbf{E}=j\omega\varepsilon'\left[1-j\frac{\sigma}{\omega\varepsilon'}\right]\mathbf{E}$$

(3.4.2.1)

For radian frequencies much larger than σ/ε' i.e., $\varepsilon'\omega >> \sigma$ the loss term is small and the approximation (3.4.1.8) to (3.4.1.10) may be used with $\varepsilon''/\varepsilon'$ replaced by $\sigma/\omega\varepsilon'$.

For radian frequencies much below σ/ε' i.e., $\omega\varepsilon' << \sigma$ the material may be considered a good conductor. If we make use of the fact that $\omega\varepsilon' << \sigma$ in (3.4.1.3) we find

$$jk = \alpha + j\beta = j\omega\sqrt{\frac{\mu\sigma}{j\omega}} = (1+j)\sqrt{\pi f\mu\sigma} = \frac{1+j}{\delta}$$

(3.4.2.2)

where $\delta = \dfrac{1}{\sqrt{\pi f\mu\sigma}}$ is the penetration depth.

The propagation factor for the wave shows that the wave decreases in magnitude exponentially, and has decreased to *1/e* of its original valued after propagating a distance equal to depth of penetration of the material.

For a good conductor the intrinsic impedance is

$$\eta = \sqrt{\frac{\mu}{\varepsilon}} = \sqrt{\frac{j\omega\mu}{\sigma}} = (1+j)\sqrt{\frac{\pi f\mu}{\sigma}} = (1+j)R_s$$

(3.4.2.3)

where R_s is the surface resistivity or high-frequency skin effect resistance per square of plane conductor of great depth.

Eq. (3.4.2.3), shows that electric and magnetic field are 45 degrees out of time phase for the wave propagating in a good conductor. Also since R_s is very small (0.014 Ω for copper at 3 GHz), the ratio of electric field to magnetic field in the wave is small.

3.5 Losses mechanisms in Dielectric materials

3.5.1 Representation of dielectric relaxation losses by circuit parameters

Let's have a look to what happen when a sinusoidal electric field is applied to dielectric materials where the main loss mechanism is due to the dielectric relaxation. Suppose the following applied electric field

$$E = E_0 \cos(\omega t)$$

(3.5.1.1)

the dipolar orientation will be delayed with respect to ***E.*** The higher the angular frequency ω, the greater the delay $\delta(\omega)$ of the displacement current with respect to the electric field E

$$D = D_0 \cos(\omega t - \delta(\omega))$$

(3.5.1.2)

Now, in order to easy the formulation we can adopt the phasor concept:
Given a certain sinusoidal function:

$$x(t) = X_0 \cos(\omega t + \Phi)$$

(3.5.1.3)

then we can define the rotating phasor associated to *x(t)* as:

$$\dot{X}(\omega,t) = X_0 e^{j(\omega t+\Phi)} = X_0 \cos(\omega t + \Phi) + jX_0 \sin(\omega t + \Phi)$$

(3.5.1.4)

as a consequence we have:

$$x(t) = \mathrm{Re}\{\dot{X}(\omega,t)\}$$

(3.5.1.5)

The phasors associated to electric field and to electric displacement are:

$$\dot{E}(\omega,t) = E_0 e^{j(\omega t)} \quad \Rightarrow \quad E = \mathrm{Re}\{\dot{E}(\omega,t)\}$$
$$\dot{D}(\omega,t) = D_0 e^{j(\omega t-\delta(\omega))} \quad \Rightarrow \quad D = \mathrm{Re}\{\dot{D}(\omega,t)\}$$

(3.5.1.6)

Electric displacement vector and electric field vector are related to each other by

$$\dot{D}(\omega,t)=\varepsilon_0\tilde{\varepsilon}_r\dot{E}(\omega,t)$$

(3.5.1.7)

but:

$$\tilde{\varepsilon}_r=\varepsilon_r^{'}(\omega)-j\varepsilon_r^{''}(\omega)$$

(3.5.1.8)

as a consequence:

$$\begin{aligned}
&\dot{D}(\omega,t)=\varepsilon_0\tilde{\varepsilon}_r\dot{E}(\omega,t)=\varepsilon_0\left(\varepsilon_r^{'}(\omega)-j\varepsilon_r^{''}(\omega)\right)\dot{E}(\omega,t)\\
&D_0e^{j(\omega t-\delta(\omega))}=\varepsilon_0\tilde{\varepsilon}_rE_0e^{j(\omega t)}=\varepsilon_0\left(\varepsilon_r^{'}(\omega)-j\varepsilon_r^{''}(\omega)\right)E_0e^{j(\omega t)}\\
&D_0e^{j(\omega t)}e^{-j(\delta(\omega))}=\varepsilon_0\left(\varepsilon_r^{'}(\omega)-j\varepsilon_r^{''}(\omega)\right)E_0e^{j(\omega t)}\\
&D_0e^{-j(\delta(\omega))}=\varepsilon_0\left(\varepsilon_r^{'}(\omega)-j\varepsilon_r^{''}(\omega)\right)E_0\\
&D_0\cos(\delta(\omega))-jD_0\sin(\delta(\omega))=\varepsilon_0\varepsilon_r^{'}(\omega)E_0-j\varepsilon_0\varepsilon_r^{''}(\omega)E_0
\end{aligned}$$

(3.5.1.9)

taking real and imaginary part we have

$$\left.\begin{aligned}
&D_0\cos(\delta(\omega))=\varepsilon_0\varepsilon_r'\ (\omega)E_0\\
&-jD_0\sin(\delta(\omega))=-j\varepsilon_0\varepsilon_r''\ (\omega)E_0
\end{aligned}\right\}\Rightarrow\begin{cases}
\varepsilon_r'\ (\omega)=\dfrac{D_0\cos(\delta(\omega))}{\varepsilon_0E_0}\\
\varepsilon_r''\ (\omega)=\dfrac{D_0\sin(\delta(\omega))}{\varepsilon_0E_0}
\end{cases}$$

(3.5.1.10)

Observations:

$$\text{when } \omega = 0 \quad \text{(static field)}, \qquad \delta(0) = 0 \quad \Rightarrow \begin{cases} \varepsilon_r'(\omega) = \dfrac{D_0}{\varepsilon_0 E_0} \\ \varepsilon_r''(\omega) = 0 \end{cases}$$

$$\text{if dielectirc material has no losses then } \delta(\omega) = 0 \quad \Rightarrow \begin{cases} \varepsilon_r'(\omega) = \dfrac{D_0}{\varepsilon_0 E_0} \\ \varepsilon_r''(\omega) = 0 \end{cases}$$

Suppose now to apply a sinusoidal voltage to the capacitor

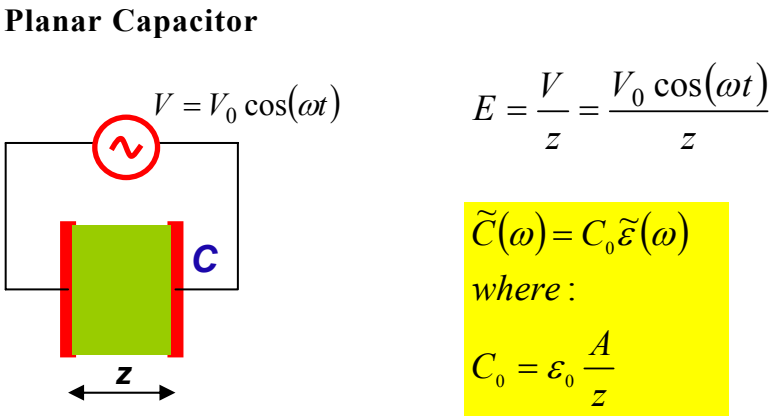

Fig.(3.5.1.1). Representation of dielectric losses in terms of real capacitor

Using Phasor we have:

$$\dot{V}(\omega,t) = V_0 e^{j\omega}$$

$$\dot{I}(\omega,t) = \frac{\dot{V}(\omega,t)}{1/j\omega\tilde{C}(\omega)} = j\omega\tilde{C}(\omega)\dot{V}(\omega,t) = j\omega C_0 \tilde{\varepsilon}_r(\omega)\dot{V}(\omega,t)$$

$$= j\omega C_0 \left(\varepsilon_r'(\omega) - j\varepsilon_r''(\omega)\right)\dot{V}(\omega,t) = \omega C_0 \left(\varepsilon_r''(\omega) + j\varepsilon_r'(\omega)\right)\dot{V}(\omega,t) =$$

$$= \omega C_0 \varepsilon_r''(\omega)\dot{V}(\omega,t) + j\omega C_0 \varepsilon_r'(\omega)\dot{V}(\omega,t) =$$

$$= \frac{\dot{V}(\omega,t)}{\frac{1}{\omega C_0 \varepsilon_r''(\omega)}} + \frac{\dot{V}(\omega,t)}{\frac{1}{j\omega C_0 \varepsilon_r'(\omega)}} = \frac{\dot{V}(\omega,t)}{R(\omega)} + \frac{\dot{V}(\omega,t)}{Z_C(\omega)} = \dot{V}(\omega,t)\left[\frac{1}{R(\omega)} + \frac{1}{Z_C(\omega)}\right] = \dot{V}(\omega,t)Y$$

(3.5.1.11)

where:

$$Y(\omega) = \frac{1}{R(\omega)} + j\omega C(\omega)$$

This expression is compatible with the following circuit where losses are summarized in a parameter represented by the resitance ***R***

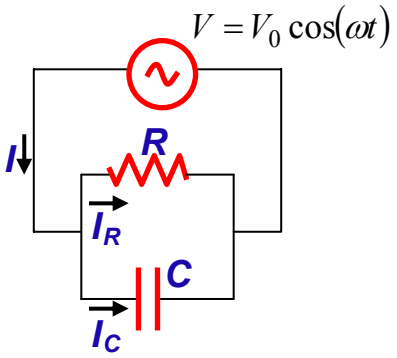

$$Y = \frac{1}{R} + j\omega C$$

Fig.(3.5.1.2). Representation of dielectric losses in terms of circuit parameters

3.6 Microwave dielectric characterization of materials

In this section Dielectric characterization of materials is performed using transmission line method and network approach [5]. In the line method, the microwave properties of the transmission lines or resonant structures are represented by their equivalent lumped elements. Network approach is developed from the line method. In the network approach, we do not care the distributions of electromagnetic fields within a microwave structure, and we are only interested in how the microwave structure responds to external microwave signals. Microwave network method studies the responses of a microwave structure to external signals, and it is a complement to the microwave field theory that analyzes the field distribution inside the microwave structure.

This section is organized in fourth main subsection. The first introduces the concept of transmission lines and scattering parameters, the second speaks about vector network analyzer (VNA) and measurements techniques. Several measuring methods are possible, like wave guide, coaxial line, free space antennas, resonant cavities, and so on. In this work the wave guide method has been adopted: the reason for such

choice is due to the problems intrinsically arising with other methods where all the boundary conditions are difficult to be correctly taken into account, thus affecting the dielectric permittivity values determination by introducing errors. The frequency band considered is in the range 5 to 18 GHz.

The third subsection introduces some algorithms to extract dielectric parameters.

The last subsection consists in the application of presented measurements methods and algorithms for microwave dielectric characterization epoxy-resin manufactured composite materials. Characterization is made in terms of dielectric parameters, electrical conductivity, skin-dept, intrinsic characteristic impedance.

3.6.1 Transmission line and scattering parameters

In microwave environment most analysis and synthesis concepts usually used for the linear network analysis are valid and some components can continue to be idealized.

In most cases some concepts adopted for low frequencies circuits design can be generalized and transferred in millimetric and microwave circuits design, as an example impedance matrix.

Nevertheless there are some operative difficulties. In fact, as an example, at low frequencies in the definition of admittance, the connections, weldings, ecc, have physical length equal to zero.

In the case of millimetric wave instead, even a short piece of connection conductor, became a *line of transmission* characterized by a proper *characteristic impedance* Z_i and by a proper *electric length* θ.

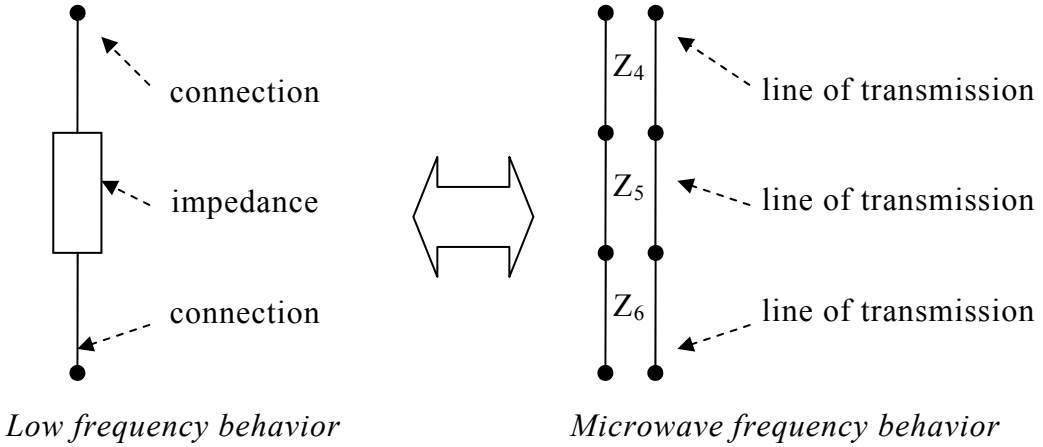

Fig. (3.6.1.1). Different propagation concepts at low and microwave frequencies.

Since in *microwave* each component can be treated as a *line of transmission* then, its become fundamental the application of *transmission line concepts*.

As a second example let us to consider the following situation in which the low frequency circuit (circuits elements dimensions lower than wavelength λ), is represented like an admittance connected to two cable.

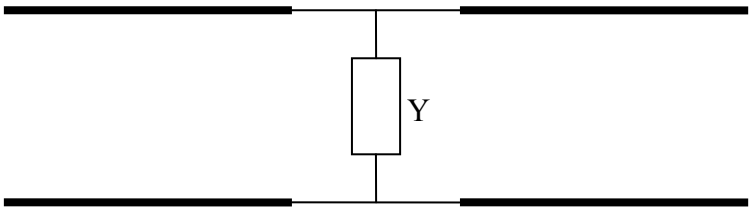

Fig. (3.6.1.2). Low frequency situation where circuit element dimensions are lower than the wavelength λ

Now at millimetric frequencies the same circuit consists of a parallel component and a series component due to the connection of the element to the circuit; as a consequence, we must to revise the element as a *2-port network*:

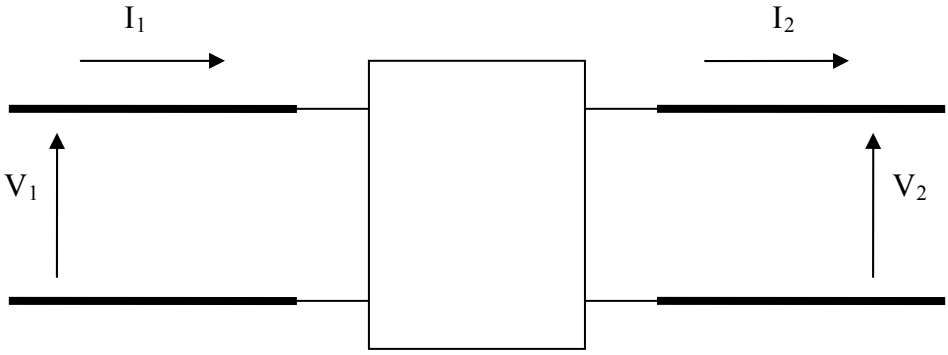

Fig. (3.6.1.3). Equivalent circuit at millimetric wavelength

We can conclude that at high frequencies, the pure parallel or series connections do never exists and in place of lumped elements, we need to apply *transmission line concepts*. Since composite materials have proper dielectric parameters as permittivity, permeability and characteristic impedance, than we can treat them as a transmission lines taking advantages in applying microwave theory and analysis.

3.6.1.1 ABCD Matrix or Matrix of Connection

Suppose a *network* like in the previous figure, where the elements are linear; under this hypothesis is it possible to use the matrix representation like *ABCD* matrix in which:

$$\begin{aligned} V_1 &= AV_2 + BI_2 \\ I_1 &= CV_2 + DI_2 \end{aligned} \quad \rightarrow \quad \begin{pmatrix} V_1 \\ I_1 \end{pmatrix} = \begin{pmatrix} A & B \\ C & D \end{pmatrix} \begin{pmatrix} V_2 \\ I_2 \end{pmatrix} \quad \text{where:} \quad A = \left.\frac{V_1}{V_2}\right|_{I_2=0} \qquad B = \left.\frac{V_1}{I_2}\right|_{V_2=0}$$

(3.6.1.1.1)

Besides since the connection between elements is usually a cascade of connections, the *ABCD* matrix is quite useful:

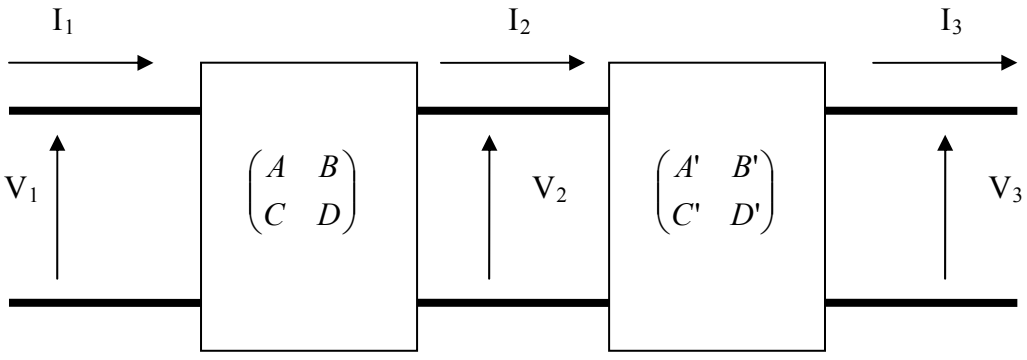

Fig. (3.6.1.1.1). Two ABCD matrix connected

$$\begin{pmatrix} V_1 \\ I_1 \end{pmatrix} = \begin{pmatrix} A & B \\ C & D \end{pmatrix} \begin{pmatrix} V_2 \\ I_2 \end{pmatrix} \quad \text{and} \quad \begin{pmatrix} V_2 \\ I_2 \end{pmatrix} = \begin{pmatrix} A' & B' \\ C' & D' \end{pmatrix} \begin{pmatrix} V_3 \\ I_3 \end{pmatrix} \rightarrow \begin{pmatrix} V_1 \\ I_1 \end{pmatrix} = \begin{pmatrix} A & B \\ C & D \end{pmatrix} \begin{pmatrix} A' & B' \\ C' & D' \end{pmatrix} \begin{pmatrix} V_3 \\ I_3 \end{pmatrix}$$

(3.6.1.1.2)

A,B,C,D parameters are complex number in general, besides they are not dimensionally homogeneous to each other.

In fact *A,D* are dimensionless while *B* is an impedance (ohm) and *C* is an admittance (mho).

Lets starts with two examples respectively one with Series Element and one with Parallel Element.

1) SERIES

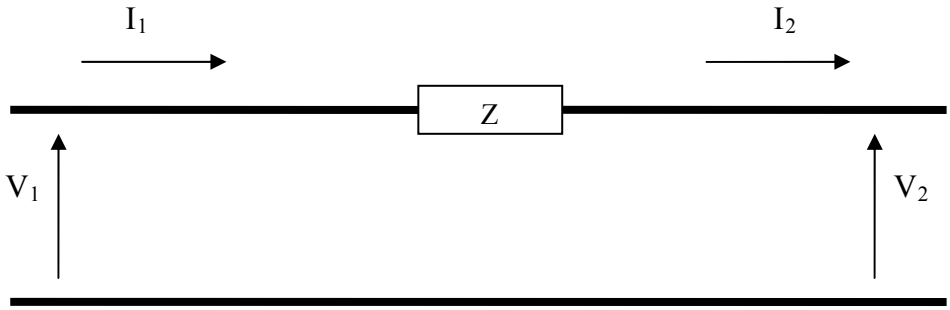

Fig. (3.6.1.1.2). Series Element

$$\begin{cases} V_1 = V_2 + ZI_1 \\ I_1 = I_2 \end{cases} \Rightarrow \begin{cases} V_1 = 1 \cdot V_2 + ZI_1 \\ I_1 = 0 \cdot V_2 + 1 \cdot I_2 \end{cases} \Rightarrow \begin{bmatrix} A & B \\ C & D \end{bmatrix} = \begin{bmatrix} 1 & Z \\ 0 & 1 \end{bmatrix}$$

(3.6.1.1.3) Series elements

2) PARALLEL

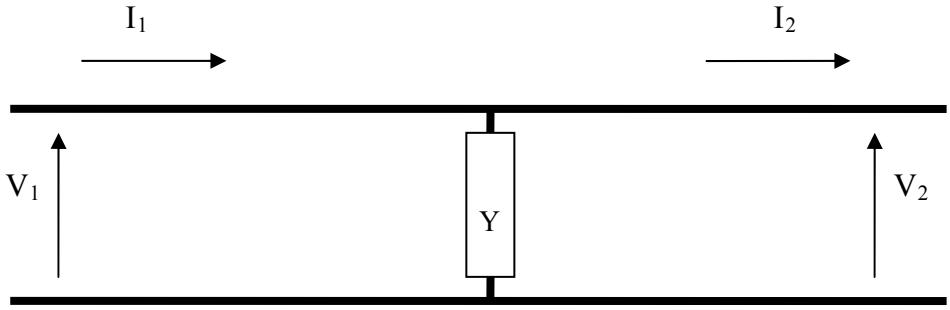

Fig. (3.6.1.1.4).Parallel elements

$$\begin{cases} V_1 = V_2 \\ I_1 = YV_2 + I_2 \end{cases} \Rightarrow \begin{cases} V_1 = 1 \cdot V_2 + 0 \cdot I_2 \\ I_1 = Y \cdot V_2 + 1 \cdot I_2 \end{cases} \Rightarrow \begin{bmatrix} A & B \\ C & D \end{bmatrix} = \begin{bmatrix} 1 & 0 \\ Y & 1 \end{bmatrix}$$

(3.6.1.1.4) Parallel Element

If we were working at low frequencies then *ABCD* matrix would be enough to describing the system.

On the contrary, at millimetric regime, the cable elements can't be neglected since they do not have a negligible length. These transmission line elements are responsible of phase changing and we are able to describe it using *ABCD* matrix.

Let us to consider a coaxial cable line and be its length *L*, now considering the electrical length θ:

$$\vartheta = \frac{2\pi L}{\lambda} = \frac{2\pi f L}{\lambda f} = \frac{\omega L}{\frac{\mathrm{v}}{f} f} = \frac{\omega L}{\mathrm{v}} = \frac{\omega L}{\frac{c}{n}} \qquad where:$$

$$\mathrm{v} = \frac{c}{n} = \text{phase\_velocity} \quad \text{and} \quad \lambda = \text{wave length} = \frac{\mathrm{v}}{f} \quad \text{and} \quad f = \text{frequency}$$

(3.6.1.1.5)

We can have two simple case:

1. when $L<<\lambda$, then $\theta \rightarrow 0$, and equivalently we can observe that at low frequencies cable do not cause any change of the phase i.e., in any point of the cable the phase is the same.
2. when $L>=\lambda$, then $\theta=f(L)$ and in general is not zero. The phase changes along the cable.

Using the properties defined above we start now to compute the *ABCD* matrix for a line of transmission as a function of the parameter *L* and Z_0.

Here Z_0 is the characteristic impedance of the line where the meaning of the line is referred to a cable but it could also be free-space, waveguide, dielectrics.

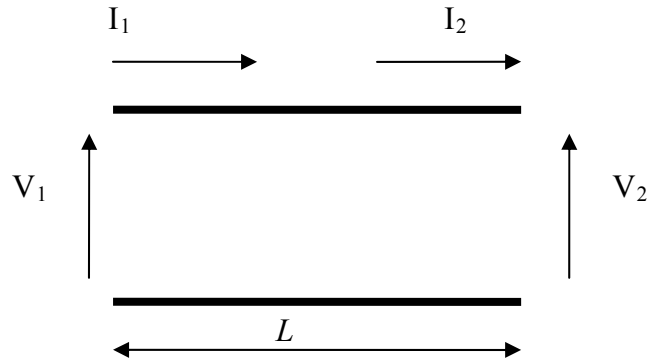

Fig. (3.6.1.1.5). ABCD matrix for a piece of line

Then the first parameter A can be computed as follows

$$A = \left.\frac{V_1}{V_2}\right|_{I_2=0} = \cos(\theta) \quad \text{i.e.} \quad V_1 = V_2\cos(\theta)$$

(3.6.1.1.6)

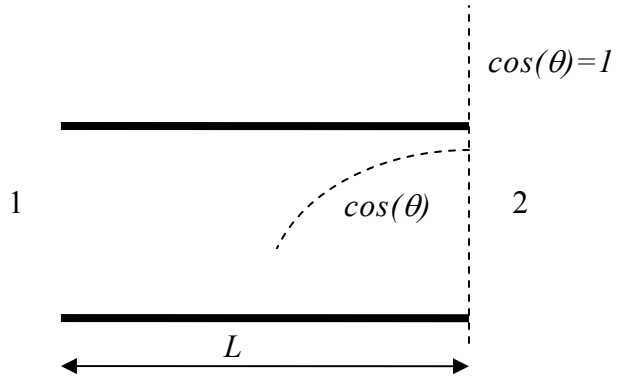

Fig. (3.6.1.1.6). V max

In fact, $I_2=0$ means "open circuit" at port 2. But at an open circuit corresponds a maximum of the electric field i.e., a maximum of voltage *V*. The Current *I* changes and decreases towards the port 1 with harmonic law. Now I(t) could have *sin* or

cosine solutions but since we have to take a real solution then we have to take the *cosine* solution.

In the same way we can compute the parameter D. In this case we need to consider that V_2=0 at port 2 means that there is a maximum of magnetic field i.e. a maximum of current I. This situation can be represented using the "short circuit" idea.

$$B = \left.\frac{I_1}{I_2}\right|_{V_2=0} = \cos(\vartheta)$$

(3.6.1.1.7)

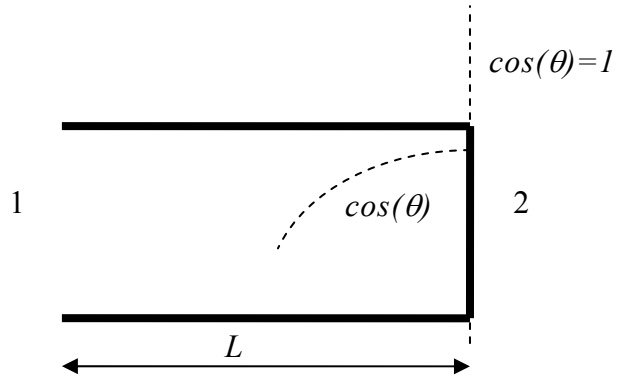

Fig. (3.6.2.1.7). I max

Now in order to compute the parameter *B*, we have to take into account that it represents an impedance (*V/I* exactly), consequently in the equation must appear the line impedance Z_0.

Now since between V_1 and I_2 there is a phase shift of π/2, then there is also e "reactive ratio" and we represent this with the complex symbol *j*:

$$B = \left.\frac{V_1}{I_2}\right|_{V_2=0} = jZ_0 \sin(\theta)$$

(3.6.1.1.8)

Using the same method we find the parameter C:

$$C = \left.\frac{I_1}{V_2}\right|_{I_2=0} = jY_0 \sin(\theta)$$

(3.6.1.1.9)

In previous equation, we considered *Y* because the ratio is *I/V*.

Finally, the ABCD matrix of the line can be rewritten as:

$$\begin{pmatrix} A & B \\ C & D \end{pmatrix} = \begin{pmatrix} \cos(\theta) & jZ_0 \sin(\theta) \\ jZ_0 \sin(\theta) & \cos(\theta) \end{pmatrix}$$

(3.6.1.1.10) ABCD matrix for an element of transmission line

Supposing absence of losses (i.e. Z_0 real), then:

1. *A,D* are real;
2. *B,C* are imaginary (complex); plus in the circuits where there is a symmetrical longitudinal plane, it is possible to exchange the port 1 with the port 2 and vice versa.
3. A=D (in the longitudinal symmetry circuits only);
4. AD-BC=1 (or det ABCD=1); this means reciprocity. The reciprocity proerty means that exchanging the port 1 with the port 2 we can observe the same circuit behavior. The reciprocity property does not imply the symmetry property. The non-reciprocity imply the existence if the girotropic macroscopic properties, i.e. such that there is a different interaction for the electromagnetic wave when it propagates from port 1 to port 2 with respect to port 2 to port 1. In general, the non reciprocal element causes transmission energy losses too.

3.6.1.2 Scattering matrix and S_{11}, S_{21}, S_{12}, S_{22} scattering parameters

The *ABCD* matrix is useful in order to represent a cascade of connections but it is not good to describe the input and output amplitude of signals. This is because at high frequencies is difficult to measure voltage and current, in fact, the instrument probe would became a sort of stub which in turn is able to affect the system under test causing false measurements.

At the other hand there are some instruments that, once a certain signal is sent across the circuit, are capable to measure the reflection and transmission of the signal in amplitude an phase.

As a consequence the best we can do is to define another matrix type which is able to connect the input and output circuit quantities using the reflection and transmission coefficient.

Let's start using a network as in figure below:

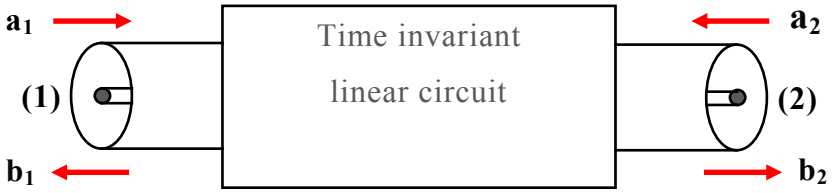

Fig. (3.6.1.2.1).

The hypotheses are:

1. The circuit is linear. In fact if not, it would not be possible to define the circuit matrix, plus the linearity is essential in order to describe the phenomena independently from the input signal.
2. The circuit is time-invariant. This means that the circuit characteristics remain the same in time.
3. The input and output impedance at port 1 and 2 are adapted. This means that there is not reflected power back to source.

Consider now a wave of voltage (or Transverse Electric field) $\mathbf{a_1}$ at the input of port(1). We are interested in finding the reflected wave $\mathbf{b_1}$ at the output of the port(1). In the same way $\mathbf{a_2}$ and $\mathbf{b_2}$ at port (2).

The relationship between $\mathbf{a_1},\mathbf{a_2},\mathbf{b_1},\mathbf{b_2}$ is formally expressed using the scattering matrix:

$$\begin{pmatrix} b_1 \\ b_2 \end{pmatrix} = S \cdot \begin{pmatrix} a_1 \\ a_2 \end{pmatrix} \Rightarrow \begin{pmatrix} b_1 \\ b_2 \end{pmatrix} = \cdot \begin{bmatrix} S_{11} & S_{12} \\ S_{21} & S_{22} \end{bmatrix} \begin{pmatrix} a_1 \\ a_2 \end{pmatrix} \Rightarrow \begin{cases} b_1 = S_{11} \cdot a_1 + S_{12} \cdot a_2 \\ b_2 = S_{21} \cdot a_1 + S_{22} \cdot a_2 \end{cases}$$

(3.6.1.2.1)

Where the $\boldsymbol{S_{ij}}$ parameters, are complex.

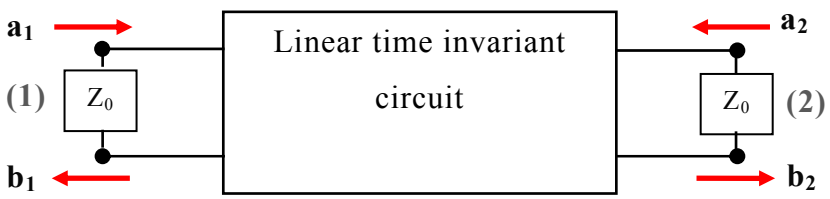

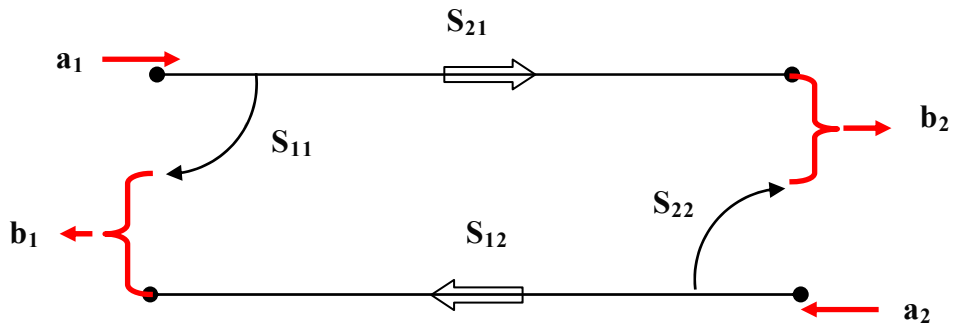

Fig. (3.6.1.2.2). Circuit representation

The S_{ij} parameters are the following:

$$S_{11} = \left.\frac{b_1}{a_1}\right|_{a_2 = 0}$$

(3.6.1.2.2)

S_{11}: Measure the reflection at port (1) when the incidence is unitary, there is no signal at port (2) and the port (2) is impedance loaded matched (a_2=0 does not mean short circuit);

$$S_{12} = \left.\frac{b_1}{a_2}\right|_{a_1 = 0}$$

(3.6.1.2.3)

S_{12}**:** Measure the transmission of the signal from port (2) to port (1) when at port (1) there is no signal applied;

$$S_{21} = \left.\frac{b_2}{a_1}\right|_{a_2 = 0}$$

(3.6.1.2.4)

S_{21}**:** Measure the transmission of the signal from port (1) to port (2) when at port (2) there is no signal applied;

$$S_{22} = \left.\frac{b_2}{a_2}\right|_{a_1 = 0}$$

(3.6.1.2.5)

***S_{22}*:** Measure the reflection at port (2) when the incidence is unitary, there is no signal at port (1) and the port (1) is impedance loaded adapted (a_1=0 does not mean short circuit);
Since the S_{ij} parameters are complex number, then, we need to consider 8 real parameters i.e., 2 c per each coefficient.

Note: it is possible to observe a difference between *ABCD* matrix and *S* matrix: in fact, the *ABCD* matrix need of an even number of port, vice versa in the S matrix we can have any number of port, as a consequence it result a more general representation (it need only for the linearity and time-invariant conditions).

Now let's have a look to how the *a* and *b* parameters are connected to the voltage and current in the circuits.
If *a* and *b* are voltage waves, then the total voltage at the single port will be the sum of input and output wave i.e., forward and reflected waves, as a consequence considering both port we have:

$$\begin{cases} V_1 = a_1 + b_1 \\ V_2 = a_2 + b_2 \end{cases}$$

(3.6.1.2.6)

As far as the currents are concerned, if we consider the input current as positive, then we have:

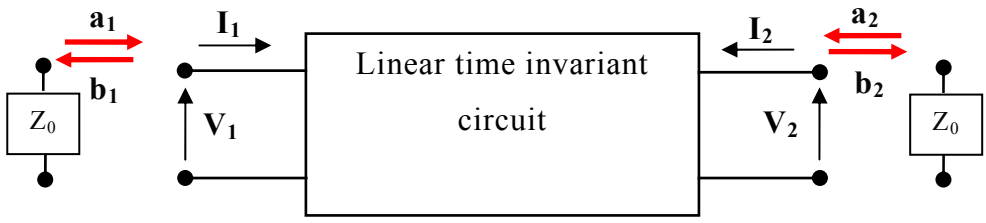

Fig. (3.6.1.2.3). Connection between *a* and *b* parameters with voltage and current

$$\begin{cases} I_1 = \dfrac{a_1}{Z_0} - \dfrac{b_1}{Z_0} = \dfrac{1}{Z_0}(a_1 - b_1) \\ I_2 = \dfrac{a_2}{Z_0} - \dfrac{b_2}{Z_0} = \dfrac{1}{Z_0}(a_2 - b_2) \end{cases}$$

(3.6.1.2.3)

As a consequence we have:

$$\begin{cases} a_1 = Z_0 I_1 + b_1 \\ a_2 = Z_0 I_2 + b_2 \end{cases} \Rightarrow \begin{cases} V_1 = a_1 + b_1 = Z_0 I_1 + b_1 + b_1 = Z_0 I_1 + 2b_1 \\ V_2 = a_2 + b_2 = Z_0 I_2 + b_2 + b_2 = Z_0 I_2 + 2b_2 \end{cases} \Rightarrow \begin{cases} b_1 = \dfrac{V_1 - Z_0 I_1}{2} \\ b_2 = \dfrac{V_2 - Z_0 I_2}{2} \end{cases}$$

(3.6.1.2.8)

Using the same method we can find a_1 and a_2:

$$\begin{cases} b_1 = a_1 - Z_0 I_1 \\ b_2 = a_2 - Z_0 I_2 \end{cases} \Rightarrow \begin{cases} V_1 = a_1 + b_1 = a_1 + a_1 - Z_0 I_1 = 2a_1 - Z_0 I_1 \\ V_2 = a_2 + b_2 = a_2 + a_2 - Z_0 I_2 = 2a_2 - Z_0 I_2 \end{cases} \Rightarrow \begin{cases} a_1 = \dfrac{V_1 + Z_0 I_1}{2} \\ a_2 = \dfrac{V_2 + Z_0 I_2}{2} \end{cases}$$

(3.6.1.2.9)

As a consequence the power at the port (1) and (2) will be:

$$P_1 = \frac{1}{2}\mathrm{Re}\left[VI^*\right] = \frac{1}{2}\mathrm{Re}\left[V_1 I_1^* + V_1^* I_1\right]$$
$$P_2 = \frac{1}{2}\mathrm{Re}\left[VI^*\right] = \frac{1}{2}\mathrm{Re}\left[V_2 I_2^* + V_2^* I_2\right]$$

(3.6.1.2.10)

Substituting the expressions of V and I in the expression of power we have:

$$P_1 = \frac{1}{2}\mathrm{Re}\left[V_1 I_1^* + V_1^* I_1\right] = \frac{1}{2}\mathrm{Re}\left[\left(a_1 + b_1\right)\frac{\left(a_1 - b_1\right)^*}{Z_0} + \left(a_1 + b_1\right)^* \frac{\left(a_1 - b_1\right)}{Z_0}\right] =$$
$$= \frac{1}{2}\mathrm{Re}\left[\left|a_1\right|^2 - \left|b_1\right|^2 - a_1 b_1^* + a_1^* b_1 + \left|a_1\right|^2 - \left|b_1\right|^2 - a_1^* b_1 + a_1 b_1^*\right] =$$
$$= \frac{1}{Z_0}\left\{\left|a_1\right|^2 - \left|b_1\right|^2\right\}$$

$$P_2 = \frac{1}{2}\mathrm{Re}\left[V_2 I_2^* + V_2^* I_2\right] = \frac{1}{2}\mathrm{Re}\left[\left(a_2 + b_2\right)\left(a_2 - b_2\right)^* + \left(a_2 + b_2\right)^*\left(a_2 - b_2\right)\right] =$$
$$\frac{1}{2}\mathrm{Re}\left[\left|a_2\right|^2 - \left|b_2\right|^2 - a_2 b_2^* + a_2^* b_2 + \left|a_2\right|^2 - \left|b_2\right|^2 - a_2^* b_2 + a_2 b_2^*\right] =$$
$$= \frac{1}{Z_0}\left\{\left|a_2\right|^2 - \left|b_2\right|^2\right\}$$

(3.6.1.2.11)

Now normalizing with respect to Z_0 we obtain:

$$\begin{cases} I_1 = a_1 - b_1 \\ I_2 = a_2 - b_2 \end{cases}$$

(3.6.1.2.12)

We can see that because of normalization, *V* and *I* have the same dimensions

As a consequence we have:

$$\begin{cases} a_1 = I_1 + b_1 \\ a_2 = I_2 + b_2 \end{cases} \Rightarrow \begin{cases} V_1 = a_1 + b_1 = I_1 + b_1 + b_1 = I_1 + 2b_1 \\ V_2 = a_2 + b_2 = I_2 + b_2 + b_2 = I_2 + 2b_2 \end{cases} \Rightarrow \begin{cases} b_1 = \dfrac{V_1 - I_1}{2} \\ b_2 = \dfrac{V_2 - I_2}{2} \end{cases}$$

(3.6.1.2.13)

Using the same method we can find a_1 and a_2:

$$\begin{cases} b_1 = a_1 - I_1 \\ b_2 = a_2 - I_2 \end{cases} \Rightarrow \begin{cases} V_1 = a_1 + b_1 = a_1 + a_1 - I_1 = 2a_1 - I_1 \\ V_2 = a_2 + b_2 = a_2 + a_2 - I_2 = 2a_2 - I_2 \end{cases} \Rightarrow \begin{cases} a_1 = \dfrac{V_1 + I_1}{2} \\ a_2 = \dfrac{V_2 + I_2}{2} \end{cases}$$

(3.6.1.2.14)

Now let's have a look to the power related to per port (1) and (2), under the hypothesis of no power loss, then the power is a real quantity expressed by:

$$P = \mathrm{Re}\left[VI^*\right]$$

(3.6.1.2.15)

As a consequence the power at the port (1) and (2) will be:

$$P_1 = \frac{1}{2}\mathrm{Re}\left[VI^*\right] = \frac{1}{2}\mathrm{Re}\left[V_1 I_1^* + V_1^* I_1\right]$$
$$P_2 = \frac{1}{2}\mathrm{Re}\left[VI^*\right] = \frac{1}{2}\mathrm{Re}\left[V_2 I_2^* + V_2^* I_2\right]$$

(3.6.1.2.16)

Substituting the expressions of *V* and *I* we have:

$$P_1 = \frac{1}{2}\mathrm{Re}\left[V_1 I_1^* + V_1^* I_1\right] = \frac{1}{2}\mathrm{Re}\left[(a_1 + b_1)(a_1 - b_1)^* + (a_1 + b_1)^*(a_1 - b_1)\right] =$$
$$= \frac{1}{2}\mathrm{Re}\left[|a_1|^2 - |b_1|^2 - a_1 b_1^* + a_1^* b_1 + |a_1|^2 - |b_1|^2 - a_1^* b_1 + a_1 b_1^*\right] =$$
$$= |a_1|^2 - |b_1|^2$$

$$P_2 = \frac{1}{2}\mathrm{Re}\left[V_2 I_2^* + V_2^* I_2\right] = \frac{1}{2}\mathrm{Re}\left[(a_2 + b_2)(a_2 - b_2)^* + (a_2 + b_2)^*(a_2 - b_2)\right] =$$
$$\frac{1}{2}\mathrm{Re}\left[|a_2|^2 - |b_2|^2 - a_2 b_2^* + a_2^* b_2 + |a_2|^2 - |b_2|^2 - a_2^* b_2 + a_2 b_2^*\right] =$$
$$= |a_2|^2 - |b_2|^2$$

(3.6.1.2.17)

Observing the above equations we can see that the net power at each single port, is equal to the difference between the input and output power at that port.

As a consequence, for a *n*-port circuit we have:

$$P_n = |a_n|^2 - |b_n|^2$$

(3.6.1.2.18)

Now let's have a look to how the *S* matrix elements play their role:

We know that the scattering matrix is:

$$\vec{b} = S\vec{a}$$

(3.6.1.2.19)

Where:

$$\vec{b} = \begin{pmatrix} b_1 \\ b_2 \\ \\ b_n \end{pmatrix} \quad \text{and} \quad \vec{a} = \begin{pmatrix} a_1 \\ a_2 \\ \\ a_n \end{pmatrix}$$

(3.6.1.2.20)

The total net power is the sum of all port power:

$$P = \sum_{n=1}^{N} P_i = \sum_{n=1}^{N} \left\{ |a_n|^2 - |b_n|^2 \right\} = \sum_{n=1}^{N} |a_n|^2 - \sum_{n=1}^{N} |b_n|^2$$

(3.6.1.2.21)

Now we know that the $\sum_{n=1}^{N}|a_n|^2$ represent the NORMA of vector $\vec{a}$; in fact, the NORMA is given by the expression:

$$\left(a_1^*, a_2^*, a_3^*, ..., a_n^*\right)\begin{pmatrix} a_1 \\ a_2 \\ . \\ . \\ an \end{pmatrix} = |a_1|^2 + |a_2|^2 + |a_3|^2 + ... + |a_n|^2$$

(3.6.1.2.22)

The vector $\left(a_1^*, a_2^*, a_3^*, ..., a_n^*\right)$ is the $\vec{a}$ conjugated and transposed vector. By definition it is called Hermitian conjugated: $\vec{a}^+$

As a consequence, we have that $\overline{a}^+ \cdot \overline{a} = \sum_{i=1}^{n}|a_n|^2$ and the power can be rewritten as:

$$P = \vec{a}^+ \cdot \overline{a} - \vec{b}^+ \cdot \vec{b}$$

(3.6.1.2.23)

Now since: $\vec{b} = S\vec{a}$ then also $\vec{b}^+ = \left[S\vec{a}\right]^+ = \left[S^\bullet \vec{a}^*\right]^T = \vec{a}^{*T} \cdot S^{*T} = \vec{a}^+ S^+$ is a valid equation. As a consequence, the power became:

$$P = \vec{a}^+ \cdot \overline{a} - \vec{b}^+ \cdot \vec{b} = \vec{a}^+ \cdot \overline{a} - \vec{a}^+ S^+ \cdot \vec{b} = \vec{a}^+ \cdot \overline{a} - \vec{a}^+ S^+ \cdot \vec{a}S$$

(3.6.1.2.24)

Rewriting in a more compacted form we have:

$$P = \vec{a}^+ I\overline{a} - \vec{a}^+ S^+ \vec{a}S = \vec{a}^+\left[I\overline{a} - S^+ \vec{a}S\right] = \vec{a}^+\left[I\overline{a} - S^+ S\vec{a}\right] = \vec{a}^+\left[I - S^+ S\right]\overline{a}$$

(3.6.1.2.25)

Now supposing that within the circuit there are neither sources nor losses elements, the total power is conserved an so the difference between the total input power and the total output power should be equal to zero:

$$P = \vec{a}^{+}\left[I - S^{+}S\right]\vec{a} = 0$$

(3.6.1.2.26)

In order to verify this equation, three different scenarios can happen:

1. $\vec{a} = 0$;
2. $\vec{a}$ is orthogonal to $\vec{a}^{+}$
3. $\left[I - S^{+}S\right] = 0$

While the first and second scenarios are particular case of excitation and so they give us no information about power conservation, the third case instead is general and independent form the excitation.

Therefore the condition:

$$\left[I - S^{+}S\right] = 0 \quad \textbf{i.e} \quad S^{+}S = I$$

(3.6.1.2.27)

represent the POWER CONSERVATION law.

The condition above, imply for a *n*-port circuit, n^2 scalar equations. As an example in the case of 2-port system, we obtain 4 scalar equations:

$$\begin{bmatrix} S_{11}^{*} & S_{21}^{*} \\ S_{12}^{*} & S_{22}^{*} \end{bmatrix} \cdot \begin{bmatrix} S_{11} & S_{12} \\ S_{21} & S_{22} \end{bmatrix} = \begin{bmatrix} 1 & 0 \\ 0 & 1 \end{bmatrix}$$

(3.6.1.2.28)

This means:

1. $\left|S_{11}\right|^2 + \left|S_{21}\right|^2 = 1$
2. $S_{11}^{*} \cdot S_{12}^{*} + S_{21}^{*} \cdot S_{22}^{*} = 0$
3. $S_{12}^{*} \cdot S_{11}^{*} + S_{22}^{*} \cdot S_{21}^{*} = 0$
4. $\left|S_{12}\right|^2 + \left|S_{22}\right|^2 = 1$

The first and fourth equations have a precise physical meanings, in fact, considering again the two port scheme, and supposing that $a_1=1$ and $a_2=0$ (i.e. there is not source at port (2)).

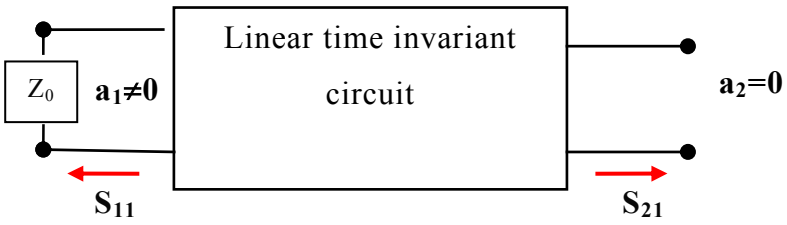

Fig. (3.6.1.2.4).

This means that:

$$S_{11}=\left.\frac{b_1}{a_1}\right|_{a_2=0}=\frac{b_1}{1}\Rightarrow S_{11}=b_1$$

(3.6.1.2.29)

S_{11}: Measure the reflection at port (1) when the incidence is unitary, there is no signal at port (2) and the port (2) is impedance loaded adapted (a_2=0 does not mean short circuit);

$$S_{21}=\left.\frac{b_2}{a_1}\right|_{a_2=0}=\frac{b_2}{1}\Rightarrow S_{21}=b_2$$

(3.6.1.2.30)

***S_{21}*:** Measure the transmission of the signal from port (1) to port (2) when at port (2) there is no signal applied;

As a consequence since we supposed the unitary power at the input (a_1=1), then the relation:

$$\left|S_{11}\right|^2+\left|S_{21}\right|^2=\left|b_1\right|^2+\left|b_2\right|^2=1$$

(3.6.1.2.31)

is the power conservation principle at port (1). In other words, the sum of the reflected power $|S_{11}|^2 = |b_1|^2$ and the transmitted power $|S_{21}|^2 = |b_2|^2$ are equal to the input power at port (1).

The same scheme can be applied to the fourth equation but this time, referred to port (2).

3.6.2 Vector network analyzer and dielectrics measurement

Measurement of dielectric properties involves measurements of the complex relative permittivity ε_r and complex relative permeability μ_r of the materials [6]. A complex dielectric permittivity consists of a real part and an imaginary part. The real part of the complex permittivity, also known as dielectric constant is a measure of the amount of energy from an external electrical field stored in the material. The imaginary part is zero for lossless materials and is also known as loss factor. It is a measure of the amount of energy loss from the material due to an external electric field. The term $\tan\delta$ is called loss tangent and it represents the ratio of the imaginary part to the real part of the complex permittivity. The loss tangent is also called by terms such as tangent loss, dissipation factor or loss factor.

The complex permeability also consists of a real part which represents the amount energy from an external magnetic field stored in the material whereas the imaginary part represents the amount of energy dissipated due to the magnetic field. Measurement on the complex permeability is only applicable to magnetic materials. Most materials are non-magnetic and thus, the permeability is near to the permeability of free space. Table (3.6.2.1) shows some examples of materials with their dielectric constant and loss tangent at room temperature.

Material	Dielectric constant	Loss-tangent
Alumina	9.0	0.0006
Bacon (smoked)	2.50	0.05
Beef (frozen)	4.4	0.12
Beef (raw)	52.4	0.3302
Blood*	58	0.27
Butter (salted)	4.6	0.1304
Butter (unsalted)	2.9	0.1552
Borosilicate glass	4.3 0	0047
Concrete (dry)	4.5	0.0111
Corn oil	2.6	0.0077
Cottonseed oil	2.64	0.0682
Sandy soil (dry)	2.55	0.0062
Egg white	35.0	0.5
Fused quartz	4.0	0.0001
Fat*	5.5	0.21
Glass ceramic	6.0	0.0050
Lard	2.5	0.0360
Lung*	32	0.3
Muscle*	49	0.33
Nylon	2.4	0.0083
Olive oil	2.46	0.0610
Paper	3-4	0.0125–0.0333
Soda lime glass	6.0	0.02
Teflon	2.1	0.0003
Thermoset polyester	4.0	0.0050
Wood	1.2–5	0.0040–0.4167
*At 37°C		

Tab. (3.6.2.1) – Example of characteristics of some dielectric materials at room temperature and at frequency 2.45 GHz

There are many techniques developed for measuring the complex permittivity and permeability and each technique is limited to specific frequencies, materials, applications etc. by its own constraint:

- transmission/reflection line technique,
- open ended coaxial probe technique,
- free space technique,
- resonant technique.

In the present work we applied transmission/reflection line technique. Tab. (3.6.2.2), describes some examples of materials, s-parameters and dielectric properties measured using various measurement techniques

Measurement techniques	Materials	S-parameters	Dielectric properties
Transmission/Reflection Line	Coaxial line, waveguides	S11, S21	ε_r, μ_r
Open-ended coaxial probe	Liquids, biological specimen, semi-solids	S11	ε_r
Free space	High temperature material, large flat solid, gas, hot liquids	S11,S21	ε_r, μ_r
Resonant Technique (Cavity)	Rod shaped solid materials, waveguides, liquids	Frequencies, Q-factors	ε_r, μ_r

Tab. (3.6.2.2) – Comparison between the measurement techniques

Transmission/Reflection line technique is a popular broadband measurement technique. In such technique, only the fundamental waveguide mode (TEM mode in coaxial line and TE mode in waveguides) is assumed to propagate. In our measurements, we choose the wave guide method due to two main reasons:

1. Manufacturing of sample which assure the best electric contact, with no air-gaps, between sample and sample holder. This assure that any uwanted microwave infiltration can affect the measurements result;
2. Possibility to characterize dielectric properties of materials along the two main Electric field polarization directions. Such possibility has been demonstrated particularly useful for analyses of composite materials based on aligned nanostructures along certain directions.

The Open-ended co-axial probe technique is a non-destructive technique and the technique assumes only the TEM or TE mode is propagating.Th e resonant technique provides high accuracies and assumes the TE or TM propagation mode but is quite effective only in a short range of frequencies. The free space technique is for broadband applications and assumed only the TEM propagation mode. Here after will be discussed the Transmission/Reflection Line technique using wave guide method as in Fig.(3.6.2.1).

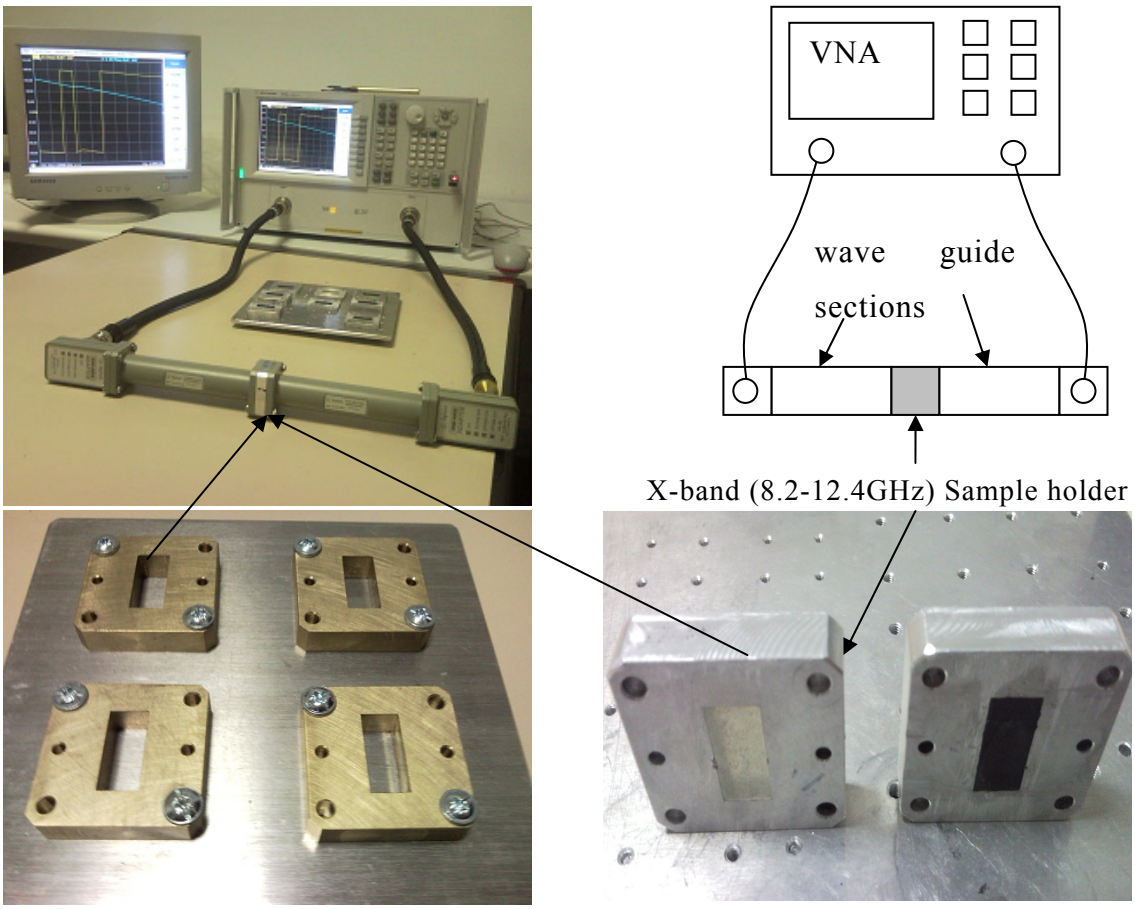

Fig (3.6.2.1). Agilent Network analyzer (PNA), on top, and sample holder in the x-band on bottom, respectively empty (left), and filled with Composite materials based on epoxy matrix reinforced with several species of carbon nanomaterials (right).

A measurement using the Transmission/Reflection line technique involves placing a sample in a section of waveguide or coaxial line and measuring the two ports complex scattering parameters with a vector network analyzer (VNA). The sample is inserted between two wave guide sections such as in Fig. (3.6.2.1).

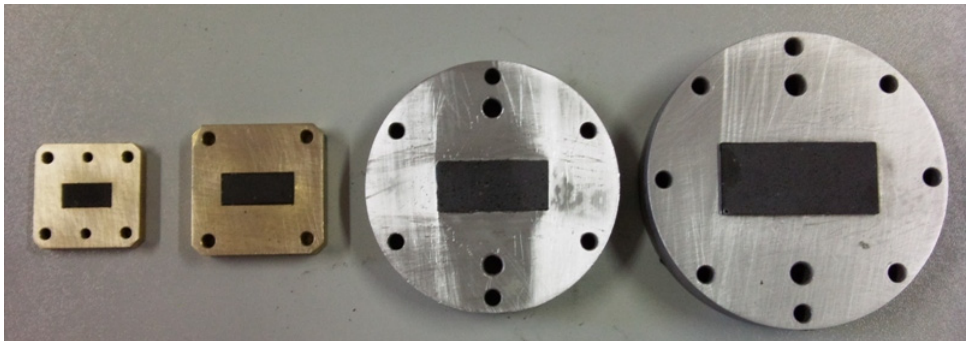

(a)

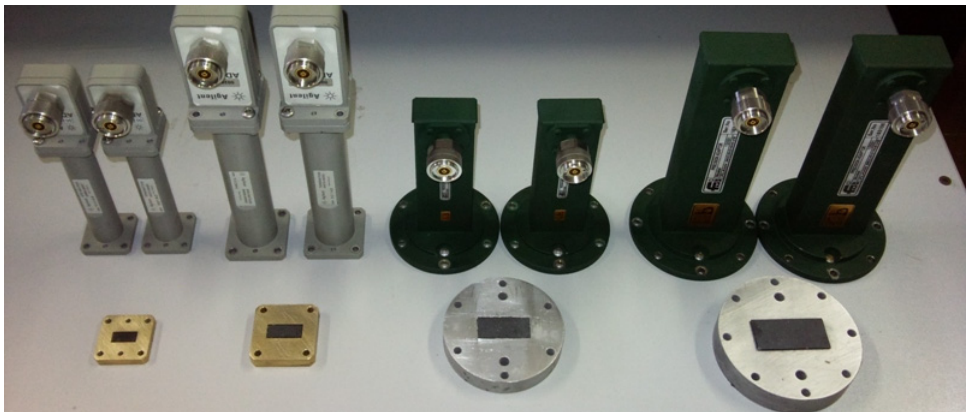

(b)

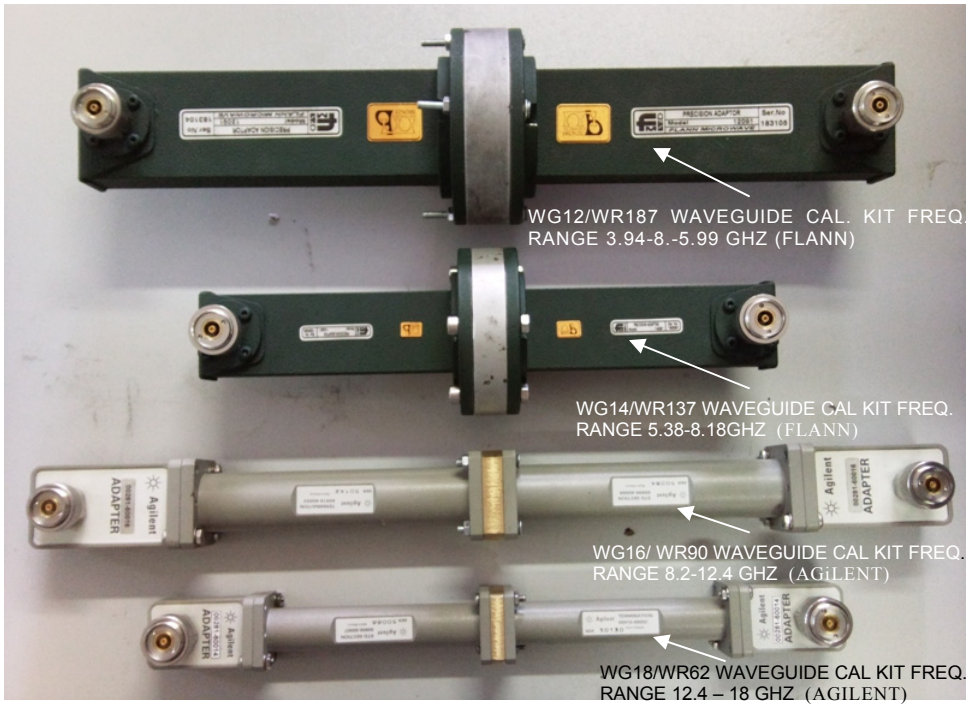

(c)

Fig (3.6.2.2). a): sample holder for (4-18 GHz), b,c): sample holder and waveguide sections for (4-18 GHz),

Wave guide sections have been chosen of proper length so as to reduce the higher-order electromagnetic modes keeping the monomodal regime (TE10).

In Fig. (3.6.2.2), different sample holder and waveguide sections are shown in order to cover 4 to 18 GHz frequency band. Wave guide section and sample holders are Agilent (8.2 to 18 GHz) and Flann (4-8.2 GHz).

A measurement of the reflection from and/or transmission through a material along, with knowledge of its physical dimensions provides the information to characterize the permittivity and permeability of the material. Vector network analyzers [7] make swept high frequency stimulus-response measurements from 300 kHz to 110 GHz or even higher. A vector network analyzer consists of a signal source, a receiver and a display Fig. (3.6.2.3).

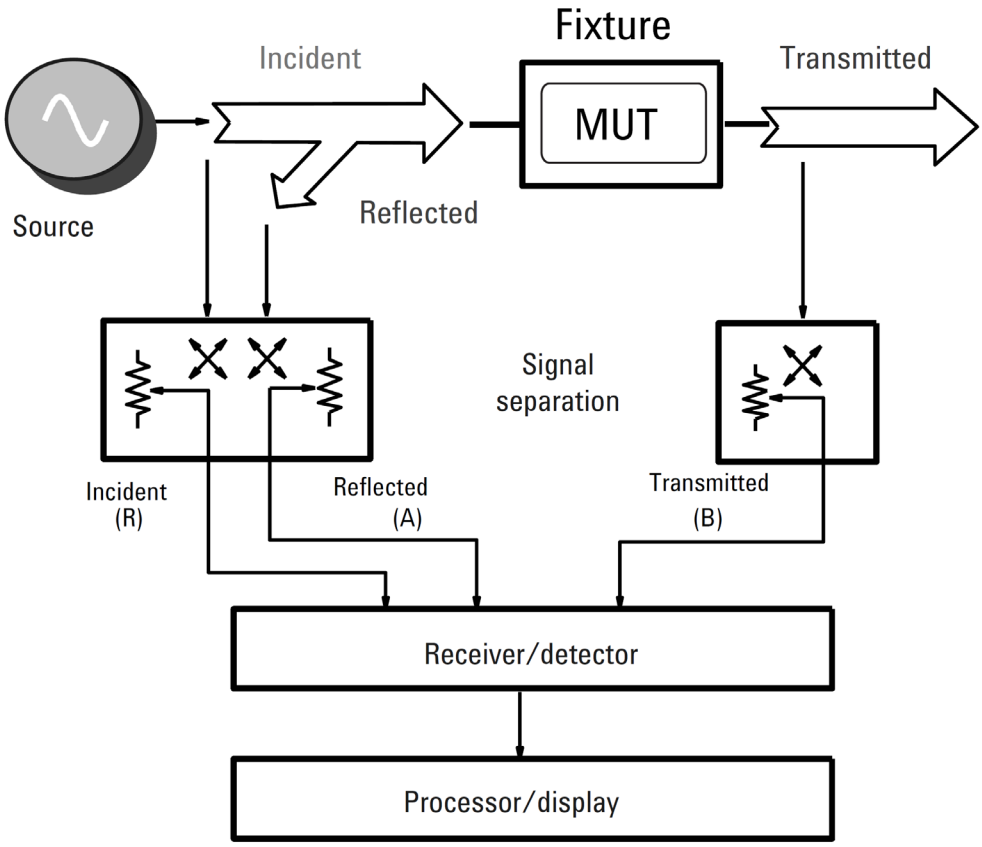

Fig (3.6.2.3). Vector Network Analyzer

The source launches a signal at a single frequency to the material under test. The receiver is tuned to that frequency to detect the reflected and transmitted signals from the material. The measured response produces the magnitude and phase data at that frequency. The source is then stepped to the next frequency and the measurement is

repeated to display the reflection and transmission measurement response as a function of frequency.

Simple components and connecting wires that perform well at low frequencies behave differently at high frequencies. At microwave frequencies wavelengths become small compared to the physical dimensions of the devices such that two closely spaced points can have a significant phase difference. Low frequency lumped-circuit element techniques must be replaced by transmission line theory to analyze the behavior of devices at higher frequencies.

Additional high frequency effects such as radiation loss, dielectric loss and capacitive coupling make microwave circuits more complex and expensive.

It is time consuming and costly to try to design a perfect microwave network analyzer. Instead, a measurement calibration is used to eliminate the systematic (stable and repeatable) measurement errors caused by the imperfections of the system. Random errors due to noise, drift, or the environment (temperature, humidity, pressure) cannot be removed with a measurement calibration. This makes a microwave measurement susceptible to errors from small changes in the measurement system. These errors can be minimized by adopting good measurement practices, such as visually inspecting all connectors for dirt or damage and by minimizing any physical movement of the test port cables after a calibration.

For solid materials, an air gap between the probe and sample can be a significant source of error unless the sample face is machined to be at least as flat as the probe face. A key feature in reliable sample preparation requires that no gaps between sample holder and the material are present. In the present work, this target has been obtained injecting the final composite directly into the sample holder, while keeping the composite in the liquid status at room temperature. This strategy assures the best electrical continuity between the sample and its holder. This process improves the traditional method of wave guide measurements where the sample is obtained machining the materials so as to fit the sample holder section at the cost of introducing air gaps.

The sample must also be thick enough to appear “infinite” to the probe. There is a simple equation [8], to calculate the approximate thickness of the sample for the high

temperature probe sample and suggested thickness for the slim probe sample. A simple practical approach is to put a short behind the sample and check to see if it affects the measurement results.

Calibration must be carried out before making the measurement. The technique involves measurement of the reflected (S_{11}) and transmitted signal (S_{21}). The relevant scattering parameters are related closely to the complex permittivity and permeability of the material by equations. The conversion of s-parameters to complex dielectric parameter is computed by solving the equations using a program.

3.6.3 Conversion of scattering parameters in electric permittivity and magnetic permeability

In a transmission/reflection method, the material under test (MUT), is inserted into a segment of transmission line, such as waveguide or coaxial line. From the relevant scattering equations relating the scattering parameters of the segment of transmission line filled with the sample under study to the permittivity and permeability of the sample, we can get the electromagnetic properties of the sample [9].

In a transmission/reflection method, all the four scattering parameters can be measured, so we have more data at our disposal than in reflection measurements. For a transmission/reflection measurement, the relevant scattering equations contain variables including the complex permittivity and permeability of the sample, the positions of the two reference planes, and the sample length.

These relevant scattering equations are generally overdetermined and therefore can be solved in various ways.

3.6.3.1 Nicolson -Ross -Weir procedure

The working principles for transmission/reflection methods have been systematically analyzed in literatures [10]. The sample under study is inserted into a segment of transmission line, whose axis is in x-direction.

Scattering equations are often used to analyze the electric fields at the sample interfaces. We assume the electric fields at the three sections of the transmission line as E_I,E_{II}, and E_{III}. For a normalized forward wave, we have [10].

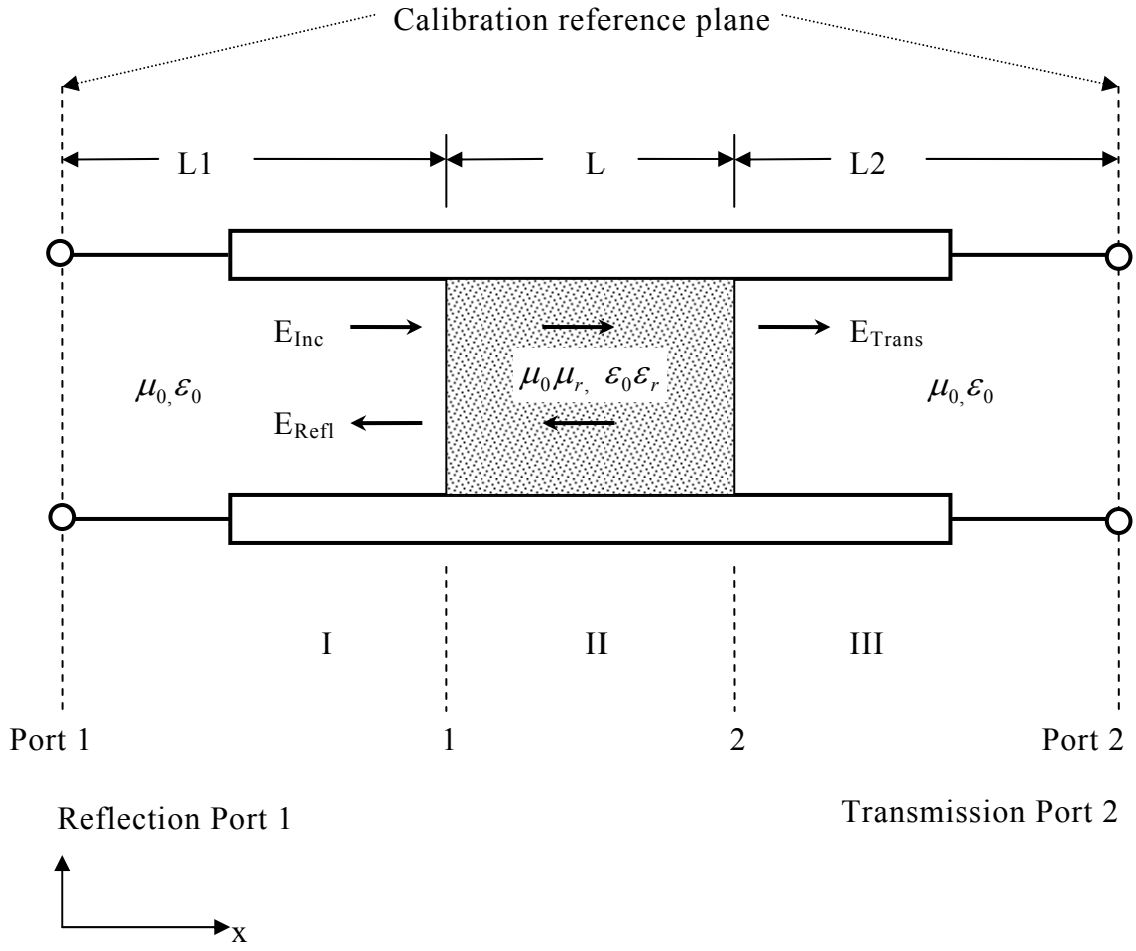

Fig. (3.6.3.1.1). A dielectric sample in a transmission line and the incident(Inc) and reflected (Refl) electric field distributions in the regions I, II, and III.
Port1 and port2 denote calibration reference plane positions (from James Baker-Jarvis NIST tech note 1990)

Let us suppose the electric fields E_I, E_{II}, and, E_{III} in either the TEM mode in a coaxial line or the TE_{10} mode in a waveguide, (with a time dependence of $e^{j\omega t}$) in the regions I, II, and III, [10], we can write the spatial distribution of the electric field for an forward field normalized to 1:

$$E_I = e^{-\gamma_0 x} + C_1 e^{+\gamma_0 x}$$

(3.6.3.1.1)

$$E_{II} = C_2 e^{-\gamma x} + C_3 e^{+\gamma x}$$

(3.6.3.1.2)

$$E_{III} = C_4 e^{-\gamma_0 x}$$

(3.6.3.1.3)

with

$$\gamma = j\sqrt{k^2 - \beta^2} = j\sqrt{\frac{\omega^2 \mu_r \varepsilon_r}{c_{vac}^2} - \left(\frac{2\pi}{\lambda_c}\right)^2},$$

$$\gamma_0 = j\sqrt{k_0^2 - \beta^2} = j\sqrt{\frac{\omega^2}{c_{lab}^2} - \left(\frac{2\pi}{\lambda_c}\right)^2}.$$

$$\varepsilon = \left[\varepsilon_r' - j\varepsilon_r''\right]\varepsilon_0 = \varepsilon_r \varepsilon_0,$$

$$\mu = \left[\mu_r' - j\mu_r''\right]\mu_0 = \mu_r \mu_0.$$

(3.6.3.1.4)

Here $j = \sqrt{-1}$, c_{vaq} and c_{lab} are the speed of light in vacuum and laboratory, ω is the angular frequency, λ_c, is the cutoff wavelength of transmission line, ε_0 and μ_0 are the permittivity and permeability of vacuum, ε_r and μ_r are the complex permittivity and permeability relative to a vacuum, and γ_0, γ are the propagation constants in vacuum and material respectively. The constants C_i are determined from the boundary conditions. The boundary condition on the electric field is the continuity of the tangential component at the interfaces. The tangential component can be calculated from Maxwell's equations given an electric field with only a radial component.

$$E_I(x = L_1) = E_{II}(x = L_1)$$
$$E_{II}(x = L_1 + L) = E_{III}(x = L_1 + L)$$

(3.6.3.1.5)

where $L_{air} = L_1 + L_2 + L$ is the length of the air line, L_1 and L_2 are the distances from the respective ports to sample faces, and L is the sample length. The boundary condition on the magnetic field requires the additional assumption that no surface currents are generated. If this condition holds, then the tangential component of the magnetic field is continuous across the interface. The tangential component can be calculated from Maxwell's equations for an electric field with only a radial component.

$$H_I(x=L_1)=H_{II}(x=L_1)$$
$$H_{II}(x=L_1+L)=H_{III}(x=L_1+L)$$
$$\Downarrow$$
$$\frac{1}{\mu_0}\frac{\partial E_I}{\partial x}(x=L_1)=\frac{1}{\mu}\frac{\partial E_{II}}{\partial x}(x=L_1)$$
$$\frac{1}{\mu}\frac{\partial E_{II}}{\partial x}(x=L_1+L)=\frac{1}{\mu_0}\frac{\partial E_{III}}{\partial x}(x=L_1+L)$$

(3.6.3.1.6)

For a two-port device the expressions for the measured scattering parameters are obtained by solving Eqs (3.6.3.1.1) - (3.6.3.1.3) subject to the boundary conditions. We assume that $S_{12} = S_{21}$. The explicit expressions are given by

$$S_{11}=R_1^2\left[\frac{\Gamma\left(1-P^2\right)}{1-\Gamma^2P^2}\right],$$
$$S_{22}=R_2^2\left[\frac{\Gamma\left(1-z^2\right)}{1-\Gamma^2P^2}\right],$$
$$S_{21}=R_1R_2\left[\frac{P\left(1-\Gamma^2\right)}{1-\Gamma^2P^2}\right],$$

(3.6.3.1.7)

where

$$R_1=e^{-\gamma_0L_1}$$
$$R_2=e^{-\gamma_0L_2}$$

(3.6.3.1.8)

The above expressions of S_{11}, S_{22}, S_{12} S_{21} have already been shown in chapter 1 in (1.2.7) and (1.2.13): $S_{21}=T_{(z=0^+)}=\frac{P\left(1-\Gamma^2\right)}{1-\Gamma^2P^2}$, $S_{11}=\Gamma_{(z=-d)}=\frac{\Gamma\left(1-P^2\right)}{1-\Gamma^2P^2}$.

Here R_1, R_2, are the respective reference plane transformation expressions. The expression of the *propagation factor P* is

$$P=e^{-\gamma L}$$

(3.6.3.1.9)

The wave number can be expressed for the empty wave guide as γ_0 and for the non-empty wave guide as γ:

$$\gamma_0 = j\beta_0 = j\sqrt{\omega^2\mu_0\varepsilon_0 - \omega_c^2\mu_0\varepsilon_0} = j\sqrt{\mu_0\varepsilon}_0\sqrt{\omega^2\left(1-\frac{\omega_c^2}{\omega^2}\right)} = j\omega\sqrt{\mu_0\varepsilon}_0\sqrt{1-\left(\frac{f_c}{f}\right)^2} =$$

$$\gamma_0 = j2\pi f\sqrt{\mu_0\varepsilon}_0\sqrt{1-\left(\frac{f_c/c}{f/c}\right)^2} = j2\pi\frac{f}{c}\sqrt{1-\left(\frac{\lambda_o}{\lambda_c}\right)^2} = j\frac{2\pi}{\lambda_o}\sqrt{1-\left(\frac{\lambda_o}{\lambda_c}\right)^2}$$

(3.6.3.1.10)

$$\gamma = j\beta_g = j\sqrt{\omega^2\mu_0\varepsilon_0\mu_r\varepsilon_r - \omega_c^2\mu_0\varepsilon_0} = j\sqrt{\mu_0\varepsilon}_0\sqrt{\omega^2\left(\mu_r\varepsilon_r-\frac{\omega_c^2}{\omega^2}\right)} = j\omega\sqrt{\mu_0\varepsilon}_0\sqrt{\mu_r\varepsilon_r-\left(\frac{f_c}{f}\right)^2} =$$

$$\gamma = j2\pi f\sqrt{\mu_0\varepsilon}_0\sqrt{1-\left(\frac{f_c/c}{f/c}\right)^2} = j2\pi\frac{f}{c}\sqrt{\mu_r\varepsilon_r-\left(\frac{\lambda_o}{\lambda_c}\right)^2} = j\frac{2\pi}{\lambda_o}\sqrt{\mu_r\varepsilon_r-\left(\frac{\lambda_o}{\lambda_c}\right)^2}$$

(3.6.3.1.11)

where

$c = \frac{1}{\sqrt{\mu_0\varepsilon}_0} \cong 3\cdot 10^8 \quad [\text{m/s}]$

f_c is the trnsmission line cut off frequency $[\text{Hz}]$

f is the electromagnetic wave frequency $[\text{Hz}]$

$\lambda_0 = \frac{c}{f}$ is the wavelenght in the empty space $[\text{m}]$

$\lambda_c = \frac{c}{f_c}$ is the cut off wavelenght of the transmission line $[\text{m}]$

The wave impedance of the empty and filled cell can be written as:

$$Z_0 = \frac{j\omega\mu_0}{\gamma_0} = \frac{j2\pi f\mu_0}{j\frac{2\pi}{\lambda_o}\sqrt{1-\left(\frac{\lambda_o}{\lambda_c}\right)^2}} = \frac{f\lambda_o\mu_0}{\sqrt{1-\left(\frac{\lambda_o}{\lambda_c}\right)^2}} = \frac{c\mu_0}{\sqrt{1-\left(\frac{\lambda_o}{\lambda_c}\right)^2}} = \frac{\mu_0}{\sqrt{\varepsilon_0\mu_0}\sqrt{1-\left(\frac{\lambda_o}{\lambda_c}\right)^2}} = \frac{\sqrt{\frac{\mu_0}{\varepsilon_0}}}{\sqrt{1-\left(\frac{\lambda_o}{\lambda_c}\right)^2}}$$

(3.6.3.1.12)

$$Z = \frac{j\omega\mu_0\mu_r}{\gamma} = \frac{j2\pi f\mu_0\mu_r}{j\frac{2\pi}{\lambda_o}\sqrt{\varepsilon_r\mu_r - \left(\frac{\lambda_o}{\lambda_c}\right)^2}} = \frac{f\lambda_o\mu_0\mu_r}{\sqrt{\varepsilon_r\mu_r - \left(\frac{\lambda_o}{\lambda_c}\right)^2}} = \frac{c\mu_0\mu_r}{\sqrt{\varepsilon_r\mu_r - \left(\frac{\lambda_o}{\lambda_c}\right)^2}} = \frac{\sqrt{\frac{\mu_0}{\varepsilon_0}}\mu_r}{\sqrt{\varepsilon_r\mu_r - \left(\frac{\lambda_o}{\lambda_c}\right)^2}}$$

(3.6.3.1.13)

In case of coaxial line where the cutoff frequency is zero, then the above expressions reduce to.

$$Z_{0_{(TEM)}} = \frac{j\omega\mu_0}{\gamma_0} = \frac{\sqrt{\frac{\mu_0}{\varepsilon_0}}}{\sqrt{1 - \left(\frac{\lambda_o}{\infty}\right)^2}} = \sqrt{\frac{\mu_0}{\varepsilon_0}}$$

(3.6.3.1.14)

$$Z_{(TEM)} = \frac{j\omega\mu_0\mu_r}{\gamma} = \frac{\sqrt{\frac{\mu_0}{\varepsilon_0}}\mu_r}{\sqrt{\varepsilon_r\mu_r - \left(\frac{\lambda_o}{\infty}\right)^2}} = \sqrt{\frac{\mu_0}{\varepsilon_0}}\sqrt{\frac{\mu_r}{\varepsilon_r}} = \sqrt{\frac{\mu}{\varepsilon}}$$

(3.6.3.1.15)

As a consequence the reflection coefficient is:

$$\Gamma = \frac{Z - Z_0}{Z + Z_0} = \frac{j\omega\frac{\mu_0\mu_r}{\gamma} - j\omega\frac{\mu_0}{\gamma_0}}{j\omega\frac{\mu_0\mu_r}{\gamma} + j\omega\frac{\mu_0}{\gamma_0}} = \frac{\frac{\mu_r}{\gamma} - \frac{1}{\gamma_0}}{\frac{\mu_r}{\gamma} + \frac{1}{\gamma_0}} = \frac{\gamma_0\mu_r - \gamma}{\gamma_0\mu_r + \gamma}$$

(3.6.3.1.16)

which in case of coaxial line become:

$$\Gamma_{(TEM)} = \frac{Z - Z_0}{Z + Z_0} = \frac{\sqrt{\frac{\mu_0}{\varepsilon_0}}\sqrt{\frac{\mu_r}{\varepsilon_r}} - \sqrt{\frac{\mu_0}{\varepsilon_0}}}{\sqrt{\frac{\mu_0}{\varepsilon_0}}\sqrt{\frac{\mu_r}{\varepsilon_r}} + \sqrt{\frac{\mu_0}{\varepsilon_0}}} = \frac{\sqrt{\frac{\mu_r}{\varepsilon_r}} - 1}{\sqrt{\frac{\mu_r}{\varepsilon_r}} + 1}$$

(3.6.3.1.17)

The *propagation factor P* within the material can also be written as

$$P = e^{-\gamma L} = e^{-j\omega\sqrt{\mu_0\varepsilon_0}\sqrt{\mu_r\varepsilon_r}L} = e^{-j\frac{2\pi f}{c}\sqrt{\mu_r\varepsilon_r}L} = e^{-j\frac{2\pi}{\lambda_0}\sqrt{\mu_r\varepsilon_r}L}$$

(3.6.3.1.18)

$$\frac{1}{P} = e^{j\frac{2\pi}{\lambda_0}\sqrt{\mu_r\varepsilon_r}L}$$

(3.6.3.1.19)

$$\ln\left(\frac{1}{P}\right) = \ln\left(e^{j\frac{2\pi}{\lambda_0}\sqrt{\mu_r\varepsilon_r}L}\right)$$

(3.6.3.1.20)

$$\ln\left(\frac{1}{P}\right) = j\frac{2\pi}{\lambda_0}\sqrt{\mu_r\varepsilon_r}L$$

(3.6.3.1.21)

$$\left[\frac{\lambda_0}{j2\pi L}\ln\left(\frac{1}{P}\right)\right] = \sqrt{\mu_r\varepsilon_r}$$

(3.6.3.1.22)

$$-\left[\frac{\lambda_0}{2\pi L}\ln\left(\frac{1}{P}\right)\right]^2 = \mu_r\varepsilon_r$$

(3.6.3.1.23)

Now we can equal the expressions of both propagation constant, i.e.,

1) $$\gamma = j\omega\sqrt{\mu_0\varepsilon_0}\sqrt{\mu_r\varepsilon_r} = j2\pi f\sqrt{\mu_0\varepsilon_0}\left[\frac{\lambda_0}{j2\pi L}\ln\left(\frac{1}{P}\right)\right] = j2\pi\frac{c}{\lambda_0}\frac{1}{c}\left[\frac{\lambda_0}{j2\pi L}\ln\left(\frac{1}{P}\right)\right]$$

(3.6.3.1.24)

2) $$\gamma = j\frac{2\pi}{\lambda_o}\sqrt{\mu_r\varepsilon_r - \left(\frac{\lambda_o}{\lambda_c}\right)^2}$$

(3.6.3.1.25)

$$j\frac{2\pi}{\lambda_o}\left[\frac{\lambda_0}{j2\pi L}\ln\left(\frac{1}{P}\right)\right]=j\frac{2\pi}{\lambda_o}\sqrt{\mu_r\varepsilon_r-\left(\frac{\lambda_o}{\lambda_c}\right)^2}$$

$$\left[\frac{\lambda_0}{j2\pi L}\ln\left(\frac{1}{P}\right)\right]=\sqrt{\mu_r\varepsilon_r-\left(\frac{\lambda_o}{\lambda_c}\right)^2}$$

$$-\left[\frac{\lambda_0}{2\pi L}\ln\left(\frac{1}{P}\right)\right]^2=\mu_r\varepsilon_r-\left(\frac{\lambda_o}{\lambda_c}\right)^2$$

$$-\left[\frac{1}{2\pi L}\ln\left(\frac{1}{P}\right)\right]^2=\frac{\mu_r\varepsilon_r}{\lambda_0^2}-\left(\frac{\lambda_o}{\lambda_c}\right)^2=\left[\frac{\mu_r\varepsilon_r}{\lambda_0^2}-\frac{1}{\lambda_c^2}\right]$$

$$\Downarrow$$

$$\frac{1}{\Lambda^2}=-\left[\frac{1}{2\pi L}\ln\left(\frac{1}{P}\right)\right]^2=\left[\frac{\mu_r\varepsilon_r}{\lambda_0^2}-\frac{1}{\lambda_c^2}\right]$$

(3.6.3.1.26)

For nonmagnetic materials, Eq. (3.7.1.6) and (3.7.1.7) contains $\varepsilon_r', \varepsilon_r'', L, R_1, R_2$, as unknown quantities. Additionally for the empty sample holder

$$S_{21}^0=R_1R_2\left[\frac{P\left(1-\Gamma^2\right)}{1-\Gamma^2P^2}\right]=R_1R_2\left[\frac{P\left(1-0\right)}{1-0P^2}\right]=R_1R_2e^{-\gamma_0L}$$

(3.6.3.1.27)

Since the equations for S12 and S21 are equivalent for isotropic materials, we have four complex equations, plus the equation for the length of the air line, or equivalently nine real equations for five unknown [10]. Thus, the system of equations is overdetermined, and it is possible to solve the equation in various combinations.

Nicolson and Ross [11] and Weir [12], combined the equations for S_{11} and S_{12} and discovered a formula for the permittivity and permeability. This procedure works well at frequencies where the sample length is not a multiple of one-half wavelength in the material. At these latter frequencies, however, the solution procedure completely breaks down.

In the Nicolson- Ross-Weir algorithm writing:

$$V_1 = S_{21} + S_{11}$$
$$V_2 = S_{21} - S_{11}$$

(3.6.3.1.28)

and if

$$X = \frac{1 - V_1 V_2}{V_1 - V_2} = \frac{1 - (S_{21} + S_{11})(S_{21} - S_{11})}{(S_{21} + S_{11}) - (S_{21} + S_{11})} = \frac{S_{11}^2 - S_{21}^2 + 1}{2S_{11}}$$

(3.6.3.1.29)

The reflection coefficient is given explicitly in terms of scattering parameters

$$\Gamma = X \pm \sqrt{X^2 - 1}$$

(3.6.3.1.30)

The correct root is chosen by requiring $|\Gamma| \leq 1$.

The propagation factor, *P*, for the Nicolson-Ross-Weir procedure is given by

$$P = \frac{V_1 - \Gamma}{1 - V_1 \Gamma} = \frac{S_{21} + S_{11} - \Gamma}{1 - (S_{21} + S_{11})\Gamma}$$

(3.6.3.1.31)

The complex dielectric constant ε_r and permeability μ_r can be determined from *P* and Γ. In the coaxial line is very simple since from

$$\Gamma_{(TEM)} = \frac{\sqrt{\frac{\mu_r}{\varepsilon_r}} - 1}{\sqrt{\frac{\mu_r}{\varepsilon_r}} + 1} \qquad \Rightarrow \qquad \frac{\mu_r}{\varepsilon_r} = \frac{\left(1 + \Gamma_{(TEM)}\right)^2}{\left(1 - \Gamma_{(TEM)}\right)^2} = c_1$$

(3.6.3.1.32)

and from

$$\mu_r \varepsilon_r = -\left[\frac{\lambda_0}{2\pi L} \ln\left(\frac{1}{P}\right)\right]^2 = c_2$$

(3.6.3.1.33)

is easy to find:

$$\boxed{\begin{aligned}\mu_r &= \sqrt{c_1 c_2} \\ \varepsilon_r &= \sqrt{\frac{c_2}{c_1}}\end{aligned}}$$

(3.6.3.1.34)

More generally instead, in waveguide or coaxial line we have:

$$\boxed{\mu_r = \frac{\lambda_{0g}}{\Lambda}\left(\frac{1+\Gamma}{1-\Gamma}\right) = \frac{1+\Gamma}{\Lambda(1-\Gamma)\sqrt{\frac{1}{\lambda_0^2}-\frac{1}{\lambda_c^2}}}}$$

(3.6.3.1.35)

where, λ_0, is the free space wavelength and λ_c is the cutoff wavelength, λ_{0g} is the wavelength in the empty cell

$$\lambda_{0g} = \frac{1}{\sqrt{\frac{1}{\lambda_0^2}-\frac{1}{\lambda_c^2}}}$$

(3.6.3.1.36)

The permittivity is given by:

$$\boxed{\varepsilon_r = \frac{\lambda_0^2}{\mu_r}\left\{\frac{1}{\Lambda^2}+\frac{1}{\lambda_c^2}\right\} = \frac{\lambda_0^2}{\mu_r}\left\{\frac{1}{\lambda_c^2}-\left[\frac{1}{2\pi L}\ln\left(\frac{1}{P}\right)\right]^2\right\}}$$

(3.6.3.1.37)

Equation (3.7.1.16) has an infinite number of roots for magnetic materials, since the logarithm of a complex number is multi-valued. In order to pick out the correct root it is necessary to compare the measured group delay to the calculated group delay. The calculated group delay is related to the change of the wave number, *k*, with respect to angular frequency

$$\tau_{calc.group(n)} = L\frac{d}{df}\left(\sqrt{\frac{\varepsilon_r\mu_r}{\lambda_0^2}-\frac{1}{\lambda_c^2}}\right)_n$$

(3.6.3.1.38)

where *f* is the frequency in hertz and $\tau_{calc.group(n)}$ is the group delay in seconds for the *n*-th solution of Eq (3.6.1.20), and (3.6.1.25),

The measured group delay is determined from the slope of the phase of the propagation factor versus frequency

$$\tau_{meas.group} = -\frac{1}{2\pi}\frac{d\phi}{df}$$

(3.6.3.1.39)

where ϕ is the measured phase in radians of *P*.

To determine the correct root, the calculated group delays are found from Eq (3.6.3.1.39) for various values of *n* in the logarithm term in Eq (3.6.1.23), using $\ln(z) = \ln|(z)| + j(\theta + 2\pi n)$, where $n = 0,\pm1,\pm2....,$ and compared to the measured value from Eq (3.7.1.29). The comparison yields the correct value of *n*.

Accuracy in the determination of *n*, may be increased by applying numerical differentiation techniques [13] where the slope is computed using data for three or more frequencies. The correct root, $n = k$, is found when

$$\tau_{calc.group(k)} - \tau_{meas.group} \cong 0$$

(3.6.3.1.40)

Besides the group-delay method, the problem of phase ambiguity can also be solved using *phase unwrapping method* (Hock 2002). It is possible to divide this problem into two parts: determination of the initial phase and phase unwrapping. Consider a sample with constant permittivity over a wide frequency range, such as Teflon. Fig.(3.6.3.1.2) shows the phase of T calculated from Eq. (3.6.3.1.31), which gives an answer between ±π. It is clear from the figure that phase ambiguity arises from the phase-wrapping effect.

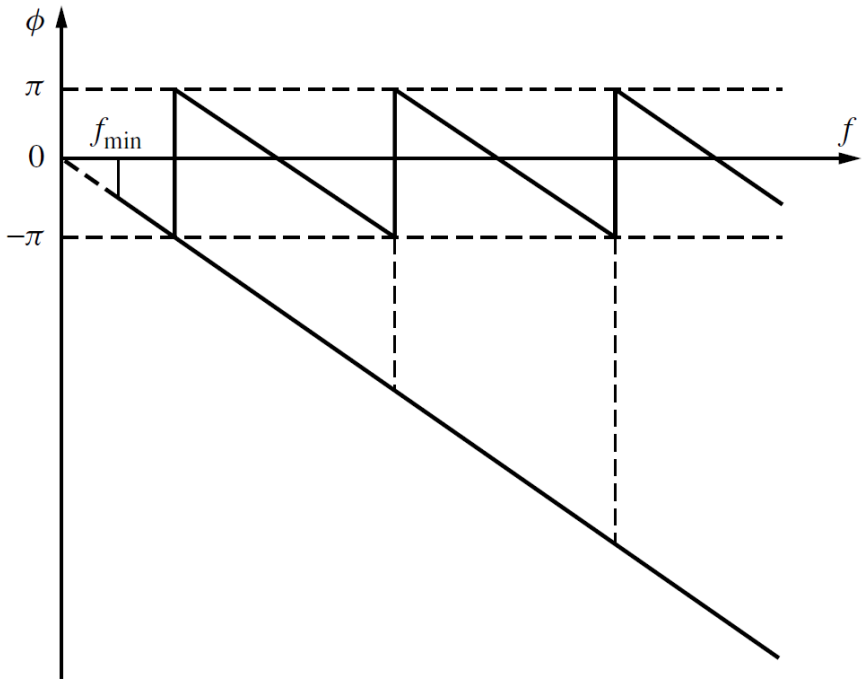

Fig. (3.6.3.1.2). Wrapping and unwrapping of phase of transmission coefficient

Obtaining the correct additive constant of $2n\pi$ for the logarithm in Eq. (3.6.3.1.39) is then equivalent to phase unwrapping. The unwrapped phase is also shown in Fig. (3.6.3.1.2).

The phase-unwrapping can be done in a simple way. The phase can be unwrapped by detecting a jump in phase value of, say, more than π from one measurement frequency to the next, and then shifting all the subsequent phases by 2π in the opposite direction. This is a commonly used phase-unwrapping method. As long as the noise is less than π, such an unwrapping is reliable.

Besides the phase ambiguities discussed above, as will be discussed later, spurious peaks for permittivity and permeability can be observed when the sample length is a multiple of half wavelength of the microwave within the sample. In most of the transmission/reflection measurements, the determinations of permittivity and permeability are based on the NRW algorithm. To get the correct permittivity and permeability results, the phase ambiguities and spurious peaks should be eliminated.

The phase unwrapping procedure is the following one:

Freq	Phase	$\Delta\Phi$	Unwrapped Phase
f1	Φ1		UnwrΦ1= Φ1
f2	Φ2	$\Delta\Phi$2	UnwrΦ2
f3	Φ3	$\Delta\Phi$3	UnwrΦ3
f_i	Φ_i	$\Delta\Phi_i$	UnwrΦ_i
f_{i+1}	Φ_{i+1}	$\Delta\Phi_{i+1}$	UnwrΦ_{i+1}
f_n	Φ_n	$\Delta\Phi_n$	UnwrΦ_n

Tab. (3.6.3.1.1). Example of phase unwrapping procedure

The algorithm we could implement for phase unwrapping is reported below as pseudocode:

if $(\Phi_{i+1}<\Phi_i)$ && $abs(\Phi_{i+1}-\Phi_i)>180$

$\Delta\Phi_{i+1}=\Phi_{i+1}-\Phi_i+360;$

elseif $(\Phi_{i+1}<\Phi_i)$ && $abs(\Phi_{i+1}-\Phi_i)<180$

$\Delta\Phi_{i+1}=\Phi_{i+1}-\Phi_i;$

elseif $(\Phi_{i+1}>\Phi_i)$ && $abs(\Phi_{i+1}-\Phi_i)>180$

$\Delta\Phi_{i+1}=\Phi_{i+1}-\Phi_i-360;$

elseif $(\Phi_{i+1}>\Phi_i)$ && $abs(\Phi_{i+1}-\Phi_i)<180$

$\Delta\Phi_{i+1}=\Phi_{i+1}-\Phi_i;$

end

$Unwr\Phi_{i+1}= Unwr\Phi_i+\Delta\Phi_{i+1};$

In Fig. (3.6.3.1.3). the phase unwrapping when phase increases is shown

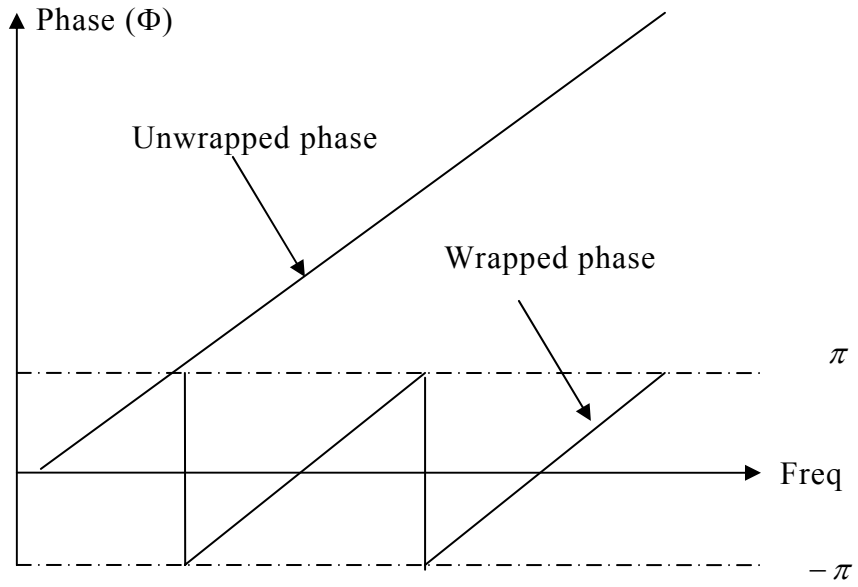

Fig. (3.6.3.1.3). Wrapping and unwrapping of the phase of the transmission coefficient

In Fig. (3.6.3.1.4). Epoxy resin S_{21} scattering parameter wrapped and unwrapped phase is shown.

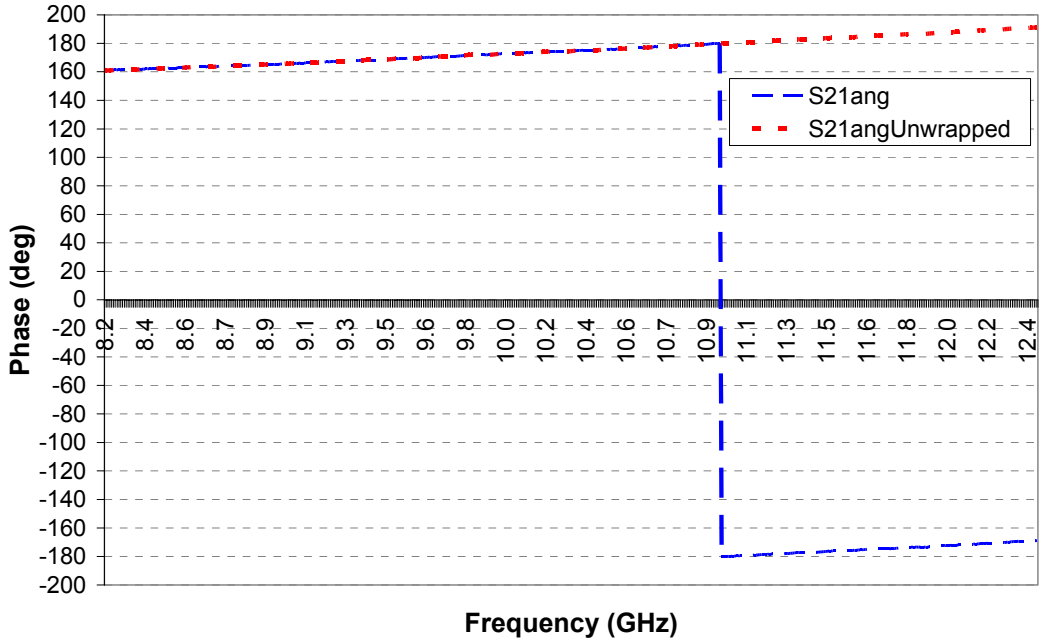

Fig. (3.6.3.1.4). Epoxy resin scattering parameter S_{21}, wrapped and unwrapped phase.

3.6.3.2 New Non Iterative Method for dielectric Materials

It is well known that for low-lossy materials, the NRW procedure presents divergence at frequencies corresponding to integer multiples of one half wavelength in the sample. This is illustrated in Fig. (3.6.3.2.1), where the real permittivity and permeability of a polytetrafluoroethylene (PTFE) sample is plotted against of frequency in 8.2–12.4 GHz band waveguide. At these particular frequencies, the magnitude of the measured parameter is particularly small (thickness resonance) and the phase uncertainty becomes large. This leads to the appearance of inaccuracy peaks on the permittivity and permeability curve.

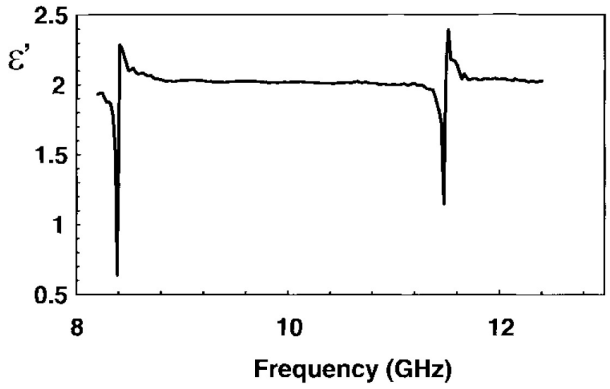

(a)

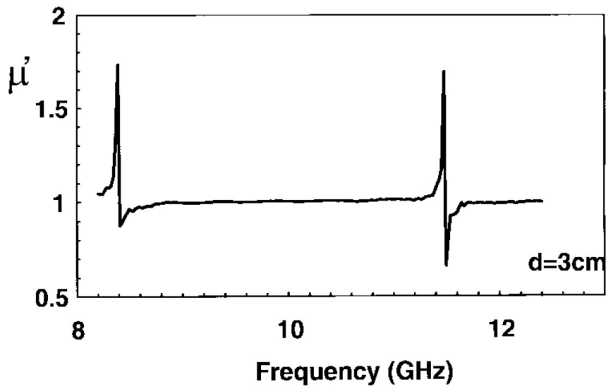

(b)

Fig (3.6.3.2.1). Real permittivity (a) and permeability (b) of a PTFE sample characterized in X band waveguide (NRW procedure).

At points corresponding to one-half wavelength the scattering parameter $|S_{11}|$ gets very small. Also, for small $|S_{11}|$ the uncertainty in the measurement of the phase of S_{11} on a network analyzer is very large. Thus, this uncertainty dominates the solution

at these frequencies. To bypass this problem many researchers resort to short sample lengths in the coaxial line. Use of short samples lowers the measurement sensitivity, however. In fact, in minimizing the uncertainty for low-loss, a low permittivity material, a relatively long sample is preferred.

Equations (3.6.3.1.35) and (3.6.3.1.37) reveal that the two terms $\left(\frac{1+\Gamma}{1-\Gamma}\right)$ and $\frac{\lambda_{0g}}{\Lambda}$, occur in the calculation of the complex permittivity and permeability. In Fig. (3.6.3.1.2), has been represented the variation of these two terms (magnitude and phase) corresponding to the previous PTFE sample versus the frequency. We can notice that the inaccuracy peaks are visible only on the term $\left(\frac{1+\Gamma}{1-\Gamma}\right)$ and not on $\frac{\lambda_{0g}}{\Lambda}$ although these two terms depend on the S_{11} parameter. Hence, the term $\left(\frac{1+\Gamma}{1-\Gamma}\right)$ is only responsible for the inaccuracy peaks observed on the electromagnetic parameters.

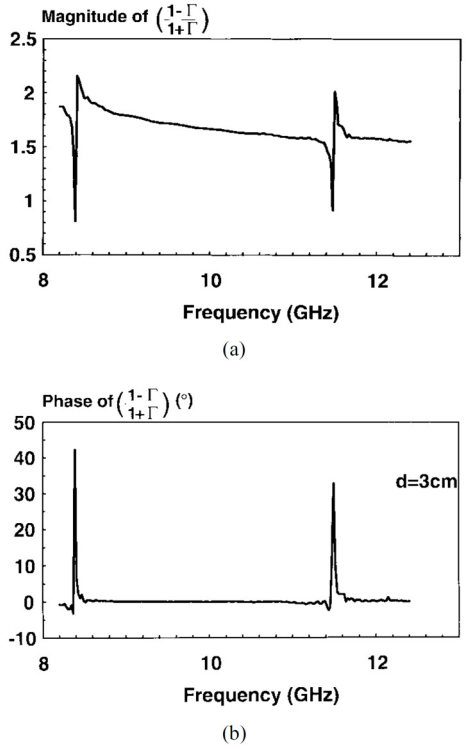

Fig (3.6.3.1.2). Evolution of magnitude (a) and phase (b) of the term $\left(\frac{1+\Gamma}{1-\Gamma}\right)$ for PTFE sample versus frequency.

1) Different Formulation of the NRW Method:

In the following equations, a different formulation of the NRW method is proposed:

$$S_{11}, S_{21}$$
$$\Downarrow$$
$$X = \frac{S_{11}^2 - S_{21}^2 + 1}{2S_{11}}$$

(3.6.3.1.1)

The reflection coefficient is given explicitly in terms of scattering parameters

$$\Gamma = X \pm \sqrt{X^2 - 1}$$

(3.6.3.1.2)

The correct root is chosen by requiring $|\Gamma| \le 1$.

The propagation factor, *P*, for the Nicolson-Ross-Weir procedure is given by

$$P = \frac{S_{21} + S_{11} - \Gamma}{1 - (S_{21} + S_{11})\Gamma}$$

(3.6.3.1.3)

$$\frac{1}{\Lambda^2} = -\left[\frac{1}{2\pi L}\ln\left(\frac{1}{P}\right)\right]^2 = \left[\frac{\mu_r \varepsilon_r}{\lambda_0^2} - \frac{1}{\lambda_c^2}\right]$$

(3.6.3.1.4)

Equations (3.6.3.1.1)– (3.6.3.1.4) are unchanged, and an intermediate step is added by introducing the effective electromagnetic parameters $\mu_{eff}^*, \varepsilon_{eff}^*$ [14], These parameters presuppose a TEM propagation mode in the cell. These effective electromagnetic parameters are deduced using mathematical expressions (3.6.3.1.5) and (3.6.3.1.6) of reflection Γ and the transmission coefficient *P* which in turn give:

$$\Gamma = \frac{\sqrt{\frac{\mu^*_{eff}}{\varepsilon^*_{eff}}} - 1}{\sqrt{\frac{\mu^*_{eff}}{\varepsilon^*_{eff}}} + 1}$$

(3.6.3.1.5)

$$P = e^{-j\frac{2\pi}{\lambda_{og}}\sqrt{\mu^*_{eff}.\varepsilon^*_{eff}}L}$$

(3.6.3.1.6)

$$\Downarrow \Downarrow$$

$$\mu^*_{eff} = \frac{\lambda_{0g}}{\Lambda}\left(\frac{1+\Gamma}{1-\Gamma}\right)$$

(3.6.3.1.7)

$$\varepsilon^*_{eff} = \frac{\lambda_{0g}}{\Lambda}\left(\frac{1-\Gamma}{1+\Gamma}\right)$$

(3.6.3.1.8)

$$\Downarrow \Downarrow$$

$$\begin{cases} \left(\frac{1-\Gamma}{1+\Gamma}\right) = \frac{\lambda_{0g}}{\Lambda}\frac{1}{\mu^*_{eff}} \\ \varepsilon^*_{eff} = \frac{\lambda_{0g}}{\Lambda}\left(\frac{1-\Gamma}{1+\Gamma}\right) = \frac{\lambda_{0g}}{\Lambda}\frac{\lambda_{0g}}{\Lambda}\frac{1}{\mu^*_{eff}} = \left(\frac{\lambda_{0g}}{\Lambda}\right)^2\frac{1}{\mu^*_{eff}} \end{cases}$$

(3.6.3.1.9)

$$\Downarrow \Downarrow$$

$$\varepsilon^*_{eff}\mu^*_{eff} = \left(\frac{\lambda_{0g}}{\Lambda}\right)^2$$

(3.6.3.1.10)

if $\mu_r = \mu^*_{eff} = 1$ then

$$\boxed{\varepsilon^*_{eff} = \varepsilon^*_{eff}\mu^*_{eff} = \left(\frac{\lambda_{0g}}{\Lambda}\right)^2}$$

(3.6.3.1.11)

This formulation is still valid to calculate the material permittivity, in particular as far as the rectangular wave guide cell is concerned.

The sample electromagnetic parameters ε_r, μ_r are then deduced from the effective ones equating the expression of P and γ:

$$\begin{cases} \gamma = j\dfrac{2\pi}{\lambda_0}\sqrt{\mu_r\varepsilon_r - \left(\dfrac{\lambda_0}{\lambda_c}\right)} \\ \gamma = \gamma_0\sqrt{\mu^*_{eff},\varepsilon^*_{eff}} \end{cases}$$

(3.6.3.1.12)

$$\begin{cases} Z = \dfrac{j\omega\mu_0\mu_r}{\gamma} \\ Z = Z_0\sqrt{\dfrac{\mu^*_{eff}}{\varepsilon^*_{eff}}} \end{cases}$$

(3.6.3.1.13)

⇓ ⇓

Solving the system of (3.7.2.12) and (3.7.2.13), we obtain:

$$\mu_r = \mu^*_{eff}$$

(3.6.3.1.14)

$$\boxed{\varepsilon_r = \left(1 - \frac{\lambda_0^2}{\lambda_c^2}\right)\varepsilon^*_{eff} + \frac{\lambda_0^2}{\lambda_c^2}\frac{1}{\mu^*_{eff}}}$$

(3.6.3.1.15)

$\mu_r = \mu^*_{eff} = 1$

$$\boxed{\varepsilon_r = \left(1 - \frac{\lambda_0^2}{\lambda_c^2}\right)\varepsilon^*_{eff} + \frac{\lambda_0^2}{\lambda_c^2} = \left(1 - \frac{\lambda_0^2}{\lambda_c^2}\right)\left(\frac{\lambda_{0g}}{\Lambda}\right)^2 + \frac{\lambda_0^2}{\lambda_c^2}}$$

(3.6.3.1.16)

In the last equations the term $\left(\frac{1+\Gamma}{1-\Gamma}\right)$ has been eliminated and we can expect the suppression of the inaccuracy peaks of permittivity.

3.7 Dielectric characterization of nanostructured composite materials

In this section measurement of permittivity of manufactured composite materials shown in chapter 2 is shown. The microwave characterization process has been carried out using waveguide method by performing scattering parameter measurements and extracting the complex electrical permittivity through canonical algorithms discussed in previous sections. *Permittivity* of materials has been used in order to compute their *electric conductivity, loss tangent, characteristic impedance, and skin-depth*.

Microwave Loss Factor% of materials has been computed by using waveguide method and computing directly scattering parameters measured by vector network analyzer.

Microwave scattering parameters (S_{ij}, i,j = 1,2, [5]) have been measured using a Vector Network Analyzer (N5230C Agilent PNA-L) and waveguide method shown in Fig.(3.7.1). Wave guide calibration kit are in the J-band (5.38-8.18 GHz), X-band (8.2-12.4 GHz), P-band (12.4-18 GHz).

Sample holders, hosting the materials under test (MUT), were built using as a shape model the thru connections of related calibration kits.

The entire frequency-band has been divided in 1536 frequency steps (start 5.38 GHz, end 18 GHz) and, for each one, the corresponding electrical permittivity has been calculated. Nanostructured composite materials taken into account are based on different weight percentage of carbon nanopowders with respect to the epoxy-resin, in particular 0.5; 1; 2; 2.5; 3 %wt for MWCNTs based composite materials and 1; 2; 3wt% for CNFs based composite materials.

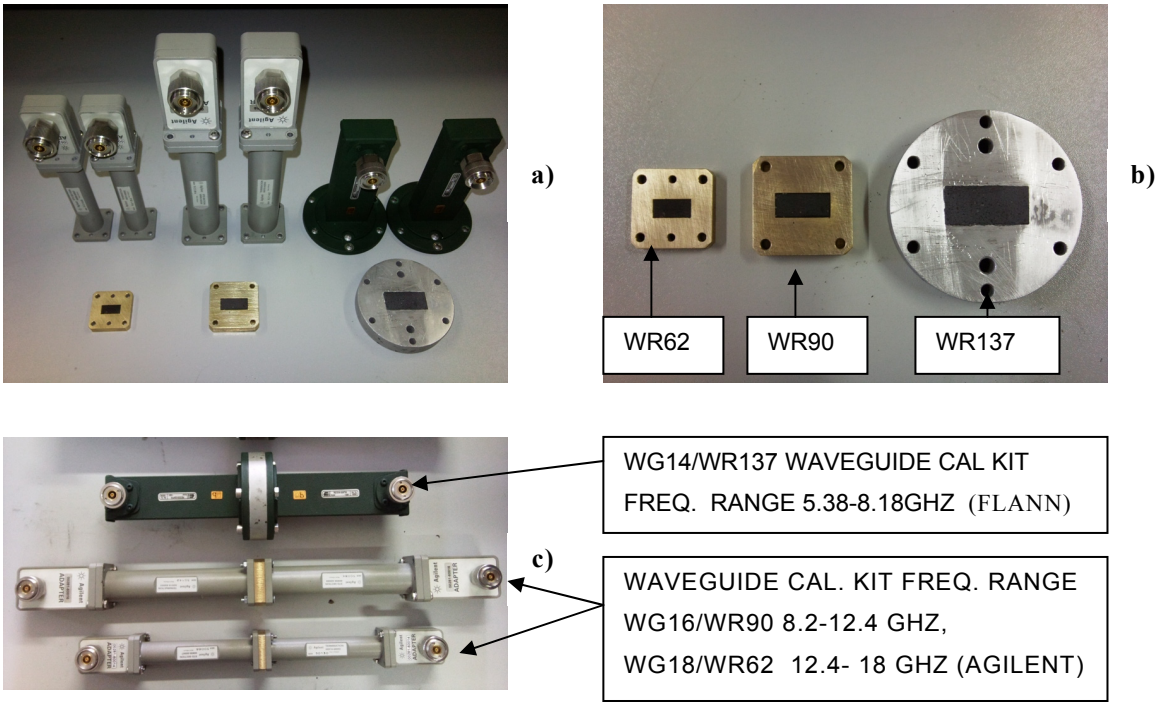

Fig (3.7.1). a,b,c) Waveguide sections and sample holders covering 5.3 to 18 GHz frequency band.

3.7.1 Complex permittivity of manufactured composite materials

We performed the permittivity retrieval by using different algorithms and comparing results. The algorithms adopted are Nicholson-Ross, NIST iterative, and non-iterative. The so obtained results can be considered accurate within the limit of the employed numerical methods.

Scattering parameters connect the input and output circuit quantities using the reflection and transmission parameters normally adopted in microwave analysis [5]. By means of such parameters it is possible to determine the real and the imaginary part of the electrical permittivity and magnetic permeability. All materials have some responses to magnetic fields but, except for ferromagnetic types, their responses are usually very small, and their permeability values differ from μ_0 by a negligible fraction. In our experiment the relative magnetic permeability is that of free space ($\mu_r = 1$) since no ferromagnetic materials are involved [15],[16].

Observing Fig.(3.7.1.1), it can be noticed that the higher the filler weight percentage the greater both the real and imaginary part of permittivity. This can be ascribed to the electric conductive characteristic of carbon powders inserted into the epoxy matrix [17].

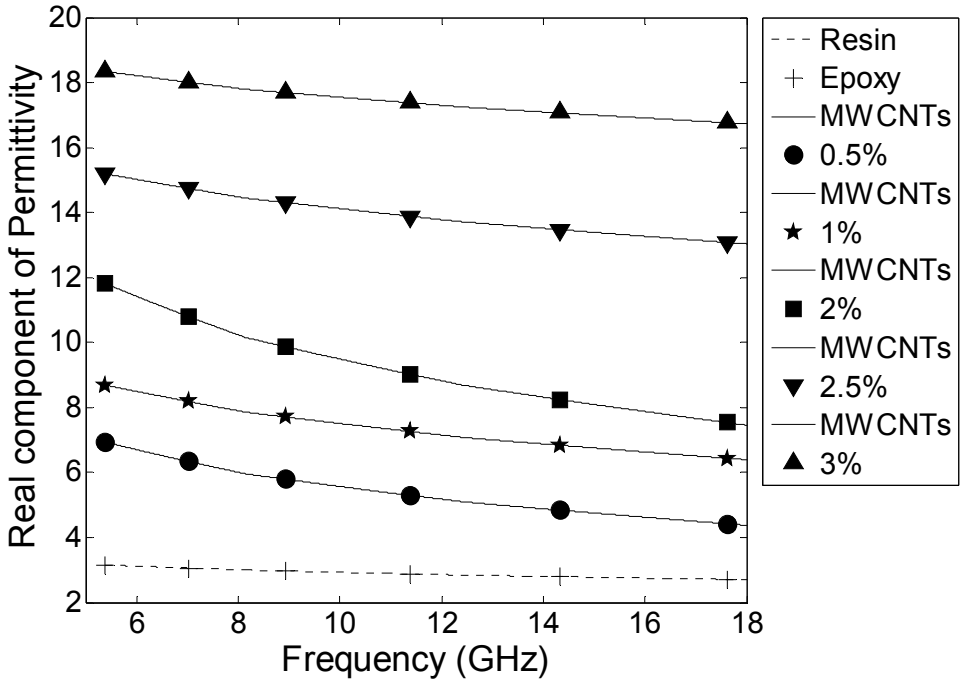

a)

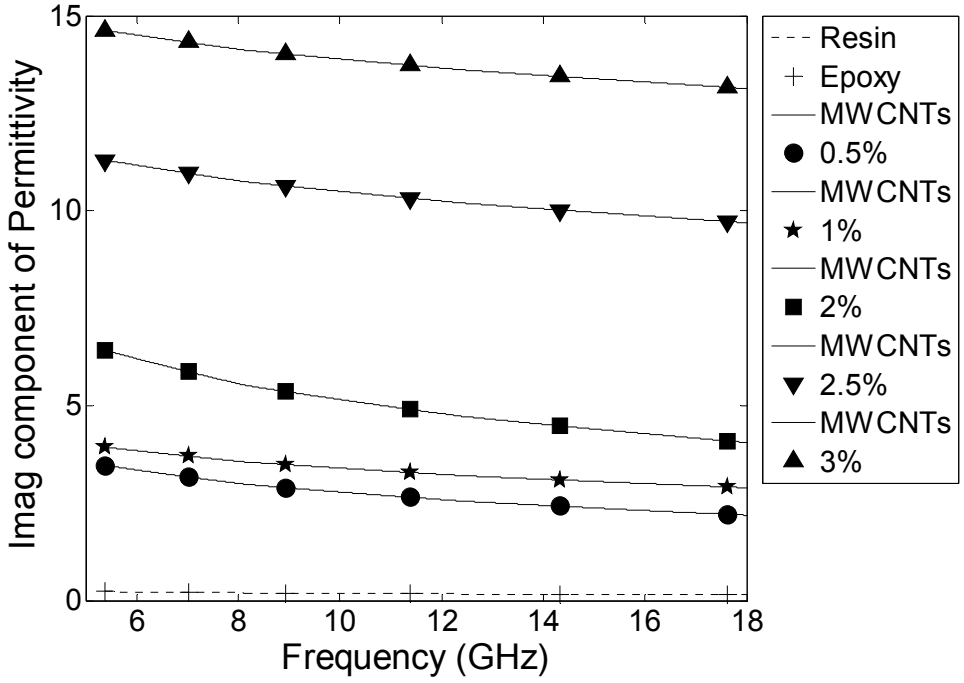

b)

Fig (3.7.1.1).

a) Real component, b) Imaginary component of permittivity of nanostructured composite materials based on MWCNTs in the 5.3 to 18 GHz frequency band

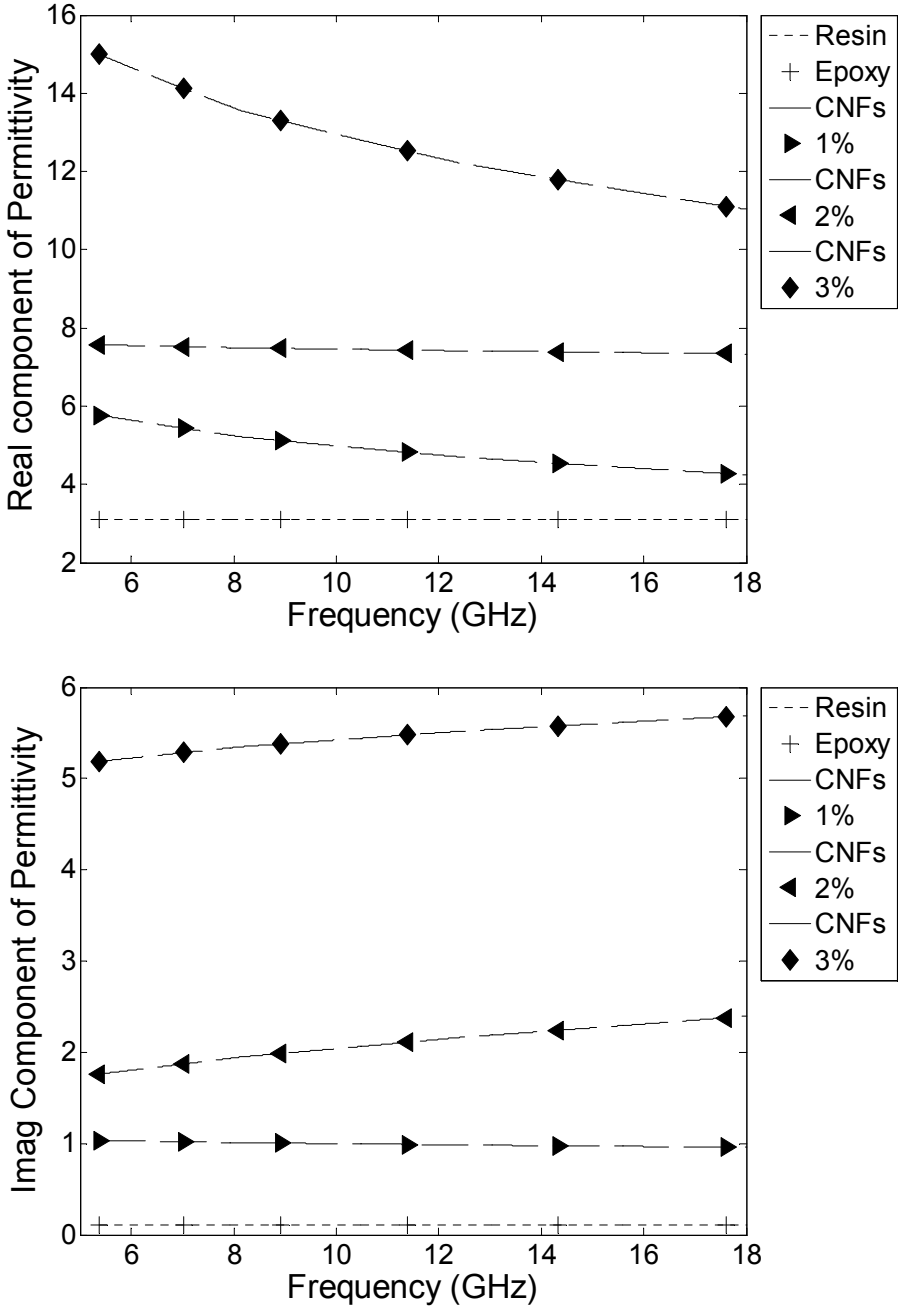

Fig (3.7.1.2).

a) Real component, b) Imaginary component of permittivity of nanostructured composite materials based on CNFs in the 5.3 to 18 GHz frequency band

3.7.2 Dielectric losses of manufactured composite materials

As explained in section 3.6.2, Loss tangent is expressed by the equation [3]

$$\tan\delta = \frac{\varepsilon_r''}{\varepsilon_r'}$$

(3.7.2.1)

This term takes into account the overall microwave dielectric losses inside the composite material under test. The higher is its value, the greater the losses.
Fig.(3.7.2.1) shows Loss tangent of all manufactured composite materials as a function of frequency. MWCNTs 3wt% have highest value of Loss Tangent.

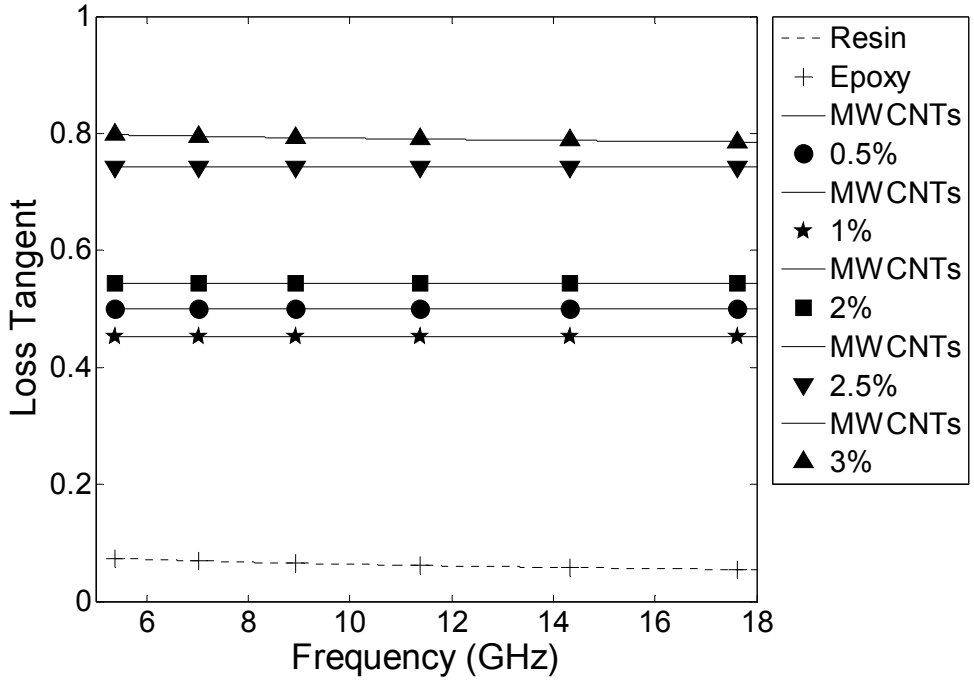

a)

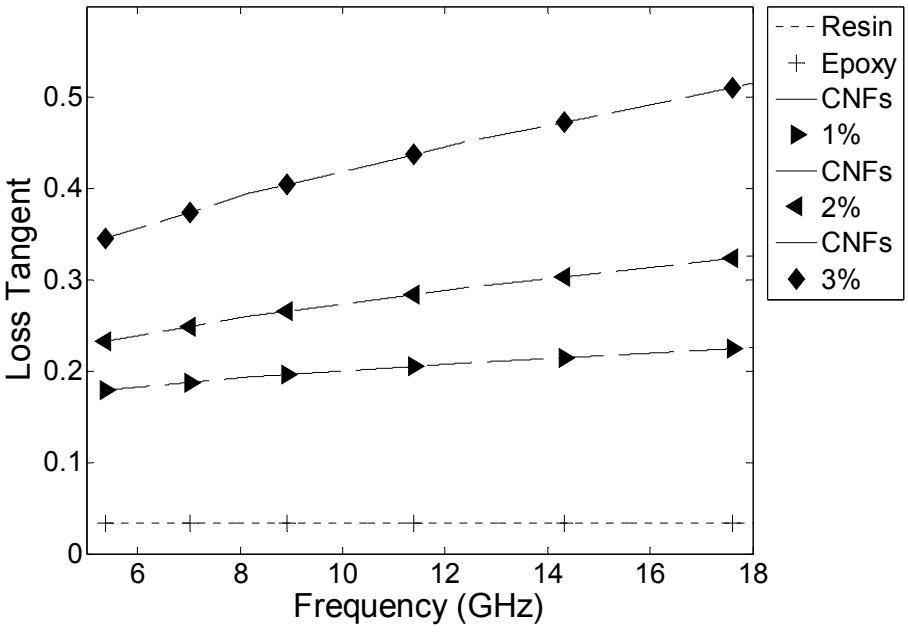

b)

Fig (3.6.4.2.1).
a) Loss Tangent MWCNTs composite materials,
b) Loss Tangent CNFs composite materials

3.7.3 Electric conductivity of manufactured composite materials

Microwave electric conductivity of a dielectric material can be evaluated by using the following equation [16]

$$\varepsilon_r'' = \frac{\sigma}{\omega\varepsilon_0} = \frac{\sigma}{2\pi f\varepsilon_0} \Rightarrow \sigma(S/m)) = 2\pi f\varepsilon_0\varepsilon''$$

(3.7.3.1)

where σ is the electric conductivity (S/m), ε_0 is the free space permittivity (8.854 × 1E-12 F/m), f is the frequency (Hz), ε'' is the imaginary component of permittivity.

In Fig. (3.7.3.1) electric conductivity as a function of frequency is reported for nanostructured composite materials.

In general, the electrical conductivity of nanopowders reinforced composite materials is due to several cause: *percolation, tunneling, capacitive,* and all of them contribute to permittivity values of nanostructure composite materials. As far as *percolation* is concerned, the high number of inter-nanostructure connections plays a role in ohmic resistivity reduction, this effect is trivially related to the concentration, and becomes dominant above the percolation threshold, when many conduction pathways cross the matrix thus forming electrical connections. This effect is also strongly dependant from morphology of carbon nanopowders hence CNTs and CNFs based composite materials have high electrical conductivity with respect to micro-graphite [16],[17]. *Capacitive effects* are explainable by thinking to the reinforced matrix as a network of nanocapacitors, where a single capacitor is constituted by two faced nanoparticles as in Fig.(3.7.3.2). The large nanoparticles specific surface area A compared to micro-sized powder results in effective capacitance C which can lowers-down the composite characteristic impedance, as stated from the fundamental capacitance impedance equation

$$Z_c = \frac{1}{j\omega C}$$

(3.7.3.2)

(where C ∝ A)

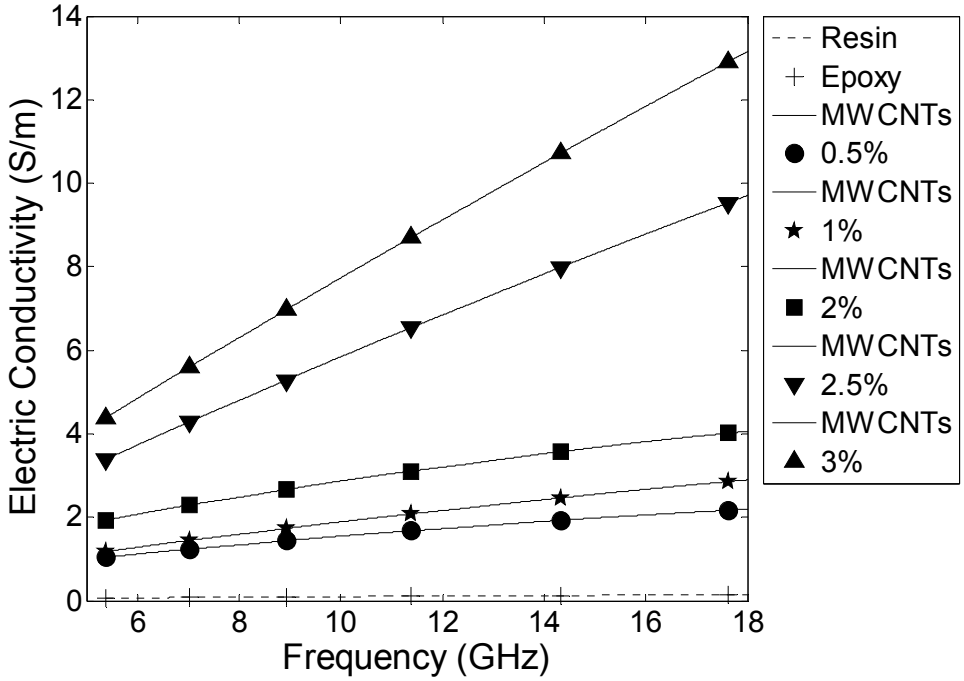

a)

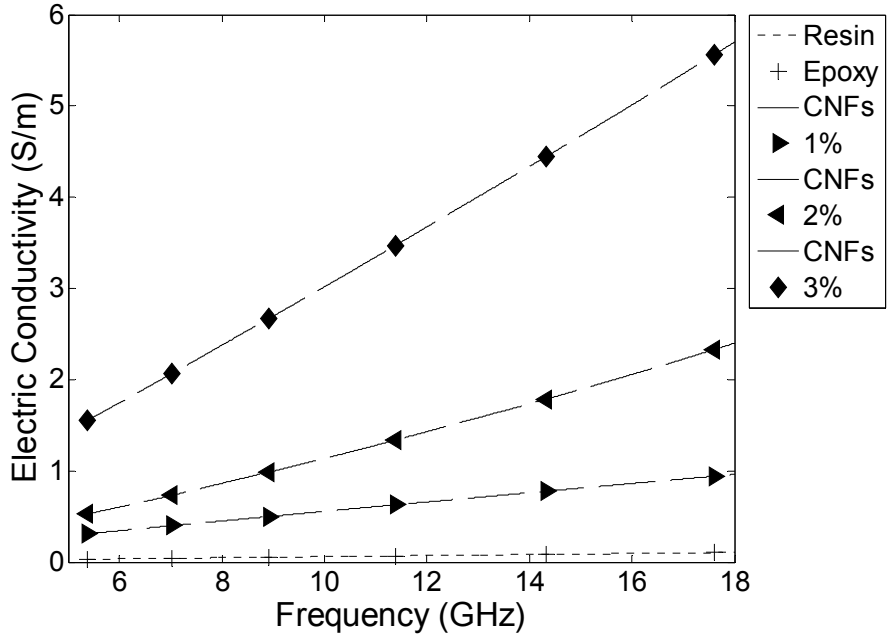

b)

Fig (3.7.3.1).

a) Electric Conductivity (S/m) of MWCNTs composite materials,

b) Electric Conductivity (S/m) of CNFs composite materials

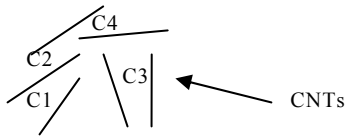

Fig.(3.7.3.2). Qualitative network of CNTs working as a network of nanocapacitors

The highest electrical conductivity is shown by MWCNTs 3wt%. Dependence of conductivity by morphology is currently under further investigation.

3.7.4 Microwave skin-depth of manufactured composite materials

The skin-depth [16], is a distance able to evaluates the ability of the electromagnetic field to propagate within a material. A Perfect Electric Conductor (PEC) has zero skin-depth, while for a good conductor like copper at microwave frequencies (10 GHz) this distance is of the order of 0.65 μm. The lower is the microwave electrical conductivity, the higher is the ability of the electromagnetic field to propagate and penetrate within the dielectric material. The skin-depth is a property which varies with the frequency of the applied wave. The relationship between frequency, electrical conductivity, magnetic permeability and skin-depth is

$$SkinDepth(mm) = 1000\frac{1}{\sqrt{\pi f \mu_0 \mu_r \sigma}}$$

(3.7.4.1)

where μ_0 is the permeability of free space (4π × 1E-7 H/m) and μ_r is the relative permeability of the material (adimensional) and σ is the electric conductivity (S/m).

The decline (i.e. attenuation) in field intensity versus depth is known as the skin effect: for high-conductivity materials the skin-depth estimates the distance over which the field intensity falls to *1/e* of its original value. Such property is valid for an electric conductor where the condition $\sigma >> 2\pi f \varepsilon_0 \varepsilon_r$ is verified, while is less strong for a dielectric material (i.e., at low microwave electrical conductivity); in any case the values obtained for the realized samples give an idea of the electromagnetic behavior of the composites materials under test. The values obtained show that skin-depth decreases at higher carbon powders wt% inclusions, and that in MWCNTs-based materials the electromagnetic field is strongly attenuated and consequently, the electromagnetic field decreases more rapidly.

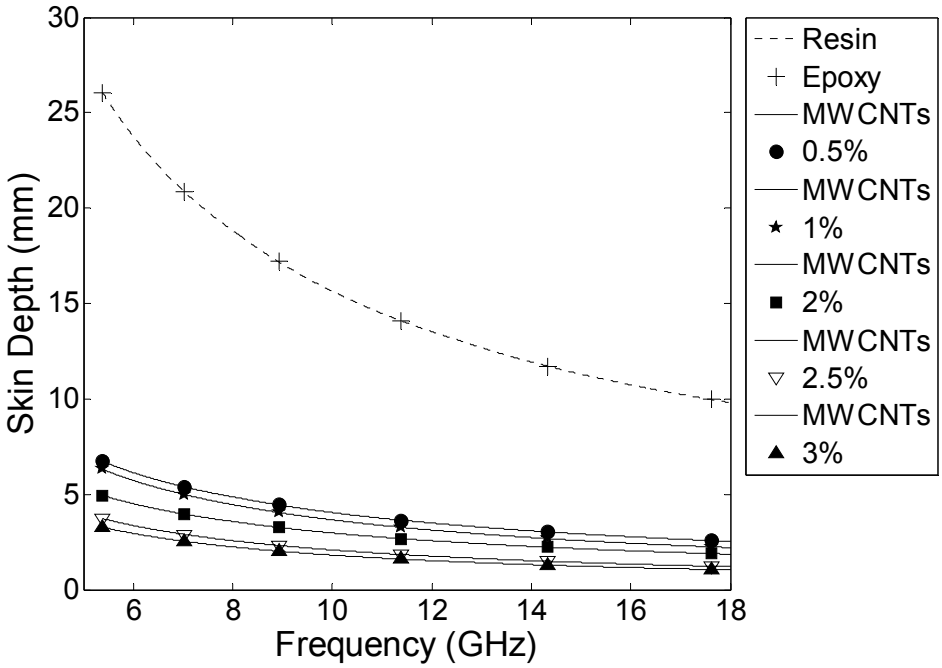

a)

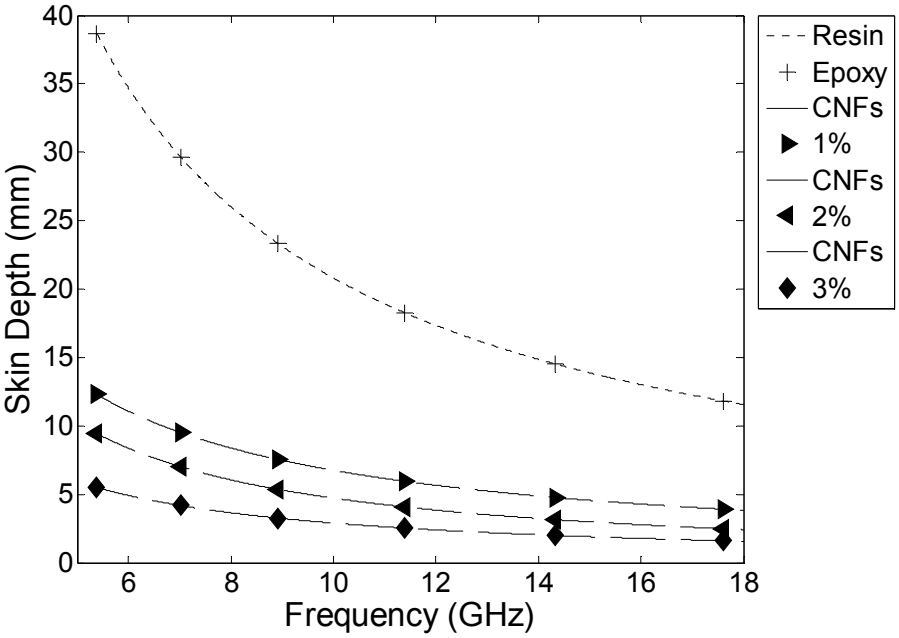

b)

Fig (3.6.4.4.1).

a) Skin Depth (mm) of MWCNTs composite materials,

b) Skin Depth (mm)of CNFs composite materials

3.7.5 Microwave loss factor of manufactured composite materials

As explained in section 3.6.1.2, if there were no losses, the sum of the squares of S_{11} and S_{21} should be equal to a unity (that is, the whole forward power is reflected and/or transmitted). On the contrary, if some loss of power is present this quantity is necessarily lower than unity, [3], [5], [16]. As a consequence, the difference between the normalized unitary forward power and the sum of the squares of the S_{11} and S_{21} represents the fractional loss of the forward power due to dielectric losses within the composite material.

$$LossFactor(\%) = 100 \times \left(1 - \left| S_{11} \right|^2 - \left| S_{21} \right|^2 \right)$$

(3.7.5.1)

In Tab.(3.7.5.1), Loss Factor of all composite materials measured using wave guide method is shown.

	Average LF(%)	Standard Deviation
Epoxyresin	18.68	6.55
MWCNTs_0.5wt%	61.83	5.01
MWCNTs_1wt%	60.14	5.92
MWCNTs_2wt%	59.43	5.45
MWCNTs_2.5wt%	50.62	4.94
MWCNTs_3wt%	51.13	5.59
CNFs_1wt%	47.22	4.88
CNFs_2wt%	51.35	8.89
CNFs_3wt%	53.27	5.29

Tab (3.7.5.1). Average and STD for LossFactor (%) of all composite materials

In Fig.(3.7.5.1), plot of Loss Factor is shown.

From electromagnetic propagation point of view, microwave absorbing mechanism is strongly related to microwave impedance matching condition within the waveguide adopted. Impedance matching condition in fact affects electromagnetic reflection coefficient. In general the higher the electrical conductivity of material the higher the reflection coefficient and the higher the reflected power too. The overall effect is a reduction of the absorbing ability of materials.

In order to understand what could happen if such materials were used in free space conditions instead of in waveguide, an analysis of microwave characteristic

impedance of carbon-based composite materials is presented in the next section and, computation of reflection coefficient of multilayer structure made of composite materials is performed.

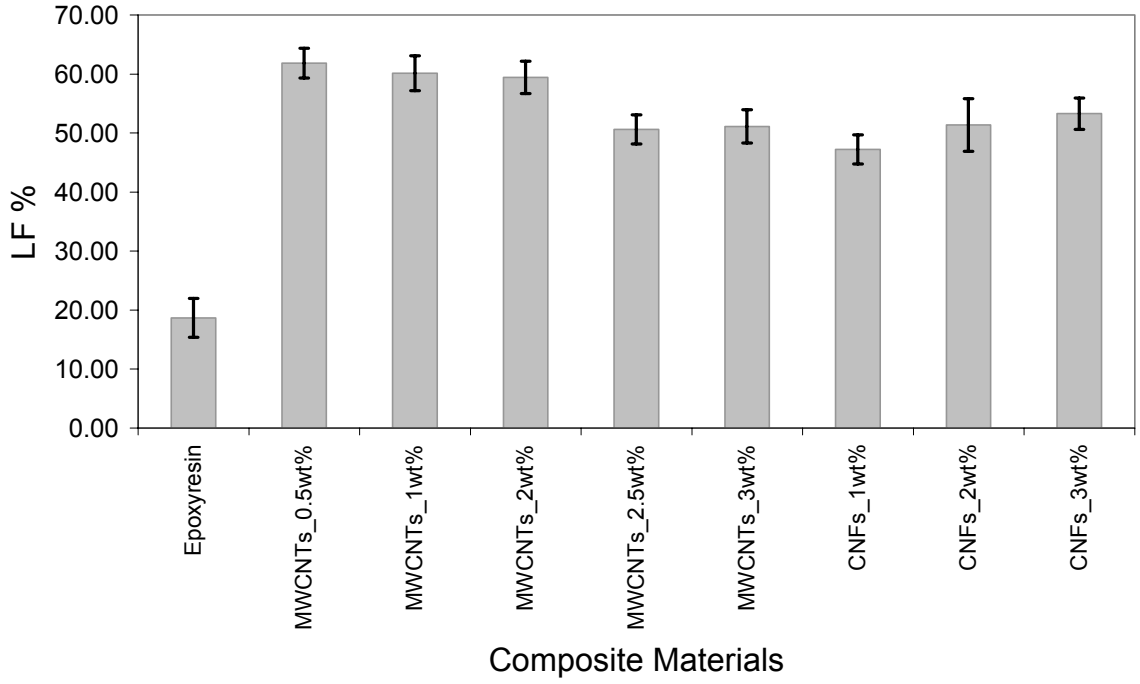

Fig (3.7.5.1). Average LossFactor (%) of composite materials with standard deviation within the frequency band 5.38-18 GHz

3.7.6 Electromagnetic intrinsic wave impedance of manufactured composite materials

From permittivity measurements results, the intrinsic wave impedances of materials have been computed using the following equation [3], [5], [16].

$$\eta_k = \sqrt{\frac{\mu_0}{\varepsilon_0}}\sqrt{\frac{\mu_{rk}}{\varepsilon_{rk}}} = \sqrt{\frac{\mu_0}{\varepsilon_0}}\sqrt{\frac{\mu_{rk}}{\varepsilon'_{rk} - j\varepsilon''_{rk}}}$$

(3.7.6.1)

where μ_{rk} is the relative permeability of the k-th composite material (equal to 1), ε_{rk} is the relative complex permittivity of k-th composite material as a function of frequency. Intrinsic wave impedances, is a complex number and its magnitude are shown in Fig. (3.7.6.1)

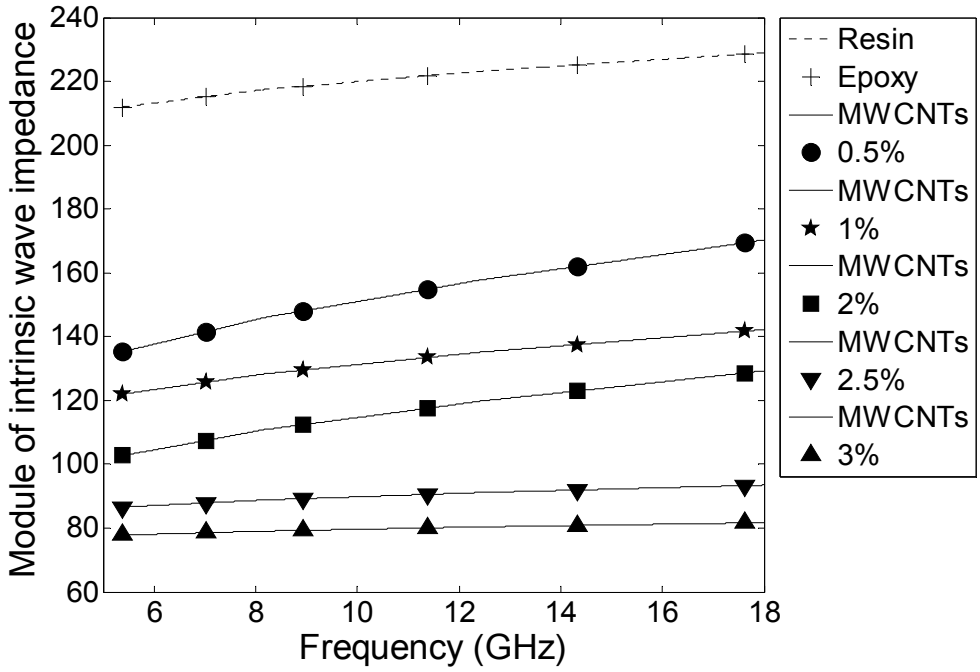

a)

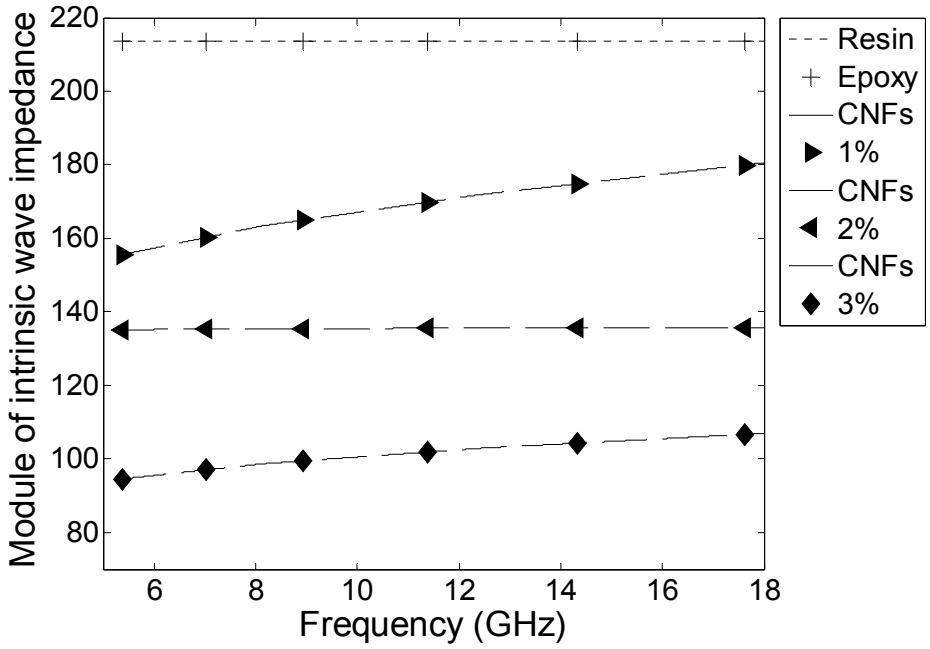

b)

Fig. (3.7.6.1).

a) Intrinsic wave impedance of nanostructured composite materials based on MWCNTs in the 5.3 to 18 GHz frequency band

b) Intrinsic wave impedance of nanostructured composite materials based on CNFs in the 5.3 to 18 GHz frequency band

Observing the intrinsic wave impedance plot, it is possible to notice that the higher the concentration of carbon nanopowders, the lower the intrinsic wave impedance of composite material. Also morphology plays a role as visible by the difference of

characteristic impedance between MWCNTs and CNFs based composite materials. As shown in [16], the wave impedance plays an important role in microwave reflection and absorbing properties of materials.

This principle is well exploited in pyramidal absorber made of lossy material in free-space applications. On the tip of the absorber the wave impedance is that of free-space ≅ 377 Ω and decreases down to that of intrinsic lossy material at the base of pyramids, Fig.(3.7.6.2). Consequently on the tip of absorber there is impedance matching condition and no back reflection of the electromagnetic wave takes place.

$$RC_{TIP} = \frac{\eta_{\text{pyramid}} - \eta_{\text{free-space}}}{\eta_{\text{pyramid}} + \eta_{\text{free-space}}} \cong \frac{\eta_{\text{pyramid}} - 377}{\eta_{\text{pyramid}} + 377} = \frac{377 - 377}{377 + 377} = 0$$

(3.7.6.2)

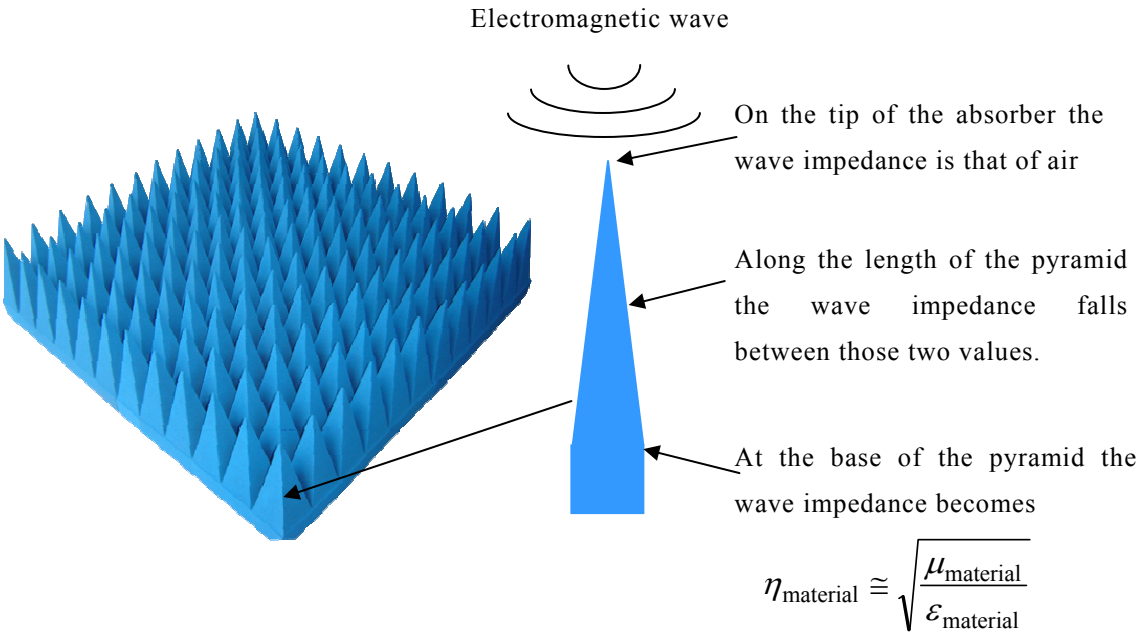

Fig.(3.7.6.2). Pyramidal absorber basic principle

Along the pyramids the impedance mismatching increases but, since materials are lossy then some energy is absorbed within the materials and converted into heat. As a consequence at the end, the amount of reflected power from pyramidal absorber results very low. In the next section absorbing effectiveness of materials, in free

space propagation condition is described in terms of impedance matching conditions and intrinsic losses of materials.

3.7.7 Microwave absorbing effectiveness of composite materials in free-space propagation conditions

The increasing demands of electromagnetic compatibility (EMC) for electronic device with different electromagnetic environment have greatly augmented the number of applications, which require electromagnetic interference (EMI) absorbing materials in frequency ranging from the kHz to GHz of micrometer and millimeter waves [18]. EMI Absorbing of materials depends on conductive materials. Rather than harnessing, capturing and grounding the EMI energy, absorber materials are designed to attenuate and absorb electromagnetic energy and convert the absorbed energy into heat. Absorber can be found in many different shape and structures, from thick pyramidal structures to single coatings and multilayer materials. This book is mainly focused in the design of EMI multilayer absorbers structures in empty space. Such structures are termed as free space absorber to distinguish form load absorbers which instead are used to absorb standing waves, which exist inside waveguides, coaxial lines, and other closed volume where microwave radiation exist.

The use of microwave absorbing materials in military applications dates back to the 1940s, spawned by the introducing of radar. With increased use of microwave electronics, such as electronic warfare (EW) systems, radar systems, identification friend- or – foe (IFF) systems, and radio frequency (RF) communication systems, EMI Interference become a mayor problem. The interference causes errors in targeting, reducing system efficiencies and limiting operating capabilities. Microwave absorbing materials are used to eliminate of reduce the EMI to manageable levels. The most known application of microwave absorbing materials is probably in stealth techniques. Such context renamed microwave absorbing materials in the most applied radar absorbing materials (RAM).

In designing absorber materials, the following equation can be used to evaluate how relative parameters affect the absorbing capability of the material [18]

$$A = \frac{1}{2}\sigma E^2 + \frac{1}{2}\omega\varepsilon_0\varepsilon_r E^2 + \frac{1}{2}\omega\mu_0\mu_r H^2$$

(3.7.7.1)

where A(W/m^3) is the electromagnetic energy absorbed per unit volume; E(V/m) is the electric field strength of the forward electromagnetic radiation; H(A/m) is the magnetic field strength of the forward radiation; σ(S/m) is the conductivity of the material; ω(sec^{-1}) is the angular speed of the electromagnetic wave, ε_0 is the dielectric permittivity of vacuum (8.854×10^{-12} F/m), ε_r is the complex permittivity of the material; μ_0 is the magnetic permeability of the vacuum (1.2566×10^{-6} A/m); μ_r is the complex permeability of material.

From equation (3.7.7.1), attenuation and absorbing of microwave energy in absorber materials basically rely on the conductivity, dielectric loss, and/or magnetic loss of absorber material. Specifically, microwave absorbers use dielectric loss to absorb the electric field portion of an electromagnetic wave, using carbon and other electrically conductive particles in many cases as filler to create the proper complex permittivity. On the other hand, microwave absorbers employ magnetic loss by filling with magnetic filler like irons and ferrites.

There are three conditions able to minimize the EMI reflection from a surface here after the explanation. When an electromagnetic wave, propagating through a free space with impedance of Z_0, happens upon a semi-infinite dielectric material boundary of impedance Z_i, a partial reflection occurs. The reflection coefficient (dB), at the interface can be expressed as [16]

$$RC(f) = 20Log_{10}\left|\frac{(Z_i - Z_0)}{Z_i + Z_0}\right|$$

(3.7.7.2)

Where:

RC = Reflection Coefficient (dB);

$Z_0 \cong 377$ (Ω) is the free space impedance;

Z_i=Input impedance at the Free space -Absorber interface;

f = frequency (Hz).

The reflection coefficient falls to -∞ when $Z_i = Z_0$, or, in other words, the composite material structure is impedance matched to the forward medium.

In order to understand the absorbing behavior of materials we report an example based on materials built using Graphite and CNTs.

Let us to suppose an electromagnetic field normally forward on a single layer of carbon composite based material backed with a PEC (Perfect Electric Conductor) plate, see Fig.(3.7.7.1). In order to neglect border effect, we assume transversal layer dimensions unlimited. Under these hypotheses we can use the transmission line theory in order to find the microwave reflection coefficient (RC), at the Air-composite material layer interface. The electromagnetic wave absorbing property, usually, can be estimated by the (3.7.7.2):

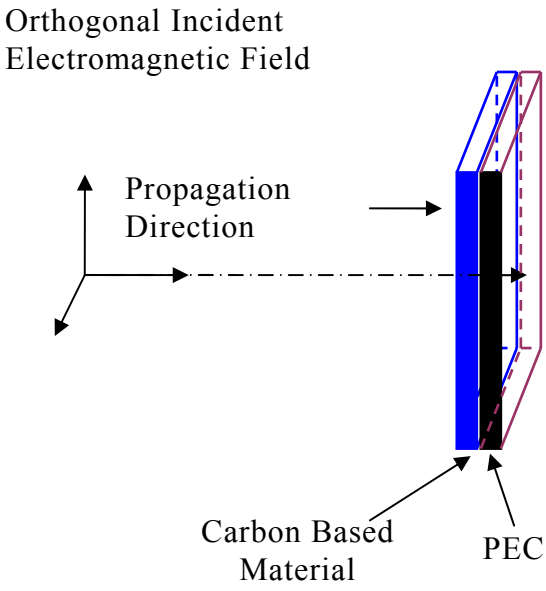

Fig. (3.7.7.1). Single microwave absorption Layer structure

The input impedance at the Free space-Absorber interface can be expressed as [16]:

$$Z_i(f) = \eta_k \frac{Z_L \cos(\beta t) + j\eta_k \sin(\beta t)}{\eta_k \cos(\beta t) + jZ_L \sin(\beta t)}$$

(3.7.7.3)

Where:

t, is *thickness* (m) of the layer absorber made of carbon composite material.

β_κ, is the *wave number*

$$\beta_k(f) = 2\pi f \sqrt{\mu_0 \varepsilon_0} \sqrt{\mu_{rk} \varepsilon_{rk}} = \\ = 2\pi f \sqrt{\mu_0 \varepsilon_0} \sqrt{\mu_{rk}(\varepsilon'_k - j\varepsilon''_k)}$$

(3.7.7.4)

η, is The *intrinsic wave impedance* of composite materials which in turns depends on dielectric parameters which in turn are function of frequency *f*:

$$\eta_k(f) = \sqrt{\frac{\mu_0}{\varepsilon_0}} \sqrt{\frac{\mu_{rk}}{\varepsilon_{rk}}} = \sqrt{\frac{\mu_0}{\varepsilon_0}} \sqrt{\frac{\mu_{rk}}{\varepsilon'_k - j\varepsilon''}}$$

(3.7.7.5)

f, is *frequency* (Hz) of the forward electromagnetic wave;

ε' is layer relative real part of *permittivity*;

ε'' is layer relative imaginary part of *permittivity*;

The equivalent electric circuit is shown in Fig.(3.7.7.2).

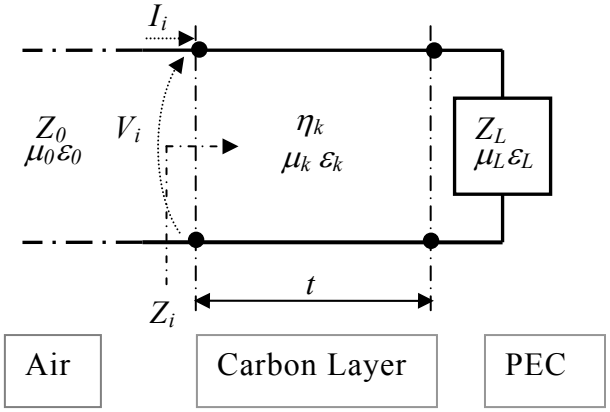

Fig.(3.7.7.2). Equivalent electric circuit of microwave absorbing layer.

Where:

$Z_0 \cong 377$ (Ω) (Air impedance assumed like that of free space)

$Z_L \cong 0$ (Ω) (PEC Load Impedance)

Z_i=wave impedance at the Air-Absorber interface (Ω)

I_i = input current related to magnetic field (A)

V_i= input voltage related to electric field (V)

η_k = Characteristic Carbon Composite material wave Impedance (Ω)

The absorbing capability of a certain dielectric material is mainly due to: "*dielectric losses*" within the composite material and "*impedance matching condition*" which in turns is a function of "thickness" of the absorbing layer.

Dielectric losses are mainly function of the imaginary part of the permittivity (ε'') while, length of the material is connected to the microwave wavelength within the material. From the Eq.(3.7.7.3) which express the impedance Z_i at the free space-layer interface, its possible to observe that for certain multiple values of quantity (βt), the imaginary part of Z_i goes to zero. When this happen, if the real part of Z_i is close to Z_0, then the *impedance matching condition* is verified and the RC quantity become null (i.e. $\rightarrow$ -∞ (dB)). Since (βt) depends from frequency, permittivity and thickness then, there will be some combinations and also periodic values of such parameters for which the impedance matching condition is close to be verified. In particular when the thickness t of the material is an odd multiple of the composite quarter wavelength, the forward and reflected waves at the air-absorber interface are out of phase 180°. As a result the reflected waves in the air-absorber interface are cancelled

$$t = n\frac{\lambda_{composite}}{4} \quad (m) \quad (\text{with} \quad n = 1,3,5,.....)$$

$$\lambda_{composite} = \frac{\lambda_0}{\left[\left|\mu_r\right|\left|\varepsilon_r\right|\right]^{1/2}} \quad (m)$$

$$\lambda_0 = \frac{c}{f} \cong \frac{3 \cdot 10^8}{f} \quad (m)$$

(3.7.7.6)

In Fig.(3.7.7.3) and (3.7.7.4),an example where t=9.7mm is presented. Here the considered composite materials are made with graphite and SWCNTs already

characterized in the [16]. We can observe that around frequency f=10 GHz, the absorbing structure made with PEC and SWCNTs 3wt%, presents a Z_i where the real part is about 300 Ω while the imaginary part is 0. This is a combination of composite material where for such values of thickness t and frequency f, the value of Z_i goes close to Z_0 (free space ≅377Ω); graphite as an example has different values. According to the electromagnetic wave theory, when an electromagnetic wave propagates across on absorber, then Z_i must be equal to Z_0 for zero reflection. In our computations we take into account both: impedance matching condition and dielectric losses of composite material, these last, by using the imaginary part of the permittivity (ε").

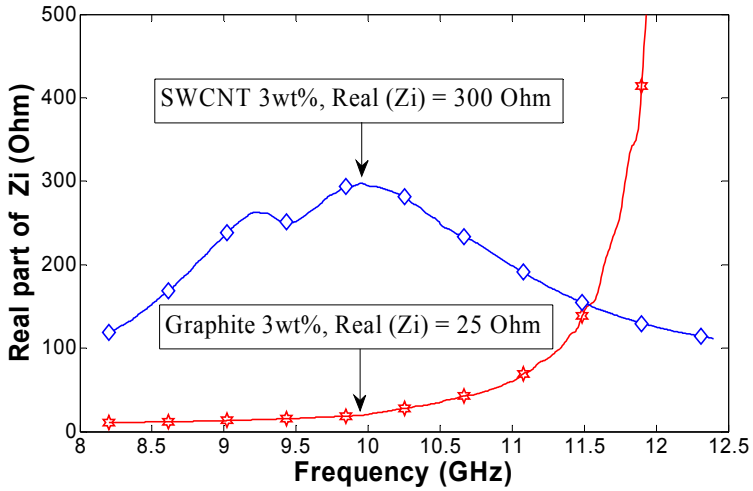

Fig.(3.7.7.3). Real part of the input impedance at Air-Absorber interface (Z_i), when sample length is 9.7 mm.

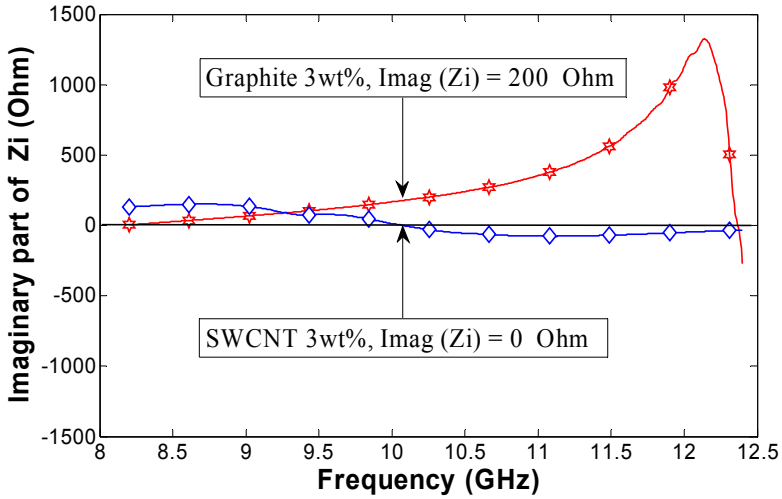

Fig.(3.7.7.4). Imaginary part of the input impedance at Air-Absorber interface (Z_i), when sample length is 9.7 mm

In Fig.(3.7.7.5) we can observe that the negative peak of reflection coefficient reach -19 dB and the filtering band is cantered around 10 GHz which is the same frequency where the impedance $Z_i \cong 300\ \Omega$.

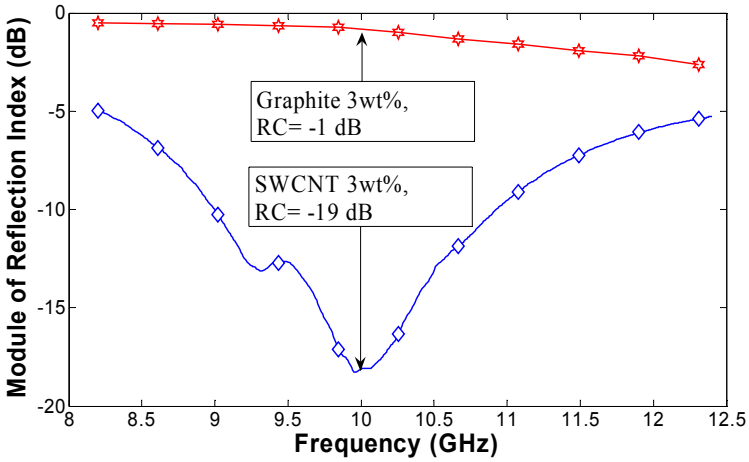

Fig.(3.7.7.5) Module of Reflection Coefficient when sample length is 9.7 mm.

Therefore, the absorbing material must be lossy (*second condition*), so that the EMI energy can be dissipated within the material and impedance matched (*first condition*), so that the forward electromagnetic wave is not reflected back being allowed to go and dissipated through material.

In order to get a large amount of attenuation, values of permeability and/or permittivity should be large; this condition could imply low values of intrinsic impedance and as a consequence large values of RC(dB). As a consequence, design of an absorber is a tradeoff between the front-face reflection coefficient and the losses per unit thickness. *One method to search the best tradeoff within the largest frequency band is the multilayer structure. Here the optimization of material of each layer and its related thickness play an important role in absorbing maximization.*

Some of these structures are characterized by a surface impedance Z_i, close as much as possible to free-space impedance (~377Ω), and then changing their intrinsic impedance inside, by gradually increasing their conductivity. This lower down the reflection coefficient at the boundary of each layer and allow the materials to convert the EMI energy into Joule heating for dissipating.

The *third condition* to obtain an absorber can be easily understood rewriting equation of reflection coefficient:

$$RC(f) = 20Log_{10}\left|\frac{(Z_i - Z_0)}{Z_i + Z_0}\right| = 20Log_{10}\left|\frac{\left(\frac{Z_i}{Z_0} - 1\right)}{\left(\frac{Z_i}{Z_0} + 1\right)}\right|$$

(3.6.6.7)

$$if \quad \mu_{rk} = \varepsilon_{rk} \quad \Rightarrow \quad \frac{Z_i}{Z_0} = \frac{\sqrt{\frac{\mu_0}{\varepsilon_0}}\sqrt{\frac{\mu_{rk}}{\varepsilon_{rk}}}}{\sqrt{\frac{\mu_0}{\varepsilon_0}}} = \sqrt{\frac{\mu_{rk}}{\varepsilon_{rk}}} = 1 \quad \Rightarrow \quad RC(dB) \to -\infty$$

(3.6.6.8)

In other words when *relative permittivity is close to relative permeability* the intrinsic impedance of material become close to free space impedance (377Ω) and reflection of electromagnetic wave tend to zero.

There are a variety of absorbers but they can be classified into two basic types of structures and materials: resonant or graded dielectric or both of them.

In the next chapter algorithms and absorbers design method are deeply analyzed.

3.8 Conclusion

In this chapter electromagnetic characterization of manufactured composite materials shown in chapter 2 has been performed.

Measurements of dielectric properties have been conducted using waveguide method.

Meanings of permittivity and electrical conductivity have been explored end has been observed that conductivity of materials is not the only requirement able to enhance the absorption properties. In fact has been concluded that electromagnetic impedance matching is the other fundamental condition needed to lower down the reflection coefficient and to further increase the electromagnetic absorption properties of composite material.

3.9 Reference Table

[1] Paolo Chiorboli, “Fondamenti di Chimica”, *UTET*, ISBN-13: 9788802039442 ,1987

[2] Sophocles J.Orfanidis, "Electromagnetic wave and Antennas"

[3] John R.Whinnery, Theodore Van Duzer. “Fields and Waves in Communication Electronics”, Thirth Edition, *John Wiley & Sons* pp 682, U.S.A 1993.

[4] J.d.Jackson, “Classical Electrodynamics”, 2nd ed., p. 311, *Wiley*, New York, 1975

[5] Davide Pozar, "Microwave Engineering" third edition, *A JOHN WILEY & SONS, INC., PUBLICATION*

[6] *Rohde & Schwarz* application note on “Measurement of dielectric material properties”, Rohde & SchwarzApplicationCenter Asia/Pacific2006

[7] Technical Overview, Agilent 85071E Materials Measurement Software, Agilent literature number 5989-0222EN, November 6, 2003

[8] .

[9] L. F. Chen, C. K. Ong and C. P. Neo. “Measurement and Materials Characterization” *National University of Singapore*. 2007.

[10] Baker-Jarvis et al. 1993, 1990; Baker-Jarvis, “Transmission/Reflection and Short-Circuit Line Permittivity Measurements”, *NIST tech note*, 1990.

[11] Nicolson, A. M. and Ross, G. "Measurement of the intrinsic properties of materials by time domain techniques*," IEEE Trans*. Instrum. hIeas.,vol.IM-19, pp.377-382, November 1970.

[12] Weir, JV. B. "Automatic measurement of complex dielectric constant and permeability at microwave frequencies," *Proc. IEEE,* vo1.62, pp.33- 36, January 1974.

[13] W. E. Milne, “Numerical Calculus”. *Princeton Univ*. ed. New York: Wiley, 1953, ch. 8. Press, 1949, ch. IV.

[14] Abdel-Hakim Boughriet, “Noniterative Stable Transmission/Reflection Method for Low-Loss Material Complex Permittivity Determination”.

[15] Davide Micheli, Roberto Pastore,Carmelo Apollo, Mario Marchetti, Gabriele Gradoni, Franco Moglie, Valter Mariani Primiani, “Carbon Based Nanomaterial Composites in RAM and Microwave Shielding Applications”, *Proc. IEEE Nano*. June 2009 Genova.

[16] D. Micheli *, C. Apollo, R. Pastore, M. Marchetti, “X-Band microwave characterization of carbon-based nanocomposite material, absorbing capability comparison and RAS design simulation”, *Composites Science and Technology 70 (2010) 400–409, Elsevier Ltd*, 2010.

[17] Davide Micheli, Carmelo Apollo, Roberto Pastore, Ramon Bueno Morles, Gabriele Gradoni and Mario Marchetti, "Nanocomposite Materials, Theory and Applications", ISBN 978-953-7619-X-X. *INTECH open publisher*, 2010.

[18] Xingcun Colin Tong, “Advanced Materials and Design for Electromagnetic Interference Shielding”, *CRC press*, 2009

Chapter 4

Numerical Design and Optimization of Microwave Multilayer absorbers

4.1 Introduction

This chapter describes the followed to design and optimize the electromagnetic absorber multilayer structures. First the design and optimization problem is introduced and the electromagnetic model of absorber described, then the most popular heuristic algorithms like genetic algorithm (GA), particle swarm optimization (PSO), and the new here proposed, winning particle optimization (WPO) method, are analyzed and applied for the numerical design of the electromagnetic absorber, here more often called microwave absorber due to the frequency band in the range 5-18 GHz. Design method and electromagnetic model of absorber are still valid for electromagnetic wave spectrum ranging up to optical frequency.

Two kinds of structures are taken into account; one explicitly required in microwave absorbing materials, the other most often adopted in electromagnetic compatibility problems.

The first commonly called radar absorbing materials (RAM) are mostly known for its applications in stealth fighters and anechoic chambers; the second is developed for enhanced shielding applications where requirements are simultaneously both: electromagnetic interference (EMI) shielding and absorbing capability of materials, i.e. interference suppression by absorbing of materials.

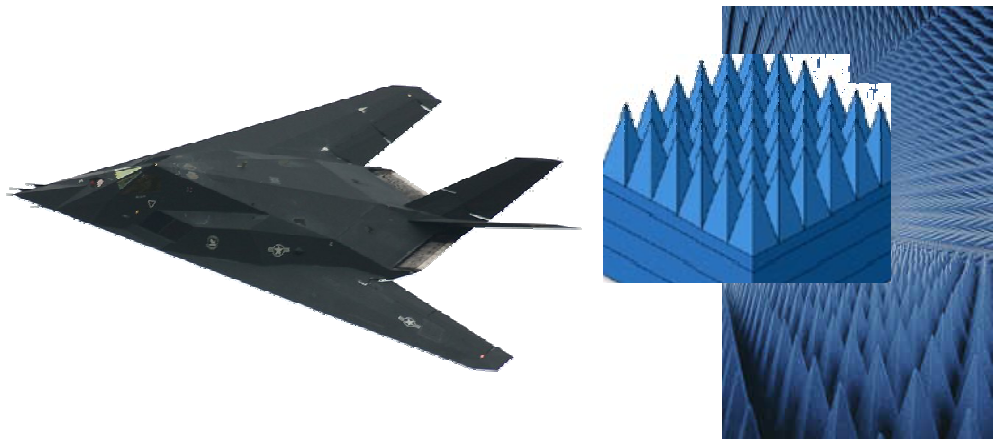

Fig.(4.1.1). On the left RAM is used for stealthness application, on the right in anechoic chamber

The use of such structures is relevant in aerospace/aeronautics, for EM protection from natural phenomena (lightning), and intentional interference with radar

absorbing materials (RAM) [1], [2], [3], in nuclear physics, for shields adopted in particle accelerators [4], and for nuclear EM pulses (NEMP) protection [5], in electromagnetic compatibility (EMC), for equipment-level shielding [6], [7], high-intensity radiated fields (HIRF) protection [3], anechoic chambers (for the realizations of wedges and pyramidal arrays) [8], and human exposure mitigation [9].
Nature of filling media plays a central role in achieving best absorbing performances. When dealing with composite aggregates, electromagnetic properties of final materials are mainly given by electrical features of filling particles, which could also exhibit several different properties such as isotropic, anisotropic or bi-anisotropic behavior, as well as chiral or non-reciprocal behaviors. Traditional composites are loaded by graphene/graphite micrometric mixtures, able to absorb good fraction of EM energy upon a few millimeters to a centimeter of thickness – e.g., -11 dB of reflection coefficient at 1 GHz for a 5.5 mm nickel-zinc panel [10]. More recently, particular carbon based reinforced composites have been proposed to improve performances of traditional materials reducing the overall multilayer thickness – e.g., -20 dB of reflection coefficient in the range 9-18 GHz for a 5.5 mm panel [11].
In this work, we propose an inhomogeneous multilayer absorber nanometric carbon particles (MWCNTs, CNFs, at different wt%). Thus, an improvement of the traditional absorbers (graphite based), has been achieved upon optimization through an in-house genetic algorithm (GA), an in-house Particle Swarm optimization (PSO), and an in-house Winning Particle Optimization (WPO), this last proposed as new evolutionary algorithm. Main goal of the work is to achieve lower values (< -10 dB) of both reflection and transmission coefficients for angular apertures within 40°.

As far as electromagnetic shielding is concerned, the most common type of EMI occurs in the radio frequency (RF) range of the electromagnetic (EM) spectrum, from 10^4 to 10^{12} Hertz. This energy can be radiated by computer circuits, radio transmitters, fluorescent lamps, electric motors, overhead power lines, lightning, and many other sources.
Device failures caused by interference—or "noise"—from electromagnetic energy are increasing due to the growing number of products that contain sensitive electronic components. The smaller size and faster operating speeds of these components make it more difficult to manage the EM pollution they create. Increased devices

frequencies (applications over 10 GHz are now common) cause proportionally decreased wavelengths that can penetrate very small openings in housings and containers.

Increasingly strict regulations address product's emissions. At the same time, product's immunity to external EMI determines its commercial success or failure. To comply with regulations on both emissions and immunity (or susceptibility), designers and manufacturers integrate shielding in their product designs through a working knowledge of EMI behavior and shielding techniques.

Electromagnetic Interference (EMI), defined by NATO as an electromagnetic disturbance which interrupts, obstructs, or otherwise degrades the effective performance of electronic or electrical equipment.(www.glenair.com/html/emi.htm).

Electromagnetic interference can jam sensitive equipment, burn out electric circuits, and even prompt explosions. This is why drivers are directed to turn off car radios when travelling through mining areas where electronically controlled blasting is under way. In aircraft, EMI can affect everything from fly-by-wire flight control systems to a cockpit fuel gauge and in extreme cases put a plane into an uncommanded drive or shut down a critical avionic system.

Fig.(4.1.2). On the left EMI-Shielding Gasket holds up in severe environments, on the right interference during landing phase and war scenario

Historically, EMI has been a factor in aircraft construction since the 1930's when brass conduit was first used to shield cabling for newly introduced electronic communication systems from reciprocating engines and magneto ignitions. But such man-made electromagnetic "noise" generated forwardly by motors, generators, and other machinery turned out to be just one of the classes of EMI which would affect the safe operation of aircraft.

Naturally occurring radio noise originating from atmospheric disturbances (including lightning) and extraterrestrial sources (such as sunspots) can also degrade the performance of electronic equipment. Communications signals may also interfere with the operation of sensitive electronic equipment. To protect avionics systems from this class of interference, intentional radio frequency (RF) emitters like CB radios, remote-controlled toys, and walkie-talkies are banned outright on commercial airline flights. Most, but not all, airlines extend the ban to portable radios and television receivers.

a) b) c) c)

Fig.(4.1.3). a) internal shielding of a cellular phone which simultaneously generates interference and is affected by EMI problems, b) radiation and interference due to several antennas in modern telecommunication systems, c) interferences and strong electromagnetic phenomena due to lightening, d) geomagnetic storm due to solar flare can produce strong disturbances in the space around the earth and on the earth surface badly affecting all electric and telecommunication equipments like energy transportation and telecommunication devices.

Personal Electronic Devices (PED) such as laptop computers, hand held scanners, mobile phones and game players, while not intentional emitters, can produce signals in the 1MHz- 2GHz range and can therefore affect the performance of avionic equipment. As navigation cabling and other critical wiring runs along the fuselage inside the aircraft skin, it's no wonder that passengers sitting just a few feet away are warned about the indiscriminate use of such devices. Since the thin sheet of dielectric material that forms the inside of the passenger compartment - typically fiberglass - offers no shielding whatsoever; and since commercial passenger jets contain up to 150 miles of electrical wiring, it is extremely important for passengers to heed regulations on the use of disruptive electronic equipment.

Obviously, such internal sources of EMI are particularly dangerous to aircraft because they are so close to the systems they might affect. But external sources, such

as radio and radar transmitters on the ground, or radar from a passing military plane, can be even more disruptive due to the high power and frequency of such equipment. High frequency "E" (electrical) fields generated by high power systems such as avionic radars and missile targeting systems can cause interference at extreme distances.

As if the many external and internal sources of EMI were not enough of a concern, a major EMI co-conspirator in aircraft is the aluminum airframe itself, which in certain circumstances can act as a resonant cavity, or a phased array. Behaving much like a satellite dish, the airframe can compound the effects of both internal and external EMI by concentrating transient signals and broadcasting the interference into nearby equipment.

By the early 1960's, interference problems had broadened to encompass the entire electromagnetic spectrum. And the phrase "EMI" was coined to describe electromagnetic interference in its broadest sense. Practically speaking, all emitters, receptors and frequency bands are thus part of the EMI definition. Consequently, such diverse problems as interference from ground loops, mismatched impedance paths, direct magnetic/electric field coupling (AC Hum), electrostatic discharge (ESD), and power line conducted emissions and radiated emissions from other such sources all fall under the umbrella of EMI.

In scientific circles, the terms "electromagnetic compatibility" and "electromagnetic interference" are used almost interchangeably: EMC simply describes efforts to control or eliminate the problems created by EMI.

For commercial electronic and electrical equipment the Federal Communications Commission (FCC) has regulations defining allowable emission and susceptibility levels. Military equipment is regulated by **MIL-STD-461** and **MIL-STD-462** (refs 4-10 and 4-11). MIL-STD-461 defines allowable emission levels, both conducted and radiated, and allowable susceptibilities, both conducted and radiated.

Radio Frequency Interference (RFI) is a special class of EMI in which radio frequency transmissions (usually narrow-band) cause unintentional problems in equipment operation. Radio frequency interference can originate from a wide range of sources, but precautionary measures generally focus on man-made sources including 2-way radios, pagers, mobile phones, and emergency and public safety communications systems. Power lines, transformers, medical equipment,

electromechanical switches and many others unintentional emitters also produce RF energy. In common (unshielded) communications systems, RFI can degrade or completely disrupt signal quality, overall system performance, and system carrying capacity. In worst case scenarios, RFI can render an electronic system completely nonfunctional.

A recent forward on a commercial passenger plane illustrates the power of even low frequency RFI to disrupt avionic systems. In January 1993, on a flight from Denver, Colorado, to Newark, NJ, an aircraft lost all directional gyros (electromechanical devices that indicate orientation) at cruise altitude. The captain instructed the flight attendant to go through the cabin and tell all passengers to turn off their electronic devices. She reported back that about 25 passengers with portable radios had been listening to a Denver Broncos playoff game and that one passenger was also using a lap top computer. Within two minutes of the Captain's request to turn the radios off, the gyros had swung back to their correct heading. Later in the flight, several Bronco fans covertly resumed their use of the portable radios, and again the directional gyros began to malfunction. The radios were then confiscated and no further problems were experienced on the flight.

HIRF, or High Intensity Radiated Emissions (also known as High Intensity Radio Emissions) refers to emissions from radar, microwave, radio, and television transmitters, high power AM/FM radio broadcast systems, TV transmitters and other powerful communications systems. Recently, a great deal of public interest has centered on HIRF as a possible cause for the crash of TWA Flight 800, which apparently was in the proximity of a number of naval ships when it inexplicably crashed.

Whether or not HIRF from the navy ships was the cause of the crash, the FAA issued a Flight Standards Bulletin about the problem of High Intensity Radiated Fields. The bulletin states that high powered electromagnetic interference can potentially lead to disruptions in airplane navigation and communication systems and to "loss of aircraft and life."

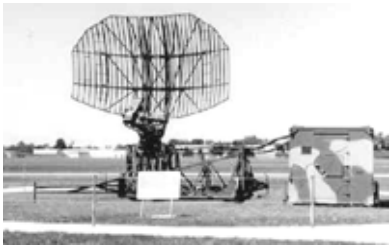

Fig.(4.1.4). High Intensity Radiated Emissions, such as those induced by radar and microwave relay stations can lead to disruptions in navigation and communication systems.

Whether or not HIRF from the navy ships was the cause of the crash, the FAA issued a Flight Standards Bulletin about the problem of High Intensity Radiated Fields. The bulletin states that high powered electromagnetic interference can potentially lead to disruptions in airplane navigation and communication systems and to "loss of aircraft and life."

TEMPEST is an acronym for Transient Electromagnetic Pulse Emanation Standard. It is both a specification for computerized equipment as well as a term used to describe the process for preventing compromising emanations from electronic equipment. The fact that computers, printers, and electronic typewriters give off electromagnetic emanations has long been a concern of the US Government. A hacker using off-the-shelf equipment could potentially monitor and retrieve classified or sensitive information as it is being processed without the user being aware that a loss is occurring. To counter this vulnerability, the US Government has long required that electronic equipment used for classified processing be shielded to reduce or eliminate transient emanations. This is typically done by shielding the device (or sometimes a room or entire building) with copper or other conductive materials.

4.1.1 EMI Management

Effective shielding of avionic devices must anticipate both "radiated susceptibility" (the degree to which outside interference affects the reliable functioning of equipment) and "radiated emissions" (the extent to which the device itself creates electromagnetic waves which can affect its function). In both cases, the techniques for managing the interference include reflecting the signals outright, reducing entry points in equipment and cable shields, absorbing the interference in permeable material and dissipating it as heat, or conducting the EMI along the skin of the device/cable and taking it to ground.

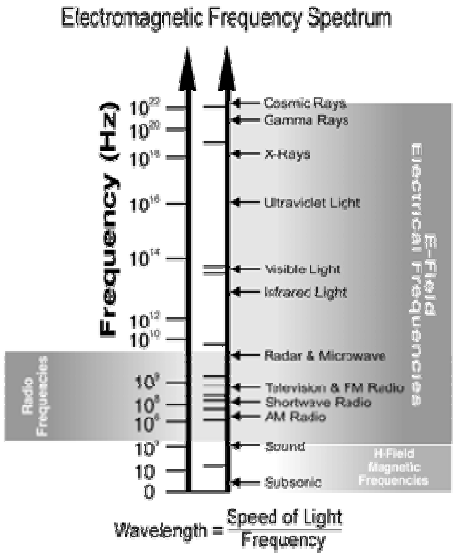

Fig.(4.1.1.1). Electromagnetic frequency spectrum

In practical terms, EMI management is accomplished by plating the skins of cases and cable shields, building up the density (thickness) of shield material, or eliminating line-of-sight entry points through which electromagnetic waves can penetrate or escape.

The frequency of the interfering signal is a critical concern when designing an effective shielding solution. Low frequency magnetic waves in the 1 to 30 Khz range, for example, are most effectively shielded by absorbing the signals in permeable material. High frequency signals (30 KHz and above) are most effectively shielded by reducing entry windows and by insuring adequate surface conductivity to ground.

In general frequency and distance of interference source strong affect the design of shielding system.

In this book far field sources are mainly considered and all subsequent considerations are referred to such kind of electromagnetic sources.

4.2 Electromagnetic model of multilayer absorber

In RAM applications, reflection coefficient (RC) at the first air-multilayer interface can been used as the main objective function (OF) which need to be reduced using numerical optimization techniques, whereas in shielding ones the most stringent requirement considered is the transmission coefficient (TC) lowering. The multilayer

absorbing is a key feature in shielding applications too, because of evident protection constraints, so it has been quantified through the so-called 'loss factor' (*LF%*), defined as [12]:

$$LF\% = \left(1 - |RC|^2 - |TC|^2\right) \cdot 100 \tag{4.2.1}$$

where:
RC is the Reflection Coefficient expressed in the linear form.
TC is the Transmission Coefficient expressed in the linear form.

Its physical meaning is related to the fraction of the forward power vanishing inside the materials due to localization and dissipation phenomena. Since the calculation of *RC* and *TC* becomes a crucial point for the optimization goal, a rigorous approach to relate transmitted and reflected waves to the forward one inside each layer has been adopted. In particular, such theoretical model relies on the *forward/backward propagation matrix* formalism introduced in chapter one, accounting for each single interface effect on the local field crossing. Both normal and oblique incidences have been evaluated during the automatic optimization. In the following text a detailed application of mathematical model of multilayer absorber introduced in chapter one is made.

Numerical optimization requires fixing for some boundary conditions related to the dimensions of the multilayer structure adopted as absorbing model [13]. For all presented absorbers, thickness of each layer can range from 0 up to 6.3 mm with step of 0.1mm for GA which works with binary chromosomes, and from 0 up to 6.3 mm with no discontinuities for PSO [14] and WPO [15] which instead work with real numbers. Number of layers of absorbers is upper-limited to maximum ten layers. The effective number of layers is established each time by the numerical optimization procedure which is able to remove one or more layers of the multilayer structure. Multilayer configuration structures are depicted in Fig. (4.2.1).

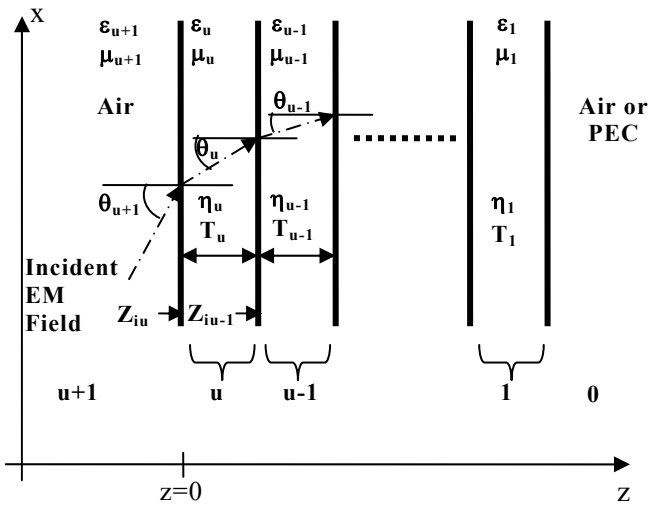

Fig. 4.2.1. General Multilayer scheme.

It could be noticed that last layer could be air (i.e. free space in this context), or a perfect electric conductor (PEC) as a function of the absorber we are interested to optimize. Usually in typically RAM application PEC is applied since is assumed that such absorber need to be applied like a coating on an existing metal based structure like an airplane or a boat. On the contrary in shielding application air usually is assumed to be the media surrounding the absorber.

The design algorithm needs to be capable not only to choose the number of layers and their thickness but the material type too. In other words in the multilayer structure, layers order is not *a priori* fixed but numerical techniques decides completely all layers parameters, from layers number and layer thicknesses up to best material which must be chosen for each layer of the multilayer structure.

In RAM applications, *RC* at the air-absorber interface can be evaluated in two main ways: adopting the classic formulation for the transmission lines or using the matrix formulation introduced in chapter one. In shielding applications instead the matrix formulation must necessarily be used to compute the transmission coefficient of the multilayer structure. We start with RAM applications adopting first the classical formulation of the transmission lines and then the formulation described in chapter one. Let us to consider the equivalent multilayer scheme based first on the transmission line concept like in Fig. (4.2.2).

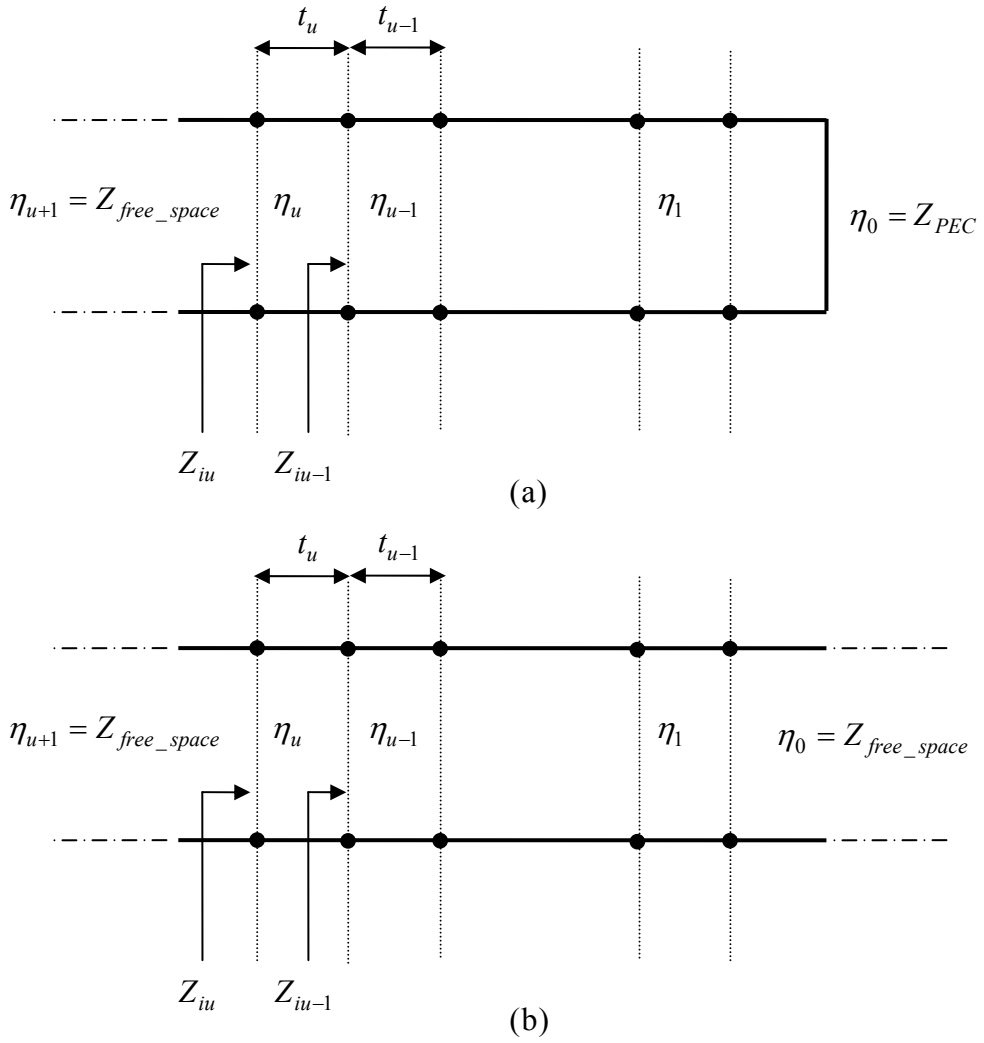

Fig. (4.2.3). Transmission line model of multilayer structure.
(a) represents the model of RAM, (b) represents the model of microwave Shielding

Then let's have to take into account the following equation for the equivalent transmission line model of the absorber which relates the free space impedance to the input impedance at the air-multilayer structure interface:

$$RC = \frac{Z_{iu} - Z_{free\_space}}{Z_{iu} + Z_{free\_space}}$$

$$RC(dB) = 20Log_{10}\left|\frac{Z_{iu} - Z_{free\_space}}{Z_{iu} + Z_{free\_space}}\right|$$

(4.2.2)

where *RC* can be expressed in linear form or in dB, $Z_{free\_space} = \sqrt{\mu_0 / \varepsilon_0} \cong 377 \quad \Omega$ is the free space impedance, and Z_{iu} is the input impedance at the first air-absorber interface. The input impedance of the multilayer at the air-absorber interface can be expressed by iterating [16][17] the relationship:

$$Z_{iu} = \eta_u \frac{Z_{iu-1}\cos(k_{uz}t_u) + j\eta_u \sin(k_{uz}t_u)}{\eta_u \cos(k_{uz}t_u) + jZ_{iu-1}\sin(k_{uz}t_u)}$$

(4.2.3)

for each layer *u*, where t_u is the thickness of the *u*-th absorber layer.

The possibility of choosing the incidence angles of the impinging electromagnetic wave as one of the input parameters for both magnetic and electric (TM/TE) transverse modes has been considered too. TM and TE impedances are:

$$Z_{iu}^{TM} = \eta_u \frac{Z_{iu-1}^{TM}\cos(k_{uz}t_u) + j\eta_u^{TE}\sin(k_{uz}t_u)}{\eta_u^{TM}\cos(k_u t_u) + jZ_{iu-1}^{TE}\sin(k_{uz}t_u)}$$

$$Z_{iu}^{TE} = \eta_u \frac{Z_{iu-1}^{TE}\cos(k_{uz}t_u) + j\eta_u^{TE}\sin(k_{uz}t_u)}{\eta_u^{TE}\cos(k_{uz}t_u) + jZ_{iu-1}^{TE}\sin(k_{uz}t_u)}$$

(4.2.4)

where

$$\eta_u^{TM} = \sqrt{\frac{\mu_0}{\varepsilon_0}}\sqrt{\frac{\mu_{ru}}{\varepsilon_{ru}}}\cos\vartheta_u = \eta_u \cos\vartheta_u$$

$$\eta_u^{TE} = \sqrt{\frac{\mu_0}{\varepsilon_0}}\sqrt{\frac{\mu_{ru}}{\varepsilon_{ru}}}\frac{1}{\cos\vartheta_u} = \eta_u \frac{1}{\cos\vartheta_u}$$

$$\vartheta_u = \arcsin\left(\frac{n_{u+1}}{n_u}\sin\vartheta_{u+1}\right) = \arcsin\left(\frac{\sqrt{\mu_{ru+1}}\sqrt{\varepsilon_{ru+1}}}{\sqrt{\mu_{ru}}\sqrt{\varepsilon_{ru}}}\sin\vartheta_{u+1}\right) =$$

$$= \arcsin\left(\frac{\frac{\eta_{free\_space}\mu_{ru+1}}{\eta_{u+1}}}{\frac{\eta_{free\_space}\mu_{ru}}{\eta_u}}\sin\vartheta_{u+1}\right) = \arcsin\left(\frac{\mu_{ru+1}}{\mu_{ru}}\frac{\eta_u}{\eta_{u+1}}\sin\vartheta_{u+1}\right)$$

(4.2.5)

The square of wave number k_{uz} along z longitudinal direction of propagation is expressed by the equation:

$$k_{uz}^2 = (2\pi f)^2 \mu_0 \varepsilon_0 \mu_{ru} \varepsilon_{ru} \cos^2 \vartheta_u = \\ = (2\pi f)^2 \mu_0 \varepsilon_0 \left(\mu_{ru}^{'} - j\mu_{ru}^{''}\right)\left(\varepsilon_{ru}^{'} - j\varepsilon_{ru}^{''}\right)\cos^2 \vartheta_u$$

(4.2.6)

where f is the frequency of the forward electromagnetic wave and ε' (ε'') are the real (imaginary) part of u-th layer permittivity, μ' (μ'') are the real (imaginary) part of u-th layer permeability. Complex waves appear in oblique incidence and lossy dielectrics problems as already explained in chapter one Sec.(1.7). Since the wave number becomes complex-valued (e.g., $\vec{k} = \vec{\beta} - j\vec{\alpha}$), both refraction and incidence angles may become complex-valued too. In calculating k_{uz} by taking square root of (4.2.6), it is necessary, in complex-wave problems, to get the correct sign of their imaginary parts such that evanescent waves are correctly described. This leads to define an 'evanescent' square root as already seen in chapter one Sec.(1.7).

In order to evaluate the propagation phenomena along transversal direction x, the wave number k_u has been further analyzed by taking component k_{ux} along x propagation direction:

$$k_{ux}^2 = (2\pi f)^2 \mu_0 \varepsilon_0 \mu_{ru} \varepsilon_{ru} \sin^2 \vartheta_u = \\ = (2\pi f)^2 \mu_0 \varepsilon_0 \left(\mu_{ru}^{'} - j\mu_{ru}^{''}\right)\left(\varepsilon_{ru}^{'} - j\varepsilon_{ru}^{''}\right)\sin^2 \vartheta_u$$

(4.2.7)

Such components has been used to compute the *constant-phase-plane-angle* (Φ) and the *constant-amplitude-plane-angle* (ψ) (see chapter 1, section 1.8).

$$\Phi = \arctan\left(\frac{\mathrm{Re}(k_{ux})}{\mathrm{Re}(k_{uz+1})}\right)$$

$$\Psi = \arctan\left(\frac{\mathrm{Im}(k_{ux})}{\mathrm{Im}(k_{uz+1})}\right)$$

(4.2.8)

The evaluation of the material absorbing and shielding performances also requires for the knowledge of the transmission properties of multilayered structure. In calculating *TC* at the last interface of the multilayer - i.e., at the absorber-air interface - a more general formalism, based on the application of boundary conditions for tangential fields, has been used in place of the transmission lines approach. Such method has been accurately described in chapter 1.

4.3 Heuristic Algorithms

Several modern heuristic algorithms have been developed for solving combinatorial and numeric optimization problems [18][19]. These algorithms can be classified into different groups depending on the criteria being considered, such as population based, iterative based, stochastic, deterministic, etc. While an algorithm working with a set of solutions and trying to improve them is called population based, the one using multiple iterations to approach the solution sought is named as iterative algorithm.

If an algorithm employs a probabilistic rule for improving a solution then it is called probabilistic or stochastic. Another classification can be made depending on the nature of phenomenon simulated by the algorithm. This type of classification mainly has two important groups of population based algorithms: evolutionary algorithms and swarm intelligence based algorithms. The most popular evolutionary algorithm is Genetic Algorithm (GA). GA attempts to simulate the phenomenon of natural evolution. In natural evolution, each species searches for beneficial adaptations in an ever-changing environment.

As species evolve, the new attributes are encoded in the chromosomes of individual members. This information does change by random mutation, but the real driving force behind the evolutionary development is the combination and exchange of chromosomal material during breeding. Although sporadic attempts have been made to incorporate these principles in optimization routines since the early 1960s, GAs were first established on a sound theoretical basis by Holland [20].

Winning particle optimization (WPO) [21], is a very simple algorithm where at each time epoch of evolution, particle which best fit the objective function (OF), is deputed to pilot the trajectory of the remaining almost-nonintelligent particles within

the multidimensional space of solutions. WPO is easy to implement and run, in fact, each single particle acts with no any knowledge about the other particles with exception of index of the best fitting particle. In WPO there is no particles neighborhoods information shearing, all particles survive but at each step of evolution only the best fitting particle is marked with its proper index while the remaining particles jump around it. Step by step this simple but quite effective method evolves toward the best solution; the iterations are stopped when all particles end to converge in a single area, which represents the optimal solution. This mean that the process can be iterated a fixed number of times or until a minimum error based on desired performance index is achieved.

In Particle Swarm Optimization (PSO), the term swarm is used to refer to any restrained collection of interacting agents or individuals. The classical example of a swarm is bees swarming around their hive but the metaphor can easily be extended to other systems with a similar architecture. An ant colony can be thought of as a swarm whose individual agents are ants; a flock of birds is a swarm of birds. An immune system [22] is a swarm of cells and molecules while a crowd is a swarm of people. Particle swarm optimization (PSO) algorithm which simulates the social behavior of bird flocking or fish schooling was introduced by Eberhart and Kennedy in 1995 [23]. PSO is a population based stochastic optimization technique and well adapted to the optimization of nonlinear functions in multidimensional space. PSO has received significant interest from researchers studying in different research areas and has been applied to several real-world problems [24].

An improved version of PSO algorithm is the Particle Swarm Inspired Evolutionary Algorithm (PS-EA) which is a hybrid model of EA and PSO [25]. It compensates the limitations of PSO when solving real-world problems. In order to avoid infeasible individuals resulted from faulty updates, PS-EA incorporates PSO with heuristics of EA in the population generator and mutation operator while retaining the workings of PSO.

For optimizing multivariable functions, Karaboga has described an artificial bee colony (ABC) algorithm [26], based on the intelligent behavior of honey bee swarm. Basturk and Karaboga compared the performance of ABC algorithm with the performance of GA in Ref. [27].

In the next section the implementation of the mathematical model of absorber using mentioned different heuristic algorithms is discussed.

GA, PSO, WPO algorithms are explained and applied and results compared in terms of absorbers overall thicknesses and absorbers electromagnetic performances.

Application of different heuristic algorithms has been made in order to be sure that implementation of absorber design method and final optimized results were not dependant by the particular heuristic algorithm type used. This is why, different algorithms, based on binary and real values, on swarm intelligence and on the almost non-intelligent method, have been applied and final results compared.

4.4 Absorber optimized using Genetic algorithm

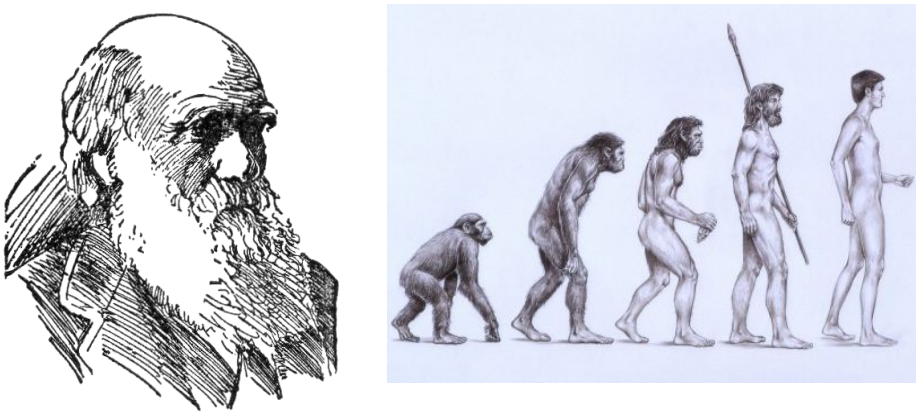

Fig.(4.4.1). Genetic Algorithm based on the imitation of genetic evolution of species

4.4.1 Genetic Algorithm principles

Genetic Algorithm is a stochastic optimization routine based on Darwin's theory of evolution and genetics [28]. An evolutionary process arrives at the optimized solution over several iterations (generations), by selecting only the best (the fittest) solutions and allowing these to survive and form the basis for calculating the next round of solutions. In the first step a population of individuals of size N is randomly generated. Each individual is described by a set of variable (genes), which gives rise to the overall characteristics of the individual. The set of variables for an individual

is termed the chromosome. An objective function or cost function uses the chromosome (variable description) of an individual in order to calculate its characteristics (i.e. a solution for optimization). The characteristics are then used as a monitor of the fitness of an individual. The number of iterations of GA can be fixed, or the algorithm can be left free to run until a certain desired minimum is obtained [29]. GA principle is shown in Fig.(4.4.1.1). The final step for the initial random chromosome population is to rank the fitness of the individuals. This is accomplished by comparing the fitness of each individual; a simple sort of the objective function can rank the individuals. Now, the initial chromosome population is created and the evolutionary loop is ready to start. The first step in the evolution is to select from the population members for mating, so that their genes are carried down to their children in the next generation. Darwin's theory of evolution states that the fittest members of a population will most likely to survive and hence propagate their genetic in formations of future generations [30]. This leads to several selection strategies that favor the fittest members of the populations. In the in-house developed version of GA the decimation selection takes place considering only the half upper family of chromosomes which presents the lowest values of the objective function [31,32], i.e., the best values. After these operations a crossover point in each couple of chromosome is chosen randomly and coupling process starts. This is one of the operations in the GA where the objective is to improve the fitness of the population. The principle is along the lines of genetics where the children of a mating pair will have chromosomes containing genes from each parent. In the developed version of GA this *random number* can range in the interval 1÷(*DimCrom*-1), where the second index *DimCrom* is the chromosome dimension decreased by one. The mutation operation has the meaning of introducing random variations into the population in order to explore new regions of the space solutions, trying to avoid local minimum, a well-known pathology of GA depicted in Fig.(4.4.1.2). As a consequence, genes which were lost earlier in the optimization are brought back into the genetic makeup of the population. The mutation acts in response to a mutation probability, randomly changing a gene to a new one i.e. from 0 to 1 or vice versa.

In this GA version, the mutation probability has been taken in the range 20% to 0.01% so that chromosomes with good fitness are not quickly lost. The mutations are applied to the children after the coupling step and act so that the closest the current

iteration to the final iterations number, the lower the percentage of genes randomly modified.

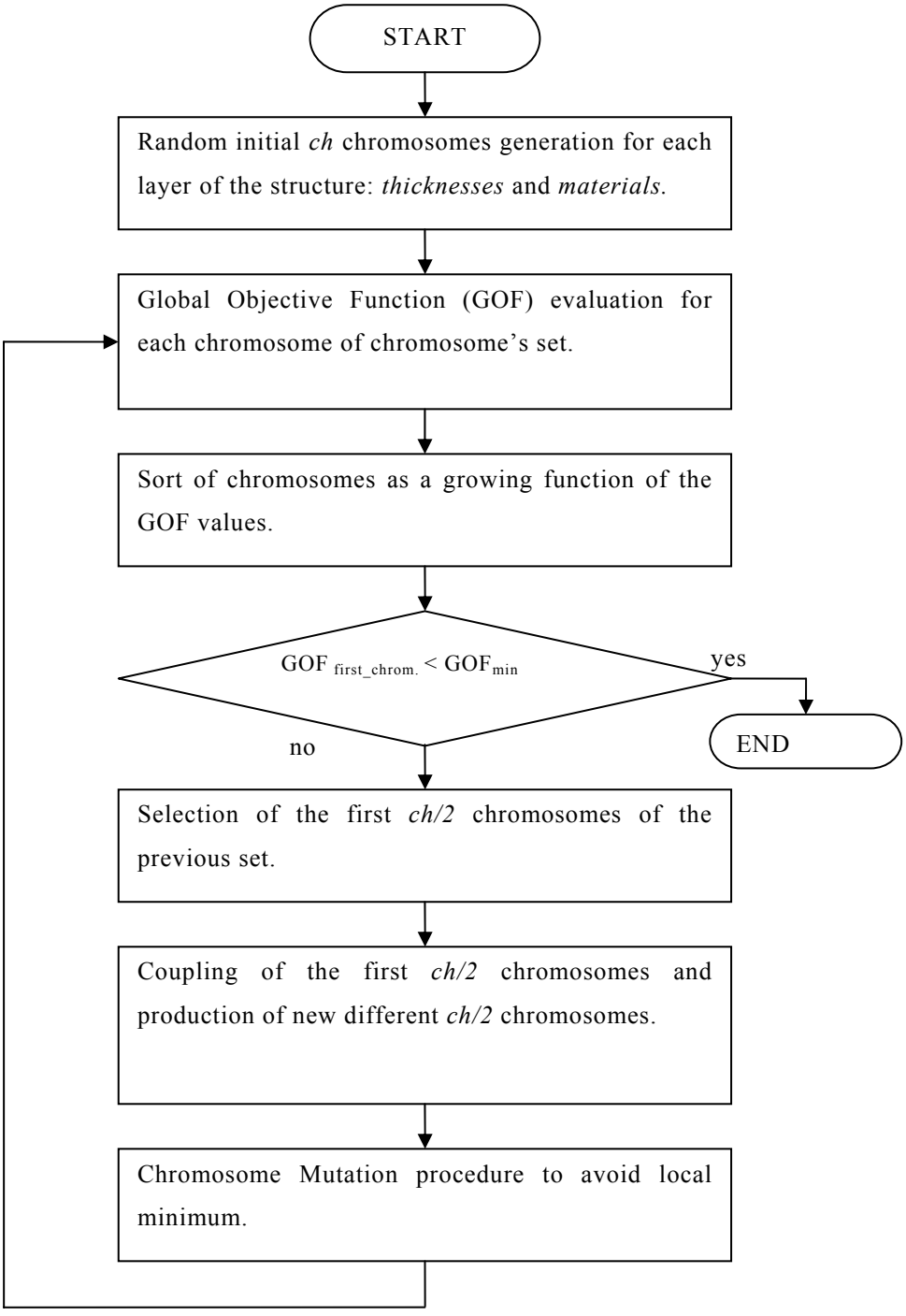

Fig. 4.4.1.1. Genetic Algorithm Description

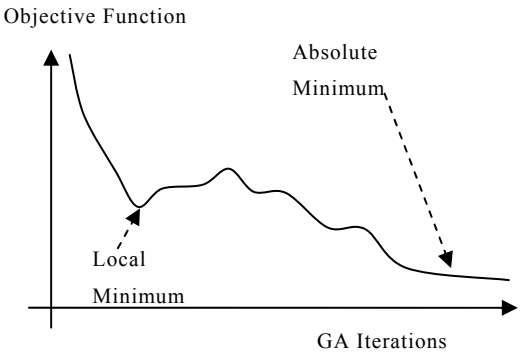

Fig. 4.4.1.2. Genetic Algorithm: local minimum of objective function

4.4.2 Absorber model and Objective functions using Genetic Algorithm

The design/optimization of the absorber is basically a *minimization* procedure which seeks the best trade-off between structure thickness (to be minimized) and absorbed electromagnetic (EM) power (to be maximized).

The multilayer structures considered in this book for the absorber structure can have up to 10 layers (so the index m=10,9,8,7,6,5,4,3,2,1) where thee last index 1 corresponds to the last layer of the multilayer structure [13,17].

The number of GA chromosomes has been fixed to 30 and number of iterations to 800.

In the GA code the thickness of each layer is binary coded using 6 bits and fixing minimum thickness to 0 mm, and minimum thickness step to 0.1 mm. as a consequence thickness of each layer can range from 0 to 6.3 mm.

As far as layer materials are concerned, each one can be chosen among 64 potential different manufactured composite materials in the database, as a consequence each layer is binary coded using 6 bits. In case database of materials were populated with a number of materials lower than 64, i.e., the maximum capability, then, it is possible to set a lower number of materials by simply changing an input parameter in the main program of algorithm. In Tab. (4.4.2.1) an example of the composite materials available in the database (DB) is reported. DB contains permittivity as a function of

frequency (GHz) of each composite material electromagnetically characterized (see Chap 3).

GA starts generating a number of binary chromosomes (ChN) containing random thicknesses and materials type. During the evolution, at each iteration, the entire set of chromosomes family is evaluated using a global objective function (GOF) which takes into account for different weighted elementary objective functions (EOF). The half chromosomes having better GOFs are used to generate new chromosomes and, at the end of the iterations the best chromosome is chosen and it represents the best choice in terms of *layers thickness, layers number, layers material type,* and *absorbed power* i.e., *LossFactor%* here referred both to absorbing and shielding materials.

In GA, the mutation probability (M-probability), changes as a function of the current iteration step, linearly decreasing from 20% to 0.01%.

TABLE 4.4.2.1
CODING OF MATERIALS IN THE DATA BASE

Available Material	Integer Number code For PSO, WPO	Binary code For GA
Epoxy- Resin	1	0001
MWCNT, 0.5wt%	2	0010
MWCNT, 1wt%	3	0011
MWCNT, 2wt%	4	0100
MWCNT, 2.5wt%	5	0101
MWCNT, 3wt%	6	0110
CNF, 1wt%	7	0111
CNF, 2wt%	8	1000
CNF, 3wt%	9	1001

The *EOF* for TM and TE modes are named as *CostRCTM*, *CostRCTE*, for reflection coefficient, *CostTCTM*, *CostTCTE*, for the transmission coefficient, *CostT*, for

thickness. Formal definitions of the *EOF* for TM and TE modes are shown in Eq. (4.4.2.1) up to (4.4.2.4).

We can observe that for each chromosome (Ch), the corresponding *EOF* is evaluated over the entire frequency band and over the entire angular forward range, adopting frequency and angular steps chosen by the user before starting the tool:

$$CostRC_{TM}(Ch)=\left[\sum_{freq=f\min}^{freq=f\max}\left(\sum_{\vartheta=\vartheta\min}^{\vartheta=\vartheta\max}RC_{TM}(Ch,freq,\vartheta)\right)\right]$$

$$CostRC_{TE}(Ch)=\left[\sum_{freq=f\min}^{freq=f\max}\left(\sum_{\vartheta=\vartheta\min}^{\vartheta=\vartheta\max}RC_{TE}(Ch,freq,\vartheta)\right)\right]$$

(4.4.2.1)

.

$$CostTC_{TM}(Ch)=\left[\sum_{freq=f\min}^{freq=f\max}\left(\sum_{\vartheta=\vartheta\min}^{\vartheta=\vartheta\max}TC_{TM}(Ch,freq,\vartheta)\right)\right]$$

$$CostTC_{TE}(Ch)=\left[\sum_{freq=f\min}^{freq=f\max}\left(\sum_{\vartheta=\vartheta\min}^{\vartheta=\vartheta\max}TC_{TE}(Ch,freq,\vartheta)\right)\right],$$

(4.4.2.2)

where *Ch* is the current chromosome, *freq* is the frequency step, *fmin* and *fmax* are the start and stop of frequency band, θ is the current angular step, and θmin and θmax represent the angular range bounds. The definition of the *EOF* for thickness is

$$CostT(Ch)=\left[thick_{10}(Ch)+thick_{9}(Ch)+....+thick_{1}(Ch)\right],$$

(4.4.2.3)

where $thick_{k}$ is the thickness of the *m-th* layer.

Two different weighting factors are introduced, one called α weighting *CostT* w.r.t. *CostRC* and *CostTC***,** one called γ*,* weighting *CostRC* w.r.t. *CostTC*. Such weighting factors are chosen by the user and their meaning has to be intended as the capability of the tool to design the multilayer structure making privilege to the electromagnetic performances w.r.t. the thickness when α tend to 1, or making privilege in lowering the transmission coefficient (shielding applications) rather than lowering the reflection coefficient (RAM applications) when γ tend to 0.

GOF is a linear combination of the described *EOF*:

$$GOF(Ch) = \alpha \cdot [\gamma \cdot OF1(Ch) + (1-\gamma) \cdot OF2(Ch)] + (1-\alpha) \cdot OF3(Ch),$$

(4.4.2.4)

where

$$OF1(Ch) = \left(\frac{CostRC_{TM}(Ch)}{A} + \frac{CostRC_{TE}(Ch)}{A} \right)$$
$$OF2(Ch) = \left(\frac{CostTC_{TM}(Ch)}{A} + \frac{CostTC_{TE}(Ch)}{A} \right),$$
$$OF3(Ch) = \left[\frac{CostT(Ch)}{C} \right]$$

α and γ are weighting coefficient ($0<\alpha<1$), ($0<\gamma<1$), A is defined as $(FreqStepNumber) \times (AngleStepNumber)$ and C is defined as $\max(LayerNumbers) \times \max(LayerThickness)$.

Here such parameters have the following values: $\alpha=0.98$, $\gamma=0.5$.

More precisely, A and C are normalization factors: they are important since all the elementary objective functions must have similar weight range within the global objective function, i.e., varying in comparable range of values.

At each iteration, for each new generation of chromosomes, a called generation of global objective function GGOF can be written as

$$GGOF = \sum_{Ch=1}^{Ch=ChN} \{\alpha \cdot [\gamma \cdot OF1(Ch) + (1-\gamma) \cdot OF2(Ch)] + (1-\alpha) \cdot OF3(Ch)\}$$

(4.4.2.5)

this latter is adopted to trace the convergence of the GA. At each iteration, for a complete available set of chromosomes, the Eq. (4.4.2.5) is plotted. The asymptotic tendency of the plotted curve shows the GA success in the optimization procedure, i.e., all final chromosomes in the optimized set make GOF convergence.

4.4.3 Final Absorbing structures optimized by Genetic Algorithm

Two different absorbing structures are taken into account, the first is radar absorbing material (RAM) multilayer structure, whereas the second has double target of absorbing and shielding microwaves and has been called microwave-shielding structure (MSS).

RAM

Radar Absorbing strucutre using GA desing is shown in Fig. (4.4.3.1). Main parameters settings in GA was: $\alpha=0.98$, $\gamma=1$, *Num_Iterations=800*, *Num_Chromosomes=30, Initial_Mutation=0.2, Final_Mutation=0.01, Num_Materials=9, Num_freq_step=1536 (i.e., range 5.38 - 18 GHz).*

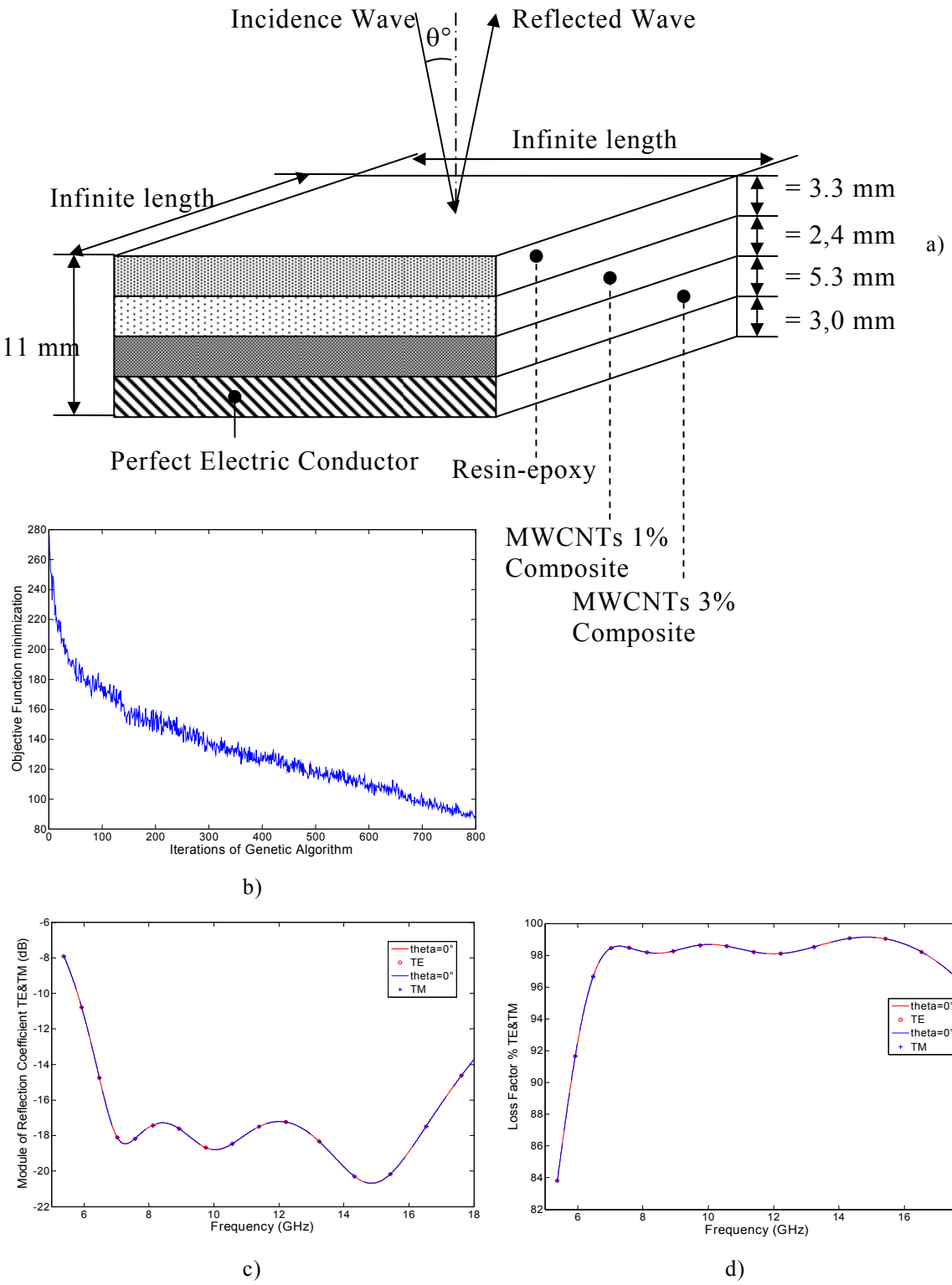

Fig. (4.4.3.1). a) Nanostrucutred composite RAM structure designed using Genetic Algorithm; b) Convergence of Genetic Algorithm in Objective Function minimization; c) Reflection coefficient (dB), and d) Loss Factor (%), for the electromagnetic wave directed normally with respect to absorber surface.

In Fig. (4.4.3.2). Module or Reflection Coefficient (dB) and Loss Factor (%) for Nanostructured composite RAM structure designed with Genetic Algorithm are shown for several incidence angles in the range 0 to 80 deg.

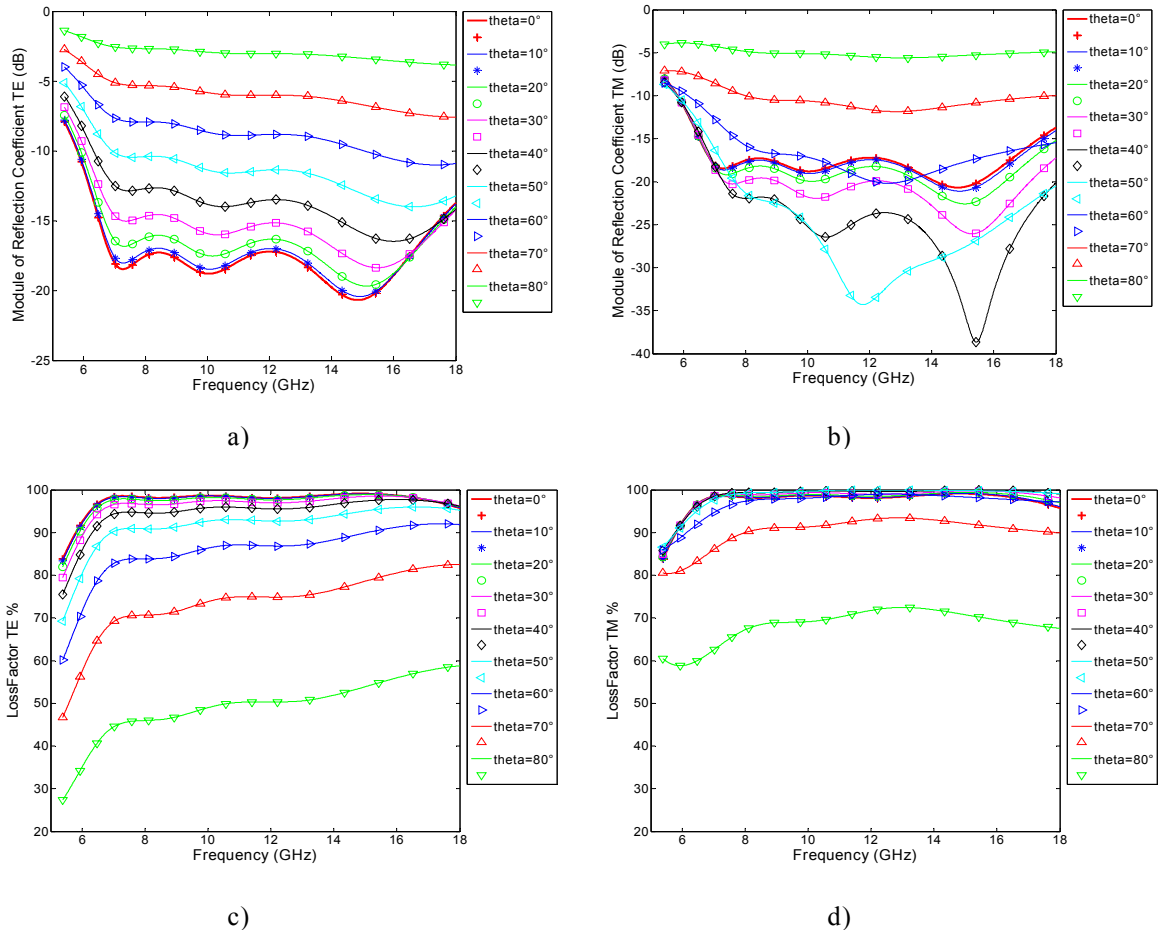

a) b)

c) d)

Fig. (4.4.3.2). Nanostructured composite RAM structure designed with Genetic Algorithm:

a) Reflection Coefficient TE (dB), incidence 0-80 deg; b) Reflection Coefficient TM (dB), incidence 0-80 deg; c) Loss Factor TE (%), incidence 0-80 deg; ; d) Loss Factor TM (%), incidence 0-80 deg.

It is possible to notice that reflection coefficient (RC) remain below -15 dB for incidence angles ranging from 0 to 30 deg for both TE and TM mode. The corresponding Loss Factor is greater than 96% within almost all the frequency band 5-18 GHz. In particular around 12GHz, for incidence angles around 50 deg and around 15.5 GHz for incidence angle of 40 deg, RAM presents for TM mode, values of TM reflection coefficient even below values at 0 deg of incidence. Such values are those corresponding to Brewster or better Zenneck angle. (see chapter 1 for explanation about Brewster and Zenneck).

MSS

Microwave shielding structure and convergence of GA design and optimization process are shown in Fig. (4.4.3.3). Main parameters settings in GA was: *α=0.97, γ=0.5, Num_Iterations=800, Num_Chromosomes=30, Initial_Mutation=0.2, Final_Mutation=0.01, Num_Materials=9, Num_freq_step=1536 (i.e., range 5.38 - 18 GHz).*

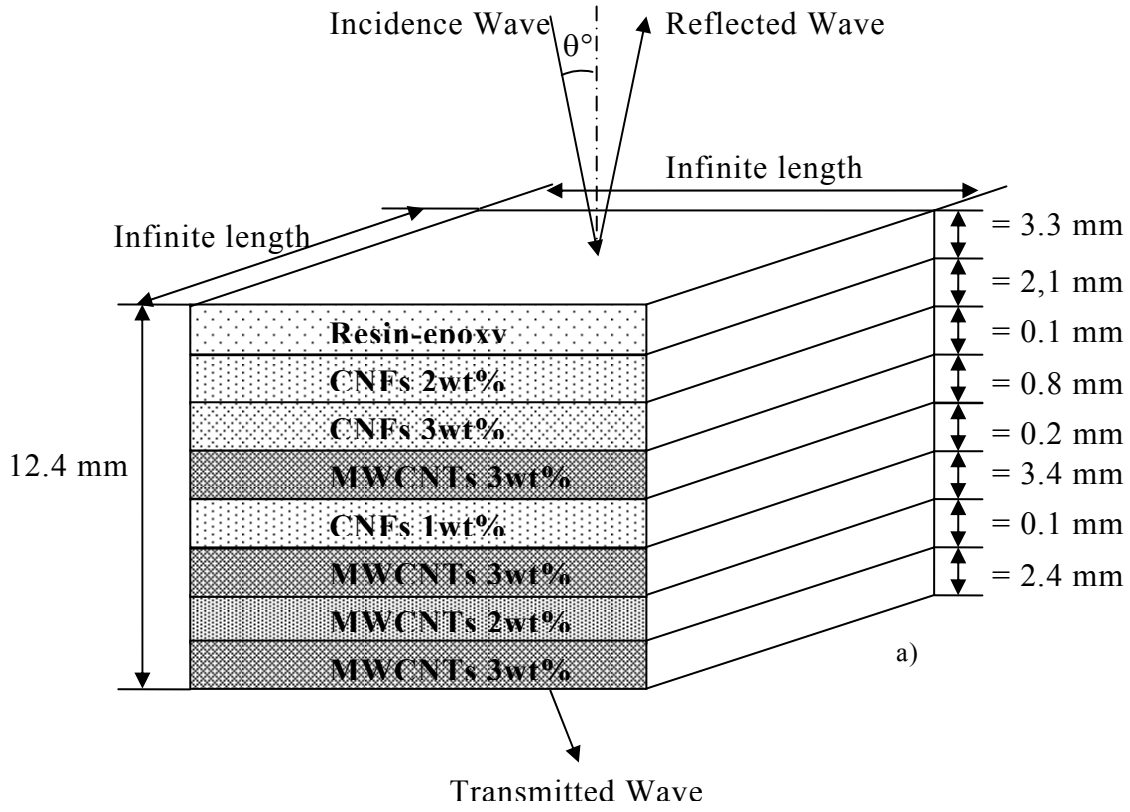

Fig. (4.4.3.3). a) Nanostructured composite MSS structure designed using Genetic Algorithm;

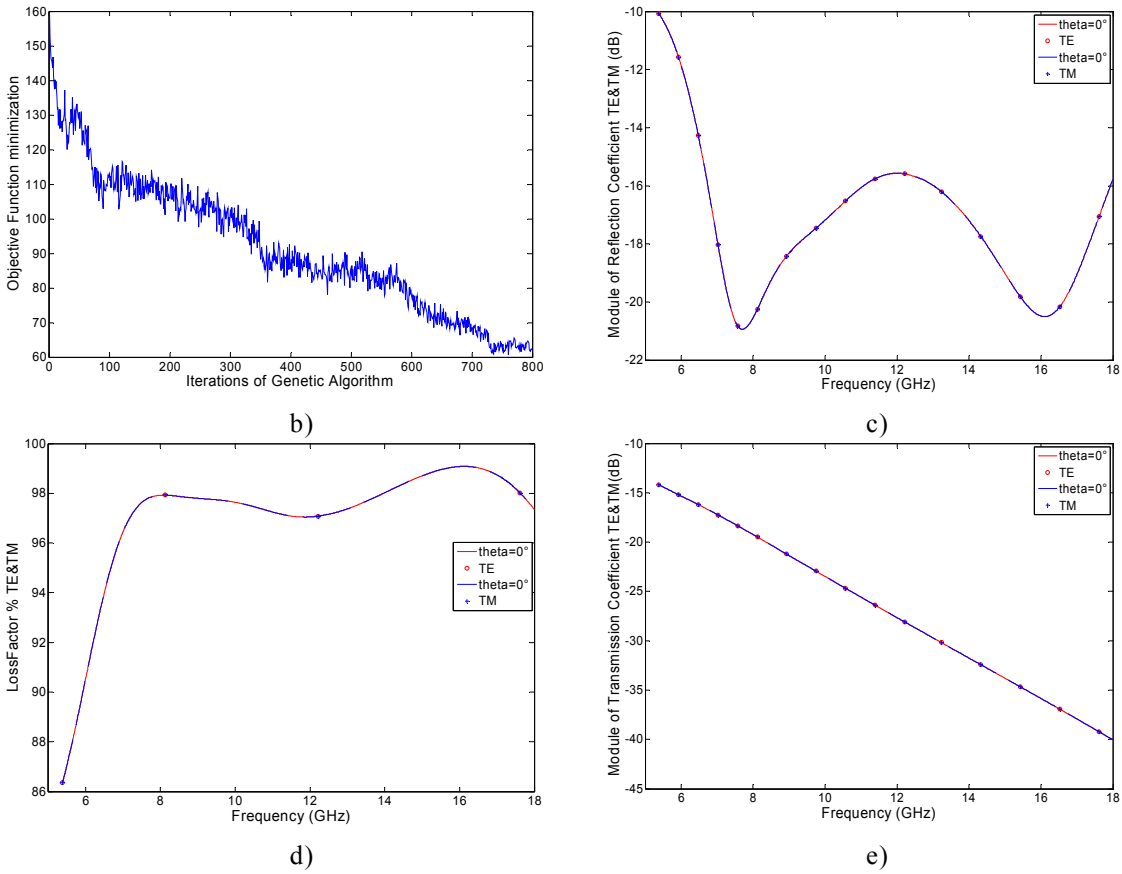

Fig. (4.4.3.3). b) Convergence of Genetic Algorithm in Objective function minimization; c) Reflection coefficient (dB); d) Loss Factor (%); e) Transmission coefficient; for electromagnetic wave normally directed with respect to absorber surface.

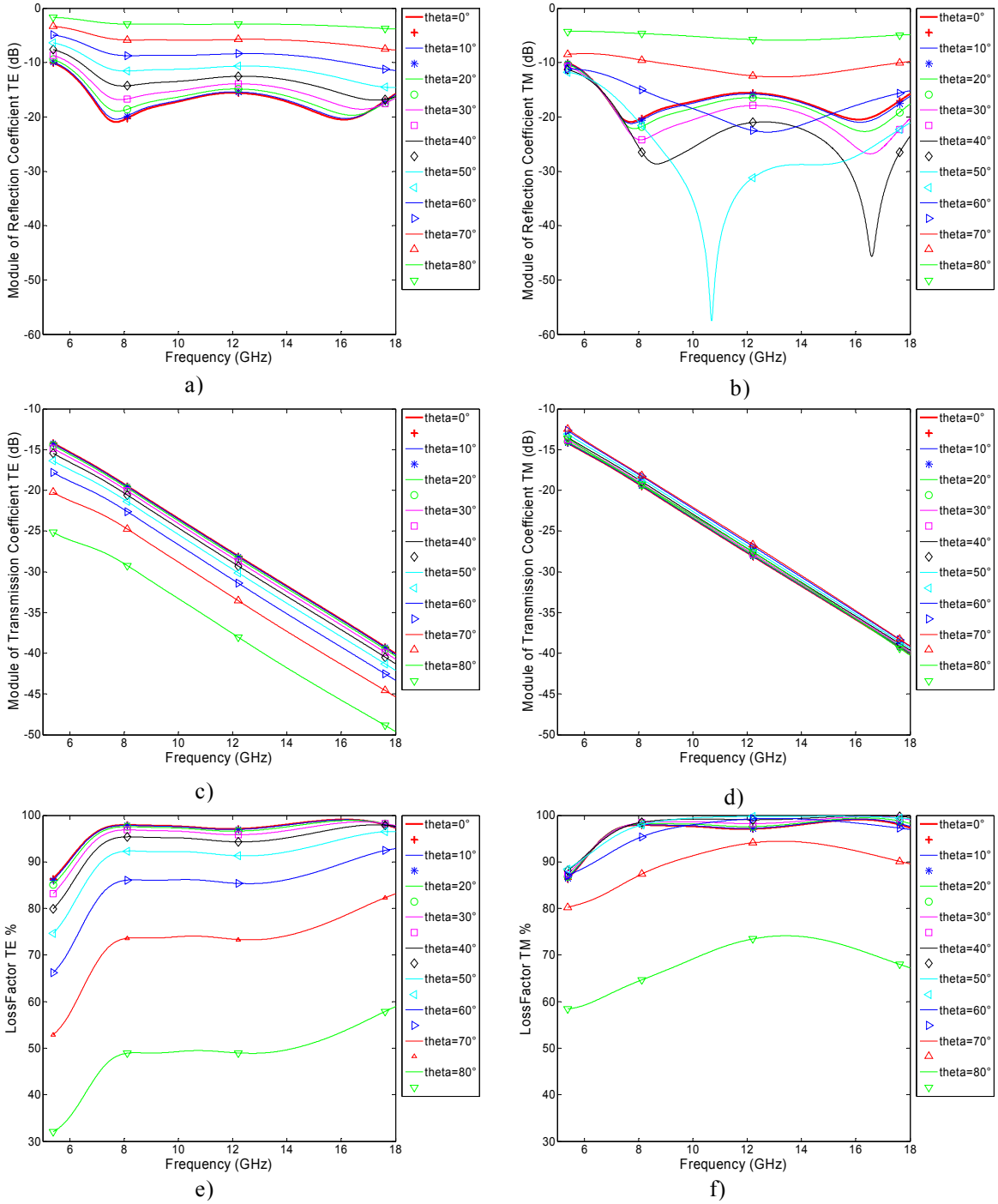

Fig. (4.4.3.4). Nanostructured composite MSS structure designed with Genetic Algorithm: a) Reflection Coefficient TE (dB); b) Reflection coefficient TM (dB); c) Transmission Coefficient TE(dB); d) Transmission Coefficient TM(dB); e) Loss Factor TE(%); f) Loss Factor TM(%), for EM wave incidence angles in the range 0-80 deg.

4.5 Absorber optimized using Particle Swarm Optimization algorithm

Fig.(4.5.1). PSO based on imitation of social behaviour of birds

4.5.1 Particle Swarm Optimization principles

Particle swarm optimization (PSO) was originally designed and introduced by Eberhart and Kennedy (Kennedy, Eberhart, 1995). The PSO is a population based search algorithm based on the simulation of the social behavior of birds, bees or a school of fishes [33]. This algorithm originally intends to graphically simulate the graceful and unpredictable choreography of a bird folk. Each individual within the swarm is represented by a vector in multidimensional search space. This vector has also one assigned vector which determines the next movement of the particle and is called the velocity vector.

The PSO algorithm also determines how to update the velocity of a particle. Each particle updates its velocity based on current velocity and the best position it has explored so far; and also based on the global best position explored by entire swarm. The PSO process then is iterated a fixed number of times or until a minimum error based on desired performance index is achieved. It has been shown that this simple model can deal with difficult optimization problems efficiently. As stated before, PSO simulates the behavior of bird flocking. Suppose the following scenario: a group

of birds is randomly searching for food in an area. There is only one piece of food in the area being searched. Not all the birds know where the food is. However, during every iteration, they learn via their inter-communications, how far the food is. Therefore, the best strategy to find the food is to follow the bird that is nearest to the food. PSO learned from this bird-flocking scenario, and used it to solve optimization problems. In PSO, each single solution is a "bird" in the search space. We call it "particle". All of particles have fitness values which are evaluated by the fitness function (the cost function to be optimized), and have velocities which direct the flying of the particles. PSO is initialized with a group of random particles (solutions) and then searches for optima by updating their position and velocity. In a single iteration, each particle is updated by following two "best" values. The first one is the position vector of the best solution (fitness) which each particle has achieved so far. The fitness value is also stored. This position is called P_{best}. The second "best" position that is tracked by the particle swarm optimizer is the best position, obtained so far, by any particle in the population. This best position is the current global best and is called G_{best} [34].

The most striking difference between PSO and the other evolutionary algorithms is that PSO chooses the path of cooperation over competition. Other algorithms commonly use some form of decimation or survival of the fittest. In contrast, the PSO population is stable and individuals are neither destroyed nor created. Individuals are affected by the best performance of their neighbors [35], and individuals eventually converge on optimal points in the problem domain. In addition, the PSO traditionally does not have genetic operators like crossover between individuals and mutation, and other individuals never substitute particles during the run. Instead, the PSO refines its search by attracting the particles to positions with good solutions.

In Fig.(4.5.1.1) a qualitative example representing evolution of the swarm in a PSO algorithm is shown. At the beginning all particles are randomly distributed in the search domain, step-by-step optimal area of solutions is defined and all particles converge toward such zone.

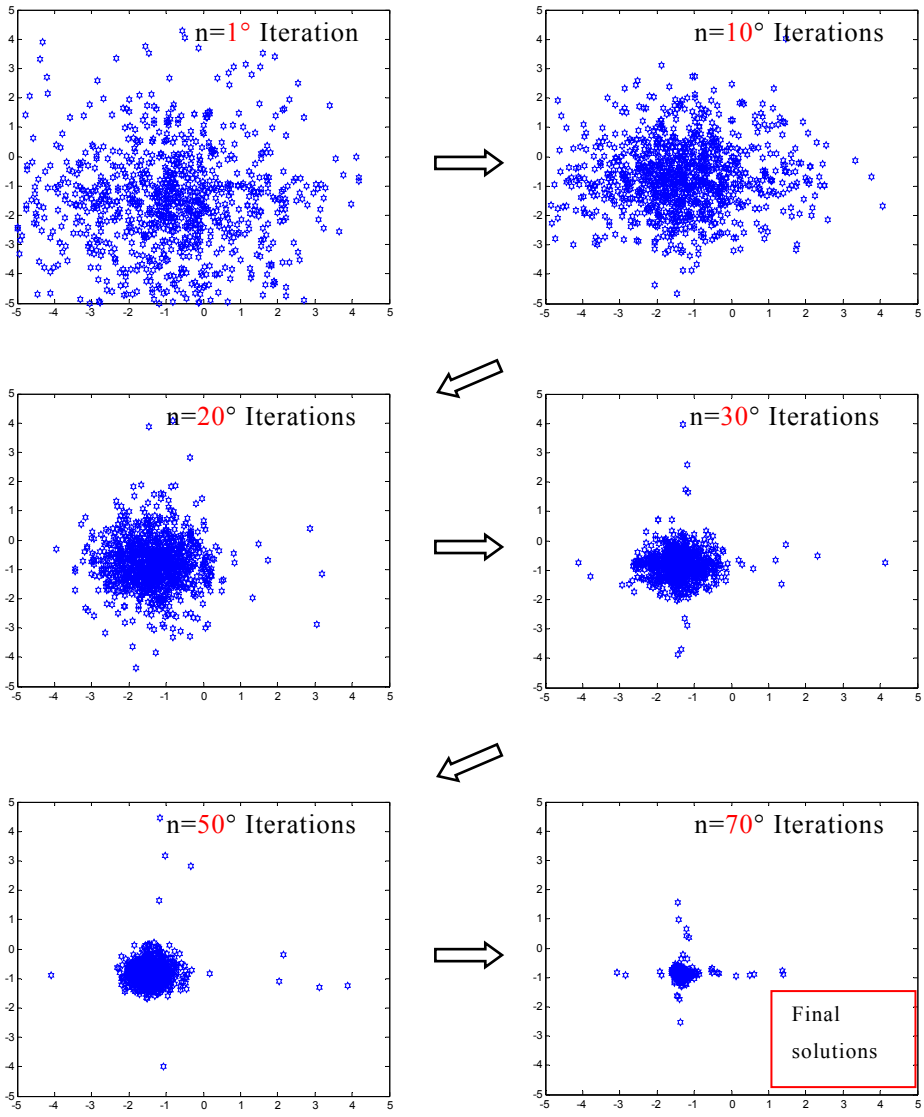

Fig.(4.5.1.1). PSO evolution example, where number of iterations is 70 and particles 500. The high the number of iterations the smaller the search area of solutions

As already seen in previous section, Genetic Algorithm (GA) is an evolutionary optimizer (EO) that takes a sample of possible solutions (individuals) and employs mutation, crossover, and selection as the primary operators for optimization [36]. In general, most of evolutionary techniques have the following steps:

1. Random generation of an initial population.
2. Reckoning of a fitness value for each subject. This fitness value depends directly on the distance to the optimum.
3. Reproduction of the population based on fitness values.

4. If requirements are met, then stop. Otherwise go back to step 2.

From this procedure, we can learn that PSO shares many common points with GA. Both algorithms start with a group of randomly generated population and both algorithms have fitness values to evaluate the population, update the population and search for the optimum with random techniques, and finally, check for the attainment of a valid solution.

On the other hand, PSO does not have genetic operators like crossover and mutation. Particles update themselves with the internal velocity. They also have memory, which is important to the algorithm (even if this memory is very simple as it stores only P_{best_i} and G_{best_k} positions).

Also, the information sharing mechanism in PSO is significantly different: In GAs, chromosomes share informations to each other. So the whole population moves like one group towards an optimal area even if this move is slow. In PSO, only Gbest gives out the information to others. It is a one-way information sharing mechanism. The evolution only looks for the best solution. Compared with GA, all the particles tend to converge to the best solution quickly in most cases as shown by Eberhart and Shi [1998] and Hassan et al. [2004].

In the PSO algorithm, each particle k of the swarm, flies in the n-dimensional space, and its *position* $X^k(i)$ and *velocity* $V^k(i)$ at a certain i-th iteration, is identified by two vectors,

$$X^k(i) = \left[x_1^k(i), x_2^k(i), \ldots\ldots, x_n^k(i)\right],$$

(4.5.1.1)

$$V^k(i) = \left[v_1^k(i), v_2^k(i), \ldots\ldots, v_n^k(i)\right]$$

(4.5.1.2)

Each $x_m^k(i)$ component, represents a quantity of the physical problem we want to optimize, m ranges in the closed interval $[1,n]$. At the start each particle is randomly located in the space of solutions and also particles velocities are randomly assigned. Particles are free to fly inside the n-dimensional space defined by the user, within the constraints defined by the n boundary conditions, which limit the extent of the search

space and, hence, the values assumed by the variables during the optimization process. At the generic *i+1*-th iteration step, the velocity of single *m*-th-dimension, of *k*-th-particle, is expressed by the following equation,

$$v_m^k(i+1) = W(i) \times v_m^k(i) + C1(i) \times rand() \times \left[P_{best,m}^k(i) - x_m^k(i)\right] + C2(i) \times rand() \times \left[G_{best,m}(i) - x_m^k(i)\right]$$

(4.5.1.3)

where $v_m^k(i)$ is the velocity along the *m*-th direction at the *i*-th iteration; $W(i)$ is the inertial weight; $C1(i)$ and $C2(i)$ are respectively the *cognitive* and the *social rate*, $P_{best,m}^k(i)$ is the best *m*-th-coordinate position found so far by the *k*-th-agent during its own flying up to *i*-th-iteration; $G_{best,m}(i)$ is the best *m*-th-coordinate position found so far by the entire swarm up to *i*-th,-iteration; $rand(\ )$ is a generator of random numbers uniformly distributed between the closed interval [*0,1*]. The *m*-th-coordinate position of each particle *k* is then simply updated according to the equation,

$$x_m^k(i+1) = x_m^k(i) + v_m^k(i) \times \Delta t$$

(4.5.1.4)

where $x_m^k(i)$ is the *m*-th-coordinate at *i*-th-iteration, of the *k*-th-particle and Δt here is equal to 1.

Flow chart of PSO algorithm is shown in Fig. (4.5.1.2)

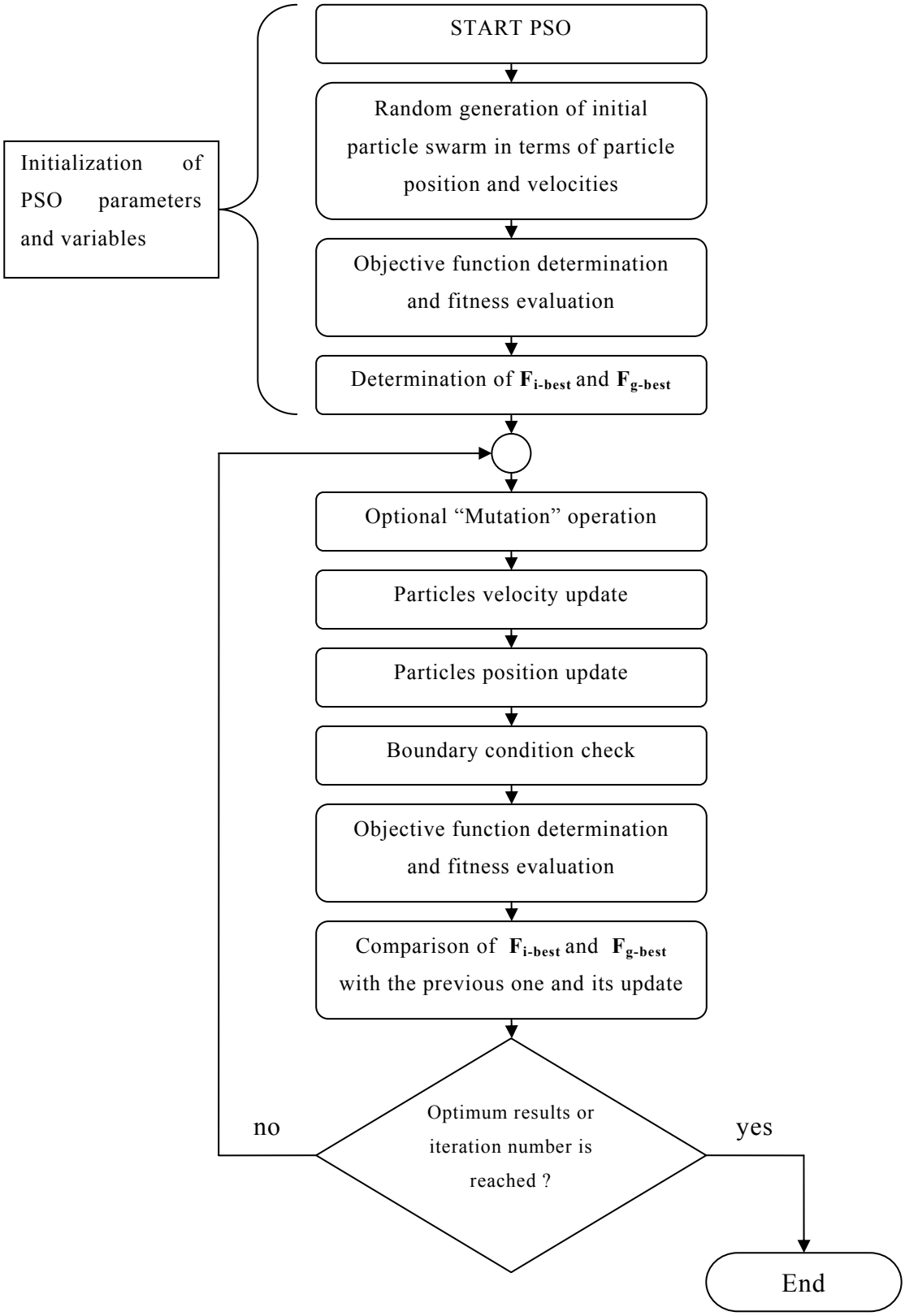

Fig. (4.5.1.2), PSO flow chart

4.5.2 Absorber model and Objective functions using Particle Swarm Optimization

In PSO no binary coding system has been adopted. Instead PSO uses real values for thickness and materials rounded to the nearest integer value. Such integer values are upper bound limited to max layer thickness and to max number of different materials available in the DB. The design/optimization is basically a minimization procedure which seeks the best trade-off between structure thickness (to be minimized) and absorbed EM power (to be maximized). In PSO algorithms particles are used in place of chromosomes.

In order to compare GA, PSO performances we have considered a number of PSO particles equal to the number of GA chromosomes. In particular the main difference between algorithms is only the engine of evolution represented respectively by:

- coupling of chromosome and mutation procedures in GA,
- computing particles velocity and particles position in PSO,

In this version of PSO the mutation operation has been introduced too in order to further enhance the global search ability of PSO by providing additional diversity in the exploration task. Such operation, like in GA, helps the optimization process to get off from local minima; in the literature, PSO which also uses mutation is sometimes called MPSO.

In PSO the search toward the global optimum solution is guided by the two stochastic acceleration factors (the cognitive part and the social part). Therefore Angeline, related these two acceleration factors to the mutation factors in evolutionary programming, whereas Shi and Eberhart [37], related these two factors to the crossover operation in genetic algorithm.

PSO, GA common procedures are called by the main program to compute: materials intrinsic impedances, in-outgoing refraction angle, TE/TM layer impedance, reflection coefficient dB, loss factor%. The same number of iterations has been adopted for PSO and GA techniques.

In PSO the mutation probability (Mprobability) change as a function of the current iteration step, linearly decreasing from 10% to 0.01%.

The multilayer structures considered in RAM design can have up to 10 layers so m=10,9,8,7,6,5,4,3,2,1. Since the optimization are for both: layer thickness and layer material, then PSO optimization algorithms need to be structured in order to take into account both quantities.

In PSO algorithm in place of (4.5.1.1) we have $XT^k(i)=\left[xt_{10}^k(i),xt_9^k(i),.....,xt_1^k(i)\right]$, as vector of layer thicknesses, where $xt_m^k(i)$ is the thickness of *m*-th layer, and $XP^k(i)=\left[xp_{10}^k(i),xp_9^k(i),.....,xp_1^k(i)\right]$, as vector of materials, where $xp_m^k(i)$ is the material associated to the *m*-th layer.

In PSO also velocity $v_m^k(i)$ of *m*-th dimension must be updated, so in place of (4.5.1.2) we have $VT^k(i)=\left[vt_{10}^k(i),vt_9^k(i),.....,vt_1^k(i)\right]$, for the thickness vector and $VP^k(i)=\left[vp_{10}^k(i),vp_9^k(i),.....,vp_1^k(i)\right]$, for the materials vector.

In order to update PSO particle coordinates, in place of (4.5.1.4), we split the problem in two equations respectively for thickness and material type of each layer:

$$XT_m^k(i+1)=XT_m^k(i)+VT_m^k(i)\times\Delta t$$
$$XP_m^k(i+1)=round\left(XP_m^k(i)+VP_m^k(i)\times\Delta t\right)$$

(4.5.2.1)

Here $\Delta t=1$. In the second of (4.5.2.1), rounded values adopted for material type, are required since the index of material of each layer can only be an integer number in the closed range 1 to 64 where 64 is the maximum amount for different materials stored in the data base.

Factor *W* is a *weighting factor* which is decreased with the iterations cycle, ranging from *W*=0.9 to *W*=0.4. The *cognitive* and the *social rate* ranges in the interval *C1*=2.5 to *C1*=0.5, *C2*=0.5 to *C2*=2.5. Values of *W,C1,C2*, in the PSO velocity equations have been chosen accordingly to [38]

$$W(i) = \left(W_i - W_f\right)\left(\frac{IN - i}{IN}\right) + W_{final}$$
$$W_{initial} = 0.9$$
$$W_{final} = 0.4$$
$$C1(i) = \left(C1_f - C1_i\right)\left(\frac{i}{IN}\right) + C1_{initial}$$
$$C1_{initial} = 2.5$$
$$C1_{final} = 0.5$$
$$C2(i) = \left(C2_f - C2_i\right)\left(\frac{i}{IN}\right) + C2_{initial}$$
$$C2_{initial} = 0.5$$
$$C2_{final} = 2.5$$

(4.5.2.2)

where IN is the PSO number of iterations and i is the current *i-th* iteration.
Number of GA chromosomes and PSO particles has been fixed to 30 and number of iterations to IN=800 for all algorithms. In particular, as far as PSO is concerned, at each iteration we do not refer to new particles generation but to the same particles with new positions in the space of solutions.

The formal definition of the objective function (OF) for TM and TE modes are the same already adopted in genetic algorithm (GA) and are shown in Eq. (4.4.2.1) up to (4.4.2.5).

4.5.3 Final Absorbing structures optimized by Particle Swarm Optimization

Two different absorbing structures are taken into account, the first is radar absorbing material (RAM) multilayer structure, whereas the second has double target of absorbing and shielding microwaves and has been called microwave-shielding structure (MSS).

RAM

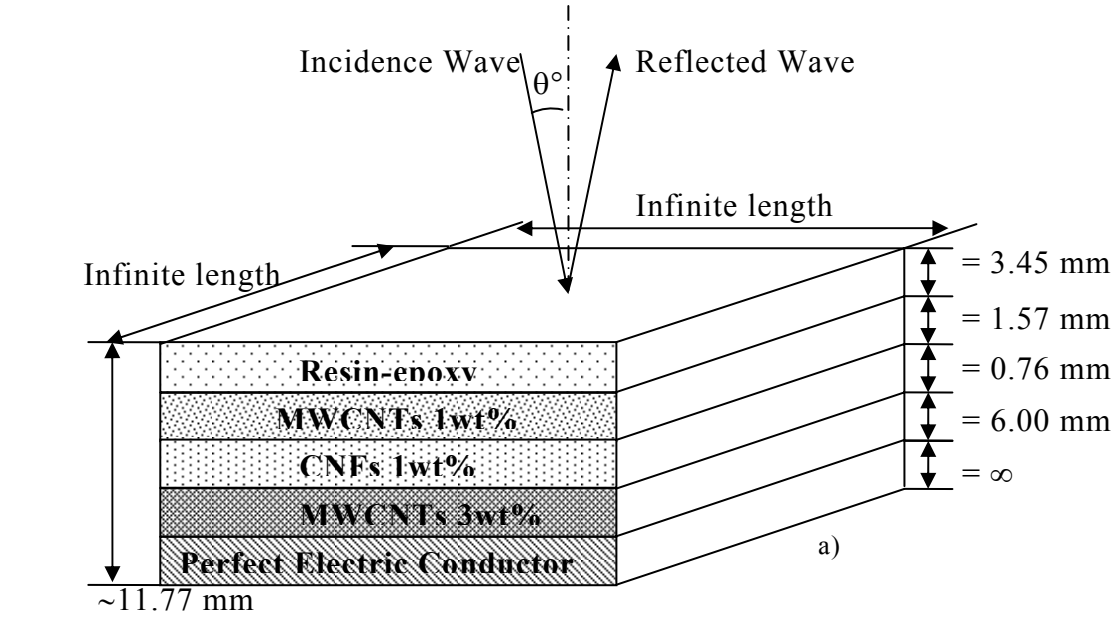

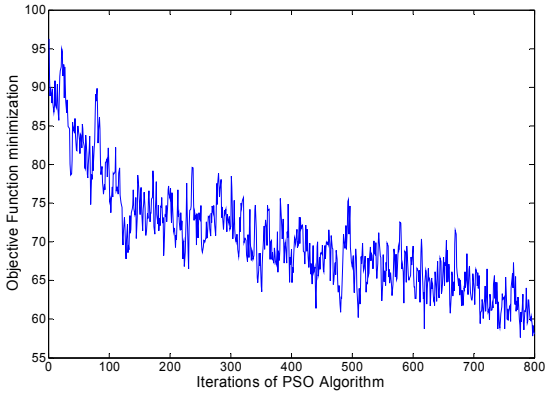

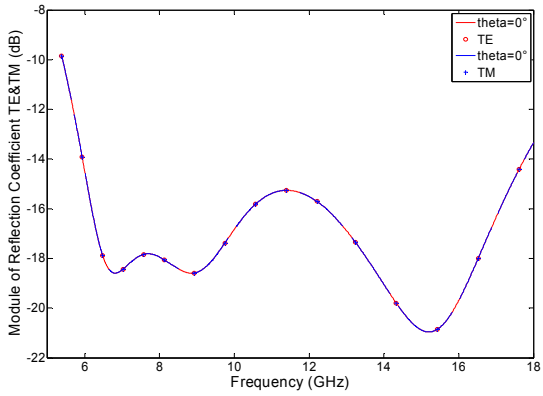

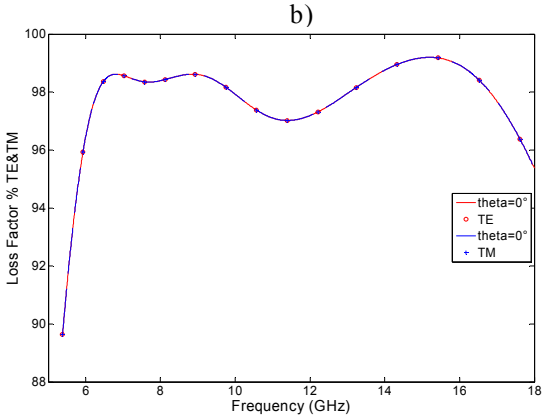

Fig. (4.5.3.1). a) Nanostructured composite RAM structure designed using Particle Swarm Optimization Algorithm; b) Convergence of PSO in Objective Function minimization; c) Reflection coefficient (dB), and d) Loss Factor (%), for electromagnetic wave normally directed with respect to absorber surface.

In Fig. (4.5.3.2), multilayer absorber characterization for several incidence angles in the range 0 – 80 deg is shown.

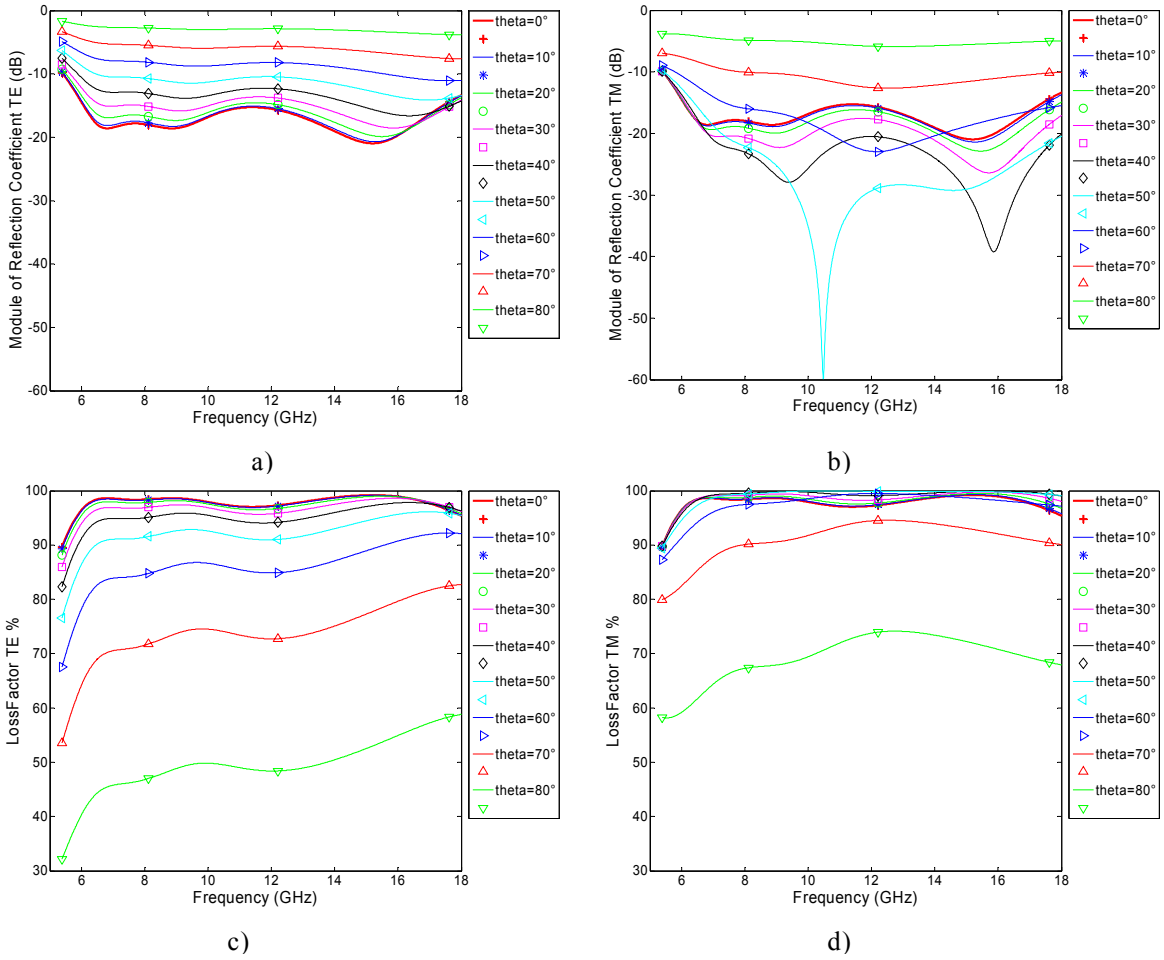

Fig. (4.5.3.2). Nanostructured composite RAM structure designed with Particle Swarm Optimization:

a) Reflection Coefficient TE(dB), b) Reflection Coefficient TM(dB); c) Loss Factor TE(%); d) Loss Factor TM (%), for electromagnetic wave incidence 0-80 deg.

In Fig. (4.5.3.2), Reflection coefficient TM shows Brewster/Zenneck behavior for 50 deg incidence angle around 10.5 GHz and for 30 and 40 deg incidence angles around 16 GHz. Values of Reflection coefficient remain always below -10 dB for incidence angles in the range 0-50 deg. This is what we were prefixed from optimization process. Loss Factor remains above 95% for electromagnetic wave incidence angles in the range 0- 30 deg.

MSS

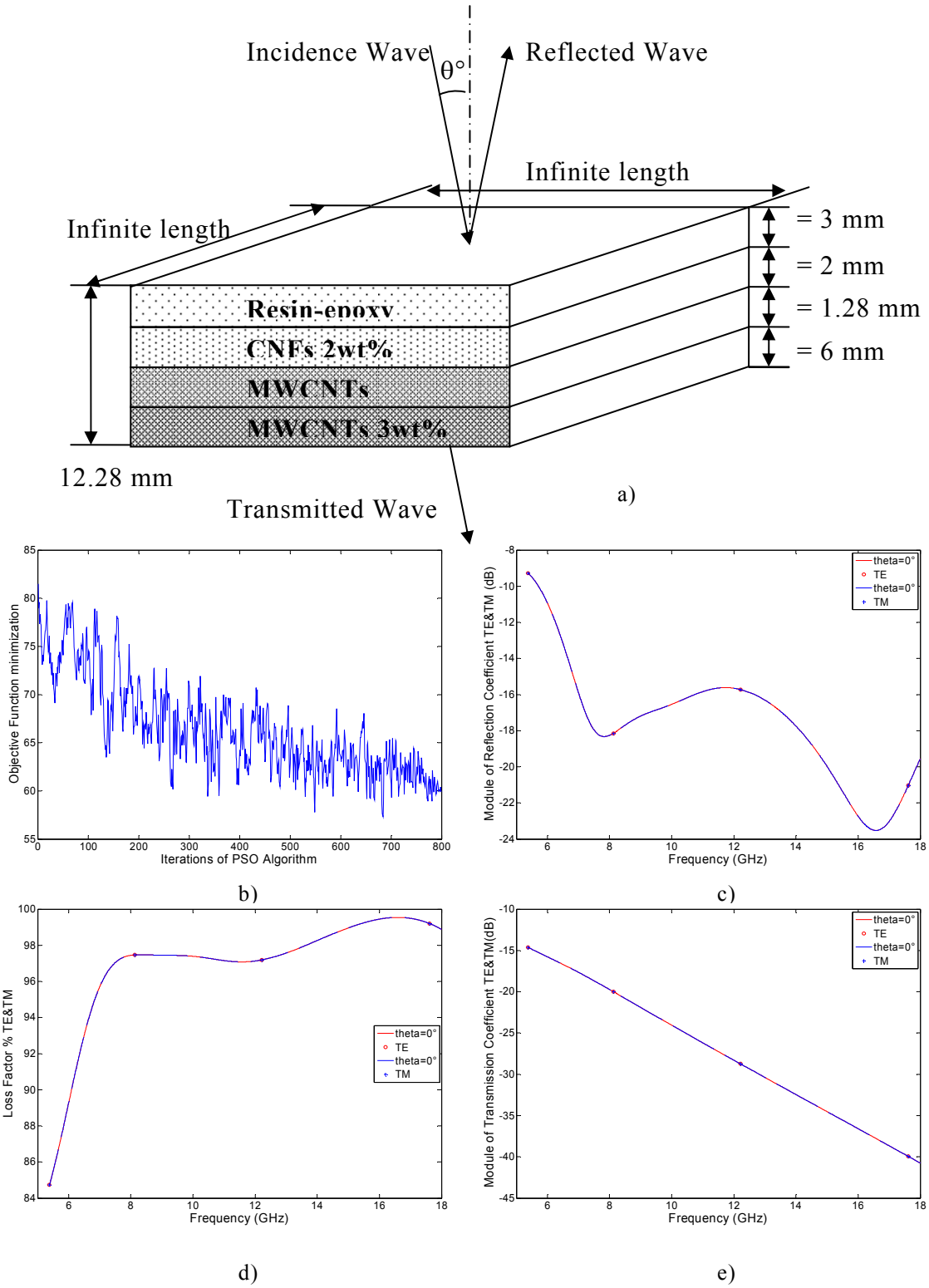

Fig. (4.5.3.3). a) Nanostructured composite MSS structure designed using Particle Swarm Optimization Algorithm; b) Convergence of PSO Algorithm in Objective function minimization; c) Reflection coefficient (dB); d) Loss Factor (%); e) Transmission coefficient; at 3 deg EM wave incidence.

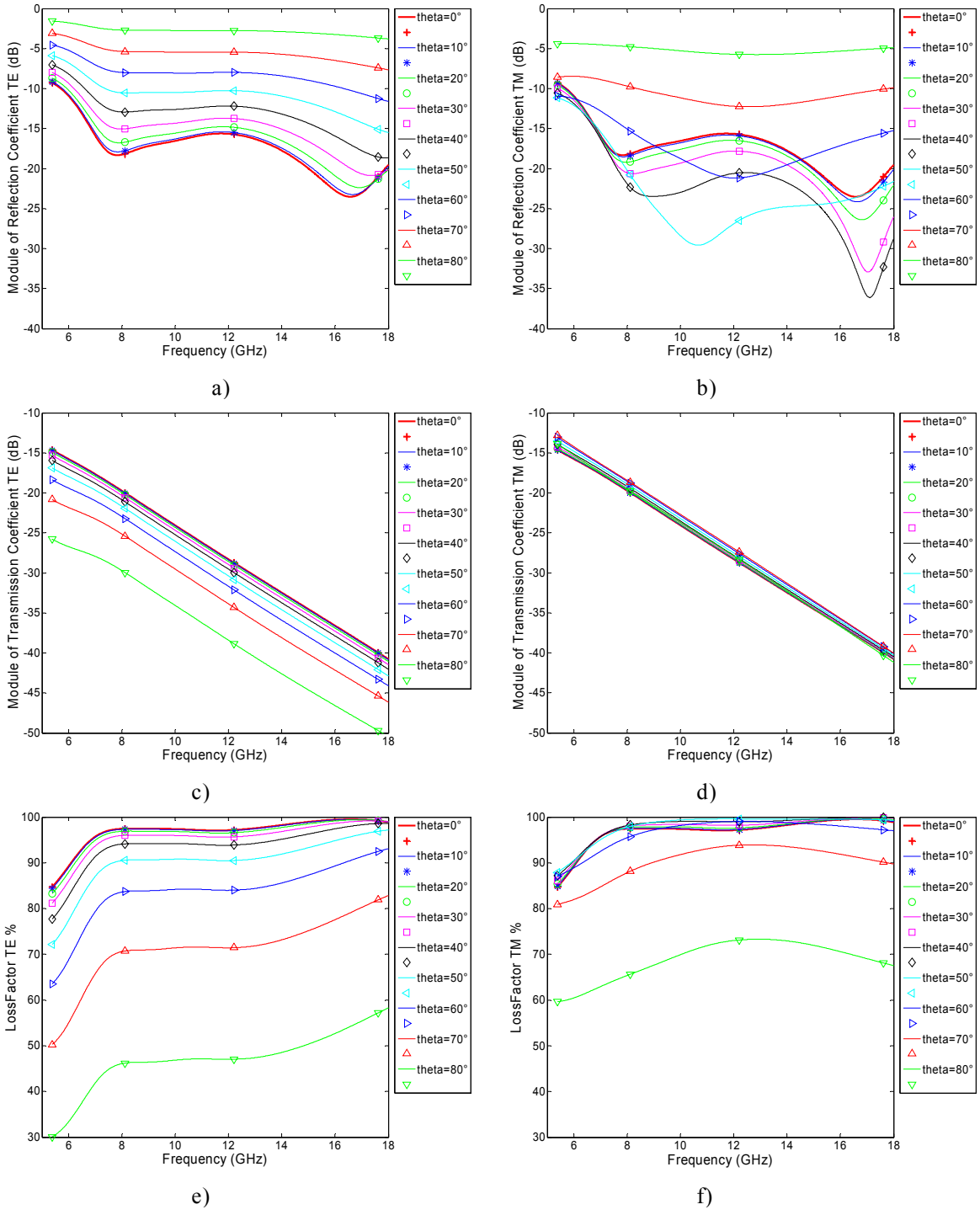

Fig. (4.5.3.4). Nanostructured composite MSS structure designed with Particle Swarm Optimization Algorithm:

a) Reflection Coefficient TE (dB); b) Reflection coefficient TM (dB); c) Transmission Coefficient TE(dB); d) Transmission Coefficient TM(dB); e) Loss Factor TE(%); f) Loss Factor TM(%), for EM wave incidence angles in the range 0-80 deg.

4.6 Absorber optimized using Winning Particle Optimization algorithm

Fig.(4.6.1). WPO based on the imitation of primordial life forms

4.6.1 Winning Particle Optimization principles

Winning particle optimization (WPO), is a very simple algorithm [15,21] where at each time epoch of evolution, particle which best fit the objective function (OF), is deputed to pilot the trajectory of the remaining nonintelligent particles within the multidimensional space of solutions.

In WPO, particles trajectories are simply defined by jumping of particles, in particular as coordinates sum or difference with respect to the current best fitting particle. The best particle represents the best position which defines the remaining particles search space and differently from the other particles, the best fitting particle is not subject to any displacement action at each iteration. It must remain in a fixed position while the other particles jump around it searching for a new best position in the space of solutions. At each WPO iteration, a new portion of the search space is explored and the same or most probably a new potential better fitting location for

each particle is always found. In Fig.(4.6.1.1), WPO flow chart is shown. At the beginning of the algorithm, particles are randomly distributed within the *n*-dimensional search space. After that at the first step of the WPO algorithm, evaluation of objective function (OF) for all the particles are computed. In the next step, particles are compared to each other using value of their objective function and the best fitting particle is marked with its proper index position, i.e., if fourth particle were the best fitting particle then such marker index would be 4. Each particle position is completely defined by its coordinates and their number represents the dimensionality of the space where particles jump in search of the optimal final solution. Trajectory of each particle, except that of the best fitting particle, is defined in the following way: if *m*-th-coordinate position of a certain particle P^k is lesser then the corresponding *m*-th-coordinate position of the current best particle PB^q, then the new *m*-th-coordinate position will result from the sum of particle and best particle *m*-th-coordinates; while if *m*-th-coordinate position of a certain particle P^k is greater then the corresponding *m*-th-coordinate position of the current best particle PB^q, then the new *m*-th-coordinate position will result from the difference between best particle and particle *m*-th-coordinates. Calling *q* the index of the best particle found at each iteration cycle, the condition which needs to be satisfied is $q \neq k$. Two different evolution strategies expressed by the (4.6.1.1) and (4.6.1.2), are possible; both of them define particles positions at $i+1$-th-iteration as a function of particles position at previous *i*-th-iteration. In the rest of work, method related to Eq.(4.6.1.1) has been applied.

$$P_m^k(i+1) = g \cdot PB_m^q(i) + \delta \cdot R_m \cdot P_m^k(i) \tag{4.6.1.1}$$

$$P_m^k(i+1) = PB_m^q(i) + g \cdot \delta \cdot R_m \cdot P_m^k(i). \tag{4.6.1.2}$$

where

$g = +1$ if $P_m^k(i) < PB_m^q(i)$

$g = -1$ if $P_m^k(i) > PB_m^q(i)$

k = Particle index in the range 1 - Particle Number

q = Best Particle index in the range 1 - Particle Number and $k \neq q$

$m = 1$ to n

n = Space Dimensions

R_m = random number in the interval [0 - 1]

δ = Convergenc e Parameter

i = current iteration

R is a random number in the closed range 0-1, which in is used to adjust the amount of jumps for each single coordinate particle dimension. Such randomization helps the search phase of optimal solution by conferring casuality to amplitude of jumps. Convergence parameter δ is defined later anyway it helps the final convergence of the WPO algorithm. Even thought mutation operation has not been applied on the subsequent reported optimizations (mutation=0%), it has to be noticed that mutation can be included in WPO algorithm. At the end of the WPO diagram, check of boundary conditions for new set of particles coordinates is required in order to avoid overcoming the admitted constraints. The entire loop cycle can be iterated several times in order to get the required objective function minimization.

In Fig.(4.6.1.2), a diagram explaining the boundary conditions checking procedure is reported, $BC_{\min}$ is the lower admitted constraints and $BC_{\max}$ is the upper admitted constraints.

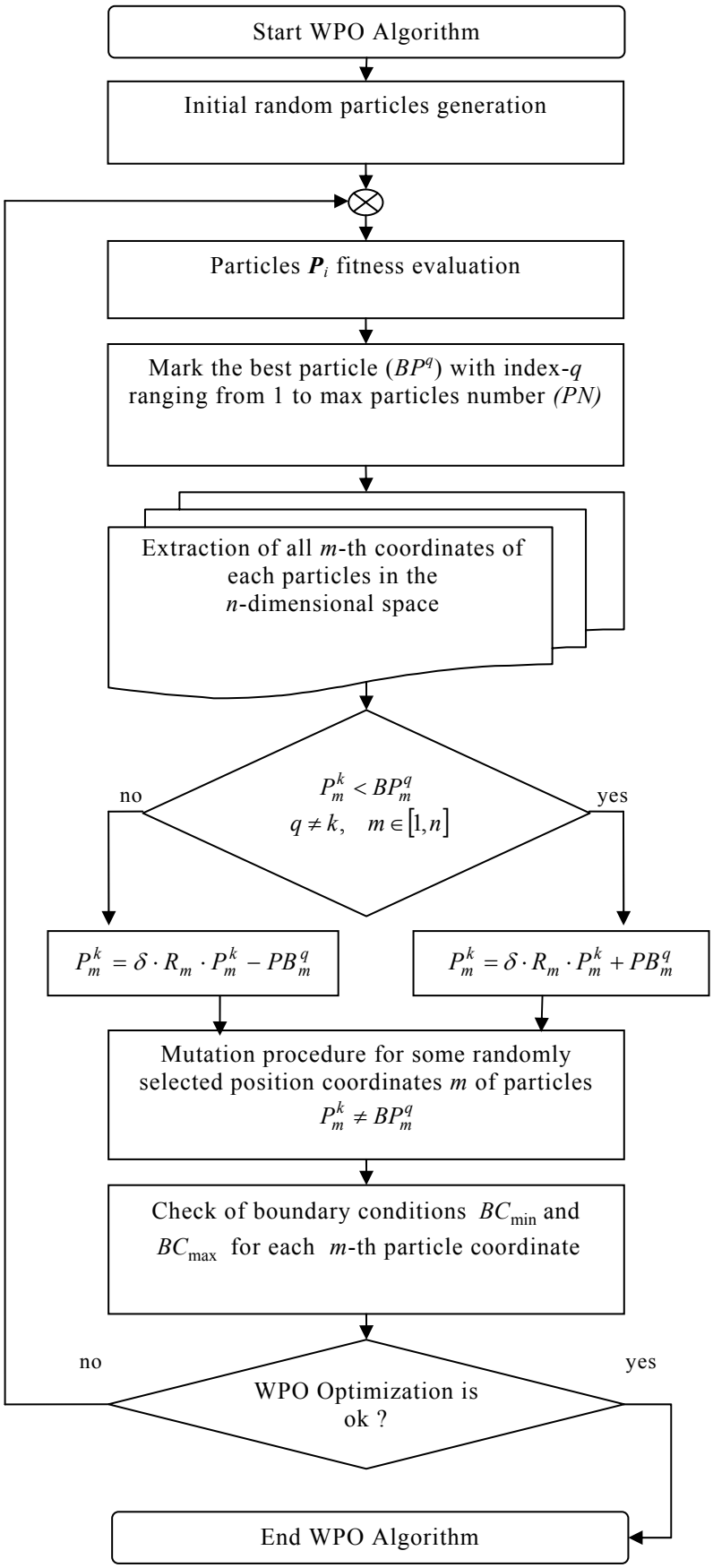

Fig. (4.6.1.1). WPO flow chart

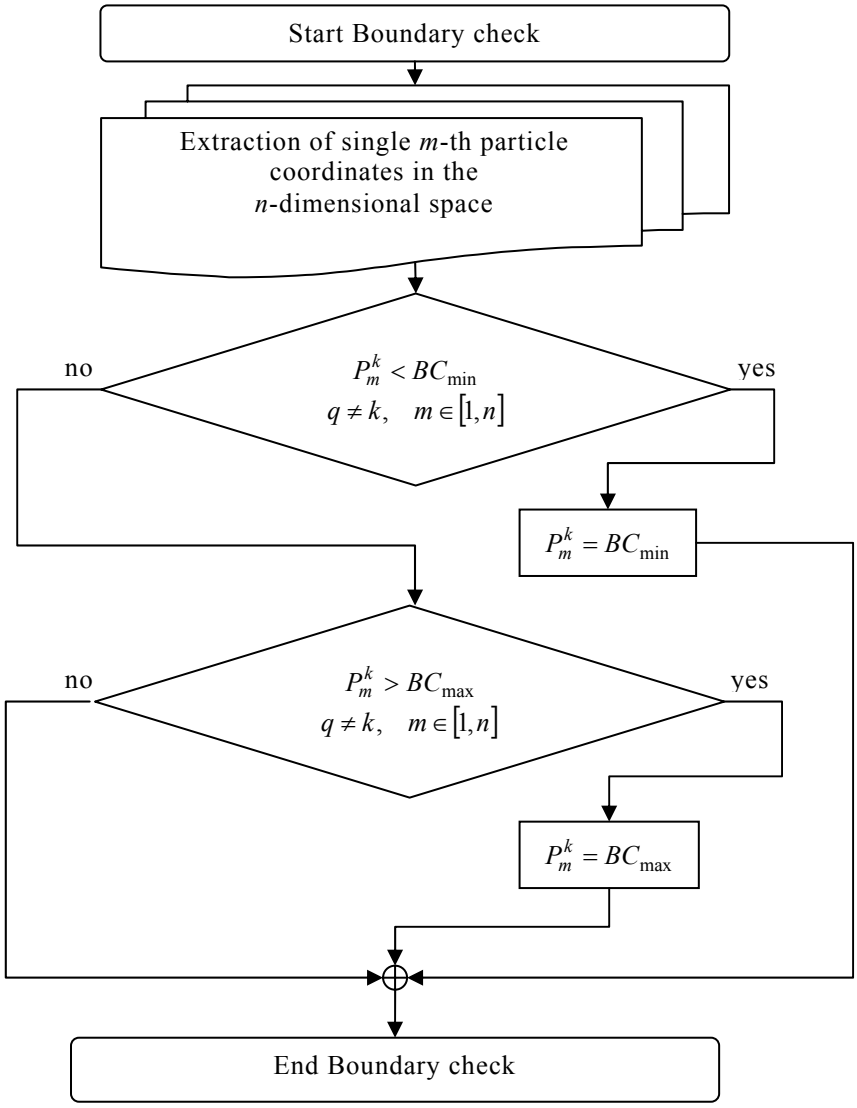

Fig. (4.6.1.2). Boundary conditions check

The idea of WPO based on quasi-random jumps of particles assures a quite effective method for solutions space exploration. In order to ease the convergence of WPO, a mechanism providing a progressive reduction of the *maximum* jumps amplitude, has been introduced and it is identified by the triplet δ, P, σ.

Even though WPO algorithm usually converges without using δ parameter, it remains useful in order to personalize the problem solving optimization too.
Calling *IN* the number of WPO iterations and supposing *i* the current *i-th* iteration, then the value of δ_i is given by Eq. (4.6.1.3).

$$\delta = \sigma\left(1 - \frac{i}{IN+1}\right)^{P}.$$

(4.6.1.3)

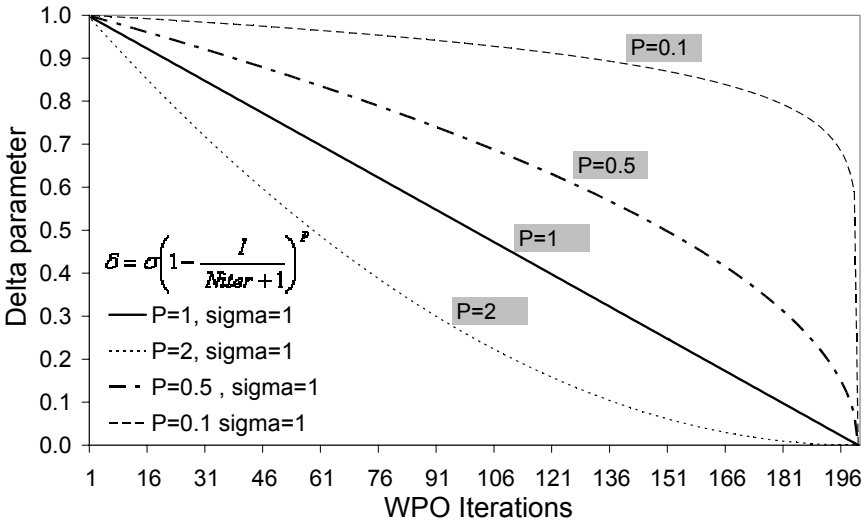

Fig. (4.6.1.4). Progressive reduction of jumps

In the Eq. (4.6.1.3), the meaning of σ,P parameters are in fast or slow convergence of the WPO algorithm. In particular the higher the σ, the greater the initial jumps amplitude and the greater the distances where particles will start to explore the search space. As far as P is concerned the higher its value, the faster the convergence to a suboptimal solution i.e., local *minimum* or *maximum*. The relationship is shown in Fig.4. The higher the current iteration number, the lower the δ parameter value.

In Fig. (4.6.1.4), a sequence of pictures, shows the convergence of WPO algorithm for some canonical test functions [40]: Sphere, Rastrigin, Griewank, Rosenbrock, Akley. Parameter δ, is decreased with the iterations number IN using $P=\sigma=1$. Two different scenarios are compared, the first referring to Iteration Number (IN)=500, Dimensions of Space Solution (DIM)=20, Number of exploring agents (Num Agents)=20; while the second refers to Iteration Number(IN)=500, Dimensions of Space Solution (DIM)=60, Number of exploring agents (Num Agents)=100.

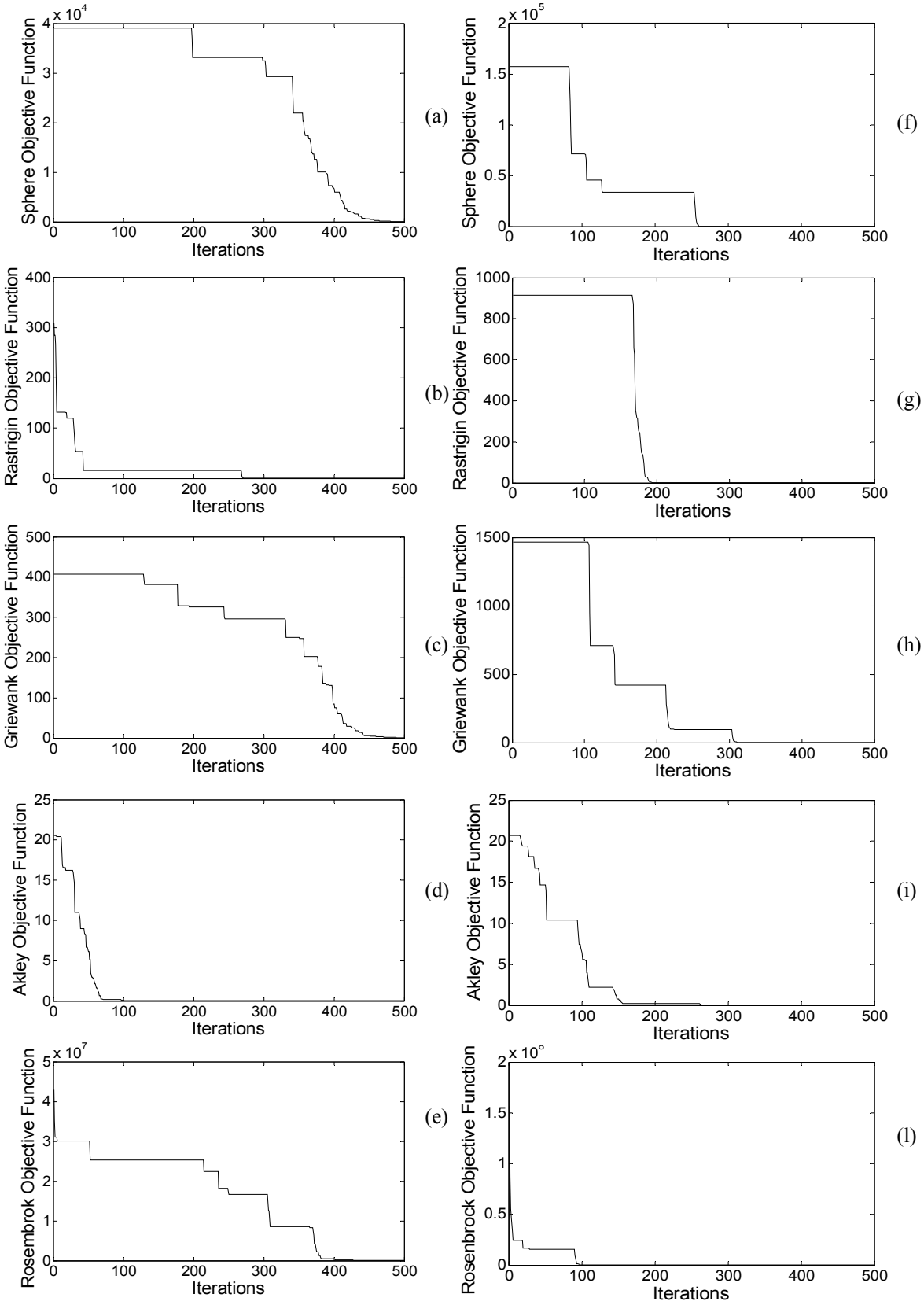

Fig. (4.6.1.4). a),b),c),d),e) Typical Objective Function minimization with: IN=500, DIM=20, AGENT=20 and

f),g),h),i),l) Typical Objective Function minimization with: IN=500, DIM=60, AGENT=100

In order to evaluate the robustness of WPO algorithm, for each test function, the algorithm as been tested repetitively for twenty times.

In Tab.(4.6.1.1) and (4.6.1.2), the mean and standard deviation values are shown for two different scenario, the first referring to Iteration Number(IN)=500, Dimensions of Space Solution (DIM)=20, Number of exploring agents (Num Agents)=20; while the second referring to Iteration Number(IN)=500, Dimensions of Space Solution (DIM)=60, Number of exploring agents (Num Agents)=100.

It can be notice that some convergence difficulties increases for Rosembrok test functions

TABLE (4.6.1.1)
WPO EVALUATION TEST: IN=500 , DIM=20,
NUM AGENT=20, RUN NUMBER=20

TEST FUNCTION	Theoretical Convergence value	WPO Mean Value	WPO Standard Deviation
Sphere	0	0	0
Rastrigin	0	0	0
Griewank	0	0	0
Rosembrock	0	58.1	0
Ackley	0	0	0

TABLE (4.6.1.2)
WPO EVALUATION TEST: IN=500 , DIM=60,
NUM AGENT=100, RUN NUMBER=20

TEST FUNCTION	Theoretical Convergence value	WPO Mean Value	WPO Standard Deviation
Sphere	0	0	0
Rastrigin	0	0	0
Griewank	0	0	0
Rosembrock	0	58.1	0
Ackley	0	0	0

4.6.2 Test Functions

In the evolutionary computation literature [41] there is a number of test functions which are used as benchmarks for contemporary optimization algorithms. In this study we used some of such functions, which has been subject of minimization A function is multimodal if it has two or more local optima. A function of variables is separable if it can be rewritten as a sum of functions of just one variable [42]. The separability is closely related to the concept of epistasis or interrelation among the variables of the function. The problem is even more difficult if the function is also multimodal. The search process must be able to avoid the regions around local minima in order to approximate, as far as possible, to the global optimum. The most complex case appears when the local optima are randomly distributed in the search space. The dimensionality of the search space is another important factor in the complexity of the problem [43]. A study of the dimensionality problem and its features was carried out by Friedman [44]. In order to evaluate the performance of the proposed WPO, we used five classical benchmark functions as given in Ref. [45]

4.6.2.1 Griewank Function

Is a continuous, multimodal function

- Number of variables: *n* variables.
- Definition:
- $$f_{GRIEWANCK} = \frac{1}{4000}\sum_{i=1}^{n} x_i^2 - \prod_{i=1}^{n} \cos\frac{x_i}{\sqrt{i}} + 1 \qquad x_i \in R^n$$ **(4.6.2.1.1)**
- Search domain*: $-600 \le x_i \le 600$, $i = 1, 2, \ldots, n$.*
- Number of local minima: several local minima.
- The global minima: $x^* = (0, \ldots, 0)$, $f(x^*) = 0$.
- MATLAB Code: download griew.m
- MATLAB Function graph: for $n = 2$.

The first function is Griewank function whose value is 0 at its global minimum (0,0,…,0) of (4.6.2.1). Initialization range for the function is [−600,600]. Griewank function has a product term that introduces interdependence among the variables. The aim is to overcome the failure of the techniques that optimize each variable independently.

The optima of Griewank function are regularly distributed. Since the number of local optima increases with the dimensionality, this function is strongly multimodal.
The multimodality disappears for sufficiently high dimensionalities (n > 30) and the problem seems unimodal.
In Fig.(4.6.2.1.1), a MATLAB visualization of Griewank Function is shown.

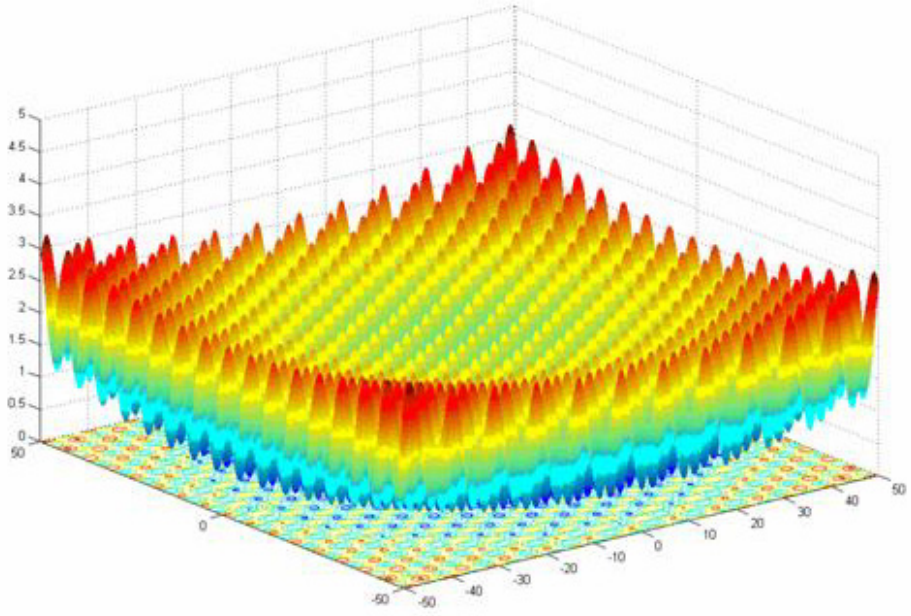

Fig.(4.6.2.1.1). Griewank Function

4.6.2.2 Rastrigin Function

Is a continuous, multimodal function

- Number of variables: *n* variables.
- Definition:
- $$f_{RASTRIGIN} = 10n + \sum_{i=1}^{n} \left(x_i^2 - 10\cos(2\pi x_i) \right) \qquad x_i \in R^n$$

(4.6.2.2.1)

- Search domain: $-5.12 \le x_i \le 5.12,\ i = 1, 2, \ldots, n.$
- Number of local minima: several local minima.
- The global minima: $x^* = (0, \ldots, 0),\ f(x^*) = 0.$
- MATLAB Code: download rast.m
- MATLAB Function graph: for $n = 2$

The second function is Rastrigin function whose value is 0 at its global minimum (0,0,…,0) of (4.6.2.2.1). Initialization range for the function is [−5.12,5.12]. This function is based on Sphere function with the addition of cosine modulation to

produce many local minima. Thus, the function is multimodal. The locations of the minima are regularly distributed. The difficult part about finding optimal solutions to this function is that an optimization algorithm easily can be trapped in a local optimum on its way towards the global optimum.

In Fig.(4.6.2.2.1), a MATLAB visualization of Rastrigin Function is shown.

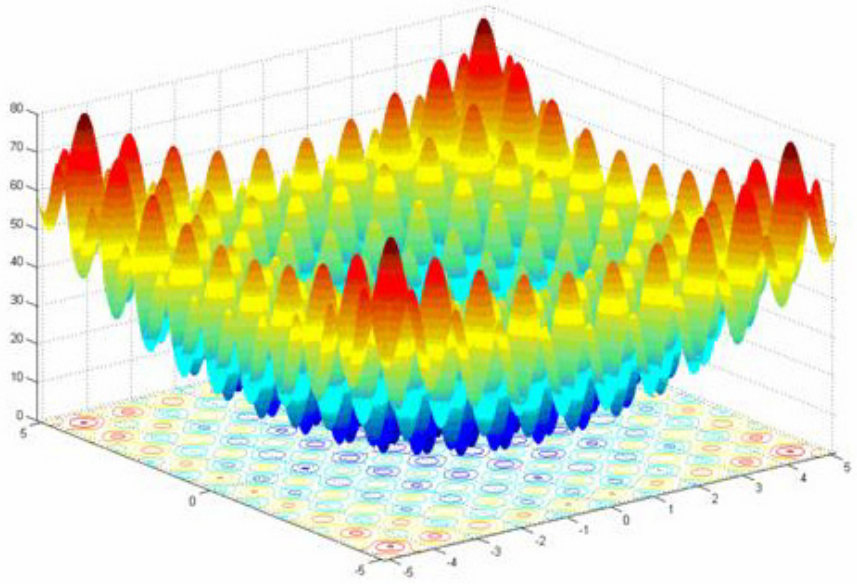

Fig.(4.6.2.2.1). Rastrigin Function

4.6.2.3 Sphere Function

Is a continuous, convex, unimodal function

- Number of variables: *n* variables.
- Definition:
- $$f_{SPHERE} = \sum_{i=1}^{n} x_i^2 \qquad x_i \in R^n$$

(4.6.2.3.1)

- Search domain: $-100 \leq x_i \leq 100,\ i = 1, 2, \ldots, n.$
- Number of local minima: no local minimum except the global one.
- The global minima: $x^* = (0, \ldots, 0),\ f(x^*) = 0.$
- MATLAB Code: download sphere.m
- MATLAB Function graph: for $n = 2$.

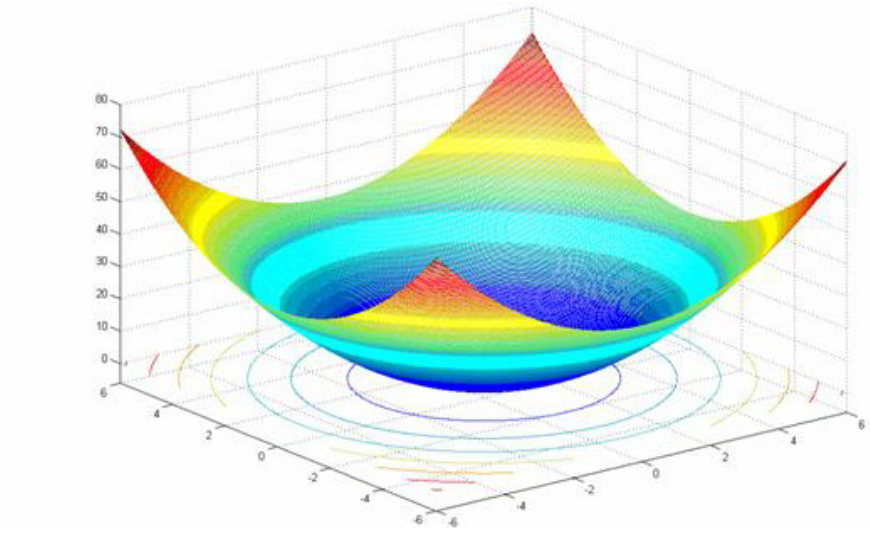

Fig.(4.6.2.3.1). Sphere Function

4.6.2.4 Schwefel Function

Is a continuous, unimodal function

- Number of variables: *n* variables.
- Definition:
- $$f_{SCHWFEL} = 418.9829n - \sum_{i=1}^{n}\left(x_i \sin\sqrt{|x_i|}\right) \qquad x_i \in R^n$$

(4.6.2.4.1)

- Search domain: $-500 \le x_i \le 500,\ i = 1, 2, \ldots, n.$
- Number of local minima: several local minima.
- The global minima: $x^* = (1, \ldots, 1),\ f(x^*) = 0.$
- MATLAB Code: download schw.m
- Function graph: for $n = 2.$

The fourth function is Schwefel function whose value is 0 at its global minimum (420.9867, 420.9867,…, 420.9867) in (4.6.2.4.1). Initialization range for the function is [−500, 500]. The surface of Schwefel function is composed of a great number of peaks and valleys. The function has a second best minimum far from the global minimum where many search algorithms are trapped. Moreover, the global minimum is near the bounds of the domain.

In Fig.(4.6.2.4.1), a MATLAB visualization of Schwefel Function is shown.

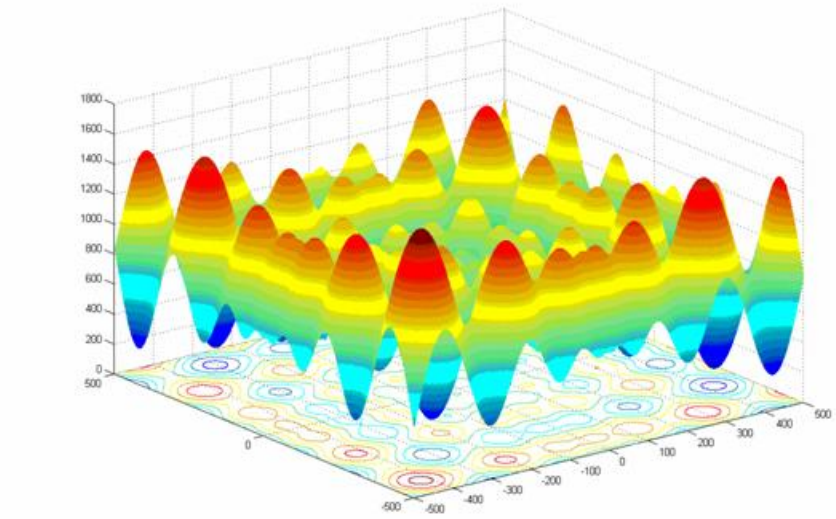

Fig.(4.6.2.4.1). Schwefel Function

4.6.2.5 Ackley Function

Is a continuous, multimodal function

- Number of variables: *n* variables.
- Definition:
- $$f_{ACKLEY} = 20 + e - 20e^{-\frac{1}{5}\sqrt{\frac{1}{n}\sum_{i=1}^{n} x_i^2}} - e^{-\frac{1}{n}\sum_{i=1}^{n}\cos(2\pi x_i)}$$ **(4.6.2.5.1)**
- Search domain: $-32.768 \le x_i \le 32.768,\ i = 1, 2, \ldots, n.$
- Number of local minima: several local minima.
- The global minimum: $x^* = (0, \ldots, 0),\ f(x^*) = 0.$
- MATLAB Code: download ackley.m
- MATLAB Function graph: for $n = 2.$

The fifth function is Ackley function whose value is 0 at its global minimum (0,0,…,0) (4.6.2.5.1). Initialization range for the function is [−32.768,32.768].Ackley has an exponential term that covers its surface with numerous local minima. The complexity of this function is moderated. An algorithm that only uses the gradient steepest descent will be trapped in a local optima, but any search strategy that analyses a wider region will be able to cross the valley among the optima and achieve better results. In order to obtain good results for this function, the search strategy must combine the exploratory and exploitative components efficiently.

In Fig.(4.6.2.5.1), a MATLAB visualization of Ackley Function is shown.

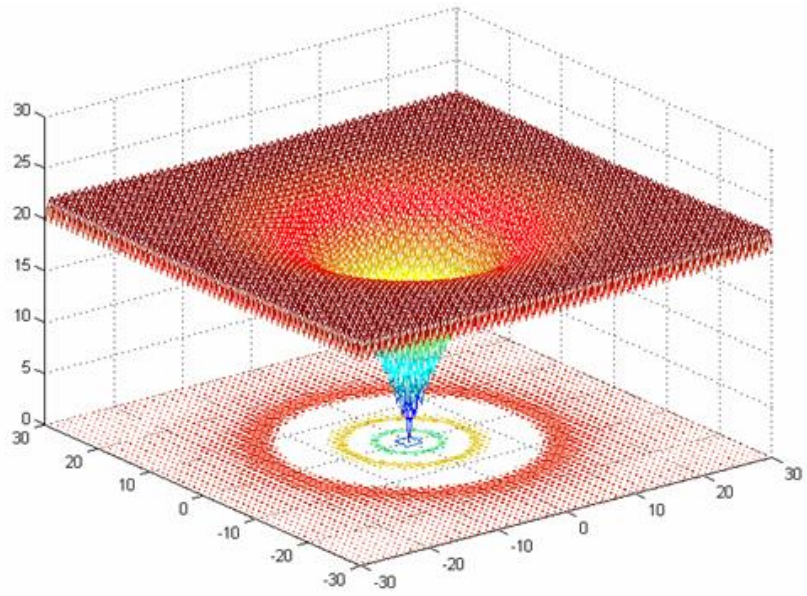

Fig.(4.6.2.5.1). Ackley Function

4.6.2.6 Rosenbrock Function

Is a continuous, unimodal function

- Number of variables: *n* variables.
- Definition:
- $$f_{ROSEMBROK} = \sum_{i=1}^{n-1}\left[100\left(x_i^2 - x_{i+1}\right)^2 + \left(x_i - 1\right)^2\right]$$

  (4.6.2.6.1)
- Search domain: $-15 \le x_i \le 15,\ i = 1, 2, \ldots, n.$
- Number of local minima: several local minima.
- The global minima: $x^* = (1, \ldots, 1),\ f(x^*) = 0.$
- MATLAB Code: download rosen.m
- MATLAB Function graph: for $n = 2$

The last function is Rosenbrock function whose value is 0 at its global minimum (1,1,…,1) in (4.6.2.6.1). Initialization range for the function is [−15,15]. The global optimum is inside a long, narrow, parabolic shaped flat valley. Since it is difficult to converge the global optimum, the variables are strongly dependent, and the gradients generally do not point towards the optimum, this problem is repeatedly used to test the performance of the optimization algorithms.

In Fig.(4.6.2.6.1), a MATLAB visualization of Rosenbrock Function is shown.

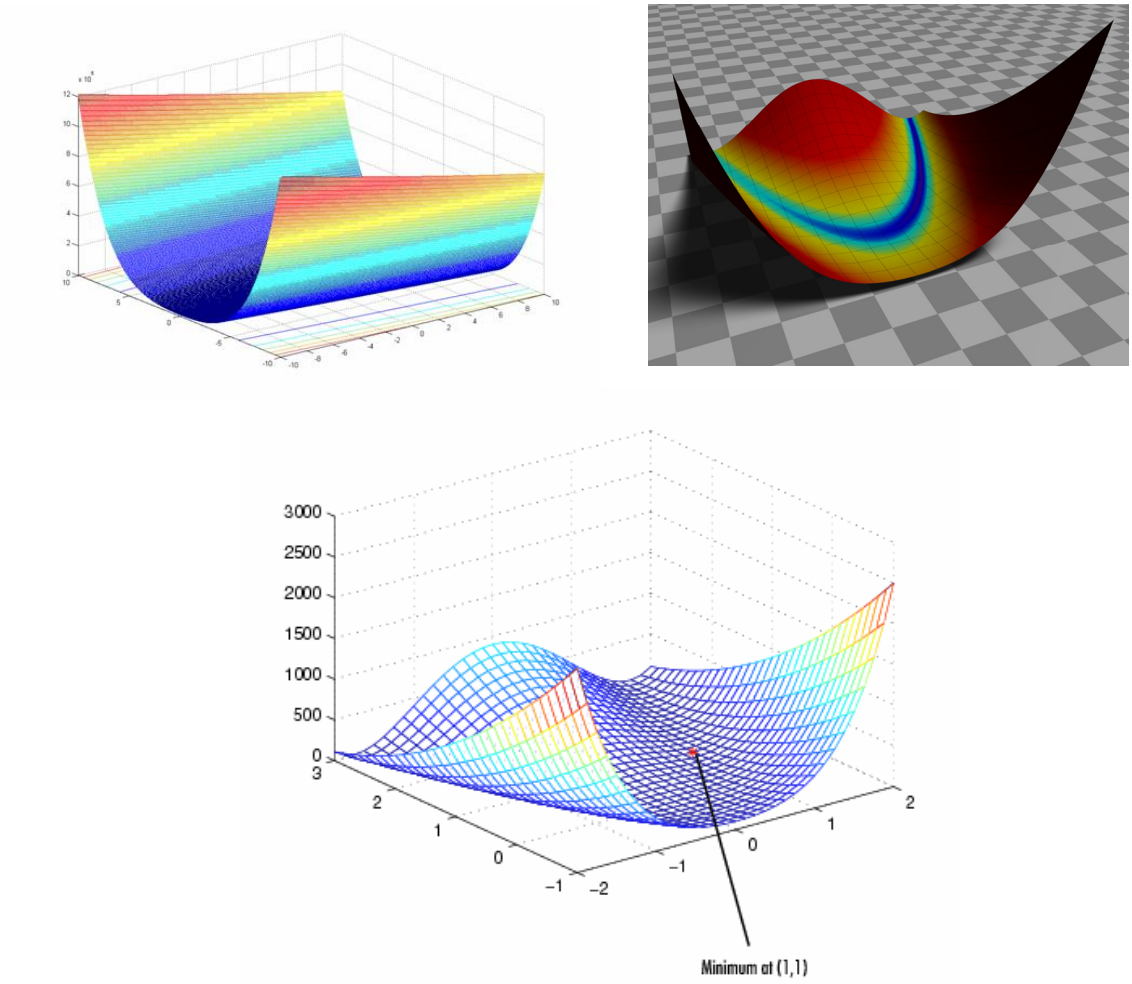

Fig.(4.6.2.6.1). Rosenbrock Function

4.6.3 Main differences between WPO, PSO and GA

WPO differentiates from GA since it does not have crossover operations and subsequent combination of particles (chromosomes in GA). As far as differences with PSO are concerned, WPO do not require any memorization (index and fitness) of the absolute best fitting particle obtained so far, in fact, in WPO, only the current iteration cycle is taken into account and only the index and not also the fitting value of best current particle is required to be stored. Another difference with PSO is that the remaining particles have no memory of their own previous best position. No memory means no intelligence and so no cognitive and social behavior like in PSO algorithm. In PSO, at each step of evolution, particles are intelligently guided towards the next better position by the particle velocity equation, which take into

account cognitive and social behavior. As a matter of fact, in PSO at each step of evolution, particles tend to gain a better position from fitness point of view, this is due to the intrinsic mechanism of PSO where the difference from best positions (Gbest. Pbest) and current positions (P) in velocity equation are used to update the current position. The immediate consequence is that PSO intrinsically tend to converge quasi-monotonically to asymptotic value as qualitatively shown in Fig. (4.6.1.6).

As far as WPO convergence mechanism is concerned, since it is intrinsically a nonintelligent method, it follows a more random approach in which particles positions are instantly determined only by their distribution around the temporally local best particle. Because of the particles jumping mechanism explained in previous section, a family of particles located at certain iteration, generally speaking, is not better then the previous family of particles from fitness point of view. Typical up and down alternating fashion of WPO convergence is shown in Fig. (4.6.1.7). This fact plays a role emphasizing the search space exploration phase, slowing down the convergence toward final global optimal solution. The immediate consequence of this slow convergence behavior are often lowest asymptotic values obtained in the minimization of OF with respect to GA and PSO.

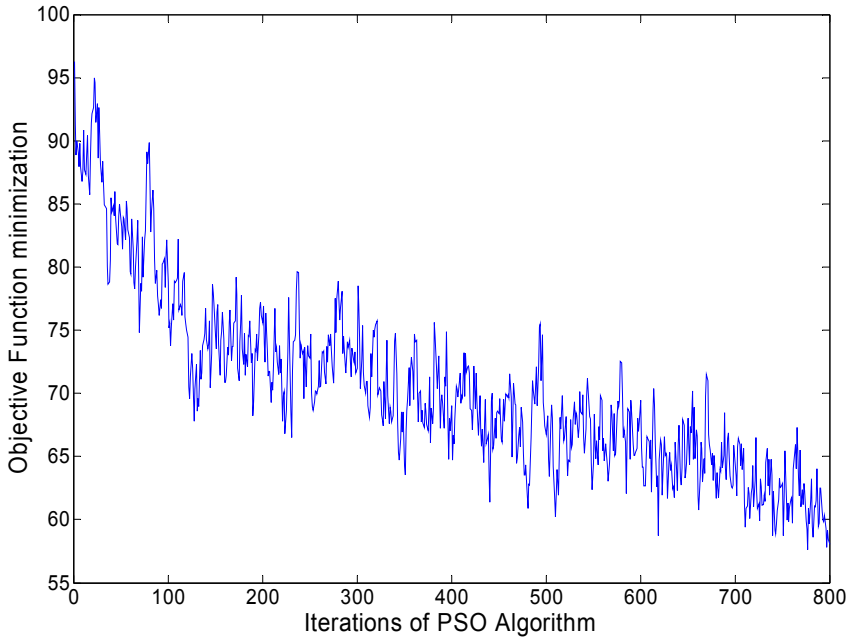

Fig. (4.6.1.6). Typical convergence of PSO Algorithm

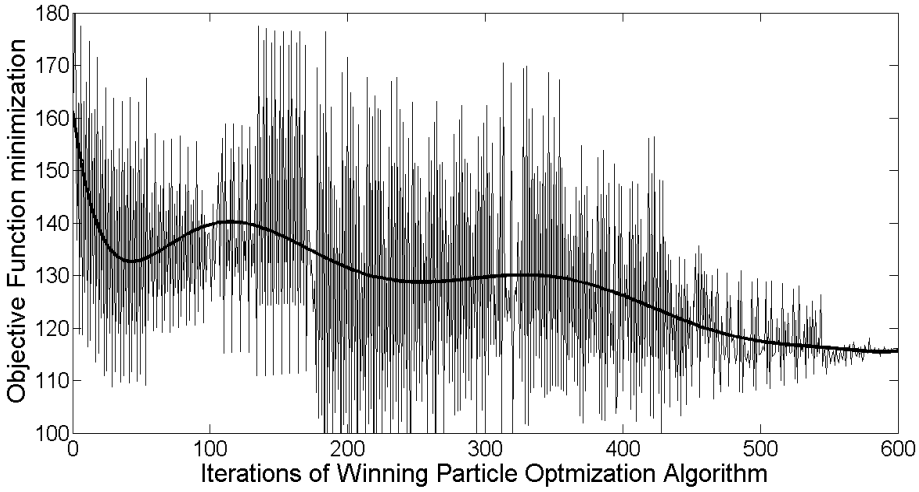

Fig. (4.6.1.7). Typical convergence of WPO Algorithm

4.6.4 Absorber model and Objective functions using Winning Particle Optimization

The formal definition of the objective function (OF) for TM and TE modes are the same already adopted in genetic algorithm (GA) and shown in Eq. (4.4.2.1) up to (4.4.2.5).

4.6.5 Final Absorbing structures optimized by Winning Particle Optimization

Two different absorbing structures are taken into account, the first is radar absorbing material (RAM) multilayer structure, whereas the second has double target of absorbing and shielding microwaves and has been called microwave-shielding structure (MSS).

RAM

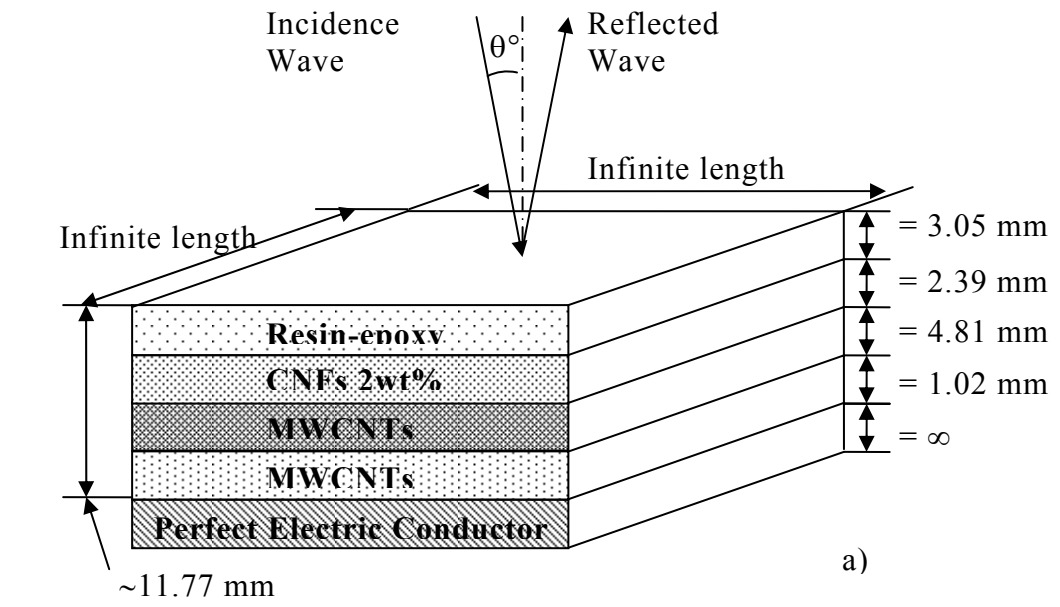

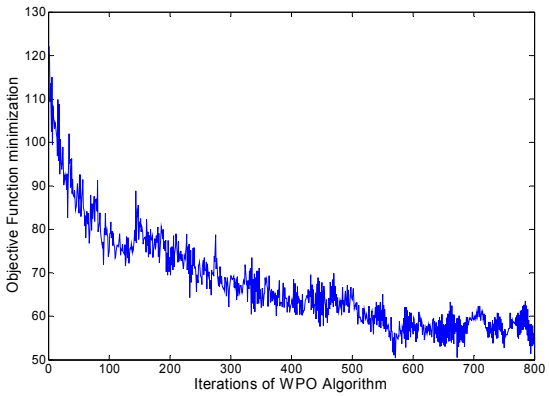

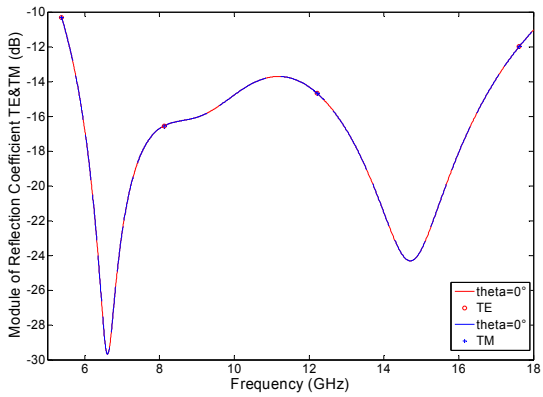

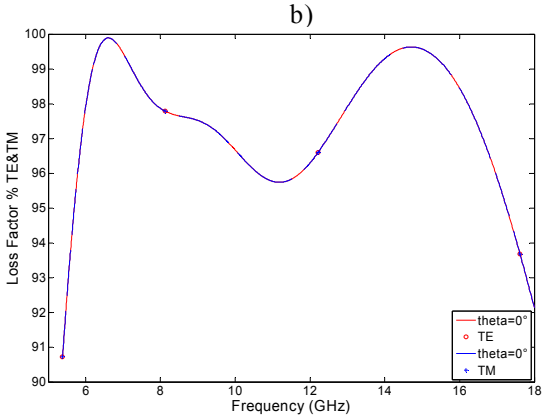

Fig. (4.6.5.1). a) Nanostructured composite RAM structure designed using Winning Particle Optimization Algorithm; b) Convergence of WPO in Objective Function minimization; c) Reflection coefficient (dB), and d) Loss Factor (%), for electromagnetic wave normally directed with respect to absorber surface.

In Fig. (4.6.5.2), multilayer absorber characterization for several incidence angles in the range 0 – 80 deg is shown.

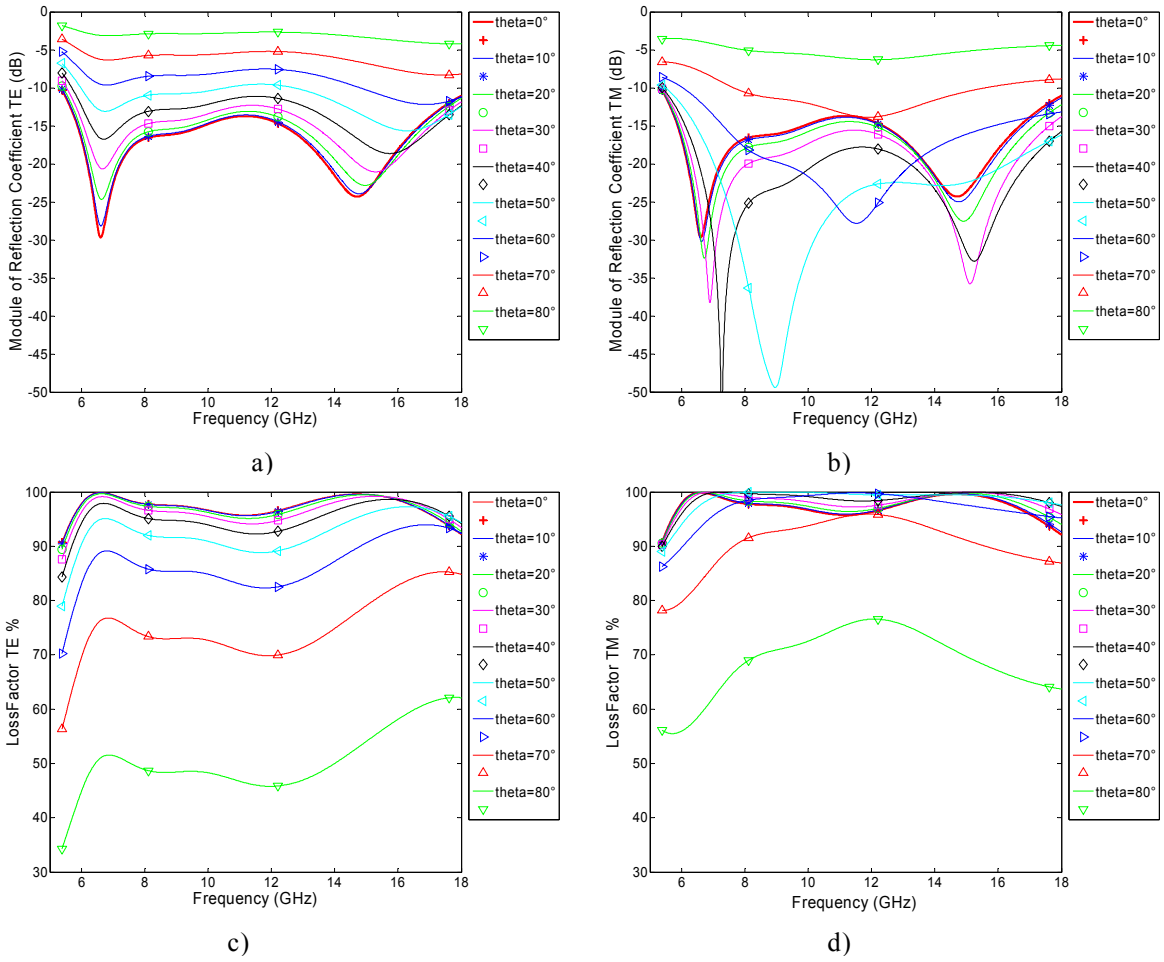

Fig. (4.6.5.2). Nanostructured composite RAM structure designed with Winning Particle Optimization Algorithm:

a) Reflection Coefficient TE(dB), b) Reflection Coefficient TM(dB); c) Loss Factor TE(%); d) Loss Factor TM (%), for electromagnetic wave incidence 0-80 deg.

Reflection coefficient TM (dB), shows values lower than that resulting from normal incidence of EM wave for frequencies around 7, 9, 12, 15 GHz. Such values are Brewster angle for lossy materials.

Loss Factor (%) remains above 95% for incidence angle up to 30 deg.

MSS

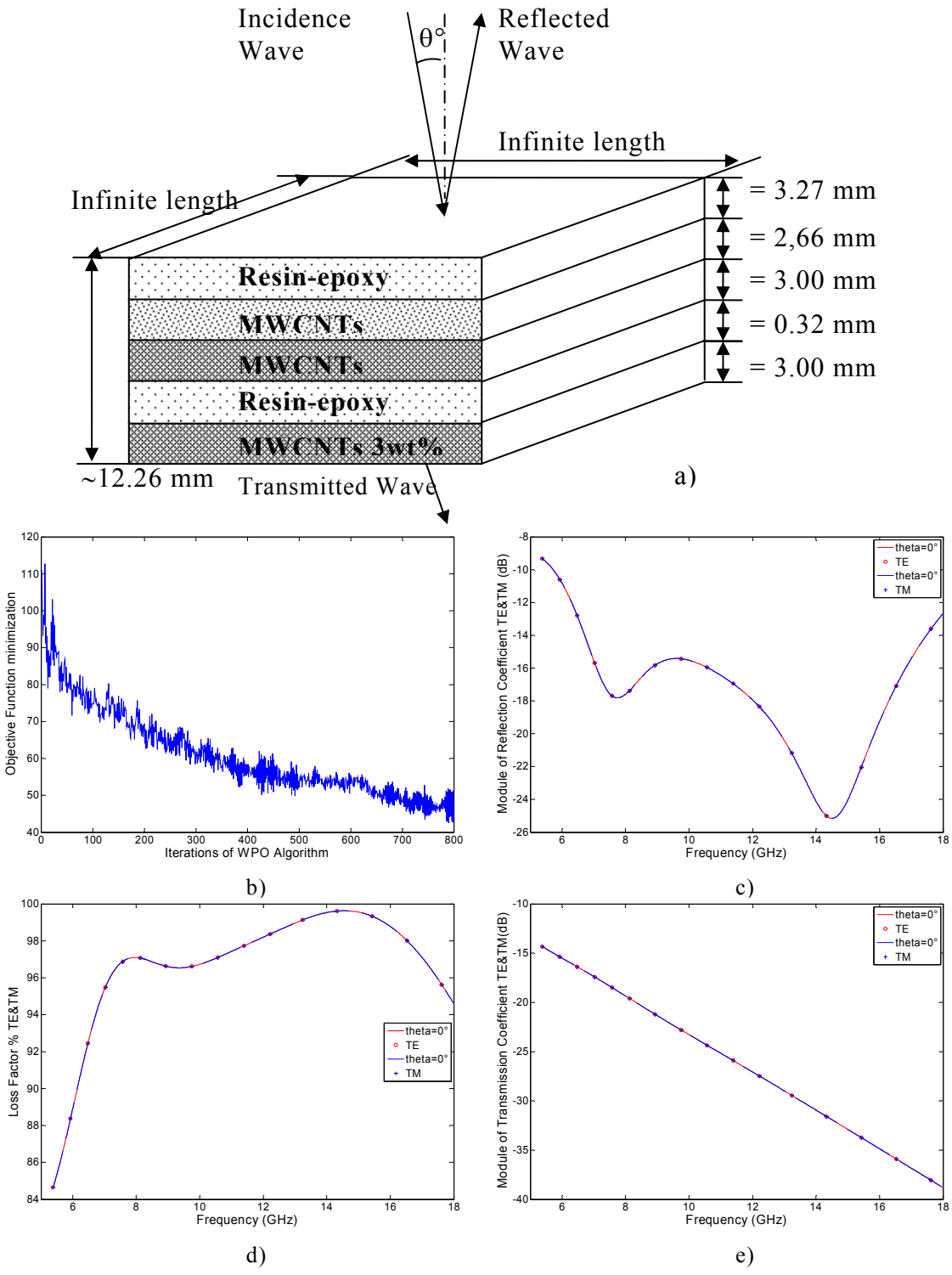

Fig. (4.6.5.3). a) Nanostructured composite MSS structure designed using Winning Particle Optimization Algorithm; b) Convergence of WPO in Objective function minimization; c) Reflection coefficient (dB); d) Loss Factor (%); e) Transmission coefficient; for electromagnetic wave normally directed with respect to absorber surface.

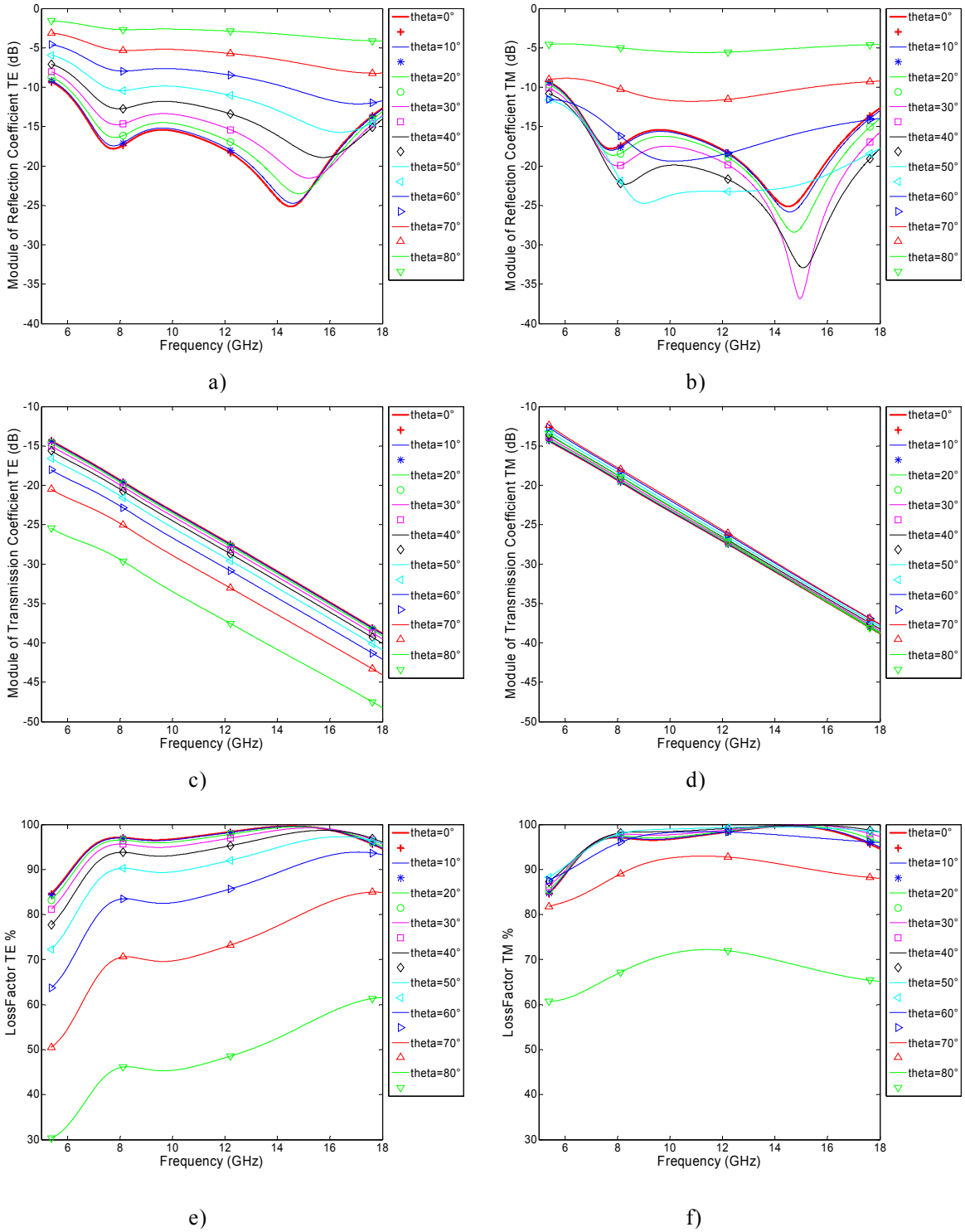

Fig. (4.6.5.4). MSS structure optimized using Winning Particle Optimization, a) Reflection Coefficient TE (dB); b) Reflection coefficient TM (dB); c) Transmission Coefficient TE(dB); d) Transmission Coefficient TM(dB); e) Loss Factor TE(%); f) Loss Factor TM(%), for EM wave incidence angles in the range 0-80 deg.

4.7 Conclusion

In this chapter, simulation of two type of absorber has been made using the same mathematical model of multilayer absorber but three different heuristic methods searching for optimal solution.

Algorithms, working on different strategies have been adopted and comparison of results shows that all absorbers are quite similar within each specific class i.e., RAM or MSS.

Both, thicknesses and absorbing relating properties are similar and this shows that at least, theoretically speaking, the absorber design method is valid.

A new algorithm, called WPO, has been introduced, deeply analyzed and applied for absorbers design.

Performances of all obtained absorbers seem to respect the proposed expectations.

If higher weight percentage of nanofillers would have been adopted then the overall thickness of absorbing structures would have been lower than 10 mm.

In the next chapter, practical realization of multilayer absorbers is presented and comparison between simulated and measured electromagnetic performances discussed.

Task of next chapter is to experimentally validate the mathematical model of absorber and the design method adopted.

4.8 Reference Table

[19] K. J. Vinoy and R. M. Jha. *Radar absorbing materials – from theory to design and characterization*, Kluwer academic publisher, Boston, 1996.
[20] Hossein Mosallaei, Yahya Rahmat-Samii, "RCS Reduction of Canonical Targets Using Genetic Algorithm Synthesized RAM," *IEEE Trans. Antennas Propagat.*, Vol. 48, N. 10, 2000.
[21] S. P. Rea, D. Linton, E. Orr and J. McConnell. "Broadband high-impedance surface design for aircraft HIRF protection," *IEE Trans. Microwaves, Antennas Propagat.*, Vol. 153, N.4, August, 2006.
[22] M. Liepe, B. Barstow and H. Padamsee. "First studies for a low temperature higher-order-mode absorber for the Cornell ERL prototype" in *Proc. of the Particle Accelerator conference,* Portland (USA), 2003.
[23] R. Carlile, A. Cavalli, W. Cramer, R. Hyde and W. Seidler. "Absorbing of energy from a large amplitude electromagnetic pulse by a collision less plasma," *IEEE Trans. Antennas Propagat.*, Vol. 27, N. 5, September, 1979.
[24] N. Li, Y. Huang, F. Du, X. He, X. Lin, H. Gao, Y. Ma, F. Li, Y. Chen, and P. C. Eklund "Electromagnetic Interference (EMI) Shielding of Single-Walled Carbon Nanotube Epoxy Composites," *Nano Lett.*, Vol. May, 2006.
[25] C.-M. Chang, J.-C. Chiu, W.-S. Jou, T.-L. Wu and W.-H. Cheng. "New package scheme of a 2.5-Gb/s plastic transceiver module employing multiwall nanotubes for low electromagnetic interference," *IEEE Journal Select. Topics Quant. Electro.*, Vol. 25, N. 5, September, 1989, pp. 1025-1031.
[26] C. L. Holloway, R. R. DeLyser, R. F. German, P. McKenna and M. Kanda. "Comparison of electromagnetic absorber used in anechoic and semi-anechoic chambers for emissions and immunity testing of digital devices," *IEEE Trans. EMC*, Vol. 39, N. 1, February, 1997, pp. 33-47.
[27] V. Bogush, T. Borbotko, N. Kolbun and L. Lynkov. "Novel composite shielding materials for suppression of microwave radiation," in *Proc. Microwaves, Radar & Wireless Communications (MIKON) International Symposium*, May, 2006, pp. 645–647.
[28] H. M. Musal and H.T. Hahn. "Thin-layer electromagnetic absorber," *IEEE Trans. Magn.*, Vol. 25, N. 5, September, 1989, pp. 3851-3853.
[29] I. M. De Rosa, R Mancinelli, F. Sarasini, M S. Sarto and A. Tamburrano. "Electromagnetic design and realization of innovative fiber-reinforced broad-band absorbing screens," to be published in IEEE Trans. EMC.
[30] D. M. Pozar, Microwave Engineering, third edition, John Wiley, 2005, pp. 174 - 180.
[31] D. Micheli, R. Pastore, C. Apollo, M. Marchetti, G. Gradoni, F. Moglie, V. Mariani Primiani, "Design of Broadband Quasi-Perfect Electromagnetic Absorbers using Carbon Nanostructure-Based Composites", *IEEE Nanotechnology*, sept 2010.
[32] Davide Micheli, Carmelo Apollo, Roberto Pastore, Mario Marchetti, "Nanomaterials in Radar Absorbing Material Design using Particle Swarm Optimization and Genetic Algorithm", *50th ISRAEL ANNUAL CONFERENCE ON AEROSPACE SCIENCES,* Conference tag number: 50IACAS-542, Feb 2010.
[33] Davide Micheli, Carmelo Apollo, Roberto Pastore, Mario Marchetti, "Modeling of Microwave absorbing structure using Winning Particle Optimization applied on Electrically Conductive Nanostructured composite material", ICEM 2010

–*XIX International Conference on Electrical Machines*, TPC-6: Theory, Modeling and Design, *Proc. IEEE*. RF-013846, Set. 2010.
[34] Ramo, Whinnery, Van Duzer, Fields and Waves in Communications Electronics, JohnWiley and Son, 1994.
[35] Davide Micheli, Roberto Pastore,Carmelo Apollo, Mario Marchetti, Gabriele Gradoni, Franco Moglie, Valter Mariani Primiani, "Carbon Based Nanomaterial Composites in RAM and Microwave Shielding Applications", *Proc. IEEE Nano*. June 2009 Genova.
[36] Dervis Karaboga · Bahriye Basturk, A powerful and efficient algorithm for numerical function optimization: artificial bee colony (ABC) algorithm, Springer, 2007.
[37] Pham, D.T., Karaboga, D. Intelligent Optimisation Techniques. Springer, London (2000)
[38] Holland, J.H.: "Adaptation in Natural and Artificial Systems". *University of Michigan Press*, Ann Arbor, MI (1975).
[39] Davide Micheli, Gabriele Gradoni, Roberto Pastore, Carmelo Apollo, Mario Marchetti, "Design of X-Band Microwave Shielding and Radar Absorbing Structures by Winning Particle Optimization Algorithm", submitted to *Elsevier*, 2010
[40] De Castro, L.N., Von Zuben, F.J.: "Artificial Immune Systems. Part I. Basic Theory And Applications". *Technical Report No. Rt Dca 01/99, Feec/Unicamp,* Brazil (1999).
[41] Kennedy, J., Eberhart, R.C.: "Particle swarm optimization2. In: *Proceedings of the 1995 IEEE International Conference on Neural Networks,* vol. 4, pp. 1942–1948. IEEE Service Center, Piscat away (1995).
[42] Fukuyama, Y., Takayama, S., Nakanishi, Y., Yoshida, H.: "A particle swarm optimization for reactive power and voltage control in electric power systems." *In: Proceedings of the Genetic and Evolutionary Computation Conference*, pp. 1523–1528. Orlando, Florida, USA (1999).
[43] Srinivasan, D., Seow, T.H.: "Evolutionary Computation", CEC '03, 8–12 Dec. 2003, 4(2003), Canberra, Australia, pp. 2292–2297.
[44] Karaboga, D., "An idea based on honey bee swarm for numerical optimization.", *Technical Report-TR06, Erciyes University, Engineering Faculty, Computer Engineering Department*, 2005.
[45] Basturk, B.,Karaboga,D.,"An artificial bee colony (ABC) algorithm for numeric function optimization.", *In: Proceedings of the IEEE Swarm Intelligence Symposium 2006*, Indianapolis, Indiana, USA, 12–14 May 2006.
[46] David E. Goldberg, "Genetic Algorithms in Search, Optimization, and Machine Learning", *Addison Wensley Publishing Company*, 1989.
[47] Davis.L;Ed. Hnadbook of Genetic Algorithms, Van Nostrand Reinhold, New York, 1991.
[48] Mitsuo Gen, Runwei Cheng, "Genetic Algorithms, 1st edition", *John Wiley & Sons*, 1999
[49] Ignace Bogaert, Femke Olyslager, Yoeri Ari¨en, Davy Pissoort, "Modeling and Optimization of Advanced Multilayered Absorbers", *Proceedings of the 37th European Microwave Conference, Department of Information Technology, Ghent University, Emerson & Cuming Microwave Products.*
[50] Paul Saville, Trisha Huber, Darren Makeiff, "Fabrication of Organic Radar Absorbing Materials", *Technical Report DRDC-Atlantic*, pp27-29 and pp213-230, 2005.

[51] J. Kennedy, R.C. Eberhart, and Y. Shi, "Swarm intelligence", *Morgan Kaufmann Publishers*, San Francisco, 2001.
[52] James Jennedy, Russell Eberhart. "Particle Swarm Optimization", *IEEE,* 1995.
[53] Maurice Clerc and James Kennedy, "The particle swarm - explosion, stability, and convergence in a multidimensional complex space", IEEE Trans. Evolutionary Computation, 6(1):58-73, 2002.
[54] Davis.L;Ed. "Hnadbook of Genetic Algorithms", *Van Nostrand Reinhold, New York,* 1991.
[55] Y.Shi and R.C.Eberhart, "Evolutionary optimization versus Particle Swarm Optimization : Philosophy and the Performance difference", *in Lecture Notes in Computer Science*, *Vol. 1447, Proc. 7th Int. Conf. Evolutionary Programming* -- Evolutionary Programming VII, Mar. 1998. pp. 600-610.
[56] Asanga Ratnaweera, Saman K. Halgamuge, Harry C.Waston. "Self-Organizing Hierarchical Particle Swarm Optimizer Whith Time-Varing Acceleration Coefficient", *IEEE TRANSACTION ON EVOLUTIONARY COMPUTATION VOL.8, NO. 3*, JUNE 2004.
[57] Dervis Karaboga, Bahriye Basturk, "A powerful and efficient algorithm for numerical function optimization: artificial bee colony (ABC) algorithm", *Springer*, 2007.
[58] Franciszek Seredynski1, Albert Y. Zomaya, and Pascal Bouvry," Function Optimization with Coevolutionary Algorithms",.
[59] Hadley, G., "Nonlinear and Dynamics Programming.", *Addison Wesley, Reading,* MA (1964).
[60] Boyer, D.O., Martnez, C.H., Pedrajas, N.G., "Crossover Operator for Evolutionary Algorithms Based on Population Features.", http://www.cs.cmu.edu/afs/cs/project/jair/pub/volume24/ortizboyer05a-html/Ortiz-Boyer.html.
[61] Friedman, J.H., "An overview of predictive learning and function approximation. From Statistics to Neural Networks, Theory and Pattern Recognition Applications", *NATO ASI Series F, vol. 136, pp. 1–61*. Springer, Berlin (1994)
[62] Srinivasan, D., Seow, T.H.: "Evolutionary Computation" , *CEC '03*, 8–12 Dec. 2003, 4(2003), Canberra, Australia, pp. 2292–2297.
[63] http://mf.erciyes.edu.tr/abc

Chapter 5

Experimental validation of theoretical Microwave absorbing structure design methods

5.1 Introduction

In this chapter experimental validation of theoretical modeling used to design microwave absorbing structures are shown and discussed.

The design method described in the previous chapter is able to predict behavior of two basic different structures: purely radar absorbing materials (RAM) and purely microwave shielding structure (MSS) but can also be quite effectively used to design multilayer structures able to satisfy both kinds of requirements i.e., to design a simultaneously absorbing and shielding structure.

Two different measurements setup are shown: the first known as *bistatic method* or *NRL arch*, is widely used in measuring reflection loss of microwave absorbing materials, the second is a new setup useful for shielding measurement effectiveness of materials for determined electromagnetic wave incidence angles. We called such technique as *directional shielding effectiveness measurement* (DSEM). In the following sections, both methods are presented and measurements results analyzed.

5.2 RAM testing using NRL Arch

The most known applications of microwave absorbing structures and materials are radar absorbing materials (RAM) applied in military applications and electromagnetic wave absorbers used in anechoic chambers. In order to test the reflection loss of nanostructured composite materials tiles, we configured an in-house NRL arch measurement system also called bistatic reflection method. In this configuration, two antennas are used for transmitting and receiving signals respectively, and the microwave reflectivity at different angles of incidence can be measured. The NRL Arch is the industry standard for testing the reflectivity of materials. Originally designed at the Naval Research Laboratory (NRL), the NRL Arch allows for quick, repeatable non-destructive testing of microwave absorbent materials over a wide frequency range.

Reflectivity is defined as the reduction in reflected power caused by the introduction of an absorbent material. This reduction in power is compared to a ‘perfect’ reflection which is approximated very well by the reflection of a flat metallic plate. An NRL arch consists of transmitting and receiving antenna which are oriented towards a metal plate. To measure normal incidence reflectivity the antennas are

located as close to each other as physically possible. Absorbent material is often used to minimize antenna cross talk. The antennas can be located anywhere on the arch to allow measurements of performance at off normal angles of incidence with the practical limitation of the ability to separate the signal from the material under test from the direct antenna to antenna cross talk. In general a network analyzer is used for bistatic measurements to provide both the stimulus and the measurement. Calibration is performed by measuring the resultant power reflecting off the metal plate over a broad frequency range. This is established as the 'perfect' reflection or 0 dB level (i.e. the reference level). The material under test is then placed on the plate and the reflected signal measured in dB. Time domain gating may be used to eliminate antenna cross talk and reduce the error introduced by room reflections.

Mainly measurements and comparison to simulations have been made in narrow frequency band and large frequency band.

In Fig.(5.2.1), Horn antennas in narrow X-band (8.2-12.4 GHz), and P-band (12-18 GHz), assembled on the NRL arch is shown.

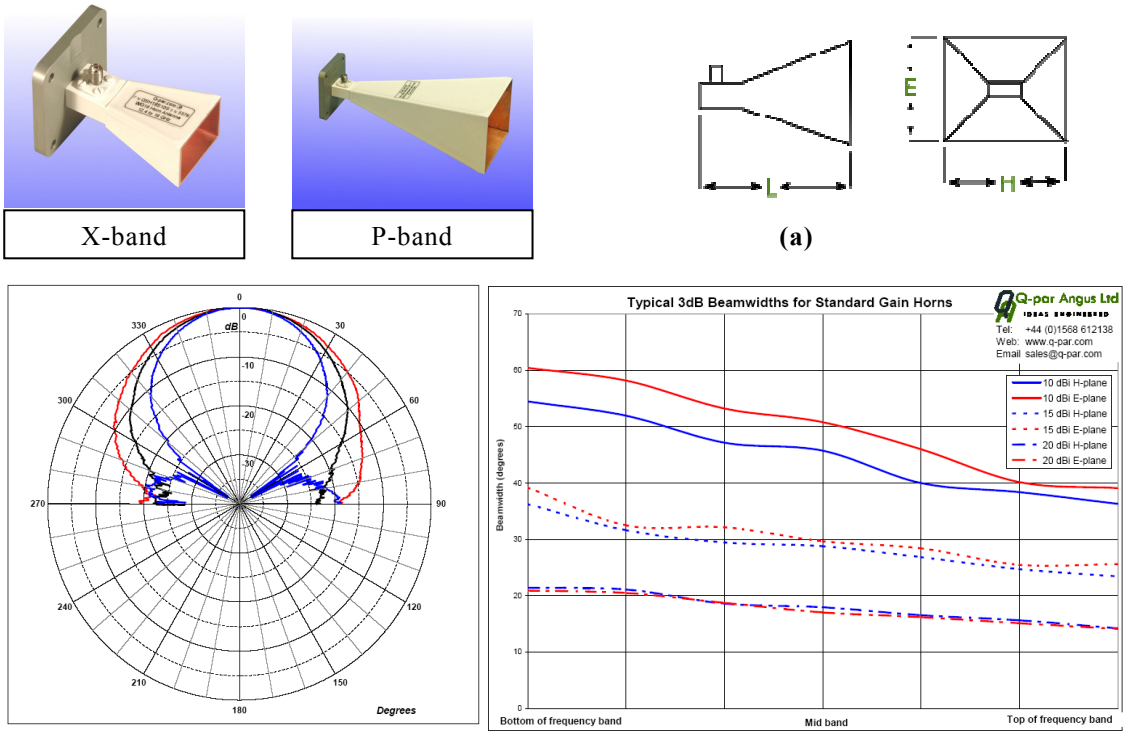

Fig.(5.2.1), a) Q-par Angus Antennas dimensions in mm, b) Typical Antenna Patterns for a 10 dBi Standard Horn - E-plane c) Typical 3dB Beamwidths for Standard Gain Horns

Narrow band Antennas and their characteristic are shown in Tab. (5.2.1)

Horn PART NO.	Frequency (GHz)	Gain (dBi)	Power (W c.w)	Connector Options	H (mm)	E (mm)	L (mm)	WG	WR	R
QSH16#10	8.2 - 12.4	10	120 (N)	N / SMA / F	45	35	75	16	90	100
QSH18#20	12.4 - 18.0	20	100 (N)	N / SMA / F	80	60	175	18	62	140

Tab. (5.2.1). Q-par Angus Antennas used in NRL ARCH system

Large frequency band Antenna is shown in Fig.(5.2.2). It is SATIMO Dual Ridge Horn SH2000 covering the frequency range 2 – 32 GHz. Satimo dual horns combine stable gain performance and low VSWR with wide band frequency operation. The horns are single linearly polarized with excellent cross-polar discrimination, ideal as reference antennas for gain calibration of antenna measurement systems or as wideband probes in classical far field test ranges.

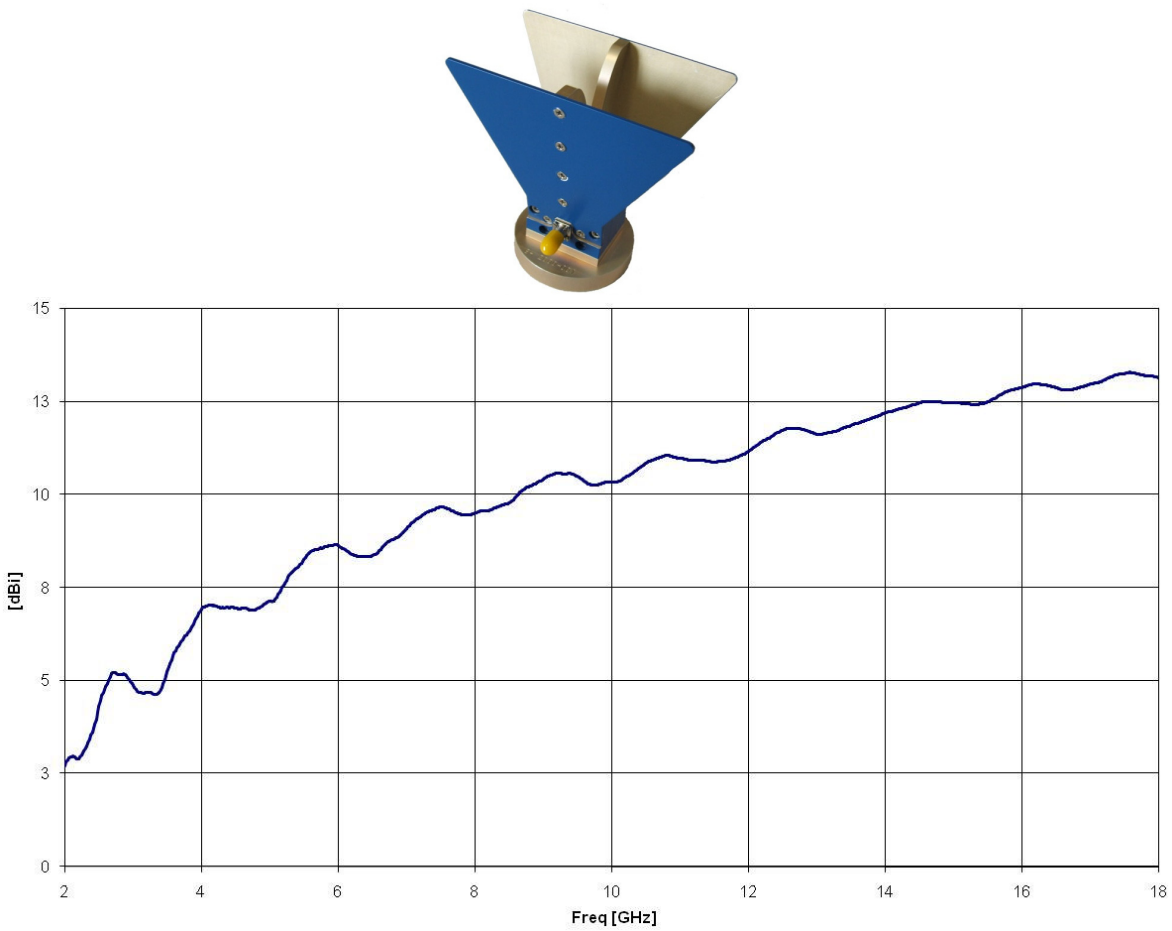

Figure 5.2.2: Typical boresight gain with frequency of SATIMO Dual Ridge Horn SH2000.

In Fig.(5.2.3), the design of the in-house manufactured NRL arch is shown. CAD picture take into account all dimensions required for far field or near-far field conditions using the above horn antennas in the frequency range 2 - 18 GHz.

$$Farfield = \frac{2\times D^2}{\lambda} = \frac{2\times D^2 \times f}{c} = \frac{2\times\left(45\times10^{-3}\right)^2\times18\times10^9}{3\times10^8} \cong 0.24 \quad m$$
$$ArchRay > 5\times Farfield$$

(5.2.1)

Using this configuration, properties of materials at different electromagnetic wave incidence directions can be evaluated. It should be noticed that in bistatic reflection measurements, the reflection is dependent on the polarization of the forward wave. Forward TE and TM waves usually result in different reflection coefficients. Besides, special calibration is needed for free-space bistatic reflection measurements [1],[2].

In Fig.(5.2.4) bistatic measurement system and the tile in composite material is shown. In this configuration, bistatic measurement system is based on Agilent software 8571E (material measurement), and Agilent PNA-L vector analyzer. Antennas Q-par Angus Ltd and are in the range 8-12 and 12-18 GHz. Calibration of the NRL bistatic system, is made taking a reference in reflection when sample holder is empty i.e., without composite material tile, (aluminum plate).

Measurement of a known sample consisting in ECCOSORB AN73 absorber (www.eccosorb.com), has been performed in order to be aware about errors in the NRL measurement setup. Confidence of measurements was within 2 dB interval with respect to reflection properties declared in the ECCOSORB data sheet.

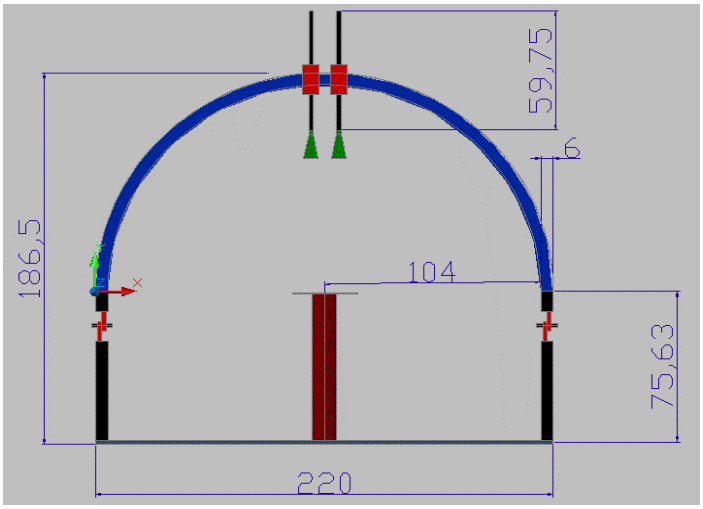

(a)

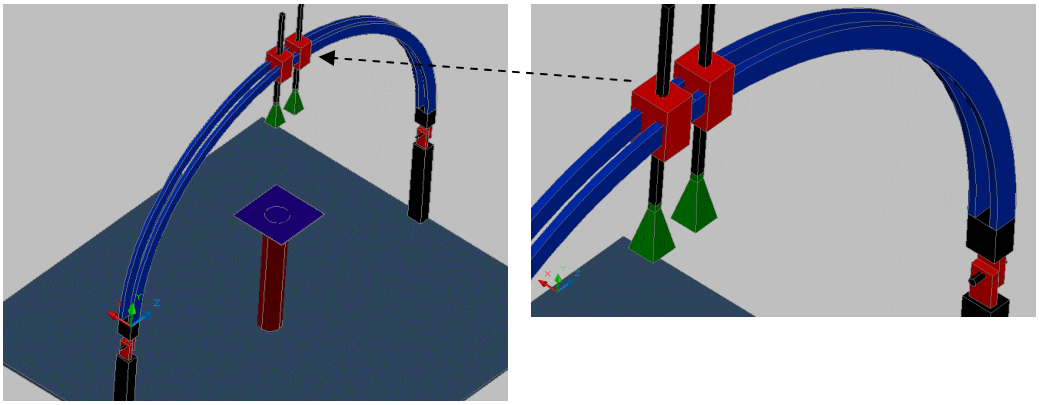

(b)

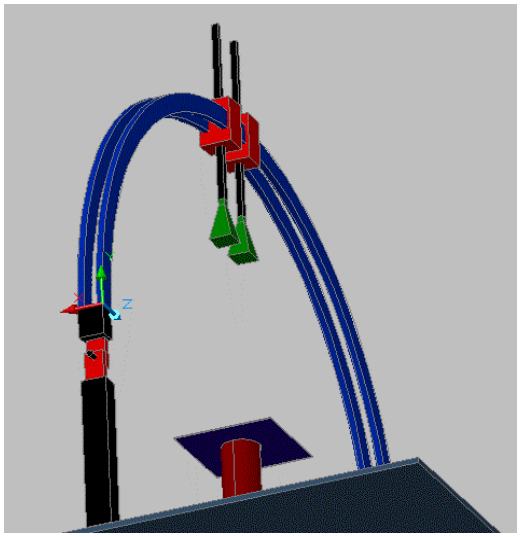

(c)

Fig. (5.2.3). a) bistatic measurement system scheme, b,c) 3D view of manufactured bistatic measurement system

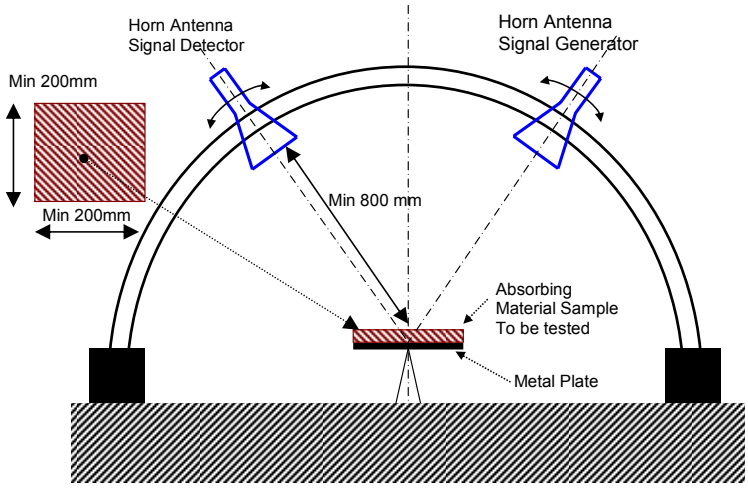

(a)

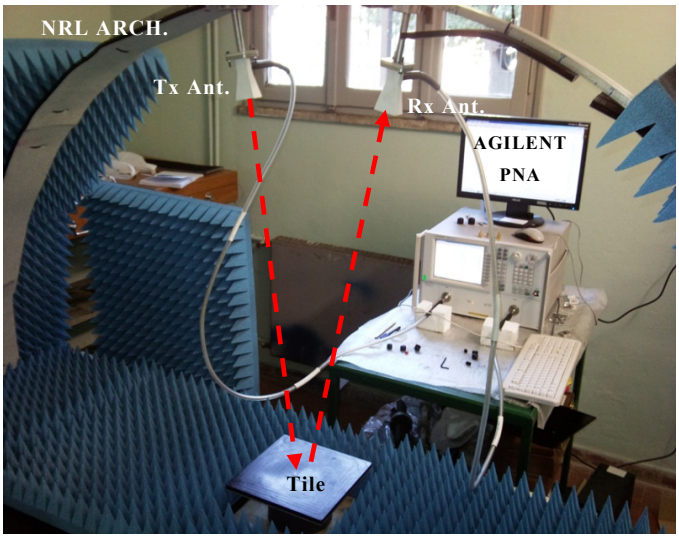

(b)

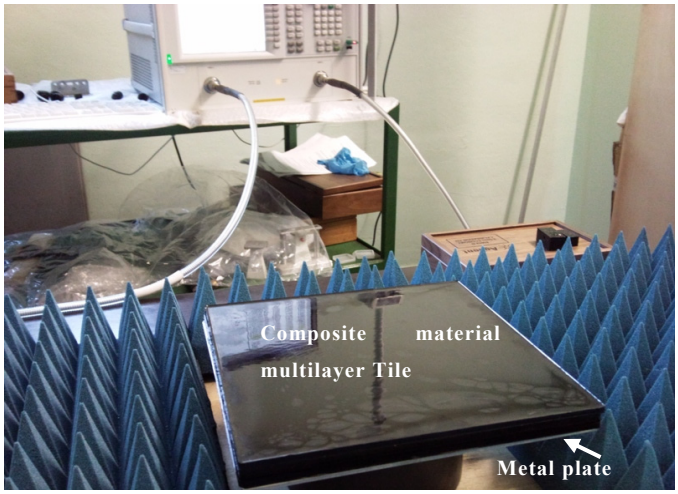

(c)

Fig. (5.2.4). a) bistatic measurement system sheme, b) bistatic measurement system located at Sapienza University of Rome, DIAEE, (www.saslab.eu); c) zoom of tile placed above the metal plate of bistatic measurement system.

In order to experimentally validate the mathematical model and the design method described in previous sections, we designed and tested different topologies of multilayer square tiles.

5.2.1 10.9 mm X-band RAM made of Epoxy-resin and Micrographite

The first RAM tile is completely based on graphite. The graphite based tile was built as composite material adopting only graphite in weight percentage respectively of 10; 5; 15 wt% with respect to epoxy-resin. The tile structure and the dimensions are schematically shown in Fig. (5.2.1.1).

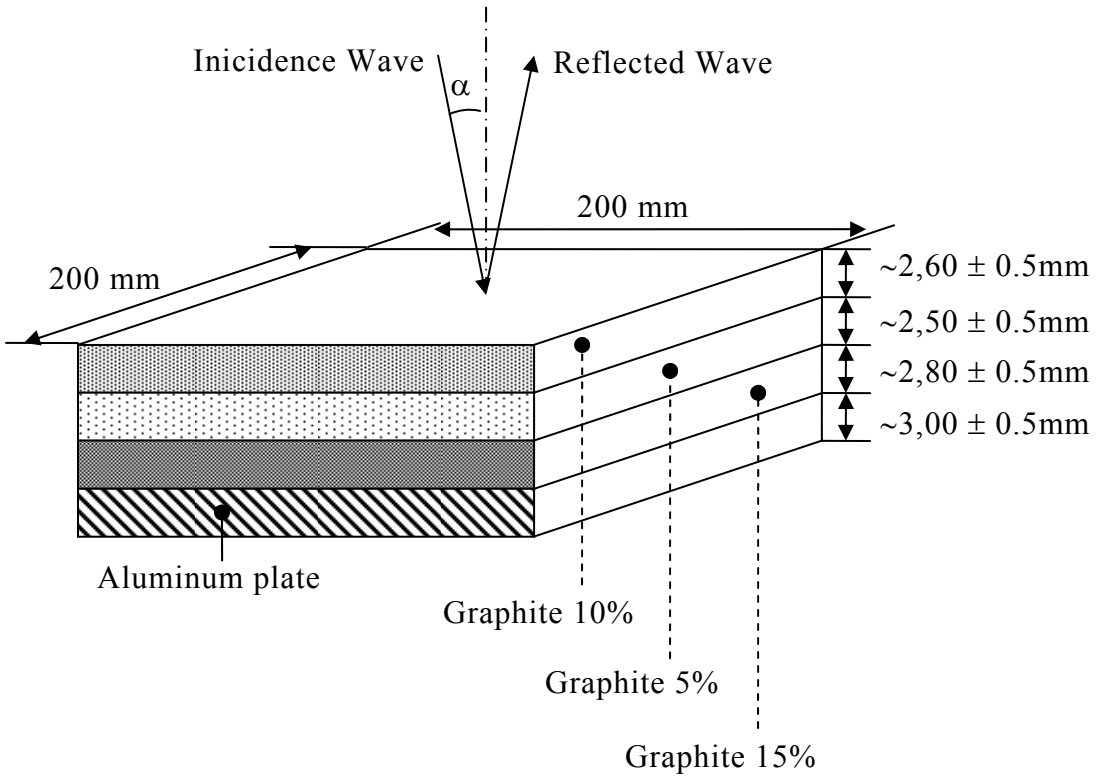

Fig. (5.2.1.1). 10.9mm Graphite based tile RAM 200x200 mm

In Fig.(5.2.1.2), comparison between simulated and measured reflection loss in dB (RL) is shown. It can be noticed a cross point around 11.8 GHz. The behavior of simulations and measurements curves is similar and in the same range of values. The average difference in the range 1÷3 dB is a good approximation in such type of

measurements. Above all, great misalignment seems to be due to the practical manufacturing process of multilayer structure. In fact, for low values of incidence angle (10 deg), TE and TM reflection loss should be quite similar. Instead, measurement shows a difference explainable if tolerances were taken into account.

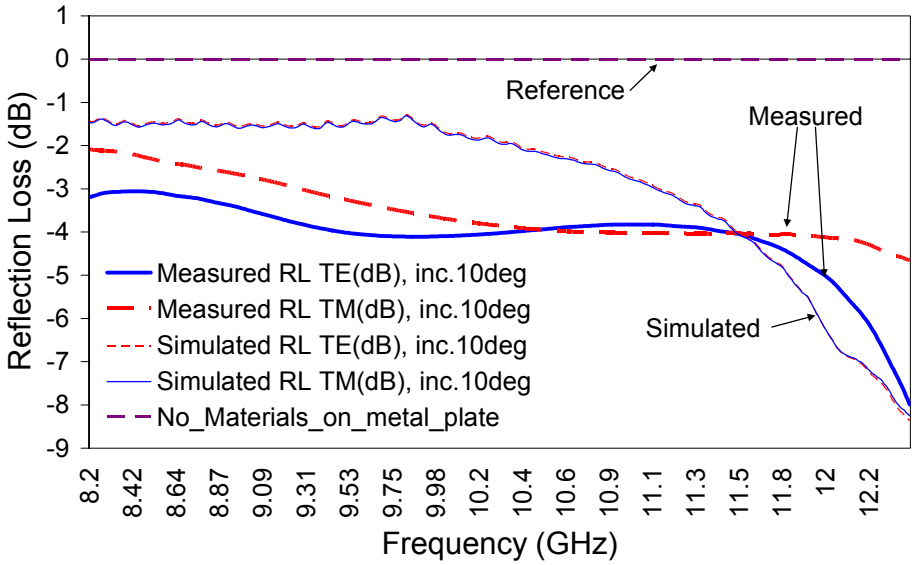

Fig.(5.2.1.2). Comparison between simulated and measured RAM based on three layers of graphite for incidence angle of 10 deg

Tolerances in question are mainly:

A) Differences in thickness along sides of each layers (due to manufacturing errors);

B) Non perfect homogeneous dispersion of carbon powders within each composite material layer (due to manufacturing errors);

C) Errors in composite materials dielectric permittivity characterization (due to errors in waveguide measurements and conversion of dielectric permittivity).

D) NRL arch measurements accuracy, which increases using lens antennas and or larger tile (our scenario is with tile 200×200 mm using usual horn antennas).

After a lot of trials and tiles manufacture and tests we estimated the following errors contributions and the accuracy in the 95% of tests:

$$Accuracy \cong \sqrt{A^2 + B^2 + C^2 + D^2} \cong \sqrt{2.5^2 + 1.5^2 + 2.5^2 + 2^2} \cong 4.3dB$$

(5.2.1.1)

5.2.2 6.9 mm X-band RAM made of Epoxy-resin and MWCNTs

The second RAM multilayer structure is based on Epoxy-resin and MWCNTs samples using respectively incidence angle of 10 deg and 5 deg. Measurements and simulations have been performed for TE and TM mode in the X-band (8.2-12.4 GHz).

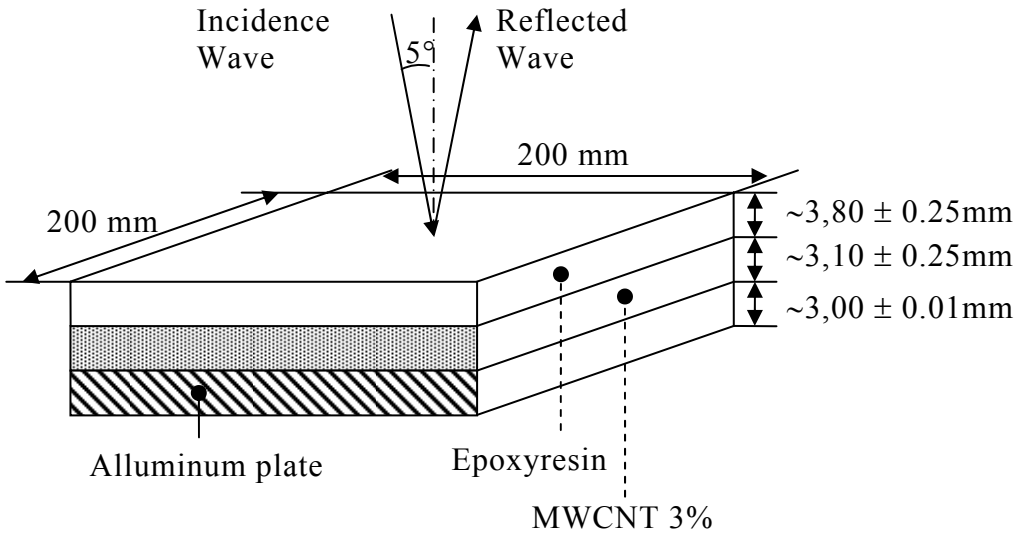

Fig. (5.2.2.1). 6.9mm Epoxyresin and MWCNTs based RAM

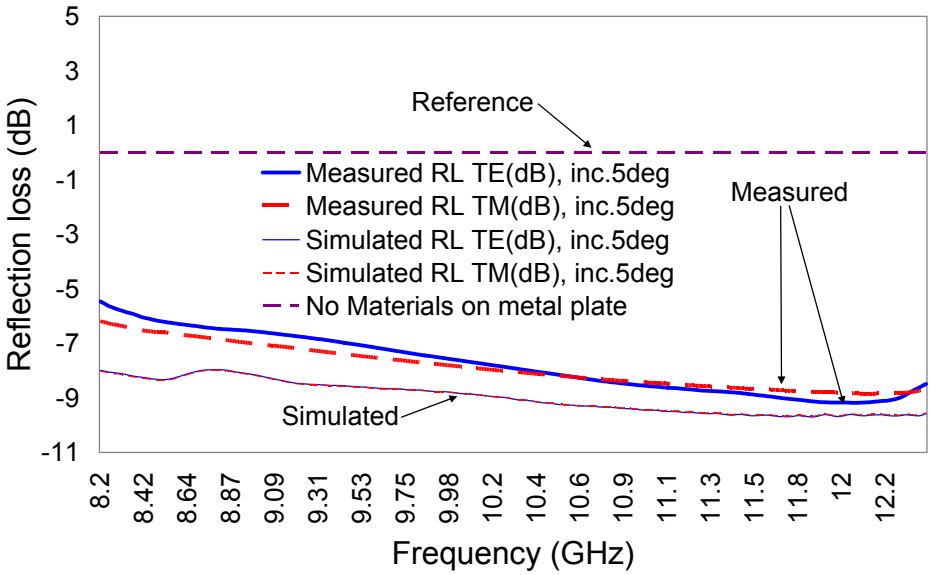

Fig.(5.2.2.2). Comparison between simulated and measured RAM based on two layers of Epoxyresin and MWCNTs for incidence angle of 5 deg

Again, manufacturing the tile with some little changes in thickness we obtained some better results:

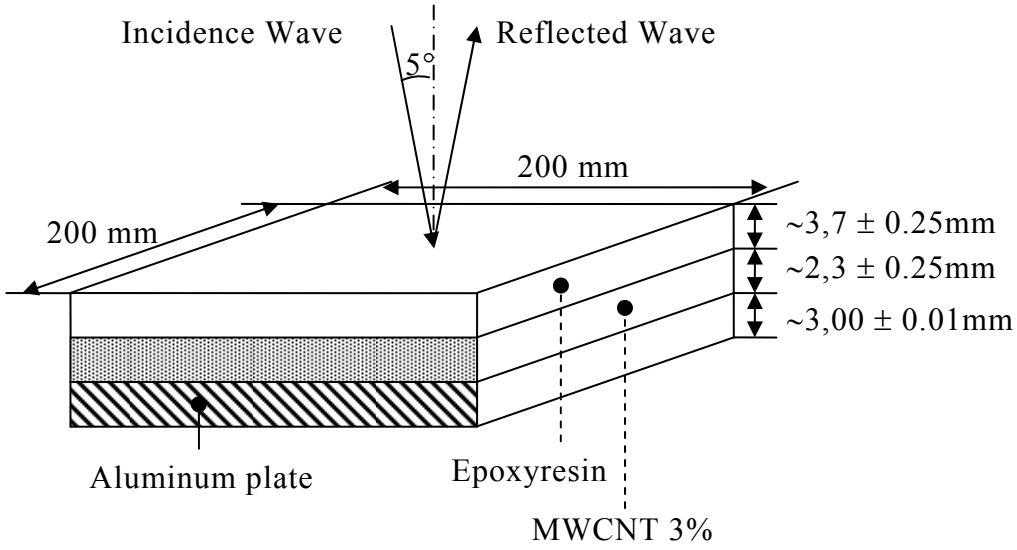

Fig. (5.2.2.3). 6 mm Epoxyresin and MWCNTs based RAM

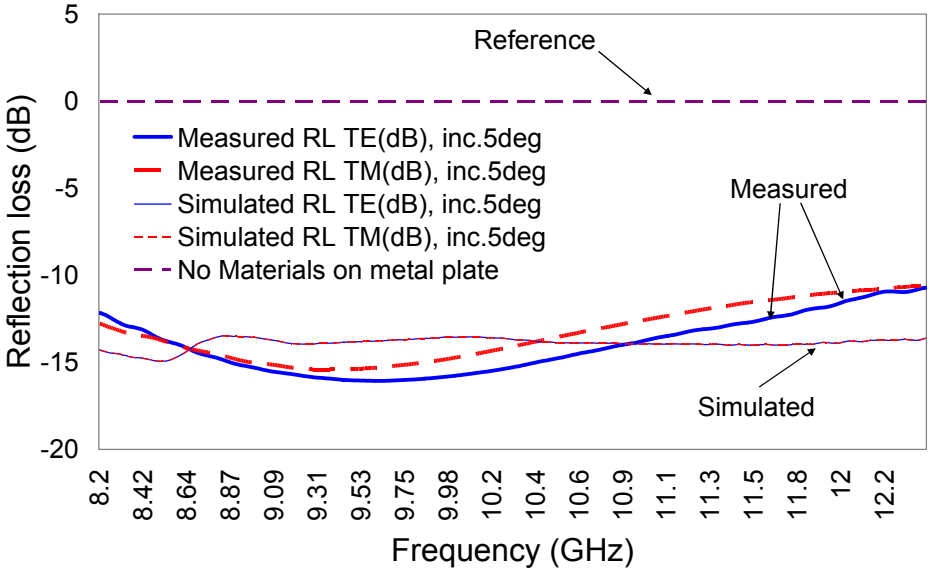

Fig.(5.2.2.4). Comparison between simulated and measured RAM based on two layers of Epoxyresin and MWCNTs for incidence angle of 5 deg

5.2.3 6.97 mm X-band RAM made of Epoxy-resin and MWCNTs

Epoxy-resin and MWCNTs based tile was built as composite material using only MWCNTs in weight percentage respectively of 1; 2; 3wt% with respect to epoxy resin. The tile structure and the dimensions are shown in Fig. (5.2.3.1)

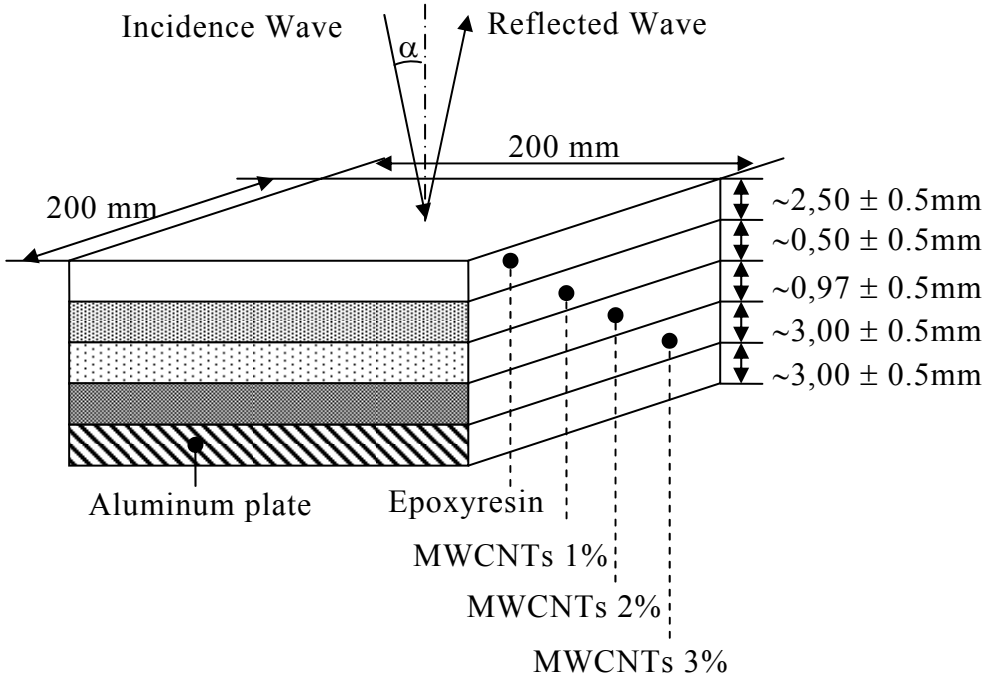

(a)

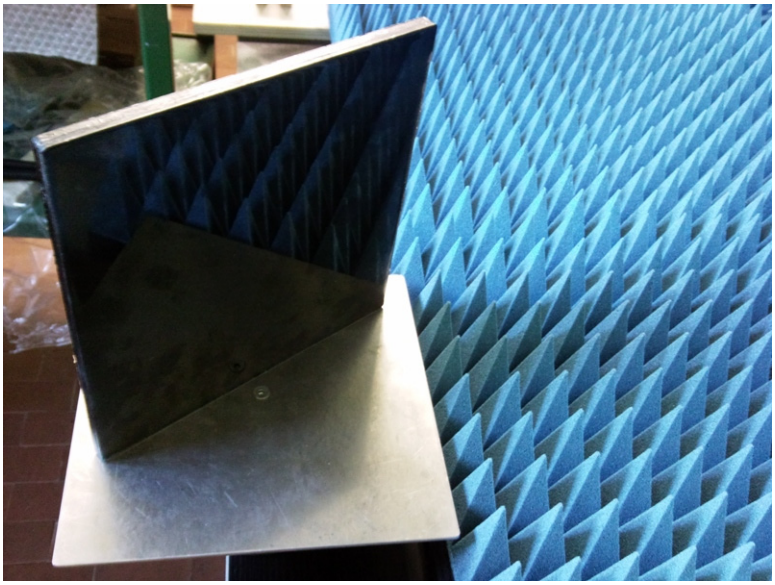

(b)

Fig. (5.2.3.1). 6.97mm RAM Epoxyresin and MWCNTs based tile; a) schematic, b) practical realization of multilayer structure

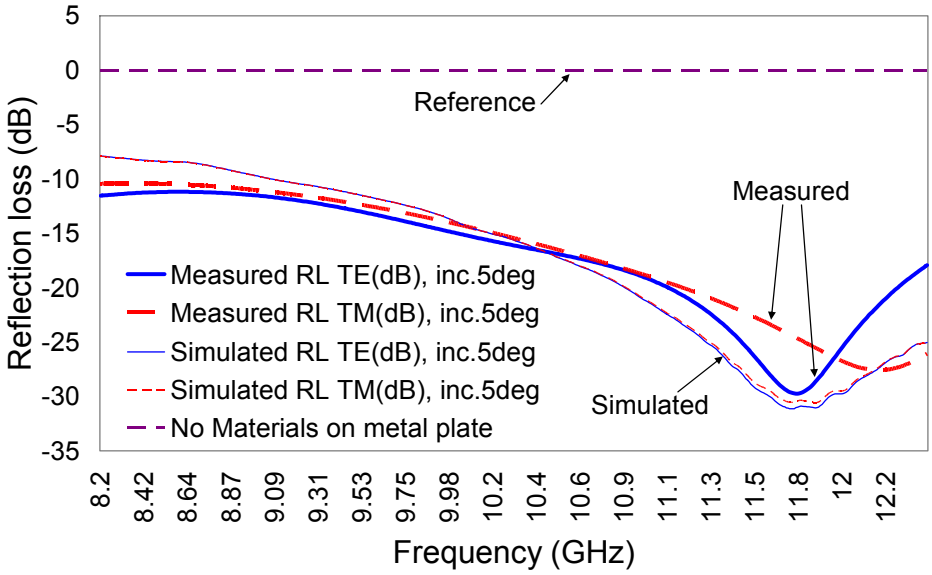

Fig.(5.2.3.1). Comparison between simulated and measured RAM based on three layers of MWCNTs for incidence angle of 5 deg

Comparing Fig.(5.2.3.1), and Fig.(5.2.1.2), we can notice the higher microwave absorbing capability of MWCNTs made absorber compared to graphite made absorber. In particular about 7 mm of MWCNTs made absorber shows from 10 to 30 dB of reflection loss greater than about 10 mm of graphite based absorber. This fact is in accordance with observations related to the poor performances of graphite with respect to carbon nanomaterials [3].

5.2.4 Extended Frequency Band RAM

In order to evaluate the mathematical model in more severe conditions, we performed some comparisons between simulations and measurements in a wide range of frequencies and for different electromagnetic wave incidence angles.

Using a couple large band antenna, NRL arch has been set using two different incidence angles: 5 deg and 30 deg. In Fig.(5.2.4.1.1) and Fig.(5.2.4.1.2), multilayer structure and the measurements/simulations comparison is shown. It can be noticed in the dashed line simulations and in continuous line measurements. The same color is adopted for each polarization of the forward electromagnetic wave field. The measurements have been made in the band 5.38 to 18 GHz i.e., where dielectric

permittivity of materials was previously measured. It can be noticed some interesting agreement between behaviors and values of simulations and measurements.

5.2.4.1 11 mm Large Band RAM, made of Epoxy-resin and MWCNTs

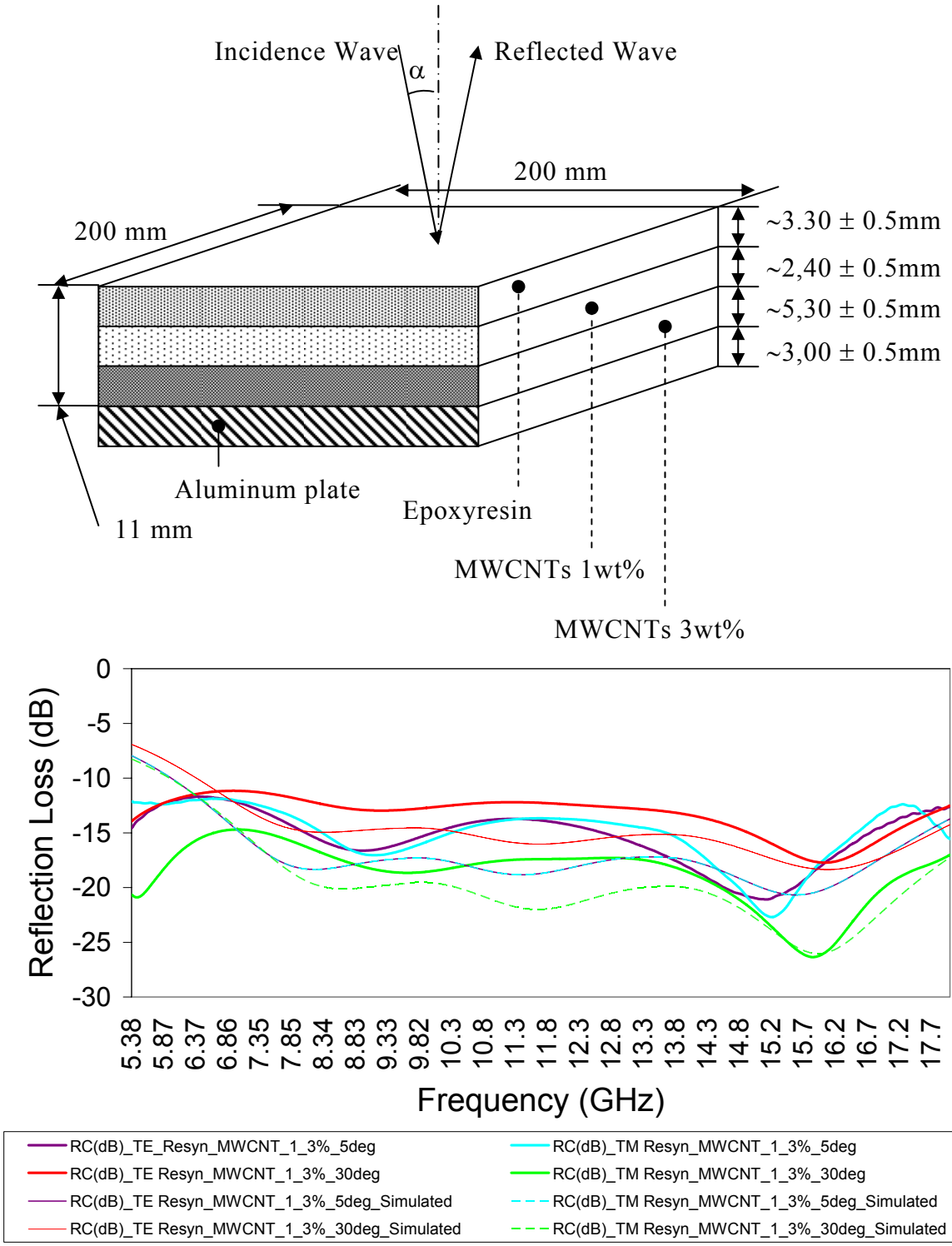

Fig. (5.2.4.1.1). 11 mm epoxyresin and MWCNTs large band RAM, 200x200 mm

5.2.4.2 2.6 mm Large Band RAM made of Epoxy-resin and MWCNTs

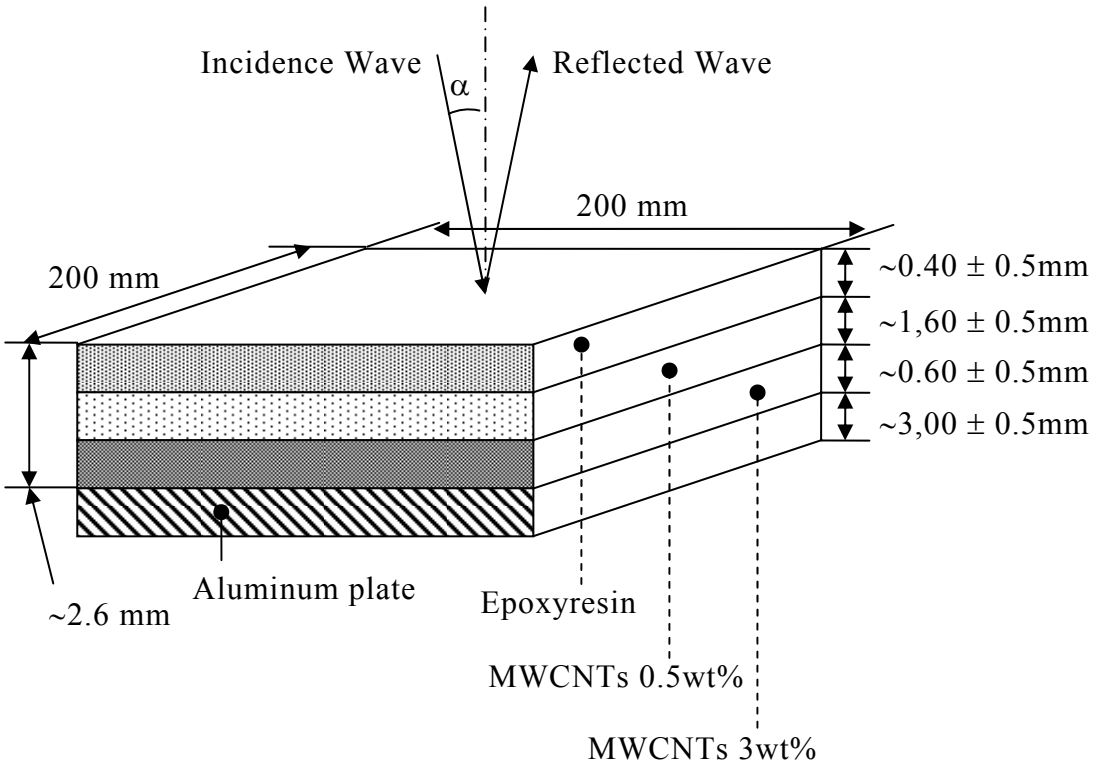

Fig. (5.2.4.2.2). 2.6 mm epoxyresin and MWCNTs large band RAM, 200x200 mm

Differences in simulated and measured reflection loss are not greater then few dBs which are acceptable in such kind of experiment.

Measured curves show better behavior of manufactured composite multilayer RAMs with respect to simulations, above all to low frequencies.

Similarities between simulations and measurements in terms of frequencies peaks and corresponding reflection loss values confirm that mathematical model of absorber can be quite effectively used to design RAM structure.

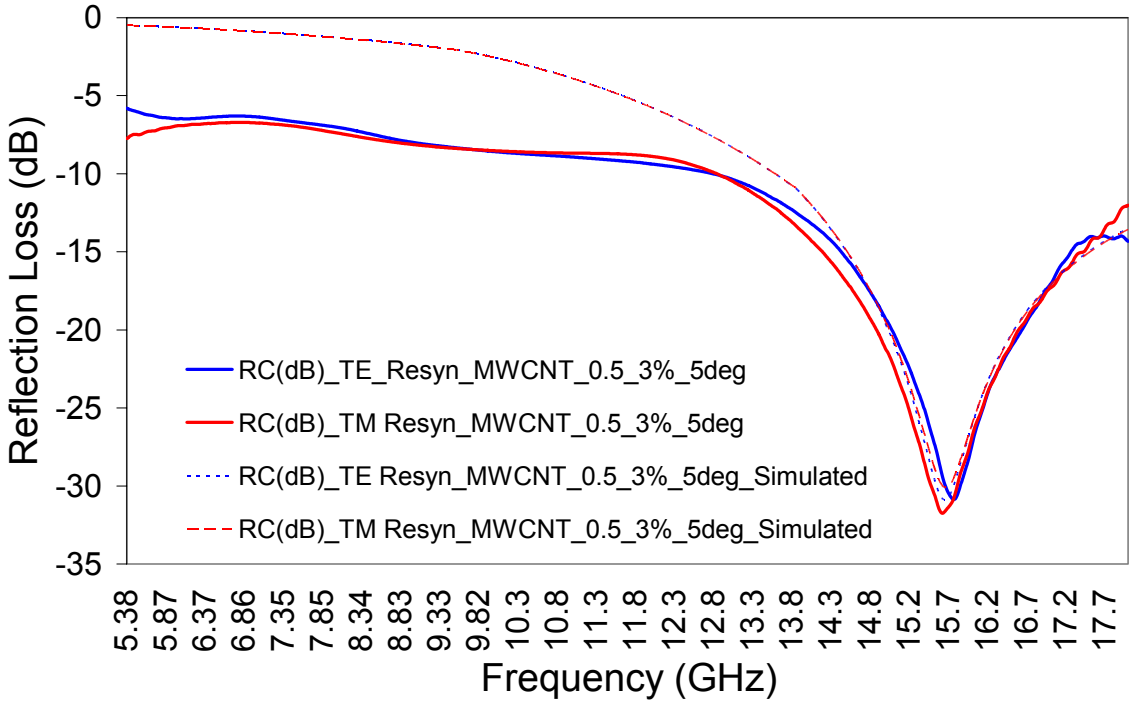

(a)

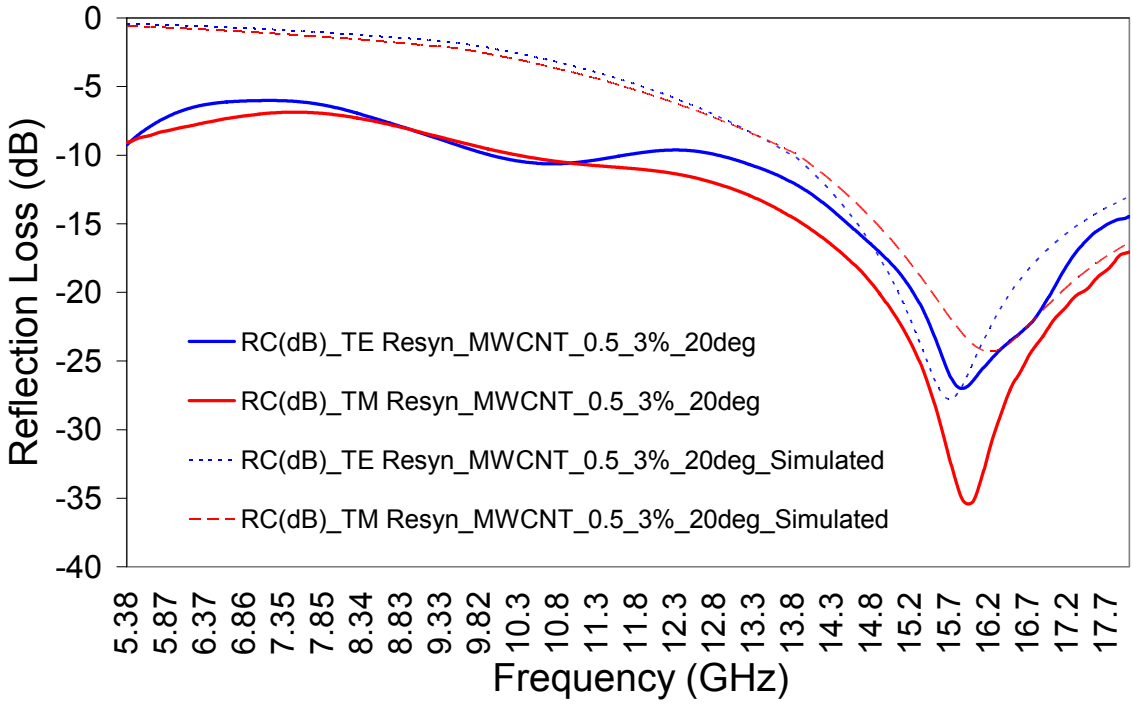

(b)

Fig. (5.2.4.2.3). 2.6 mm epoxyresin and MWCNTs large band RAM, 200x200 mm

a) Comparison of simulations and measurements for 5° incidence angle,

b) Comparison of simulations and measurements for 20° incidence angle

In the next section experimental validation of MSS mathematical model is presented.

5.3 Microwave Shielding Structures (MSS) testing using directional shielding effectiveness measurement (DSEM)

Directional shielding effectiveness measurement (DSEM) is schematically shown in Fig. (5.3.1).

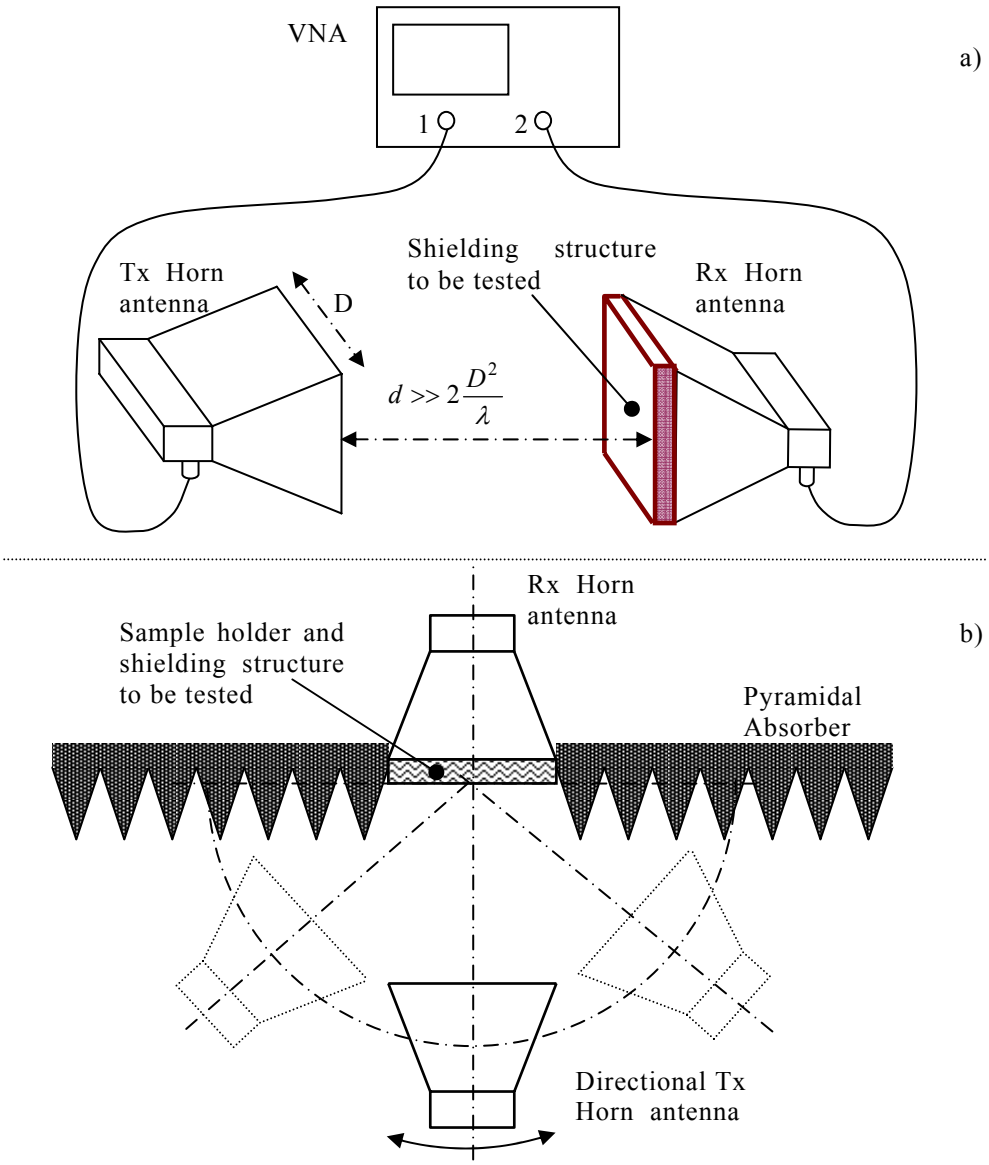

Fig.(5.3.1). Directional shielding effectiveness measurement (DSEM) scheme; a) front view, b) top view where absorbent pyramidal wall is shown

Its principle is to measure the attenuation of a microwave reference signal when it passes through a material in free space conditions with a precise incidence angle. This measurement method has been developed in collaboration with "Università

Politecnica delle Marche", Dipartimento di Ingegneria Biomedica, Elettronica e Telecomunicazioni (DIBET).

The measured attenuation represents the shielding capability of material under test.

In Fig. (5.3.2) practical realization of DSEM is shown.

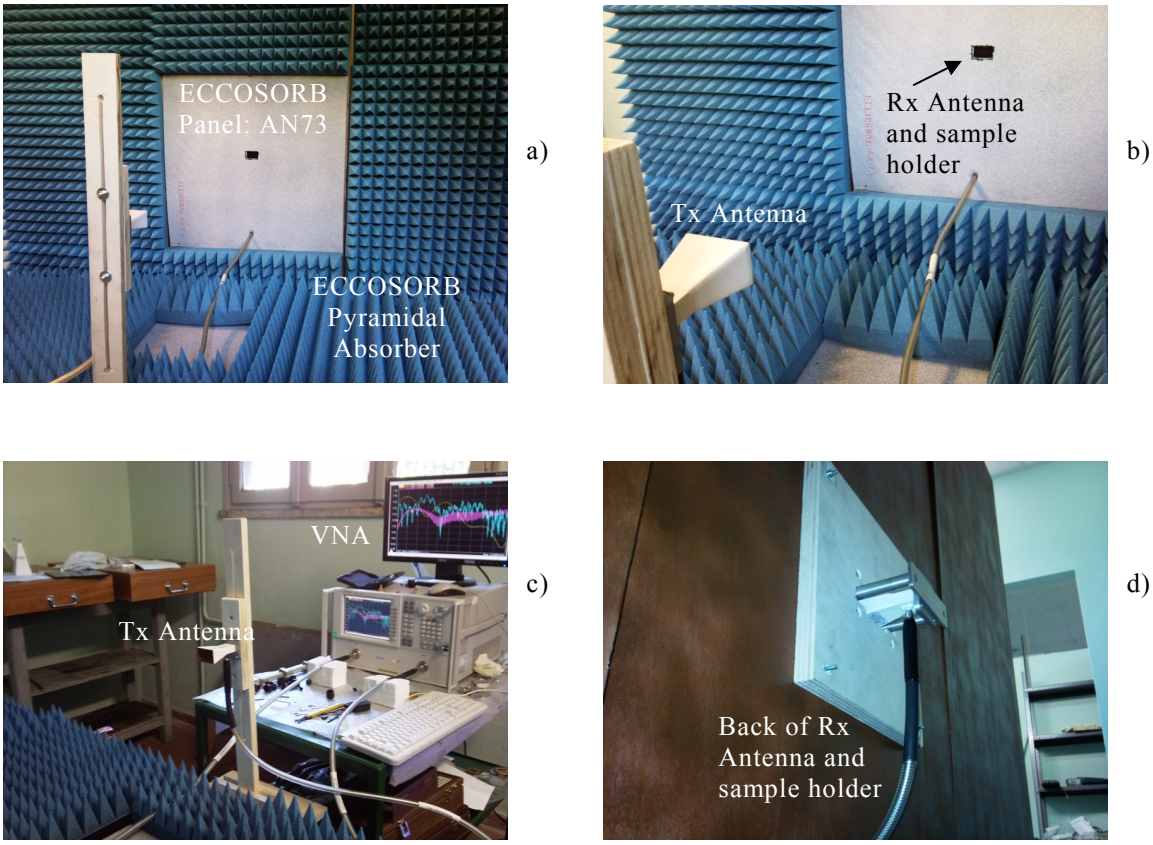

Fig.(5.3.2). Directional shielding effectiveness measurement (DSEM) practical configuration at www.saslab.eu ; a) picture of DSEM, b) zoom of Tx and Rx antenna and sample holder, c) Tx Antenna and Vector Network Analyzer, d) back of wall where is located Rx antenna and sample holder

Measurement of shielding capability of a certain structure or material is computed by means of scattering parameter $\mathbf{S_{ij}}$, available on the vector network analyzer (VNA) connected to the Tx and Rx horn antennas.

In particular, Rx horn antenna is equipped with a sample holder able to host the composite material to be tested. The measurement of shielding effectiveness (SE) is evaluated as the difference in dB or the ratio in linear scale between the transmitted signal from transmitting antenna (Tx antenna) to receiving antenna (Rx antenna) respectively when sample holder is empty and filled with materials.

Sensitivity of SE measurement system is measured closing the sample holder mouth with a metallic enclosure and performing the same ratio of scattering parameters. This last SE (short) test is an index of maximum SE measurable by the DSEM system. SE measured as in (5.3.1) give negative values which simply means that the interposition of materials between Tx and Rx antennas reduce the received signal of a certain amount in dB.

$$SE_{\text{Material}}(dB) = 10LOG\left[\frac{|S21|^2_{\text{Open}}}{|S21|^2_{\text{Material}}}\right]$$

$$SE_{\text{Reference}}(dB) = 10LOG\left[\frac{|S21|^2_{\text{Open}}}{|S21|^2_{\text{Short}}}\right]$$

(5.3.1)

Where:

- S21 is the scattering parameter measured by VNA which represents the ratio between signal transmitted by Tx antenna and signal received signal by Rx antenna. In our measurements, we are interested mainly to the absolute level of scattering parameter.
- $S21_{\text{Material}}$ is measured when shielding materials are located within sample holder;
- $S21_{\text{Open}}$ is measured when no shielding materials are located within sample holder;
- $S21_{\text{Short}}$ is measured when metallic enclosure is located above sample holder;

In order to avoid as much as possible that spurious reflected signal could have been affected measurements of SE, the Rx antenna and sample holder have been inserted in a wall made of ECCOSORB microwave absorbing materials effective in the frequency band above 5 GHz. To grant good S/N conditions, the output power of VNA has been set to +5 dBm. Used antennas are Q-par Angus horn antennas in the 8-12 GHz frequency range. In shielding measurements is required that all microwaves measured signals are the only one passing through materials to be tested, this condition is needed to perform accurate measurements of shielding properties for a certain materials/structure. Based on experience we built a sample holder as a system simultaneously able to host Rx

antenna during shielding measurements and to be used as a shape for injecting liquid composite materials and oven curing process. In Fig.(5.3.3) sample holder system is schematically shown.

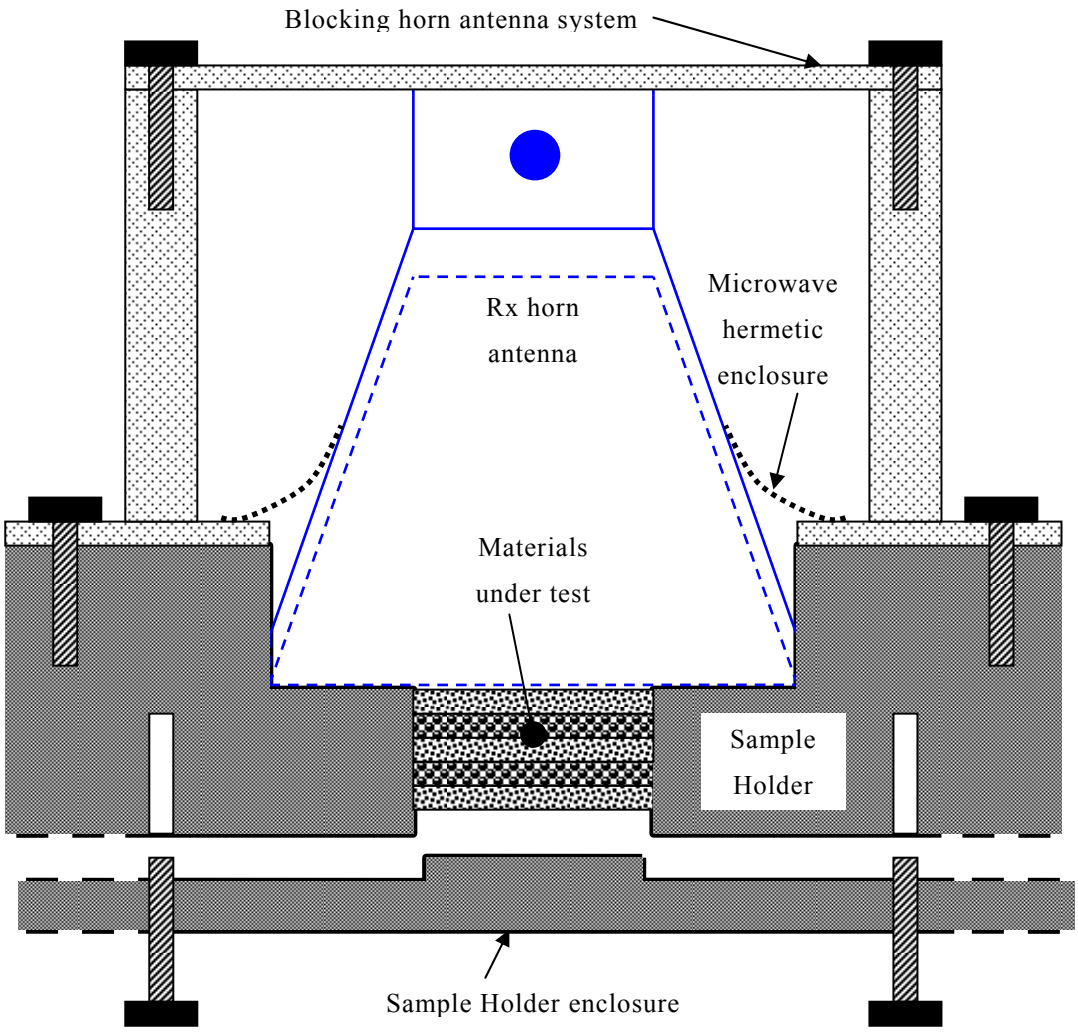

Fig.(5.3.3). Aluminum sample holder system used in manufacturing microwave shielding structure and to host horn antenna in shielding effectiveness measurement.

In Fig. (5.3.4), a simple procedure for MSS manufacturing is shown. Sample holder is closed at the base and step by step liquid composite materials are injected in the cavity. Thermal curing phase is required for each stratum of multilayer structure.

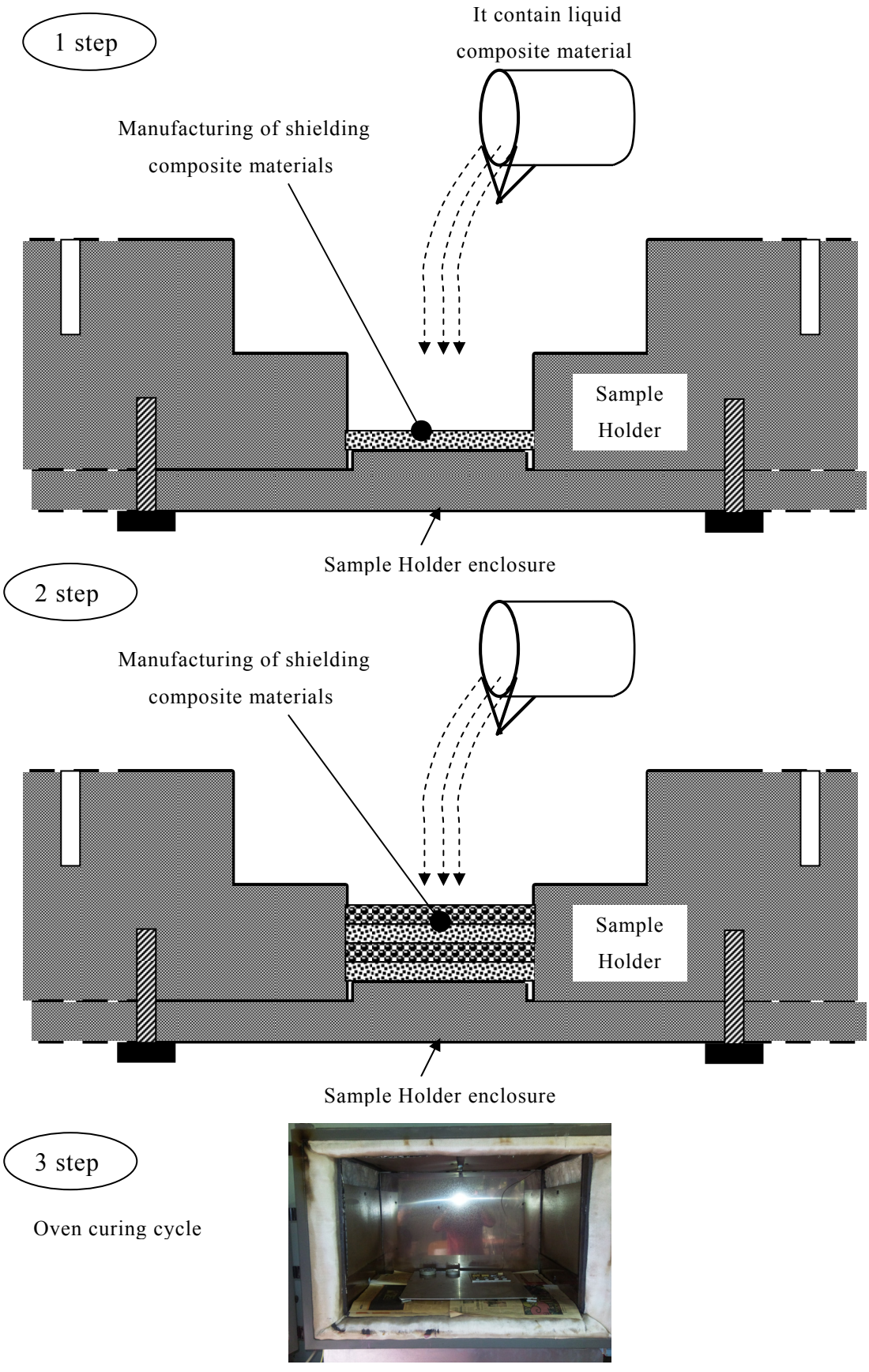

Fig.(5.3.4). Sample holder system used in shielding materials manufacturing phases

In Fig.(5.3.5) is shown the CAD plot and the pictures of realized system.

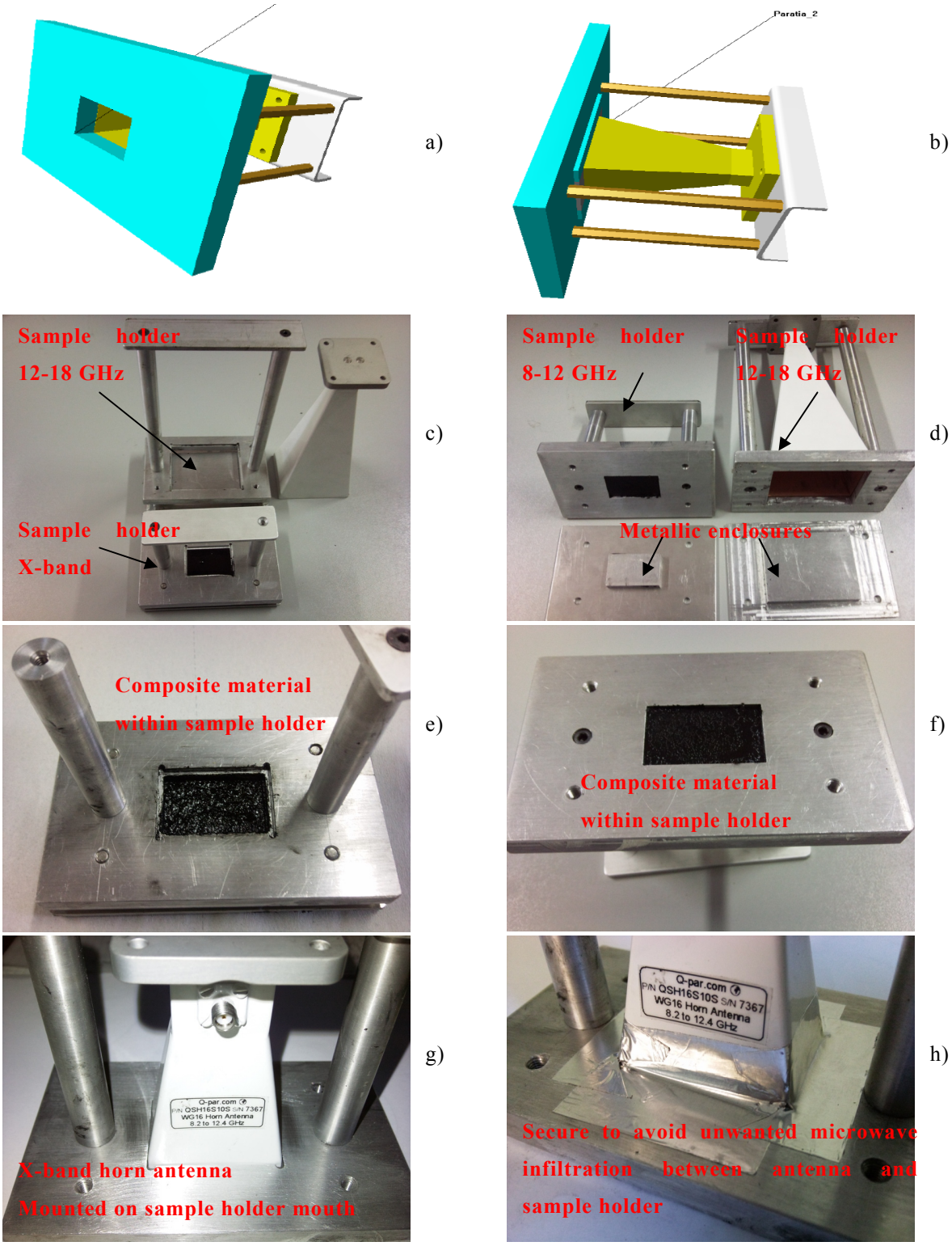

Fig.(5.3.5). Sample holder systems for MSS measurements. a,b) CAD draws, c,d) sample holder with and without horn antennas, e,f) manufactured MSS using sample holder, g,h) microwave hermetic secure for materials shielding testing.

5.3.1 MSS measurements

Materials considered are:

- Single layer: 6.5mm of CNFs 3wt%,
- Single layer: 6.5 mm of MWCNTs 6 wt%,
- Single layer: 6.5 mm of MWCNTs 10 wt%,
- Two layers: 6.9mm composed by 4mm Epoxy-resin and 1mm MWCNTs 3wt%.
- Four layers: 10mm composed by 3mm Epoxy-resin, 1mm MWCNTs 1wt%, 1mm MWCNTs 2wt%, 5mm MWCNTs 3wt%.

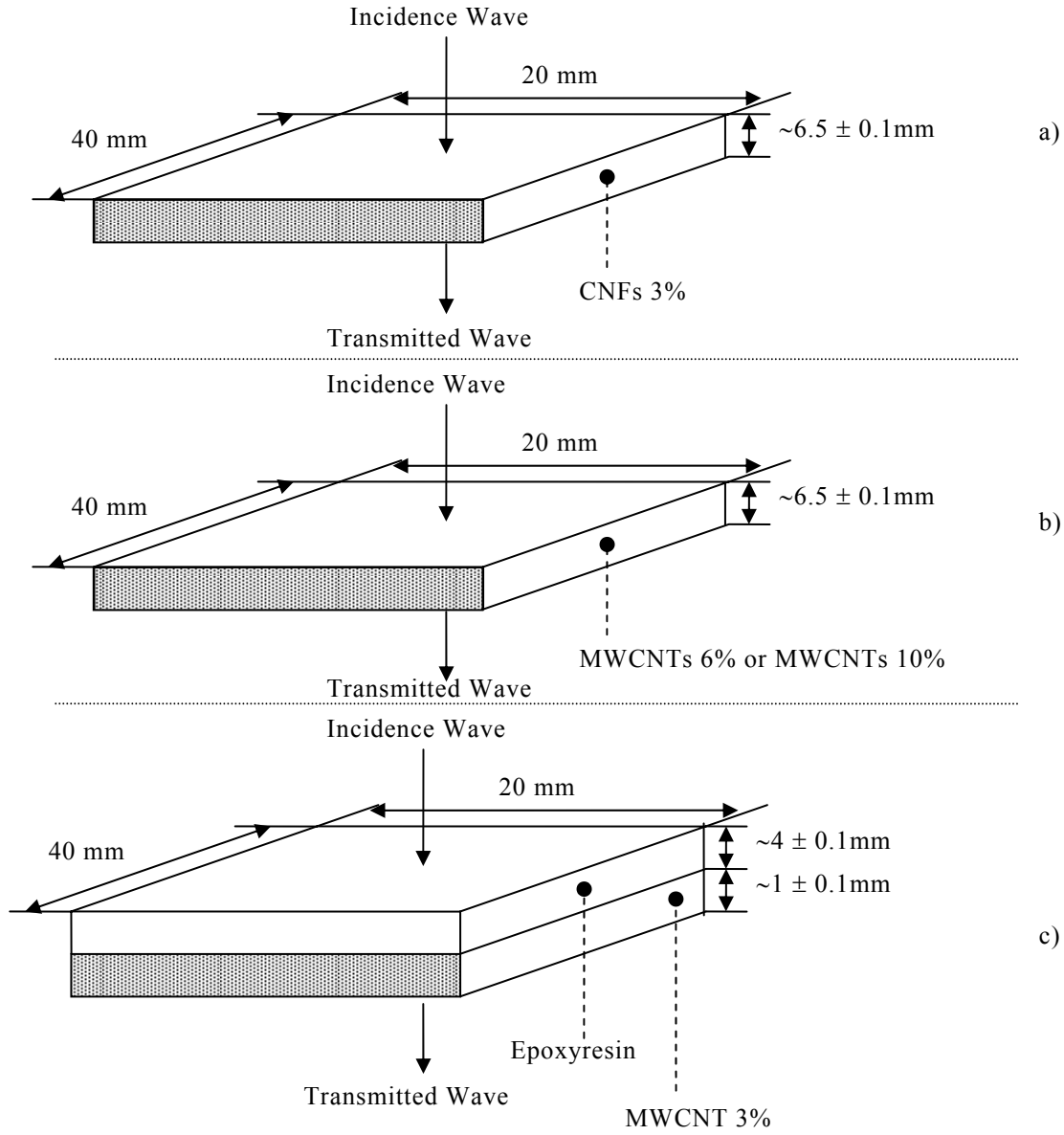

Fig. (5.3.1.1). Microwave Shielding Structure (MSS)

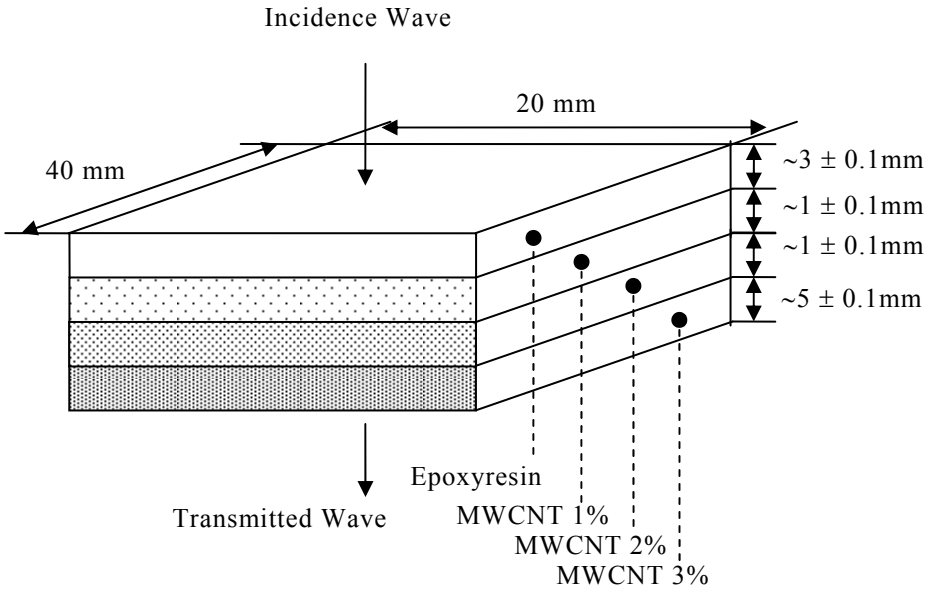

Fig. (5.3.1.2). Shielding materials and structure

In Fig.(5.3.1.3), reflection coefficient (dB), transmission coefficient (dB), i.e., SE(dB), loss factor (%) for 0 deg incidence angle are shown. It can be noticed that loss factor remain above 96% in all the frequency bandwidth.

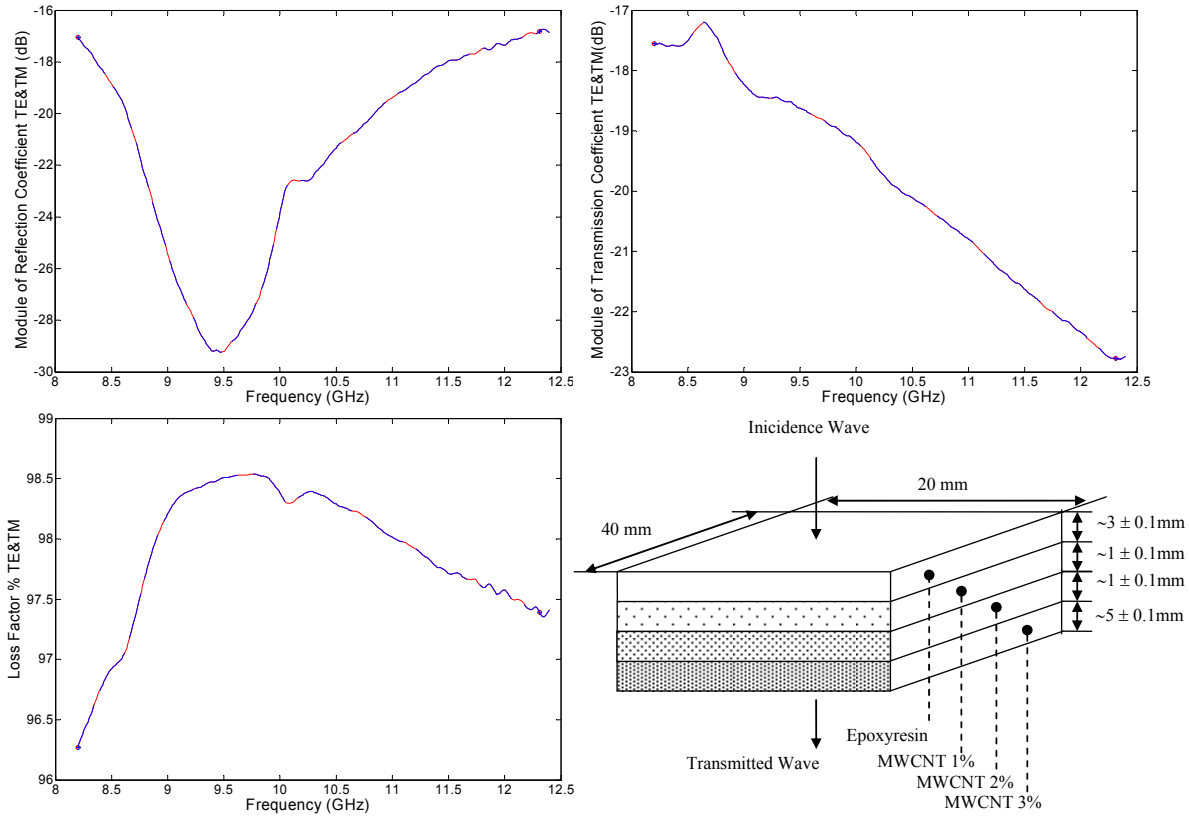

Fig. (5.3.1.3). Simulated SE of 10 mm absorber structure based on 3mmResin, 1mm MWCNT 1%, 1mmMWCNT 2%, 5mm MWCNT 3%

At the end in Fig.(5.3.1.4), comparison between simulated and measured SE of all presented composite materials epoxy-resin based is shown.

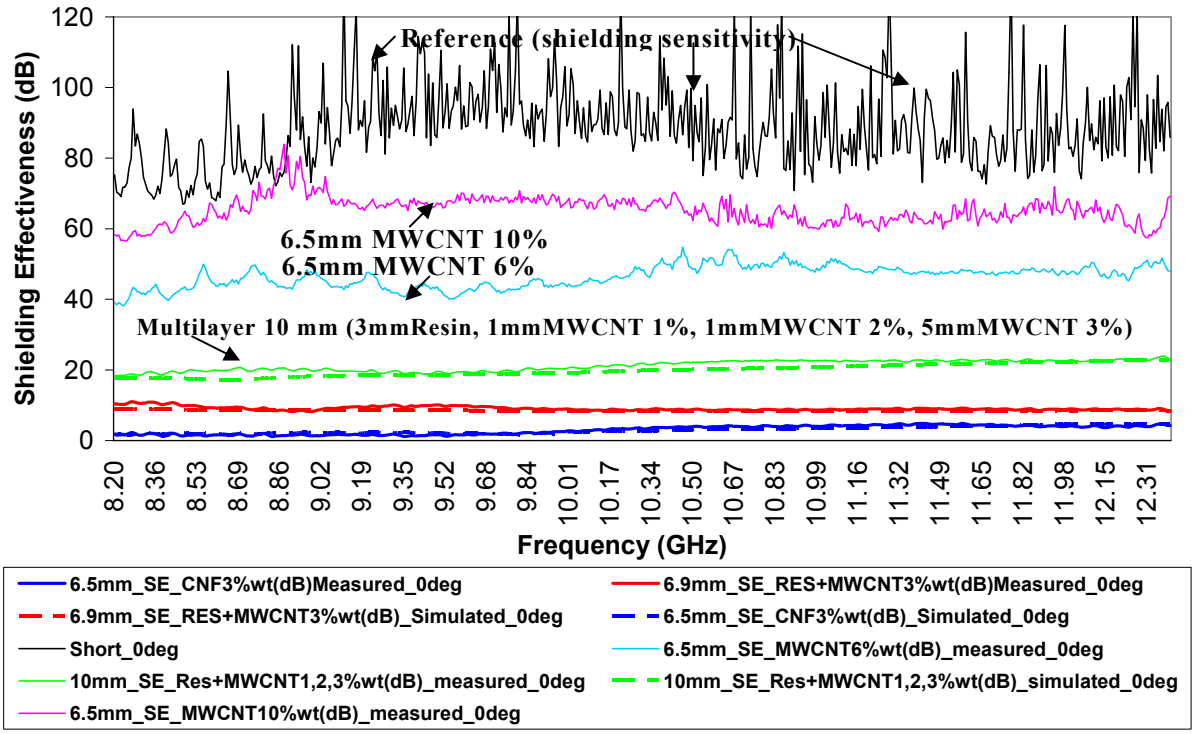

Fig. (5.3.1.4). Comparison between simulated and measured SE of composite materials.

Observing this plot, it can be noticed the good performances of 6.5mm MWCNTs 6wt% and 10wt%. The drawback of such composite materials is the high reflection coefficient which in turn means that interferences can be spread out far from the shield and consequently disturbing other electronic equipments. On the contrary, the 10mm multilayer structure, even though showing lower SE performances, has lower reflection coefficient since it is as impedance tapered structure where electromagnetic waves are gradually absorbed.

5.4 Conclusion

In this chapter, analysis of reflection loss and shielding effectiveness (SE) has been performed. Comparisons between simulations and measurements of realized structures show similar behaviors and absolute values as well.

In order to perform SE evaluation of materials, a new method has been developed able simultaneously to be used as sample holder to build composite materials and as a rack to mount antenna to perform SE measurements.

This method has been evaluated very easy to implement and able to assure optimum electric contact between sample sides and the internal walls of sample holder, i.e., reducing SE measurements errors due to unwanted microwaves infiltration.

5.5 Reference Table

[1] Emerson & Cuming Microwave Products, NRL Arch Reflectivity Testing basic notes. Available: http://www.eccosorb.com/

[2] Umari, M. H. Ghodgaonkar, D. K. Varadan, V. V. and Varadan, V. K. (1991). "A free-space bistatic calibration technique for the measurement of parallel and perpendicular reflection coefficients of planar samples", IEEE Transactions on Instrumentation and Measurement, 40 (1), 19–24.

[3] D.micheli et.al. "X-Band microwave characterization of carbon-based nanocomposite material, absorbing capability comparison and RAS design simulation", *Composites Science and Technology,* 70 (2010) 400–409.

Chapter 6

Special Materials: Microwave Absorbing and Shielding properties of Carbon-Carbon composite materials

6.1 Introduction

In this chapter, electromagnetic absorption and shielding effectiveness measurements of carbon-carbon (CC) is shown using different methods. In particular, comparison of SE(dB) is made between CC and the other composite materials analyzed in previous chapters.

Over the last decades, carbon-carbon (CC) materials have been widely investigated from the mechanical and thermodynamical point of view, exhibiting extraordinary properties at extreme temperature conditions [1]. This family of materials has been conceived in aerospace context, when NASA's Apollo projects called for special constraints imposed by Space Shuttle critical operation in crossing atmospheres [2]. Enhancing features of CC composites were responsible for their broad diffusion in automotive [3], energy [4] and communication industries, other than in space applications [5]. In particular, it is worth remarking the application of such composites for realizing lightweight and efficient dish antenna [6]. Moreover, in those applications where CC composites are employed as a protective coating, electromagnetic screening capabilities become further key properties. Here, predictions for shielding effectiveness (SE) are again allowed by the knowledge of specific electrical conductivities. Ab initio studies of electromagnetic interference (EMI) protection efficiency has been recently done by [7], showing relevant enhancements able to push SE values close to the measurement noise floor of the system. Carbon-carbon composites consist of a fibrous carbon substrate in a carbonaceous matrix. Although both constituents are the same element, this fact does not simplify composite behavior because the state of each constituent may range from carbon to graphite.

In fabrication, the fibers can be used in either continuous or discontinuous form. The directionality of the filaments can be varied ranging from unidirectional lay-ups to multidirectional weaves. The fiber volume used constitutes another variable. The higher the volume fraction of a specific high-strength fiber in a matrix, the greater the strength of the composite. The matrix can be formed via two basic approaches: (1) through the carbonization of an organic solid or liquid, such as a resin or pitch, and (2) through the chemical vapor deposition (CVD) of carbon from a hydrocarbon. A range of carbon structures can be obtained by either approach. Finally, heat

treatment of the composite material at graphitization temperatures offers additional variability to the properties that can be obtained. Typically, there is an optimum graphitization temperature at which the highest strength can be obtained for a given composite composition of fiber and matrix.

Carbon-carbon composites have low density, a high strength-to-weight ratio, and are able to withstand high temperatures. The combination of properties makes carbon-carbon composites well suited for a variety of applications and it is expected that the number of suitable applications for such materials increases.

Mechanical and physical properties of carbon-carbon composites may be widely varied through selection of efficient precursor materials and manufacturing routes. The control of properties such as strength, stiffness, fracture toughness, thermal conductivity, and biocompatibility allow use of carbon-carbon composites in challenging environments; the only major weakness of these materials is their extreme oxygen sensitivity above approximately 350 C.

Research proposed hereafter is focused on a composite with 1.48 g/cm^3 which utilizes 6K plain weave carbon fibers produced from pitch precursors in order to obtain excellent specific thermo-mechanical properties. The matrix for this class of composite is achieved through pyrolisis of a phenolic resin.

6.2 Carbon-Carbon Microwave Reflection Loss and Shielding Effectiveness in EM microwave range

In order to test the reflection loss of CC in the band 8-18 GHz, the NRL arch system described in Chapter 5, has been adopted.

In Fig. (6.2.1) a picture of NRL Arch configuration and CC are shown. It can be noticed the higher reflection behavior of CC.

Taking into account about 2 dBs of errors in the measurements of reflection loss, then we can identify CC as a good reflector in the microwave frequency range here considered.

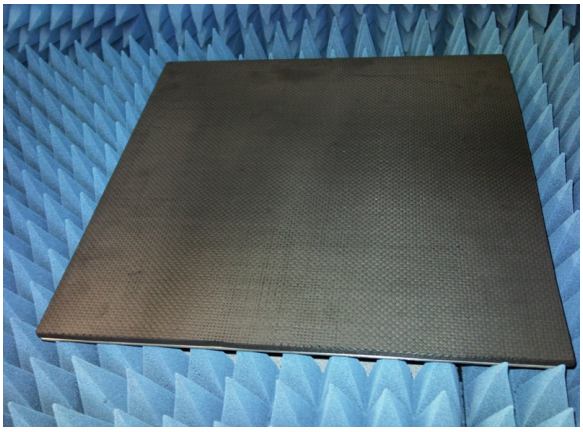

a)

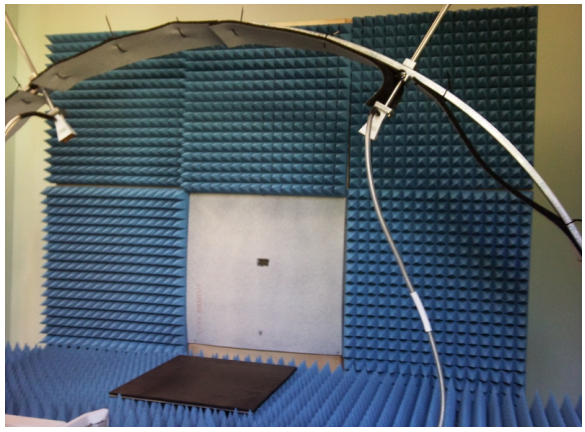

b)

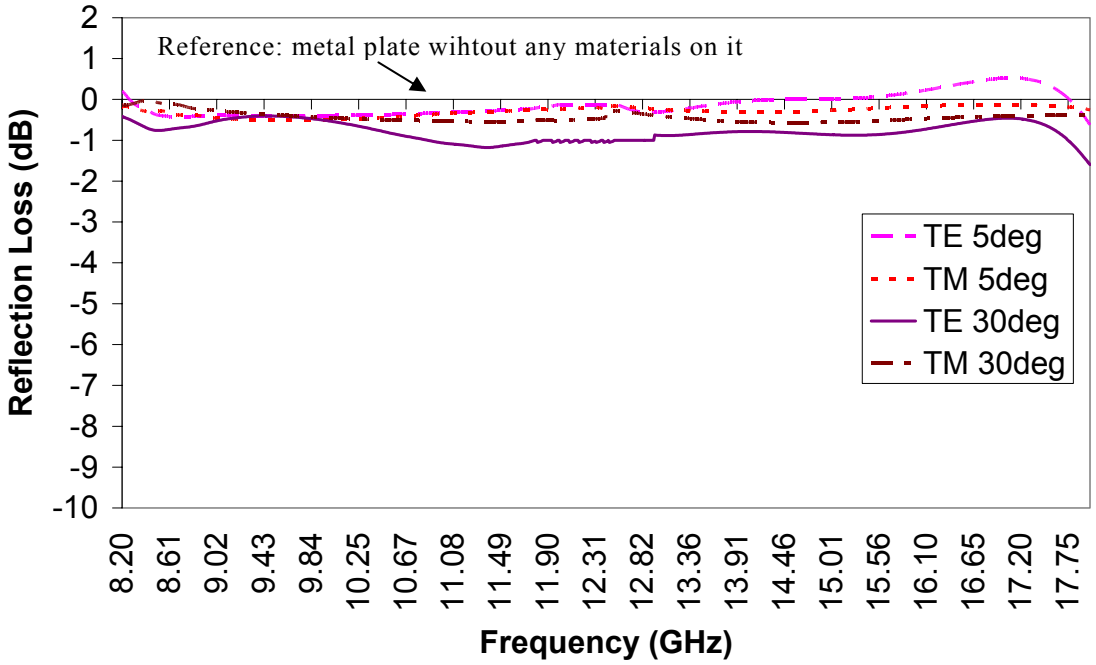

c)

Fig. (6.2.1). a) CC square tile 25mm side, 8mm thickness; b) NRL measurements system; c) Reflection loss (dB) of CC for incidence angle 5, 30, 50 deg.

As far as shielding effectiveness measurement (SE), is concerned, the following setup depicted in Fig. (6.2.2) has been adopted.

From SE measurements clearly appear the higher properties of CC materials in EMI shielding applications.

Drawback of CC materials is the poor EM microwave absorbing properties if compared to previous epoxy-resin multilayer composite materials seen in chapter 5.

This phenomenon is mainly due to the higher electrical conductivity of CC materials.

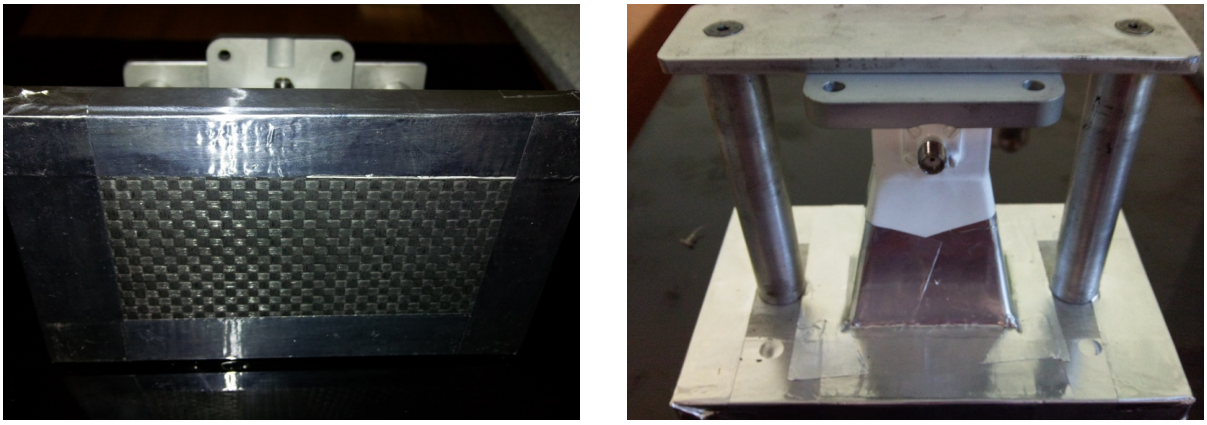

a)

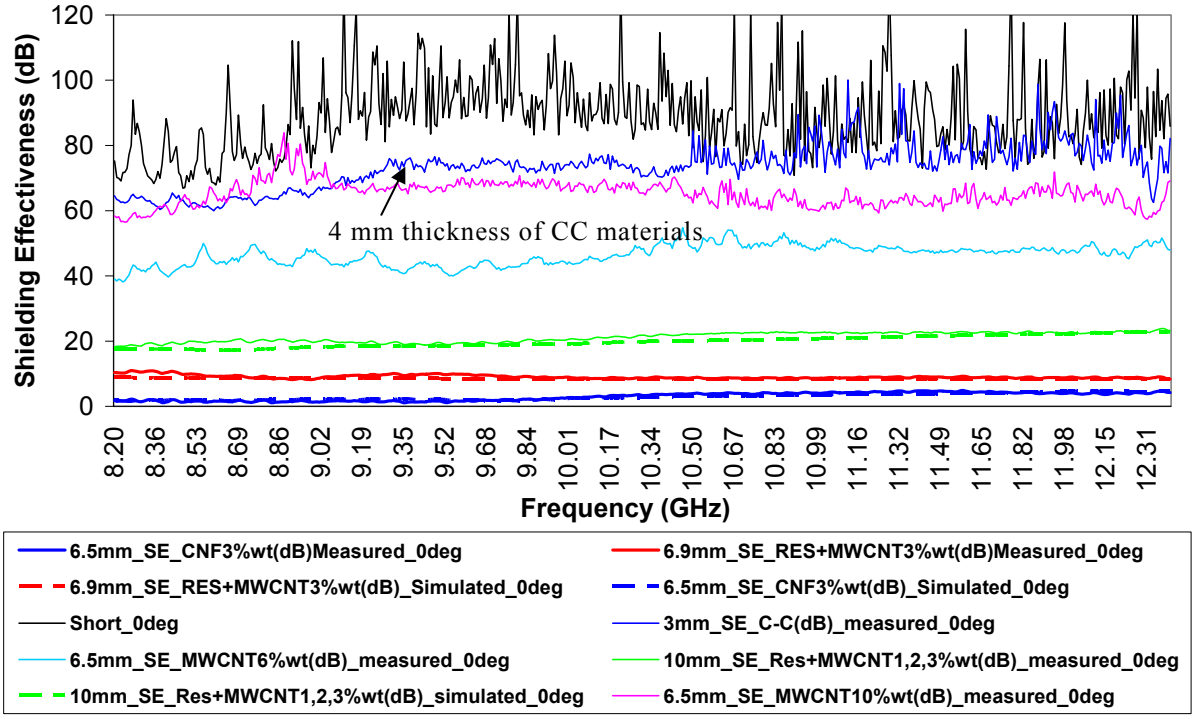

b)

Fig. (6.2.2). a) Microwave shielding measurement system, b) Comparison between measured SE of epoxyresin based composite materials and CC materials.

Obtained results in terms of reflection and shielding properties of CC, confirm those found and submitted in [9] where electrical conductivity (σ) measurements of carbon-carbon (CC) composites has been measured, resulting in the range 3500 S/m and 4500 S/m. Such values are relatively higher compared to that of composite materials seen in chapter 3 and 5, where conductivities were in the range 1-15 (S/m) max.

In the next subsection a method for measurements of CC electrical conductivity is presented and discussed.

6.2.1 Accurate electrical conductivity measurement of Carbon-Carbon material and composites

An in-house rectangular waveguide WR-28 operating at frequencies between 18 GHz to 40 GHz (K band) has been realized using CC composite. This one has been realized as a linear fibrous assembly of planar 2D shape, in particular interlacing 0° and 90° roving in a repeating pattern (or topological cell) so as to create a biaxial woven [17].

Waveguide manufacturing has been carried out by joining face-to-face two U-shaped cross-section segments like in Fig. (6.2.1.1a). Each U-shaped part has been obtained by milling or machining of an 8 mm thick laminate of carbon-carbon, using dedicated graphite milling heads. The two segments are finally joined face-to-face in order to build up the rectangular waveguide. Its cross section is of dimensions 8.2mm × 3.56mm, thus very small: this further permits to save the amount of material necessary for the device realization. In order to provide the best U-shape wall alignment as possible, a metallic frame appositely built has been adopted to maintain the two halves in correct position during bonding procedure.

Joining carbon-carbon composites is not a simple task. Unlike metals, they do not allow themselves to welding, and even brazing can be difficult because many filler metals that are commonly used in welding exhibit little or no wetting with carbon materials. Even with suitable filler metals, brazing normally requires special surface treatment, adding to the time and cost of joining. Bonding was considered the most suitable and a graphite adhesive was selected as binder since it is a carbon-based material. The graphite adhesive was applied only on the external joining surfaces once the two halves have correctly matched. The configuration is completed adding aluminum end flanges for the mechanical and electrical connection to the VNA port adapters in order to perform scattering parameter measurements.

In Fig. (6.2.1.1), manufacturing of CC waveguide, measurement setup and scattering parameters are shown [9]. Transmission (S_{21}) and reflection (S_{11}) scattering

parameters have been recorded within a frequency wideband, ranging from 23 GHz to 30 GHz (microwave K band).

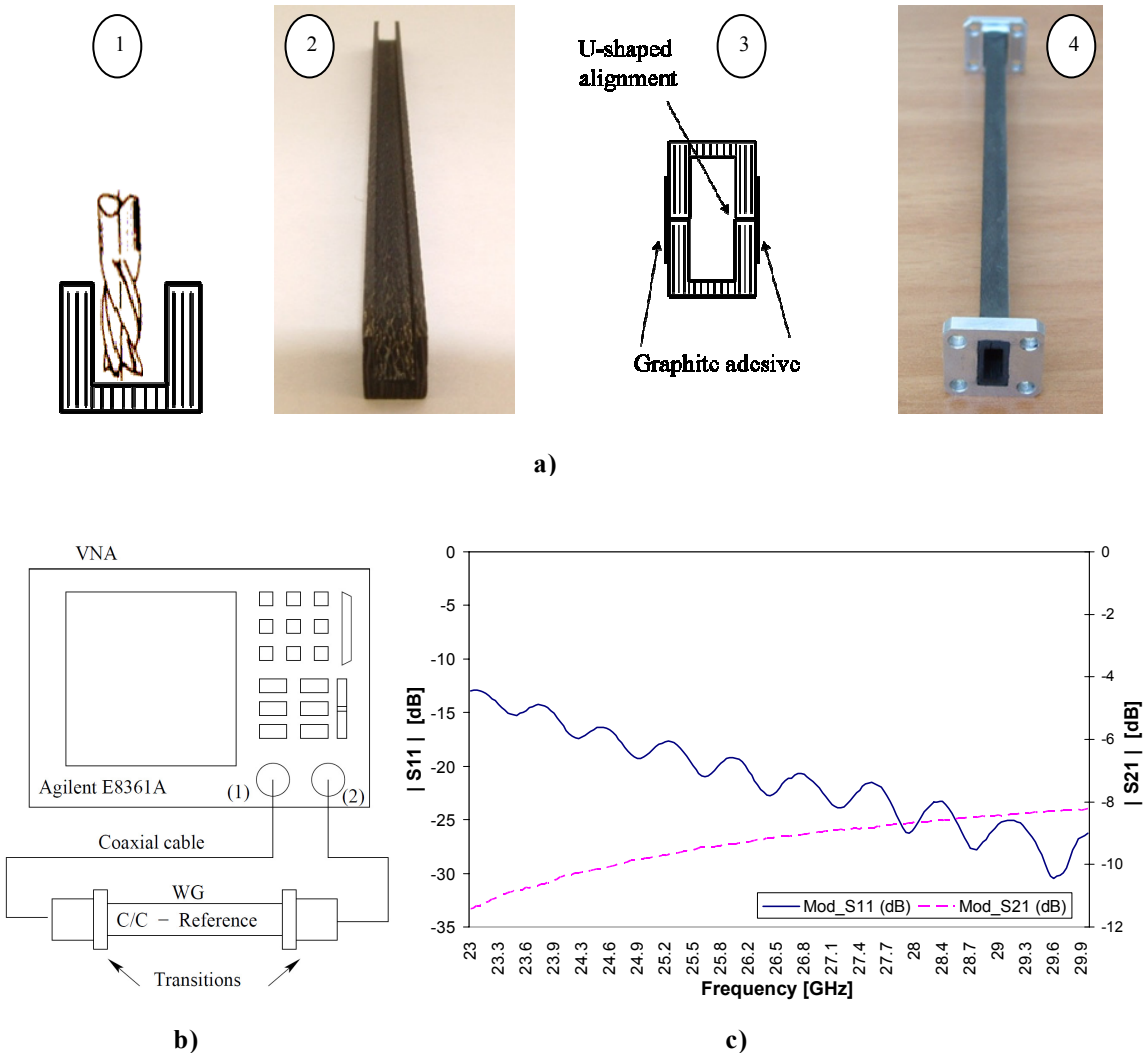

Fig. (6.2.1.1). a) CC waveguide manufacturing process; b) Scattering parameter measurement setup; c) Scattering parameters measurement

Measurements parameters are set out as follows: the injected power is P_{in} = 0 dBm, the total number of acquired samples is N = 256 – i.e. the frequency resolution is $\Delta f = 7/256 \cong 28$ MHz – and the intermediate frequency bandwidth (IFBW) is 3 kHz to lower down the noise floor of the instrument. The rectangular waveguide has been interfaced with N-type coaxial connectors of VNA through standard transitions and shielded cables.

Retrieval of σ relied on the closed-form expression of loss coefficient for the monomodal (TE_{10}) waveguide. It is worth noticing that the applied procedure gives us a rather stable value of conductivity for the realized CC composite, bounded between 3500 S/m and 4500 S/m.

From the physical point of view, the electromagnetic power impinging (P_{in}) onto the waveguide (WG) aperture gets partially reflected because of the mismatching, caused by geometrical imperfections of flanges, transitions and imperfections with respect to the nominal cross section dimensions. Injected power is attenuated proportionally to the longitudinal length D. Assuming a well tuned system, i.e., causing negligible signal reflection back to the source, and in virtue of the energy conservation, we can write the power balance for this simple problem as

$$P_{in}e^{-2\alpha L} = P_{in}\left|S_{21}\right|^2$$

(6.2.1.1)

which leads to a simple expression for the indirect estimation of the attenuation constant

$$\alpha(lin) = -\frac{1}{2L}Ln\left|S_{21}\right|^2 \quad \Rightarrow \quad \alpha\left(Np/m\right) = -\frac{1}{2L}\left|S_{21}\right|^2$$

(6.2.1.2)

where α is in Neper/m and L is the wall thickness, firstly assumed to be much more greater than the skin depth

$$\delta = \frac{1}{\sqrt{\pi f \mu_m \sigma}}$$

(6.2.1.3)

where f is the working frequency, μ_m the magnetic permeability of the coating material and σ its electrical conductivity. Condition (6.2.1.3) has the physical meaning of an injected power totally confined by the WG boundaries; hence there is no leakage due to field crossing among wall thickness. Actually, lossy-walled WG requires for more stringent conditions to assure the power bounding. It has been

turned out that an imperfect conductor of thickness d can be handled as a perfect conductor of thickness $d - \Delta r$, thus recessed of a quantity [11]

$$\Delta r = \frac{\delta \mu_m}{2\mu}$$

(6.2.1.4)

where μ is the filling medium permeability and μ_m is the conductor permeability. This physical shift is due to the surface impedance of the lossy material, which always has an inductive part to be added to the equivalent transmission line parameters. For a non-magnetic conductor, the recession is half the skin depth. We then argue that our method is valid under the assumption

$$L >> \Delta r = \frac{\delta}{2}$$

(6.2.1.5)

which serves to a fortiori estimation of the electrical conductivity.

Usually, this procedure being used with a medium filling the transverse section like the Nicholson-Ross method, the Baker-Jarvis method [11], the propagation constant method [12], and the reverberation chamber method [13], so as to obtain its dielectric parameters from the analysis of a relatively small sample.

Such a method makes the measurements critical for very good conductors –as expected for carbon-carbon composites [7] – because the strong sample reflection dramatically reduces the mismatching factor $1-|S_{11}|^2 \cong 0$, causing data processing troubles for numerical post-processing algorithms. Since we have an empty waveguide and the material to be studied is the bounding structure itself, we do not need S_{11} anymore, as noticeable in (6.2.4.1).

In this work, the waveguide is empty – i.e. vacuum filled – and the attenuation is given by the progressive dissipation of power through lossy (carbon-carbon) walls – i.e., exhibiting negligible mismatching factor. It is then straightforward to retrieve the surface resistance Rs from the attenuation constant, provided that WG operates in single TE_{10} mode regime. With this assumption and after a few algebraic arrangements of the closed-form expression for α [8, Eq. (8.18)], we get

$$Rs = \frac{\alpha\, b\, \eta \sqrt{1 - \frac{\lambda^2}{4a^2}}}{1 + \frac{b\lambda^2}{2a^3}}$$

(6.2.1.6)

where a and b are the short and long side lengths of WG respectively, η the free-space impedance and λ the free-space wavelength. Basically, (6.2.1.6) constitutes a semi-empirical estimation of Rs since only one of its parameters, α, is picked up from measurements and the whole expression refers to an ideal case, i.e., for frequencies far apart from cutoff and ideal boundary conditions.

This is not actually true in our framework as the wall losses result in a shifting of cutoff frequencies [14-15-16], closer to investigated (monomodal) band edges where the dispersion characteristics – in particular the attenuation – exhibit considerably non-flat response [8].

For a good conductor, the knowledge of Rs gives immediately electrical conductivity estimation of σ

$$\sigma = \frac{\omega\mu}{2Rs^2}$$

(6.2.1.7)

where $\mu=\mu_0\mu_r$ is the magnetic permeability of the material.

Taking into account that S_{11} is usually expressed in dB than the expression of Rs can be found equivalently as follows

$$\alpha(linear) = -\frac{1}{2D} Ln\left[\left(10^{\frac{S21}{20}}\right)^2\right]$$

(6.2.1.8)

For empty waveguide the Cutoff frequency is

$$f_{CutOff}(Hz) = \frac{1}{2a\sqrt{\mu_0 \varepsilon_0}}$$

(6.2.1.8)

Wave number is

$$BetaD = 2\pi f \sqrt{\mu_0 \varepsilon_0} \sqrt{1 - \left(\frac{f_{CurOff}}{f}\right)^2}$$

(6.2.1.9)

$$Rs_1 = \frac{\alpha \cdot BetaD \cdot b}{2\pi f \varepsilon_0} \quad \text{and} \quad Rs_2 = 1 + \left(\frac{2b}{a}\right)\left(\frac{f_{CutOff}}{f}\right)^2 \Rightarrow Rs = \frac{Rs_1}{Rs_2} = \frac{\alpha b \eta \sqrt{1 - \frac{\lambda^2}{4a^2}}}{1 + \frac{b\lambda^2}{2a^3}}$$

(6.2.1.10)

And as before, conductivity is:

$$\sigma = \frac{\omega \mu}{2Rs^2}$$

In Fig.(6.2.1.2), surface resistance and electrical conductivities of HP reference waveguide and CC waveguide materials are shown.

Computed electrical conductivity of HP reference WG is of the same magnitude order of pure aluminum, i.e., 3.7×10^7 (S/m), showing that such method is quite effective in determining electrical conductivity of materials.

Results for scattering parameters of Fig.(6.2.1.1), for S_{11} and S_{21} say that a CC waveguide structure is not efficient for communication purposes at ambient temperature because the injected signal get strongly reduced during its propagation.

Nevertheless, it could be employed aboard of satellites or aircrafts in deep space application, where extremely high temperatures lower down the electromagnetic losses – i.e. increasing the electrical conductivity in carbon based composites – while keeping excellent mechanical and thermodynamical properties. In the interpretation of obtained data we must underline that estimated values of conductivity represent a sort of average conductivity as it hides anisotropic behaviors. This is important for

C/C composites manufactured aligning relatively long filaments during processing, like continuous fiber and certain discontinuous fiber substrates, hence anisotropic properties arise [17]. Nearly isotropic composites can be achieved using short (discontinuous) carbon fibers combined with either a pyrolyzed carbon or pyrolyzed organic matrix [17].

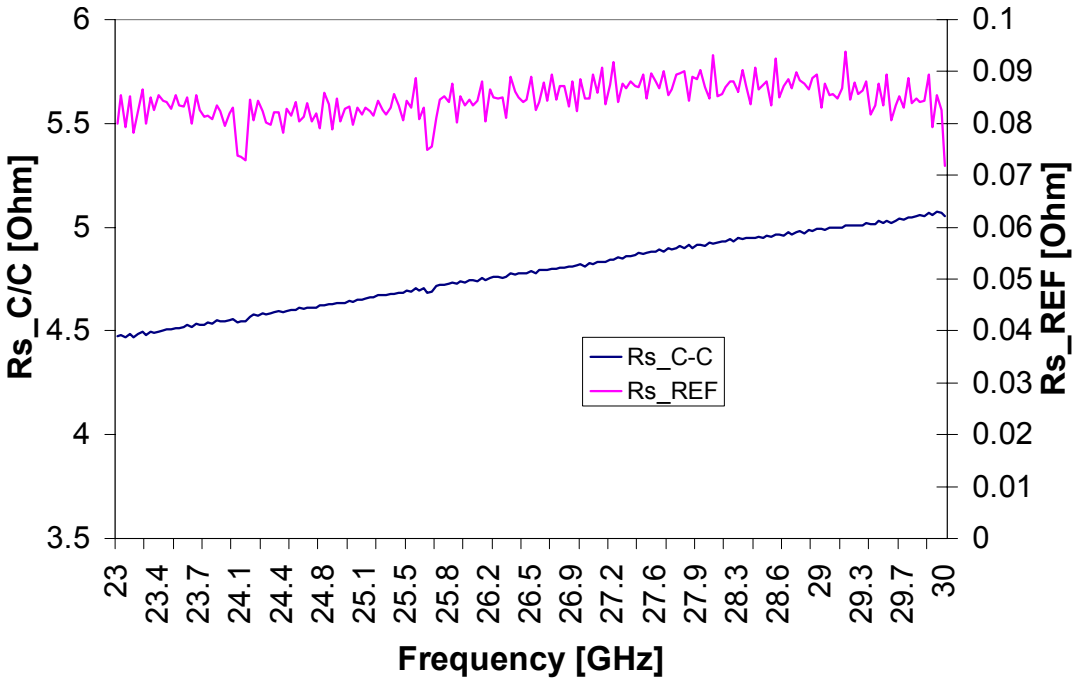

a)

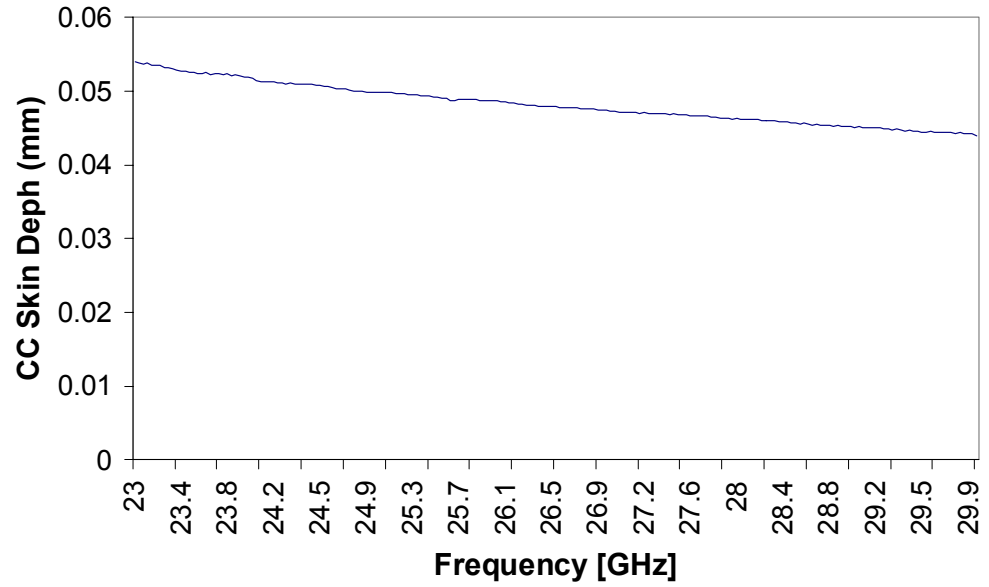

b)

Fig. (6.2.1.2). a) Surface resistance Rs of materials for reference WG and CC WG; b) skin-deph for CC WG material,

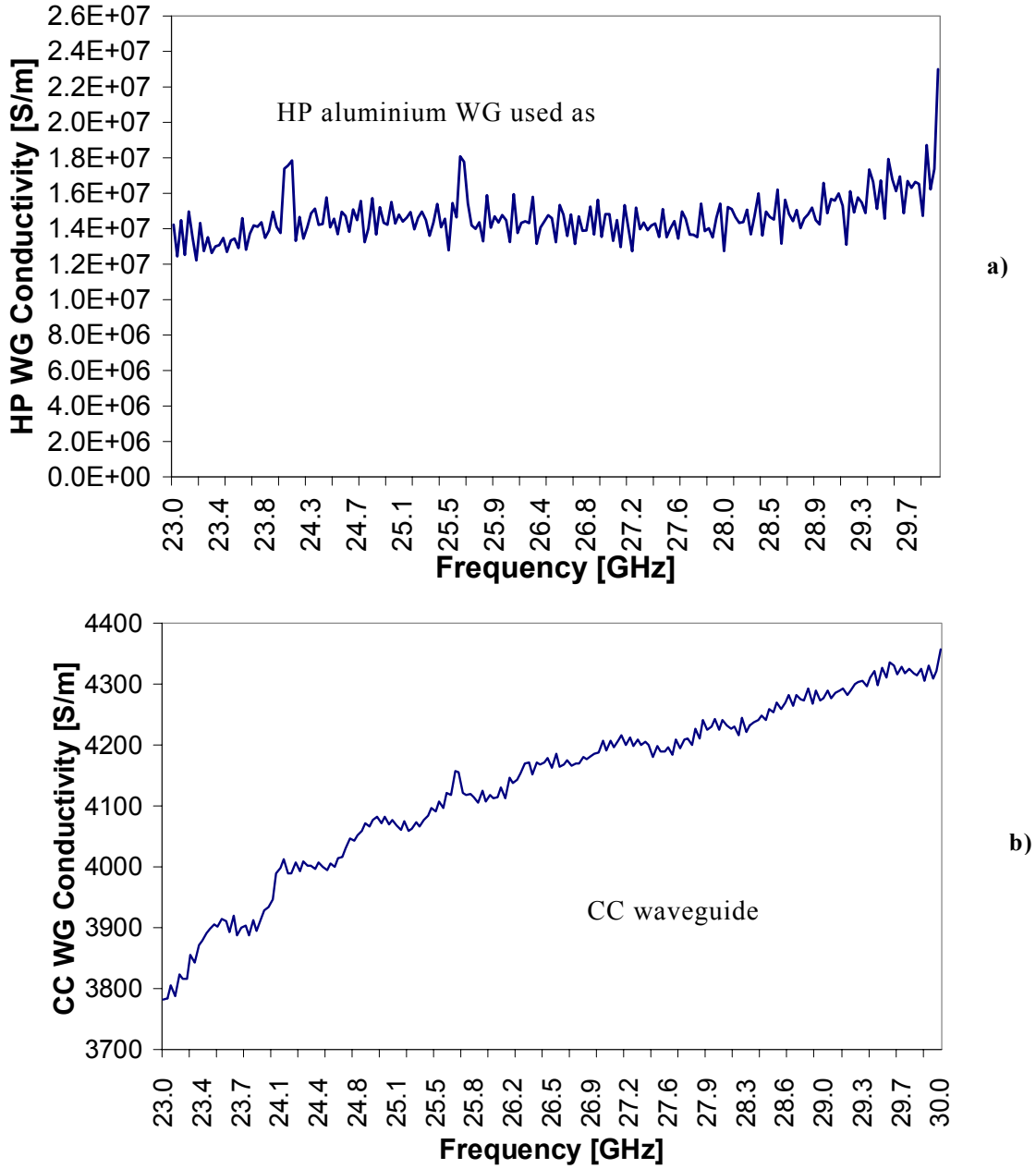

Fig. (6.2.1.2). a) Electrical conductivity of materials for HP reference WG; b) Electrical conductivity of materials for the employed CC composite WG in K-band.

As far as temperature dependence is concerned, in certain materials, when reducing Temperature to cryogenic regime, the conductivity gets strongly increased by superconductivity, while phonons density decreases ($\propto(kT)^3$) impacting the real part of permittivity. In general, the ballistic transport of electrons inside a material gets reduced by the increasing of atomic lattice defects, resulting in a lower electrical conductivity [20]. Amount of defects increases with the increasing temperature.

On the other hand, the subsequently increased thermal energy of carriers, promotes electrons in the conduction band, resulting in a higher electrical conductivity. Dominant mechanism establishes the slope sign of the curve modeling dependence of resistivity on temperature. A key parameter in quantifying this behavior is the temperature coefficient A, in $[C^{-1}]$. A negative A represents a decreasing resistivity with temperature, while a positive A represents an increasing resistivity with temperature. The former pertains to carbon, silicon and germanium; as a consequence we can suppose that an increase of working temperature can also increase the electrical conductivity of such CC material composite.

6.3 Conclusion

In this chapter, CC composite materials have been characterized in terms of microwave absorbing properties, electrical conductivity, skin-depth and surface resistivity. In particular in order to estimate electrical conductivity a new method (building a wave guide using material under test), has been proposed for materials analysis. This method is particularly useful when materials under test possess very higher electrical conductivity values with respect to dielectric materials. In such scenario conventional methods fail and dielectric permittivity and consequently electrical conductivity can not be evaluated. CC shows high microwave shielding effectiveness capability and low absorbing properties.
Measurements show a CC electrical conductivity around value of 4000 S/m which is three magnitude order greater than electrical conductivity of manufactured dielectric materials.

6.4 Reference Table

[1] G. Marsh, “Braving the heat,” *Aerosp. Compos. & Mater., vol. 1*, no. 4, pp. 28–32, Summer 1989.

[2] R. J. Diefendorf and E. Tokarsky, "High-performance carbon fibers," *Polymer Engineering & Science*, vol. 15, no. 3, pp. 150–159, March 1975.

[3] A. Taylor, "Fabrication and performance of advanced carbon-carbon piston structures," *Polymer Engineering & Science,* vol. NASA CP-3038, pp. 375–395, 1989.

[4] P. Sheehey, "LTV turbine rotor exceeds test objectives," *LTV News Release* M88-21, no. 23, August 1988.

[5] F. W. DeMario, "New world for aerospace composites," *Aerosp. America*, vol. 24, no. 42, pp. 36–40, October 1985.

[6] G. W. Labik, J. Bialek, T. K. Owens, R. Ritter, and M. Ulrickson, "TFTR carbon-carbon composite RF limiters," *Plasma Physics Lab., Princeton University*, pp. 125–128, 1987.

[7] X. Luo and D. D. L. Chung, "Electromagnetic interference shielding using continuous carbon-fiber carbon-matrix and polymer-matrix composites," *Composites Part B: Engineering*, vol. 30, no. 3, pp. 227–231,1999.

[8] S. Ramo, J. R. Whinnery, and T. V. Duzer, "Fields And Waves in Communication Electronics", *3rd ed. New York: John Wiley*, 1993.

[9] Gabriele Gradoni, Davide Micheli et.al, "Accurate electrical conductivity measurement of Carbon-Carbon material and composites". *Elsevier Editorial System(tm) for CARBON, 2010*

[10] D. M. Pozar, "Microwave Engineering, 3rd ed." New *York: John Wiley*,2005.

[11] P. I. Somlo, "Recession depth in metallic conductors at low frequencies," *Electronics Letters*, vol. 7, no. 26, pp. 776–777, 1971.

[12] J. Baker-Jarvis, J. E. Vanzura, and W. A. Kissick, "Improved technique for determining complex permittivity with the transmission/reflection method," *IEEE Transactions on Microwave Theory and Techniques,* vol. 38, no. 8, pp. 1096–1103, August 1990.

[13] M. Janezic and J. Jargon, "Complex permittivity determination from propagation constant measurements," *IEEE Microwave and Guided Wage Letters*, vol. 9, no. 2, pp. 76–78, February 1999.

[14] P. Hallbjorner, U. Carlberg, K. Madsen, and J. Andersson, "Extracting electrical material parameters of electrically large dielectric object from reverberation chamber

measurements of absorbing cross section," *IEEE Transactions on Electromagnetic Compatibility*, vol. 47, no. 2, pp. 291–303, May 2005.

[15] P. I. Somlo and J. D. Hunter, "Microwave impedance measurement, 3rd ed." *University of California: P. Peregrinus Ltd & IEE*, 2008.

[16] D. Micheli, C. Apollo, R. Pastore, and M. Marchetti, "X-band microwave characterization of carbon-based nanocomposite material, absorbing capability comparison and ras design simulation," *Composite Science and Technology*, vol. 70, no. 2, pp. 400–409, Feb 2010.

[17] J. D. Buckley and D. D. Edie, "Carbon-Carbon materials and composites, 1st ed." *Park Ridge, New Jersey, U.S.A.: Noyes Publications*, 1993.

[18] P. I. Somlo and J. D. Hunter, "On the te10-mode cutoff frequency in lossy-walled rectangular waveguides," *IEEE Transactions on Instrumentation and measurement*, vol. 45, no. 1, pp. 301–304, 1996.

[19] G. Yassin, I. Barboy, V. Dikovsky, M. Kambara, D. A. Cardwell, S. Withington, and G. Jung, "Microwave transmission through high temperature superconducting waveguides," *Physica C,* vol. 372, no. 1, pp. 523–525, 2002.

[20] Y. Quere, Physics of materials, 2nd ed. CRC Press, 1998.